Electrochemical Microfluidics in Biosensing Applications



Shaoyu Kang

Hertford College

University of Oxford

A thesis submitted for the degree of

Doctor of Philosophy

Michaelmas 2024

Faith creates great possibilities, transforming imagination into reality;

Diligence brings great achievements, turning effort into success.

Abstract

Protein biomarkers — serving as essential indicators of various biological processes, disease states, and therapeutic responses — are clinically prominent, providing valuable insights into disease progression, diagnosis and treatment monitoring. To quantify these, electrochemical biosensors offer a highly sensitive, cost-effective, and scalable platform by converting biomolecular recognition into measurable electrical signals on immunoprotein-modified electrode interfaces. Their robust assaying, however, is typically hindered by undesired biofouling, inefficient target recruitment, and slow assay turnaround times, as detailed in Chapter **1**. To address these challenges, microfluidic techniques has been integrated to streamline sample preparation, significantly improving overall assay efficiency. This integration reduces processing time, minimises reagent consumption, reduces handling errors, and facilitates high-throughput analysis. Additionally, forced convective mass transport within microfluidic channel accelerates the delivery of target analytes to the surface-bound bioreceptors while reducing nonspecific interactions, thereby increasing assay selectivity and minimising background. Exemplified by the quantification of the inflammation indicator C-reactive protein (CRP) and the cancer-relevant immunoprotein anti-p53 antibody, herein:

In Chapter **2**, building on a well-established bio-receptive polyaniline (PANI) interface, the potential of a microfluidic-integrated capacitive biosensor was explored, introducing a facile assessment of binding kinetics as a means of quantifying CRP concentration in real-time, reagentless, and label-free. By monitoring the temporal change in the capacitive fingerprint C_r of PANI films, this novel approach enables the sensitive assaying of picomolar biomarker concentration, with shorter sample-to-result time in just 15 seconds rather than over tens of minutes. Such integration provides a streamlined,

efficient, and highly sensitive platform for rapid biomarker quantification, greatly enhancing assay turnaround efficiency for real-world applications.

Based on the microfluidic configuration developed earlier, Chapter **3** introduced a novel strategy for boosting both assay sensitivity and target selectivity by leveraging microfluidic confinement. By reducing channel height to just a few micrometres, an enhanced and steady-state analyte flux generated, facilitating rapid and substantial accumulation of specific targets at the antibody-modified PANI films. As this enhancement particularly favours recognition with high binding affinity, *i.e.*, specific binding, a notable 2000% increase in sensitivity and a 300% improvement in target selectivity were observed in a manner that is streamlined, broadly applicable and COMSOL validated. Such facile strategy supported the robust assaying of CRP in serum-spiked samples on unprotected electrodes, without the need for pretreatment or blocking.

To address the issue of inefficient target recruitment resulting from limited epitope surface density on two-dimensional electrode interfaces and sluggish planar diffusion, Chapter **4** details the use of antigen-mimicking, dual-modified iron oxide nanoparticles (IONPs), combined with an alternating current (AC) magnetic field-promoted sample mixing, to specifically and efficiently recruit anti-p53 antibodies from serum under continuous flow. The tuneable surface loading and high sequence specificity of these particle-bound antigenic peptide significantly improved target recruitment efficiency, surpassing that of the full antigen under equivalent conditions by 400%. Once captured targets were pulled down to a lectin-modified screen-printed electrode, the HRP-mediated SWV response supported robustly assaying of sub-femtomolar levels of cancer-relevant antibodies in serum-spiked samples within minutes, with potential for clinical translation.

Declaration

The work presented in this thesis, titled "*Electrochemical Microfluidics in Biosensing Applications*" was conducted between Michaelmas Term 2020 and Michaelmas Term 2024 at the Department of Chemistry, University of Oxford, under the supervision of Professor Jason J. Davis. I declare that this thesis and the research presented herein, except where otherwise stated, are my own and have not been submitted previously for any other degree at this or any other university.

The following experiments were performed in collaboration:

- Atomic force microscopy (AFM) imaging of polyaniline (PANI) films was conducted by Dr. Xuanxiao Chen at the University of Oxford.
- Hydrothermal synthesis of iron oxide nanoparticles (IONPs) and the corresponding characterisations, including transmission electron microscopy (TEM), powder X-ray diffraction (PXRD), and hysteresis measurements, were performed by Dr. Daohe Yuan at the University of Oxford.

Shaoyu Kang

Oct 2024

Acknowledgements

First and foremost, I wish to express my deepest gratitude to my supervisor, Professor Jason J. Davis, for his invaluable guidance, endless encouragement, constant support throughout the course of my DPhil. His expertise and insightful feedback have been instrumental in shaping both my research and my academic growth. I am deeply appreciative of his mentorship and the opportunities he has provided.

I would also like to extend my thanks to the members of my research group: Xuanxiao, Daohe Yuan, Mohamed, Robert, Sue, Tara, Simon, and Zhen, for their effective collaboration, insightful discussions, and great assistance throughout the course of my project. Their support made the challenging days in Oxford more manageable and enjoyable.

Special thanks go to the staffs at Hertford College for their support, especially during the challenges of the pandemic, and for the delicious food served at Formal Hall, which brought moments of joy during even the most demanding days.

Finally, I am also grateful to my family and friends for their unwavering encouragement, patience, and understanding throughout this journey. To my parents, for their unconditional love and financial support, and to my friends, thank you for always being there.

Table of Contents

Chapter 1 INTRODUCTION

1.1 Biomarker and Biosensing 1

1.1.1 Protein biomarkers: structure, specific binding, and types 2

1.1.2 Examples of protein biomarkers studied in this thesis 6

1.1.3 Biosensor: types and performance evaluation 12

1.2 Electrochemical Biosensing: Fundamentals, Types, and Challenges 20

1.2.1 Concepts of electrochemistry 20

1.2.2 Electrochemical biosensors: types and challenges 28

1.3 Microfluidics and Biosensing 33

1.3.1 Concepts of microfluidics 33

1.3.2 Microfluidics in biosensing 39

1.4 Magnetic Nanoparticles and Downstream Analysis 42

1.4.1 Magnetic banoparticles: source of magnetism, structure, and synthesis ..42

1.4.2 Nanoparticle-assisted biomarker enrichment and downstream analysis ..50

1.5 Integration of Microfluidics and Electrochemical Biosensors: New Avenues Towards High-Speed and High-Sensitivity Biosensing Platforms 53

1.6 References 56

Chapter 2 ULTRAFAST BIOMARKER QUANTIFICATION THROUGH REAGENTLESS CAPACITIVE KINETICS

2.1 Background 69

2.2 Bioreceptive Polyaniline Preparation 71

2.2.1 Electrochemical Deposition of PANI 71

2.2.2 Integration of Antibodies 74

2.3 Real-Time Monitoring of Target Binding Kinetics 77

2.4 Ultrafast Biomarker Quantification 81

2.4.1 Theoretical Consideration 82

2.4.2 Ultrafast Biomarker Quantification through Reagentless Capacitive Kinetics 86

2.5 Conclusion and Future Outlook 90

2.6 References 92

Chapter 3 LEVERAGING MICROFLUIDIC CONFINEMENT IN BOOSTING ASSAY SENSITIVITY AND SELECTIVITY

3.1 Background 95

3.2 Microfluidic Confinement in Boosting Assay Sensitivity 98

3.2.1 Enhanced Analyte Flux Within Microfluidic Confinement 98

3.2.2 Boosted Assay Sensitivity Within Microfluidic Confinement 102

3.3 Enhanced Target Selectivity Inside a Confined Channel 105

3.4 Mechanistic Insights into Microfluidic Confinement: Theoretical Framework and COMSOL Simulation 109

3.4.1 Theoretical Consideration 109

3.4.2 COMSOL Simulation 114

3.5 Conclusion and Future Outlook 120

3.6 References 122

Chapter 4 ANTIGEN-MIMIC NANOPARTICLES IN ULTRASENSITIVE ON-CHIP INTEGRATED ANTI-P53 ANTIBODY QUANTIFICATION

4.1 Background 125

4.2 DO-1 Antibody Recruitment: Peptide Sequence Selection and Binding Performance Assessment 128

4.2.1 Antigen-mimicking p53 Peptide: SPR Study 128

4.2.2 Generation of a Sandwich Structure: Concanavalin A 129

4.2.3 TMB-HRP Catalysis in High-throughput SPCE Array 131

4.3 Preparation of Antigen-Mimic Dual-Functionalised Iron Oxide Nanoparticles 135

4.3.1 Hydrothermal Synthesis of IONPs 135

4.3.2 Integration with p53 Epitope and HRP: Dual-Functionalised IONPs Preparation 138

4.4 AC Magnetic Field-Assisted Immunocapture and Amplified Electrochemical p53 Antibody Quantification 142

4.4.1 AC Magnetic Field-Assisted Magnetic Separation for Enhanced Biomarker Recruitment 142

4.4.2 Amplified Electrochemical p53 Antibody Quantification 146

4.5 Conclusion and Future Outlook 149

4.6 References 151

Chapter 5 CONCLUSION AND FUTURE OUTLOOK 155

Chapter 6 EXPERIMENTAL MATERIALS AND METHODS

6.1 General Materials and Methodology 159

6.2 General Characterisations 160

6.2.1 Surface Plasmon Resonance (SPR) 160

6.2.2 Attenuated Total Reflection Fourier Transform Infrared Spectroscopy (ATR-FTIR) 161

6.2.3 Dynamic Light Scattering (DLS) and Zeta Potential Measurements 161

6.2.4 Water Contact Angle Measurements (CAM) 162

6.3 General Protocols for Electrochemical Studies 163

6.3.1 Theory of Several Key Techniques in Electrochemistry 163

6.3.2 General Protocols for CV and SWV Measurements 180

6.3.3 General Protocols for EIS and ECS Measurements 181

6.4 Experimental Protocols for Ultrafast Biomarker Quantification Studies 182

6.4.1 Materials and Instruments 182

6.4.2 Bioreceptive Interface Preparation 183

6.4.3 Continuous Flow Assays and Data Analysis 183

6.5 Experimental Protocols for Microfluidic Confinement Studies 185

6.5.1 Materials and Instruments 185

6.5.2 Boosted Assay Sensitivity and Enhanced Target Selectivity Within Microfluidic Confinement 185
6.5.3 Surface Coverage and Binding Affinity Impact on Temporal Selectivity Enhancement 186
6.5.4 COMSOL Simulation 187

6.6 Experimental Protocols for on-Chip Integrated Anti-p53 Quantification Studies 189
6.6.1 Materials and Instruments 189
6.6.2 Preparation of Antigen-Mimicking Dual-Functionalized IONPs 190
6.6.3 Micro-BCA Assay for p53 Peptide Surface Coverage Determination ... 191
6.6.4 ABTS Assay for HRP Surface Coverage Quantification 192
6.6.5 Nanoparticle-Assisted Immunoisolation 192
6.6.6 Electrochemical Enzyme-Amplified Assay 193

6.7 References 194

List of Abbreviations

Ab	Antibody
ABTS	2,2'-azino-bis(3-ethylbenzothiazoline-6-sulfonic acid)
AC	Alternating current
Ag	Antigen
AFM	Atomic force microscopy
Asn	Asparagine
Asp	Aspartic acid
AUC	The area under the ROC curve
ATR-FTIR	Attenuated total reflection Fourier transform infrared spectroscopy
BCA	Bicinchoninic acid assay
BSA	Bovine serum albumin
CA	Chronoamperometry
CAM	Contact angle measurement
Con A	Concanavalin A
CP	Chronopotentiometry
C_{dl}	Double layer capacitance
C_r	Redox capacitance
CRP	C-reactive protein
CTAB	Cetyltrimethylammonium bromide
CTCs	Circulating tumor cells
CV	Cyclic voltammetry
Cys	Cysteine

DBD	DNA-binding domain
DLS	Dynamic light scattering
DN	Dominant negative effect
ECS	Electrochemical capacitance spectroscopy
EDC	1-ethyl-3-(3-dimethylaminopropyl)carbodiimide
EIS	Electrochemical impedance spectroscopy
ELISA	Enzyme-linked immunosorbent assays
Fc	Fragment crystallizable region
FT-IR	Fourier-transform infrared spectroscopy
Gln	Glutamine
Glu	Glutamic acid
Gly	Glycine
GOF	Gain-of-function
HRP	Horseradish peroxidase
HSA	Human serum albumin
hs-CRP	High-sensitivity CRP assays
IgG	Immunoglobulin G
IHP	Inner Helmholtz layer
IL-6	Interleukin-6
Ile	Isoleucine
IONPs	Iron oxide nanoparticles
Leu	Leucine
LoC	Lab-on-a-Chip
LoD	Limit of detection

LoQ	Limit of quantification
Lys	Lysine
MAC	AC magnetic field-assisted
MDM2	Mouse double minute 2 homolog
MES	2-(N-morpholino)ethanesulfonic acid
MRI	Magnetic resonance imaging
MTL	Mass transport limited
NHS	N-Hydroxysuccinimide
NLS	Nuclear localisation signalling domain
OCP	Open-circuit potential
OHP	Outer Helmholtz plane
PANI	Polyaniline
PBS	Phosphate buffered saline
PBS-T	Phosphate buffered saline with Tween detergent
PCC	Pearson correlation coefficient
PCh	Phosphocholine
PDI	Polydispersity index
Phe	Phenylalanine
PRD	Proline-rich domain
Pro	Proline
PVP	Polyvinylpyrrolidone
PXRD	Powder X-ray diffraction
PZC	Potential of zero charge
QCM	Quartz crystal microbalance

RDE	Rotating disk electrode
R_e	Reynolds number
RE	Reference electrode
R_{ct}	Charge transfer resistance
ROC	Receiver operating characteristic
SDS	Sodium dodecyl sulfate
Ser	Serine
SHE	Standard hydrogen electrode
S/N	Signal-to-noise ratio
SPR	Surface plasmon resonance
SWV	Square-wave voltammetry
TAD	Transactivation domain
TEM	Transmission electron microscopy
TD	Tetramerisation domain
Thr	Threonine
TMB	3,3',5,5'-Tetramethylbenzidine
Trp	Tryptophan
WE	Working electrode
Val	Valine

Chapter 1

Introduction

1.1 BIOMAKRER AND BIOSENSING

Biomarkers are biomolecular indicators that reflect a wide range of biological processes,[1-4] pathogen exposures,[5, 6] pharmacological and therapeutic intervention responses.[7] These indicators can be classified by their structures into categories such as proteins,[8, 9] nucleic acids,[10] lipids,[11] metabolites,[12] and cells.[13] Their structures are intrinsically linked to functionality, influencing their specific clinical applications and significance. For example, protein-based biomarkers, such as prostate-specific antigen,[14] may reflect the presence of prostate cancer, while nucleic acid biomarkers (*e.g.*, BRCA1/BRCA2 gene mutations)[15, 16] indicate the potential for cancer development. Protein biomarkers, compared with other counterparts, are abundantly present in patient samples,[17, 18] easily accessible for measurement,[19] and highly relevant in reflecting real-time biological processes and disease states.[20] These features make protein biomarkers particularly valuable in diagnostics, offering advantages over other types of biomarkers.

The accurate quantification of protein biomarkers holds a pivotal role in clinical practice, enabling early disease detection, facilitating timely intervention, and providing continuous monitoring throughout the course of treatment, which allows for the optimisation of therapeutic strategies.[21] To translate the presence and concentration of these disease-related biomarkers into measurable signals, biosensing technologies are developed.[22, 23] In this section, the critical aspects of biomarkers and biosensing will be explored, starting with an overview of protein biomarker structure and several specific examples studied in this thesis. It will then outline the concept of specific biorecognition and its foundational role in developing biosensing assays. Following this, a brief introduction to the categories and history of biosensors will be provided, concluding with the criteria used to evaluate biosensor performance.

1.1.1 Protein Biomarkers: Structure, Specific Binding, and Types

Serving as the building blocks and primary executors of cellular functions and biological processes,[24-26] protein molecules, also known as polypeptides, are long, unbranched chains composed of amino acids. Synthesised in ribosomes via the process of translation,[24, 26] proteins play crucial roles in biological activity. For example, they act as enzymes to promote specific biochemical reactions,[27-29] serve as structural components to provide mechanical support to cells,[30, 31] and function as transporters to carry substances across membranes.[32, 33] Understanding the structural characteristics, structure-activity relationships, and categorisation of protein biomarkers is fundamental for their applications in clinical diagnostics and therapeutic monitoring. In this section, the structural organisation of proteins, their functions, particularly their specific binding mechanisms, will be outlined.

1.1.1.1 Protein Organisation at Four Structural Levels

Proteins are typically organised into four structural levels: primary, secondary, tertiary, and quaternary,[25, 26, 34] as shown in Figure **1.1**. These complex molecules are shaped by a range of covalent and non-covalent interactions across four hierarchical levels. At the primary level, amino acids are linked by peptide bonds to form a polypeptide chain,[33] while side chains impart distinct properties, such as hydrophilicity, acidity, and polarity.[35-37] The secondary structure involves stable conformations, including α helices or β sheets, which are stabilised by hydrogen bonds and hydrophobic interactions.[26, 38-40]

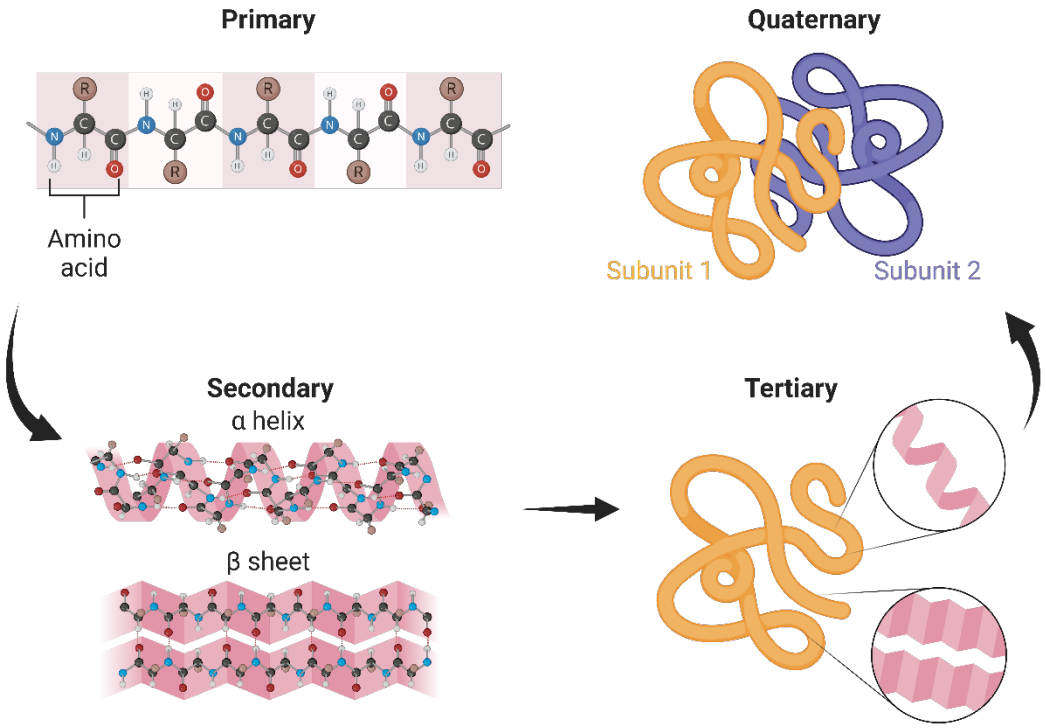


Figure 1.1. Schematic depiction of the four structural levels in proteins.[26] The primary structure is the linear sequence of amino acids in a polypeptide chain. The secondary structure involves the arrangement of adjacent segments into motifs, such as the α-helix and β sheets. The tertiary structure represents the overall three-dimensional configuration of a single polypeptide chain. The quaternary structure depicts the assembly of multiple polypeptide subunits into a functional protein complex.

Non-covalent interactions (*e.g.*, hydrogen bonds, electrostatic attractions, van der Waals attractions, and the hydrophobic effect) and covalent bonds (*e.g.*, disulfide bonds)[26] in the tertiary and quaternary structures are critical for maintaining the stability, solubility, flexibility, and biological activity of proteins.[41, 42] Understanding the protein structural organisation is fundamental to elucidating protein behaviour, predicting their functions, and advancing various biotechnological and medical applications.

1.1.1.2 Protein Binding Specificity: Structural and Functional Insights

To achieve their biological properties, proteins (*e.g.*, enzymes,[27] antibodies,[43] and receptors)[44] need to specifically interact, or bind, to other molecules.[26, 45] This means that each protein can only bind to just one or several structurally similar molecules,[26, 46] referred to as ligands or targets. The specificity of this interaction results from the precisely defined binding sites and the array of non-covalent interactions that form between their matching surface.[24, 41, 46]

When protein fold in solution, buried hydrophobic residues form surface cavities that serve as binding sites,[24, 47] precisely shaped to ensure specific ligand binding. Additionally, this binding is also energetically strong. Since individual non-covalent interaction is relatively weak (*e.g.*, bond energies of O-H homolytic cleavage $E_{\text{O-H}} = 459\ \text{kJ} \cdot \text{mol}^{-1}$ *vs.* hydrogen bond $E_{\text{O-H}\cdots\text{O}} = 21\ \text{kJ} \cdot \text{mol}^{-1}$),[48, 49] poorly matching and insufficient interactions result in weak and short-lived non-specific binding.[50] In contrast, specific binding is strong and persistent,[51] as many non-covalent bonds can generate simultaneously.[47]

To evaluate the strength and the affinity of protein binding, the association constant (K_a) and its reciprocal, the dissociation constant (K_d), are introduced, as shown in *eqn.* **1.1**, where c_{eq} denotes the equilibrium concentration of each species.

$$Protein + Ligand \underset{K_d}{\overset{K_a}{\rightleftarrows}} Complex$$

$$K_a = \frac{c_{eq,Complex}}{c_{eq,Protein} \cdot c_{eq,Ligand}};\ K_d = \frac{1}{K_a} = \frac{c_{eq,Protein} \cdot c_{eq,Ligand}}{c_{eq,Complex}} \qquad (1.1)$$

Equilibrium constants (K) are closely linked to free-energy changes (ΔG°),[52] as shown in *eqn.* **1.2**, where R is the gas constant with a value of $8.314\ \mathrm{J \cdot mol^{-1} \cdot K^{-1}}$ and T is the temperature in Kelvin.

$$\Delta G^{\circ} = -RT \ln K \tag{1.2}$$

A large K_a and a small K_d indicate the great a high affinity between the protein and its ligand,[52] signifying that the binding interaction is energetically favourable. Specific binding, characterised by high affinity, typically has nM to pM K_d,[51, 53] while non-specific interactions generally exhibit K_d values in the micromolar range or higher,[51, 54, 55] reflecting weak binding.

Specific binding enables proteins to perform diverse functions.[26] For instance, Immunoglobulins, or antibodies, are Y-shaped proteins produced by B cells in response to foreign pathogens,[56] with their general structure shown in Figure **1.2**. The hypervariable loops on antibodies form antigen-binding sites,[43, 57] which are highly specific to particular antigens. This selective binding is crucial in many biosensing assays,[58-60] as antibodies are employed to sensitively and specifically recruit antigens. However, antibodies can occasionally bind to another antigen that share structural similarities rather than the antigen of interest, a phenomenon known as cross-reactivity.[61] Cross-reactivity may compromise assay specificity, resulting in false-positive signals and reduced assay accuracy.

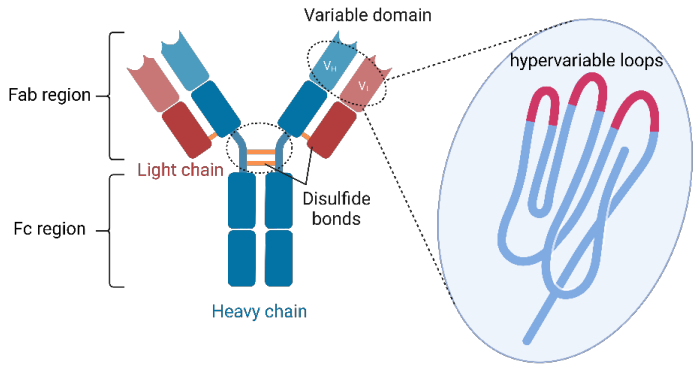


Figure 1.2. Schematic representation of an antibody structure.[26, 57] The antibody consists of two heavy chains (blue) and two light chains (red), connected by disulfide bonds. The variable domains, comprising the variable regions of the heavy (V_H) and light (V_L) chains, contain hypervariable loops responsible for antigen binding.

1.1.2 Examples of Protein Biomarkers Studied in This Thesis

Serving as indicators of physiological and pathological states, protein biomarkers are crucial in medical diagnostics and therapeutic monitoring. Building on the discussion of protein structural organisation in the previous section, herein, two specific protein biomarkers will be examined: C-reactive protein and p53 protein, due to their significant roles in inflammation and cancer, respectively.

1.1.2.1 Inflammation Indicator: C-Reactive Protein

C-reactive protein (CRP) is a widely recognised biomarker for inflammation, extensively used in diagnostics to assess inflammatory states and infections.[8, 62, 63] The name "C-reactive protein" originates from its initial identification in the 1930s by Tillett and

Francis,[64] who discovered that this substance is reactive to the C-polysaccharide of Streptococcus pneumoniae, leading to the formation of a precipitate.[63]

Structurally, CRP belongs to the pentraxin protein family composed of five identical subunits,[65, 66] each approximately 23 kDa in size and 3.6 nm in diameter, as shown in Figure **1.3**. Each subunit, consisting of 206 amino acids, forms a structure characterised by two antiparallel β-sheets with a jellyroll topology,[67] accompanied by an α-helix (residues 168-176). These subunits are held together by salt bridges and hydrogen bonds formed between residues 115-123 of one subunit and residues 40-42 and 197-202 of the adjacent subunit.[65] CRP features multiple binding sites essential for its role in the immune system and pathogen detection, including those for phosphocholine (PCh),[68] calcium ions,[65] and Fc receptors.[69] The PCh-binding sites allow CRP to attach to phosphocholine on the surfaces of dead cells and certain bacteria (*e.g.*, C-polysaccharide of Streptococcus pneumoniae),[68] thereby marking pathogens and damaged cells for phagocytosis. These binding sites are located within clefts formed by β-sheets, specifically involving residues Phe66, Leu64, and Thr76.[65, 67] The binding between CRP and PCh is calcium-dependent,[68] facilitated by two calcium ions coordinating with aspartic and glutamic acid residues. It is also suggested that several monoclonal anti-CRP antibodies recognised the PCh-binding sites.[70] Additionally, CRP can specifically bind to Fc receptors on immune cells and activate the complement system.[69, 71] Sequence homology between CRP (residues 175-185) and the immunoglobulin G (IgG) binding region suggests the functional similarities in modulating immune responses,[69, 72] highlighting its potential in therapeutic and diagnostic applications.

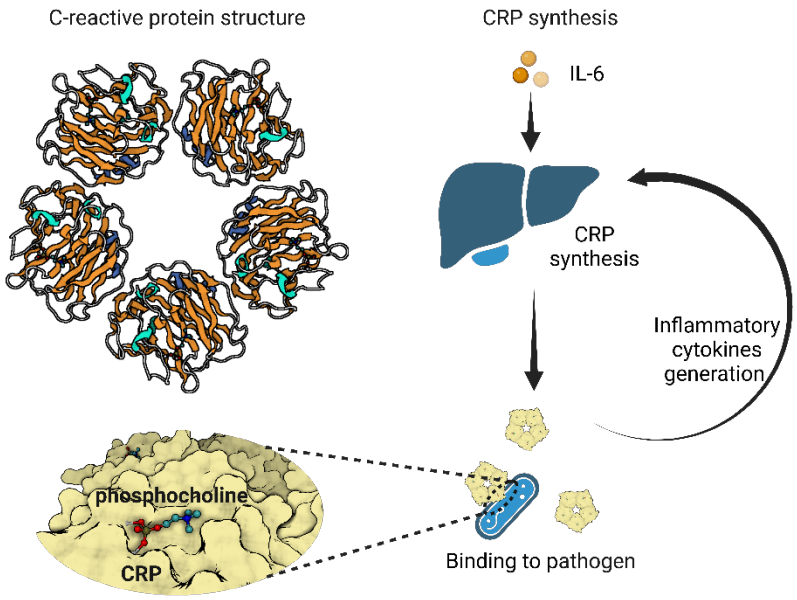


Figure 1.3. Schematic illustration of C-reactive protein structure and synthesis.[62, 63] consists of five identical subunits arranged in a pentameric structure. This pentraxin protein is synthesised in the liver in response to inflammatory cytokines. Upon release into the plasma, CRP binds to phosphocholine on the surface of pathogens, marking them for destruction.

The synthesis of this acute-phase protein, produced in the liver,[65] is primarily triggered by pro-inflammatory cytokines,[62] especially interleukin-6 (IL-6),[73, 74] which are released by immune cells (*e.g.*, T cells) in response to inflammation. Once synthesised and released into the bloodstream, CRP can bind to phosphocholine on the surfaces of pathogens and damaged cells.[68] These bound CRP proteins interact with Fc receptors on immune cells, promoting phagocytosis and the destruction of marked pathogens or apoptotic cells.[75] Meanwhile, the interaction between CRP and Fc receptors stimulates the production of pro-inflammatory cytokines further amplifying the immune response.[74] This amplification results in a dramatical increase in CRP concentration within hours of the onset of inflammation. In healthy adults, serum CRP concentration typically range from 0.8 $\mu g \cdot mL^{-1}$ to 3.0 $\mu g \cdot mL^{-1}$.[73] However, during acute inflammation, plasma CRP levels increase up to 1000-fold,[73] reaching as high as 500 $\mu g \cdot mL^{-1}$ in extreme cases.

This substantial rise makes CRP a valuable biomarker for bacterial infections, autoimmune disorders, tissue injuries and cardiovascular diseases.[8, 69, 73]

CRP levels are typically measured using nephelometric assays and high-sensitivity CRP (hs-CRP) assays.[76-78] Nephelometric assays involve measuring the intensity of scattered light after mixing antibodies with serum or plasma samples,[79] providing rapid turnaround and quick results. However, their sensitivity can be limited when biomarker concentrations are below 0.1 $\mu g \cdot mL^{-1}$.[80] To address this limitation, hs-CRP assays were developed, offering greater sensitivity through methods such as enzyme-linked immunosorbent assays (ELISA),[81] immunoturbidimetric methods,[82] and fluorescence-based assays.[83] Despite their advantages, may not always be suitable for point-of-care (PoC) testing due to the need for bulky instruments and specialized training. Developing alternative methods that are more accessible, while maintaining high sensitivity, is essential for real-world applications.[59]

1.1.2.2 The Guardian of the Genome: p53 Protein

Cancer is the uncontrolled proliferation and spread of abnormal cells, leading to tumour formation and the invasion of surrounding tissues and organs.[84, 85] As a leading cause to global mortality,[86] it was responsible for about one-sixth of all fatalities in 2020. This resulted in approximately 10 million deaths, a number projected to rise to 27 million annually over the next decade.[87] In this context, early detection is critical to improve patient outcomes. Cancer biomarkers encompass a diverse range of categories including gene mutations,[10, 16, 88] proteins,[14, 89] circulating tumour cells,[13] extracellular vesicles,[90, 91] and metabolites.[92, 93] Among these biomarkers, p53 proteins, encoded by the TP53 gene,[94]

has gained prominence due to their role in preventing cell proliferation and maintaining genomic stability.[95, 96]

Structurally, p53 is a 393-amino acid protein with a molecular weight of 43.7 kDa.[97] A protein domain is a distinct structural and functional unit within a protein.[26] As shown in Figure **1.4**, p53 consists of seven main domains,[98, 99] including two transactivation domains at the N-terminus (TAD1, residues 1-42; TAD2, residues 43-63), a proline-rich domain (PRD, residues 64-92), a central DNA-binding domain (DBD, residues 102-292), nuclear localisation signalling domain (NLS, residues 316-325), a tetramerisation domain (TD, residues 325-355) and a C-terminal regulatory domain (residues 363-393). These domains together enable p53 to effectively regulate gene expression and maintain genomic integrity. For example, under normal conditions, p53 is maintained at low levels due to its interaction with the MDM2 protein,[95, 100] which targets p53 for degradation. Upon cellular stress or DNA damage, inhibition of MDM2 and post-translational modifications (*e.g.*, phosphorylation and acetylation)[96] activate p53, allowing it to accumulate in the nucleus,[101] facilitated by the NLS domain. Once in the nucleus, the DBD recognises and binds to specific DNA sequences, with binding affinity and specificity enhanced by the TD forming a tetramer.[102] Upon binding to DNA, the TAD initiate the transcription of genes involved in cell cycle arrest and DNA repair.[103] If DNA damage is irreparable, p53 promotes apoptosis, a process facilitated by the PRD. The overall activity, stability, and interactions of p53 with other proteins are fine-tuned by the C-terminal regulatory domain through further post-translational modifications.[104] Through these mechanisms, p53 maintains genomic integrity and prevents tumour development.

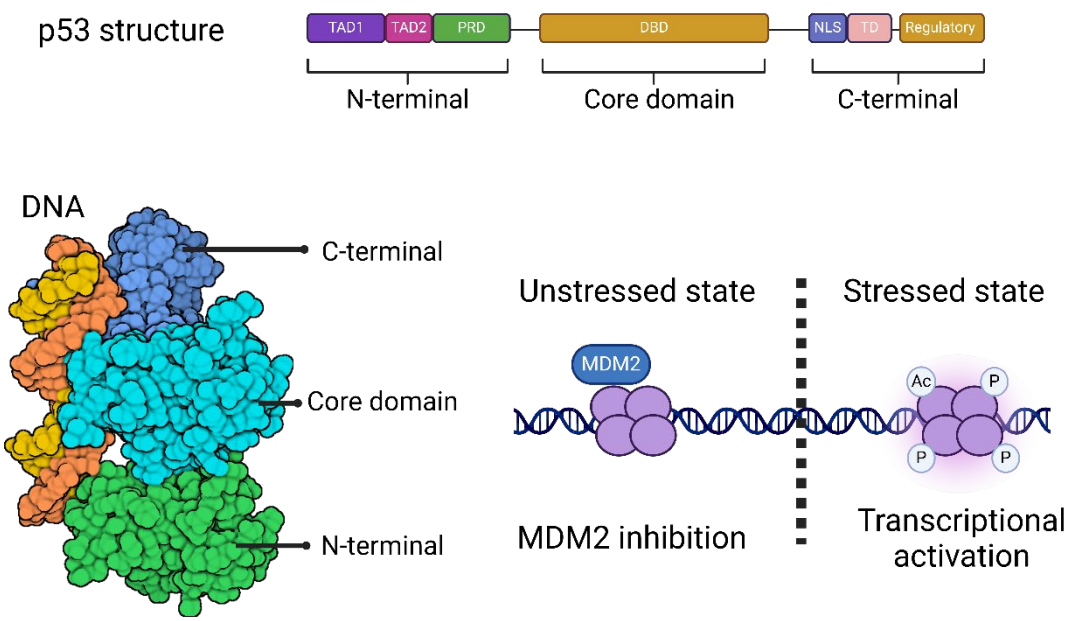


Figure 1.4. p53 protein structure and its regulation mechanism.[95, 97] The p53 protein is composed of several domains, broadly categorised into the N-terminal, core domain, and C-terminal regions. Under normal conditions, p53 activity is regulated by MDM2, which targets it for degradation. Upon cellular stress, inhibition of MDM2 and post-translational modifications activate the p53 protein. This activation initiates the transcription of genes involved in cell cycle arrest and DNA repair, thereby maintaining genomic integrity.

However, in more than 50% of human cancers,[95] mutations in the TP53 gene result in aberrant p53 proteins that are unable to effectively bind to DNA (*i.e.*, DBD mutations)[105] or interact with other regulatory proteins, leading to the accumulation of dysfunctional p53.[95] This makes p53 protein a valuable biomarker for early cancer detection. For instance, patients with gastrointestinal cancer have been found to have serum p53 concentrations more than 300% higher than those of healthy controls,[106] while patients with lung cancer show increases greater than 200%.[107] Additionally, some mutant forms exhibit dominant negative (DN) effects and gain-of-function (GOF) properties,[102, 108] inhibiting the activity of normal p53 and other tumour suppressors, thereby further promoting tumour growth and metastasis. Robust assaying of circulating p53 is, however,

challenging due to both the heterogeneity of both its mutations and post-translational modifications.[106, 109]

Alternative, assaying of anti-p53 antibodies is more accessible due to their structural consistency and rich abundance ($\sim 100\ \mathrm{ng \cdot mL^{-1}}$),[110] with levels hundreds of times higher than those of p53 in serum. Since the 1990s, the rediscovery of p53 antibodies and the growing interest in their roles in cancer progression and prognosis have inspired the generation of these antibodies through in vivo, in vitro, and recombinant approaches.[111] Most of these antibodies recognised conserved epitopes in the amino- and carboxyl-terminus of p53,[112] as exemplified by the DO-1 antibody (residues 20-25, Ser-Asp-Leu-Trp-Lys-Leu)[111] widely used in Western blotting,[113] immunohistochemistry,[114] and immunoprecipitation.[115] This structural consistency makes these antibodies effective tools for direct p53 measurement regardless of the mutant forms. Some antibodies target the DBD domain of p53.[116] Despite the high prevalence of mutations in this region, they provide valuable insights into the structural and functional impacts of specific p53 mutations. Assaying p53 antibodies involves several methods, primarily including ELISA, electrochemical biosensors, and immunofluorescence assays. However, both ELISA and electrochemical biosensors are particularly susceptible to nonspecific fouling in serum samples,[85, 117] compromising assay accuracy and reliability. Additionally, data from clinical investigations using different commercial kits or platforms often cannot be cross-referenced, making it difficult to compare results across studies.[89, 110]

1.1.3 Biosensor: Types and Performance Evaluation

To facilitate accurate quantification of protein biomarkers, biosensors are essential that combine a biorecognition component with a transducer to specifically interpret the presence and concentration of biomarkers into measurable signals. The history of biosensing dates back to 1962 when Leland C. Clark Jr. proposed the concept of the biosensor,[118] laying the groundwork for modern biosensors. Building on his pioneering work with the first practical glucose enzyme electrode in 1967,[119] the first commercially successful glucose biosensor by Yellow Springs Instrument Company was introduced in 1975,[120] marking a significant milestone in biosensing technologies. With advancements in nanotechnology, microfluidics, and bioengineering, various biosensing platforms have emerged, enhancing the sensitivity, specificity, and range of applications for these diagnostic tools. This section will explore the fundamental aspects of biosensors, focusing on their types and performance assessment.

1.1.3.1 Types of Biosensors

Biorecognition elements and transducers are two essential components to construct a biosensor. The former determines the specificity and sensitivity of biosensors,[60] while latter affect the sensitivity as transducer amplifies the biorecognition response and converts it into a measurable signal.[121] Based on the types of biorecognition elements, transduction mechanisms, the necessity of labelling, biosensors can be categorised into various types, each specified by applications and performance requirements.

The typical biorecognition elements employed in biosensing include proteins (*e.g.*, enzymes, and immunoproteins), nucleic acids, and whole cells. Protein-based biosensors leverage specific interactions between enzyme-substrate or antigen-antibody,[122, 123] as

noted in Section **1.1.1.2**, providing high specificity and sensitivity in medical diagnostics. Nucleic acid-based biosensors rely on the hybridisation between the target nucleic acid and complementary strands,[124] enabling the detection of genetic sequences with high sensitivity, which is essential for genomic studies and pathogen detection. Whole-cell biosensors employ living cells as the biorecognition component to obtain functional information about a living system responding to an environmental stimulus,[125, 126] offering applications in pharmacology, toxicology, and environmental monitoring.

Based on the transduction mechanisms, biosensors can also be categorised into optical, mechanical, electrochemical, and thermal types.[22, 121] Optical biosensors detect changes in light properties (*e.g.*, absorption, fluorescence, and surface plasmon resonance) to identify and quantify the presence of target analytes.[127] Mechanical biosensors utilise the piezoelectric effect or cantilever deflection to convert changes in mass or mechanical properties during biorecognition events into an electrical signal.[128, 129] Electrochemical biosensors, on the other hand, rely on measuring changes in electrical properties (*e.g.*, current, voltage, and impedance) and are particularly advantageous due to their simplicity and portability, making them more suitable for point-of-care applications.[130] The details of electrochemical biosensors are further discussed in Section **1.2.2**. Biochemical reactions often involve changes in enthalpy, leading to detectable temperature variations. Thermal biosensors measure heat changes to quantify biomarker concentration.[131] These biosensors are straightforward and suitable for biomolecular activity assessment, but are typically low sensitivity compared to other types.

In biosensing, labelling species can be fluorescent,[132] radioactive,[133] enzymatic,[134] or optical,[135] which can be attached to biomarkers to facilitate their transduction and enhance the sensitivity of biosensors. Depending on the necessity of labelling, biosensors

can also be categorised into label-based and label-free types.[136] Label-based biosensors provide high sensitivity and specificity, as exemplified by the well-established enzyme-linked immunosorbent assays (ELISA),[81, 137] the gold standard biosensing protocol. On the other hand, label-free biosensors streamline the biosensing process, making them more suitable for real-world applications, such as surface plasmon resonance (SPR),[138, 139] quartz crystal microbalance (QCM),[140] and electrochemical impedance spectroscopy (EIS).[141] Understanding these aspects is crucial for selecting the appropriate biosensor for a given application, ensuring accurate and reliable quantification of specific biomarkers.

1.1.3.2 Performance Assessment of Biosensors

Choosing an appropriate biosensor is not only to tailor specific applications, but also to ensure optimal performance. Several parameters will dominate biosensor performance, including signal-to-noise ratio (S/N), baseline stability, sensitivity, dynamic range, limit of detection (LoD), limit of quantification (LoQ), reproducibility, selectivity or specificity, and robustness.

In the context of biosensing, the signal refers to the measurable output biosensor produced in response to targets, while the baseline represents the background level in the absence of analytes.[142] In practice, however, random fluctuations and undesirable variations can distort the true response to the target analyte.[143] These noises include white noise or thermal noise,[143] originating from the random motion of particles caused by thermal agitation; shot noise or drift,[143] resulting from the discrete nature of carriers passing through a conductor junction; and external sources such as building vibrations.[143]

Some of these noise sources are intrinsic and unavoidable. To define the reliability of the biosensor, signal-to-noise ratio (S/N) is introduced where a high S/N ratio indicates the great precision and reliability of measurements.[142] Additionally, baseline stability, referring to the consistency of the baseline over time, is crucial for ensuring the reliability of a biosensor, especially in long-term monitoring applications where baseline drift can be prominent.

To establish a biosensing protocol, calibration is essential for determining the relationship — assuming linearity — between the measurable signal S_A of a biosensor and the known concentrations of analyte c_A, as expressed in *eqn.* **1.3**.[142]

$$S_A = k_A \cdot c_A \tag{1.3}$$

where k_A represents the proportionality constant. The sensitivity of a biosensor is then defined as the ratio of change in signal per unit change in the analyte concentration, which is equivalent to the proportionality constant, k_A. The dynamic range refers to the interval between the lowest and highest analyte concentrations that can be measured accurately, precisely, and linearly. A wide dynamic range is advantageous as it enables the biosensor to function effectively across a broad spectrum of analyte concentrations.

In the presence of noise, it is acknowledged that replicate measurements, even under the same operating conditions, may not yield identical values.[142] A range of possible values is obtained, centred at S_A with a standard deviation of σ_A. The uncertainty of measurement, represented by σ_A, reflects the precision of the biosensor and is inversely related to its reproducibility.[142] High reproducibility is indicated by a low σ_A, signifying consistent and reliable measurements. Within the framework of measurement uncertainty, the sensitivity of a biosensor can also be evaluated by the limit of detection (LoD) and

limit of quantification (LoQ).[143] LoD is defined as the lowest concentration that can be reliably distinguished from the background noise, as expressed in *eqn.* **1.4**.[142]

$$LoD = S_{blank} + 3.3 \cdot \sigma_{blank} \tag{1.4}$$

where S_{blank} is the signal for an analyte blank and σ_{blank} represents the standard deviation of blank signal. Similarly, the LoQ is the lowest analyte concentration that can be quantified with a defined precision and accuracy threshold, typically set at 10 times σ_{blank}.

Not only can the analyte generate a response, but interferents also contribute to the measured signal. In the presence of interference, the total signal S_{total} consists of the signal generated by the analyte (S_A) and that of interferents (S_I), as expressed in *eqn.* **1.5**.[142]

$$S_{total} = S_A \pm S_I = k_A \cdot c_A \pm k_I \cdot c_I \tag{1.5}$$

where $k_I$is the interferent proportionality constant and c_I is the interferent concentration. Selectivity refers to the ability of a biosensor to distinguish the target from other interferent present in the sample, evaluated by the selectivity coefficient $K_{A,I}$.[142]

$$K_{A,I} = \frac{k_A}{k_I} \tag{1.6}$$

A high $K_{A,I}$ value signifies that the biosensor is much more responsive to the analyte, indicating a high level of selectivity for the target. Specificity, on the other hand, represents the highest degree of selectivity, where the biosensor exclusively responds to the target analyte without any interference from other substances. The sensitivity and

specificity of a biosensor primarily originate from the specificity the biorecognition elements.[60]

Sensitivity and selectivity can significantly influence the occurrence of false outcomes, typically noted as false positives or false negatives.[142] In assays, false positives occur when results incorrectly indicate the presence of a target analyte, while false negatives arise when a present analyte goes undetected. These false results undermine assay performance — false positives diminish selectivity, whereas false negatives reduce sensitivity. To visualise and evaluate this trade-off, receiver operating characteristic (ROC) curves are employed,[142] plotting the true positive rate (*i.e.*, sensitivity) against the false-positive rate (*i.e.*, negative selectivity). The area under the ROC curve (*i.e.*, AUC) serves as a single metric of overall assay discrimination:[142] a perfect assay, with high sensitivity and high specificity, yields a curve that approaches the top-left corner with an AUC of 1, while a non-discriminating assay follows the diagonal line with an AUC of 0.5.

As interferents can negatively impact the biosensor performance, robustness is the prerequisite for ensuring reliable biosensing in real-world applications. Robustness refers to the capability of a biosensor to maintain accuracy under varying conditions and in the presence of interfering substances,[142, 144] which is evaluated by the sensor's recovery.

In addition to these key parameters, choosing an appropriate biosensor also need to consider other factors including equipment, time, and cost.[142] Not only the biosensor's capabilities (*e.g.*, reproducibility, sensitivity, specificity, and robustness) need to be evaluated, but also the complexity and affordability of configurations, the overall

duration, and cost-effectiveness. Balancing these factors ensures that the chosen biosensor is both high-performing and practical for real-world applications.

1.2 ELECTROCHEMICAL BIOSENSING: FUNDAMENTALS, TYPES, AND CHALLENGES

Employing electrodes as the transducer, electrochemical biosensors specifically convert the biorecognition events into electrical signals (*e.g.*, current,[145] voltage,[146] and impedance)[141], offering high sensitivity, cost-effectiveness, and portability for real-world applications. Their capability lies in the specific interaction facilitated by biorecognition elements,[60] the efficient electron transfer occurring at the electrode interface,[121] and the advanced signal processing and amplification ensuring sensitive, precise and reliable detection of target analytes. These attributes make electrochemical biosensors highly versatile and practical for a wide range of applications. At the core of electrochemical biosensing, electrochemistry allows for the precise manipulation of reaction rates and pathways by adjusting electrical parameters.[147]

In this section, the key aspects of electrochemical biosensors will be explored, beginning with the fundamental concepts of electrochemistry that underpin these devices. Following this, the challenges faced in electrochemical biosensing will be discussed, offering insights into potential advancements and future directions for this rapidly evolving technology.

1.2.1 Concepts of Electrochemistry

1.2.1.1 Electrode Reaction, Potentials, and Electrochemical Cells

Distinct from solution-phase redox reactions, electrochemical reactions occur at the interface between an electronic conductor (*i.e.*, electrode) and an ionic conductor (*i.e.*,

electrolyte).[147] In these systems, the process of charge transfer is divided: electrons flow through the external circuit connecting the electrodes, while ions carry charges through the electrolyte. The overall electrode reaction can be separated into two half-reactions,[147] where oxidation occurs at the anode, and reduction takes place at the cathode. This separation into two individual processes simplify the analysis of electrochemical reactions, providing a structured and manageable framework for understanding complex electrochemical processes.

To evaluate the tendency of a redox species to gain or lose electrons in half-reactions, electrode potentials are employed. These potentials arise from the charge separation, where a dynamic equilibrium is established at the electrode-electrolyte interface.[148] For example, in a metal electrode, spontaneous charge transfer occurs until the rate of metal dissolution equals the rate of ion deposition,[148] resulting in a stable charge separation at the interface. At this point, the Fermi level of the electrode aligns with the energy level of the dissolved ions,[147, 149] setting the electrode potential. This potential provides a reference for comparing the reactivity of different species: redox species with higher electrode potentials are more likely to be reduced, while those with lower potentials are prone to be oxidised. Not only the electrode potential determines the redox behaviour, but the concentration of redox species is also important, as described by the Nernst equation (*eqn.* **1.6**).[147, 150]

$$O + ne^- \rightleftharpoons R$$

$$E = E^\circ + \frac{RT}{nF} \ln \frac{c_O}{c_R} \tag{1.6}$$

where O and R represent the oxidised and reduced form of redox species, respectively; E represents the actual electrode potential under non-standard conditions; E° denotes the

standard electrode potential, R is the universal gas constant, valued at $8.314\ \mathrm{J \cdot mol^{-1}K^{-1}}$, T is the temperature in Kelvin; n is the number of electrons transferred; F signifies the Faraday constant, approximately $96485\ \mathrm{C \cdot mol^{-1}}$. c_O and c_R are the concentration of oxidised and reduced forms of the species involved in the half-reaction, respectively. The Nernst equation describes the dependence of the electrode potential on the concentrations of the reacting species, allowing for the prediction of equilibrium shifts with changes in concentration.

Measuring electrode potential necessitates an electrochemical cell, consisting of at least two electrodes separated by one or more electrolyte phases.[147] Practically, determining the electrode potential of a single half-reaction in isolation is impossible because potential is inherently a difference in electrochemical potential between two points, and a single electrode does not complete an electrical circuit.[147, 151] To study the electrode of interest (*i.e.*, the working electrode), a reference electrode is introduced, providing a stable and invariant baseline. By using standardised reference electrodes, any change in the cell potential is attributed to the working electrode,[147] allowing precise determination of its electrode potential. Examples of common reference electrodes include the standard hydrogen electrode (SHE), the silver/silver chloride (Ag/AgCl) electrode, and the calomel electrode (less commonly used since mercury (Hg) was banned).[147, 148] To maintain a stable electrode potential, the current passing through these reference electrodes should be minimal (~ 10^{-9} A) to preserve constant composition.[147] Otherwise, a three-electrode configuration is necessary.[148] In this setup, a third electrode called the counter electrode is introduced. The counter electrode allows for the current to pass through the system without interfering with the establishment of the potential between the working and reference electrodes,[147] thereby providing more accurate control of the

working electrode potential and improving the precision of electrochemical measurements.

1.2.1.2 Surface Matters in Electrochemistry: Electrical Double Layer and Electrode Process Kinetics

While electrode potential offers thermodynamic insights to predict the equilibrium shift of a redox reaction,[152] the exact reaction pathways and kinetics are determined by the surface characteristics of electrodes.[153] As electronic conductors, electrodes facilitate charge transfer at surfaces, where the efficiency of this transfer is heavily influenced by the electrode's electronic structure and conductivity. Additionally, the electrode surface provides active sites essential for heterogeneous chemical reactions.[147, 153] The structure and composition of the electrode surface significantly impact the reaction pathways and activities of redox species, thereby affecting the overall performance and efficiency of electrochemical processes.

The unique role of the electrode originates from the interactions at the electrode-electrolyte interface when an electrode potential is established.[154] These interactions include electrostatic attractions due to residual charges in both phases, as well as interactions with various particles in the solution (*e.g.*, solvent molecules, solvated ions, and molecules).[147] These interactions influence the local electric field, resulting in the distribution and concentration of ions near the electrode surface, known as the electrical double layer.[147, 154, 155] As shown in Figure **1.5**, specifically adsorbed ions and solvent molecules on the electrode surface form the inner Helmholtz layer (IHP). Meanwhile, long-range electrostatic attractions cause solvated ions to form the outer Helmholtz plane

(OHP) and the diffuse layer, where ion distribution in the solution compensates for the electrode charge. The presence of the double layer profoundly influences the properties of electrochemical systems, significantly contributing to the capacitance of the electrode (detailed in Section **1.2.2.3**),[147, 153] which is essential for charge storage in supercapacitors. Additionally, the strong local electric field strength (10^8 - 10^9 $V \cdot m^{-1}$) within the double layer polarise molecules and ions near electrode surface,[147] reducing activation energy and facilitating the breaking and forming of chemical bonds in electrode reactions.[156]

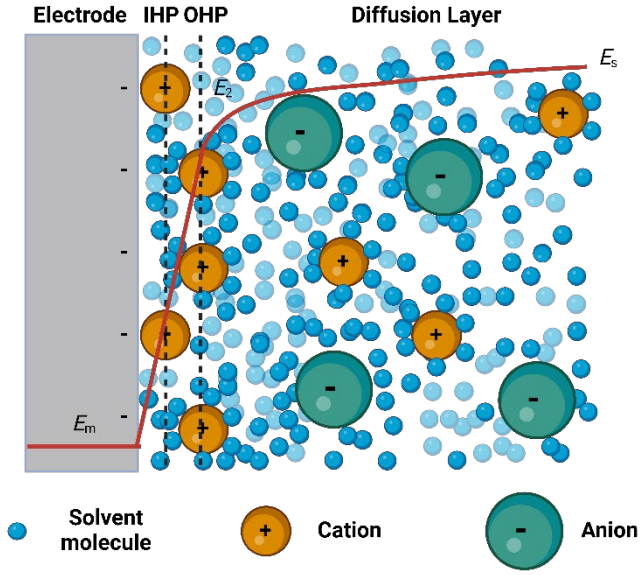


Figure 1.5. Schematic representation of electrical double layer structure on an electrode surface,[147, 155] consisting of inner Helmholtz layer (IHP), outer Helmholtz plane (OHP) and the diffuse layer. The potential gradient is indicated by the red line, showing the change in electric potential from the electrode potential (E_m) through the Helmholtz plane potential (E_2) to the solution potential (E_s).

The kinetics of electrode reactions are also significantly influenced by surface characteristics.[148, 153, 157] Specific adsorption, determined by electrode surface composition, enhances the likelihood of electron tunnelling from the electrode to the reactants, thereby improving the efficiency of charge transfer. Additionally, the strong local electric field strength within the double layer, which is modulated by overpotential, lowers activation barriers and accelerates reaction rates.[147] The rate constants for

reduction k_c, oxidation k_a, and the overall kinetics (*i.e.*, Butler-Volmer equation) for a one-step electrode reaction are expressed in *eqn.* **1.7**-**1.9**, respectively.[147, 158]

$$k_c = k^\circ \cdot \exp\left(\frac{-\alpha F\eta}{RT}\right) \tag{1.7}$$

$$k_a = k^\circ \cdot \exp\left(\frac{\beta F\eta}{RT}\right) \tag{1.8}$$

$$j = nF(k_c c_O - k_a c_R) = j^\circ \cdot [\exp\left(\frac{-\alpha F\eta}{RT}\right) - \exp\left(\frac{\beta F\eta}{RT}\right)] \tag{1.9}$$

where k° represents the standard rate constant; α and β are the transfer coefficients, with the relationship $\alpha + \beta = 1$; η is the overpotential; j is the current density in $\mathrm{A \cdot cm^{-2}}$; F is the Faraday constant; c_O and c_R are the bulk concentration of oxidised and reduced forms of the species, respectively; and j° is the exchange current density, defined as $j^\circ = nFk^\circ c_O^{1-\alpha} c_R^{\alpha}$.[147] The Butler-Volmer equation indicates that the overall current density j (or reaction rates) in an electrochemical reaction is significantly impacted by the overpotential, with a higher overpotential accelerating the reaction kinetics. This principle underpins the manipulation of electrochemical reactions in various applications, enabling precise control over reaction rates and efficiencies by adjusting the applied potentials.

1.2.1.3 Mass Transport in Electrochemical Systems

Not only are electrode kinetics regulated by overpotentials, but they are also closely related to the rate of mass transport.[153] Before charge transfer can occur, redox species need to be transported to the electrode surface and come close enough within the double

layer for the charge transfer to take place,[147] as depicted in Figure **1.6**. Efficient mass transport ensures that reactants are continuously supplied to the electrode while products are quickly removed, thereby maintaining high reaction rates and preventing concentration polarisation.

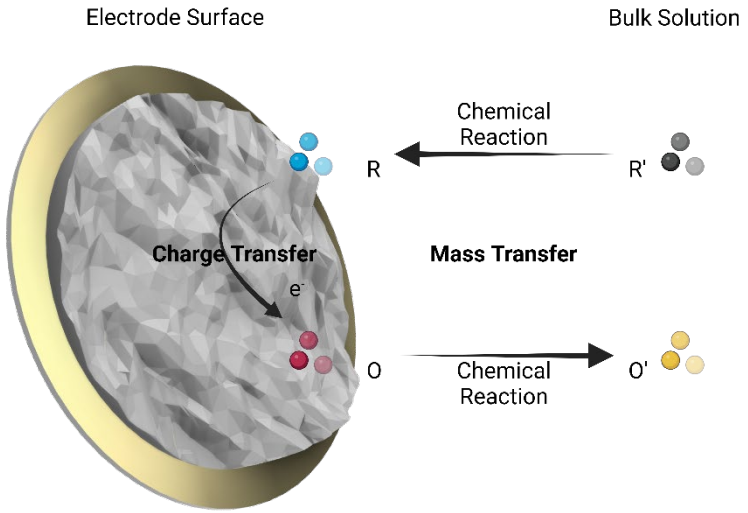


Figure 1.6. General electrode processes involved in an electrochemical reaction.[147] Species from the bulk solution are transported to the electrode surface via mass transfer. Subsequently, charge transfer occurs at the electrode surface, where electrons are either gained or lost. The overall process may be coupled with chemical reactions.

In electrochemical systems, mass transport encompasses three primary modes: diffusion, migration, and convection.[147] Diffusion is the spontaneous movement of species down their concentration gradients. Migration refers to the movement of charged species in response to an electric field. Convection is the transport of particles as a result of either natural (*e.g.*, density gradients) or forced (*e.g.*, stirring) motion of a fluid. The combined effects of these modes are expressed by the Nernst-Planck equation.[148]

$$J_j(x) = -D_j \frac{\partial c_j(x)}{\partial x} - \frac{z_j F D_j c_j(x)}{RT} \cdot \frac{\partial \phi(x)}{\partial x} + c_j(x)v(x) \qquad (1.10)$$

where $J_j(x)$ is the flux of species j in $\mathrm{mol \cdot s^{-1}cm^{-2}}$, corresponding to the number of species passing through unit area per unit time at distance x from the electrode; D_j is the diffusion coefficient of species j in $\mathrm{cm^2 s^{-1}}$; $c_j(x)$ is the concentration of species j at distance x, with $\frac{\partial c_j(x)}{\partial x}$ denominating its concentration gradient; z_j is the charge of species j; F is the Faraday constant; $\frac{\partial \phi(x)}{\partial x}$ represents the potential gradient at distance x from the electrode; and $v(x)$ is the velocity of fluid in $\mathrm{cm \cdot s^{-1}}$ along the x-axis. The three terms in *eqn.* **1.10** represent the contribution of diffusion, migration, and convection in mass transport, respectively.

Considering all three forms of mass transport simultaneously is complex. Practically, electrochemical measurements are typically performed under optimised conditions where one or two forms dominate, rendering the contributions of the others negligible.[148] For example, the addition of supporting electrolyte can reduce the transport numbers of target ions,[143, 159] resulting in a negligible migration component.[160] Additionally, convection can be largely minimised in a static solution, leaving diffusion as the primary mode of mass transport. Under these conditions, the Nernst-Planck equation simplifies to Fick's law, as shown in *eqn.* **1.11**.[148]

$$J_j(x) = -D_j \frac{\partial c_j(x)}{\partial x} \qquad (1.11)$$

This simplification allows for a more straightforward analysis of mass transport in some electrochemical techniques. In electrochemical systems, the behaviour of redox species is collectively influenced by electrode potential, surface characteristics, the local

environment within the electrical double layer, and mass transport mechanisms.[147, 153] The aims of electrochemical measurements are to establish the relationship between stimulation and response by precisely controlling and measuring parameters such as potential, current, impedance. These measurements help in elucidating the underlying mechanisms and behaviours of electrochemical systems, enabling insights into reaction kinetics, mass transport processes, and interface properties. Several key techniques in electrochemical measurements — including chronopotentiometry (CP), chronoamperometry (CA), cyclic voltammetry (CV), and square wave voltammetry (SWV), electrochemical impedance spectroscopy (EIS), and derived electrochemical capacitance spectroscopy (ECS) — are detailed in Section **6.3.1**.

1.2.2 Electrochemical Biosensors: Types and Challenges

Based on the specific transduction method, electrochemical biosensor can further be categorised into three types: potentiometric, amperometric, impedimetric/capacitive, and resistive pulse sensors.[130] Potentiometric biosensors detect the Nernstian changes in the open-circuit potential between a working electrode (WE) and a reference electrode (RE) in response to the presence and concentration of specific analytes.[161] They are advantageous due to their simplicity in setup and ease of result interpretation,[146] as they operate under equilibrium conditions. However, potentiometric sensors typically suffer from lower sensitivity and selectivity compared to other types of electrochemical sensors.[22] The potential changes in potentiometric sensors are typically small, often on the order of millivolts, making them harder to detect and differentiate from background noise, thus reducing overall sensitivity. Additionally, potentiometric sensors are

susceptible to interference from non-specific substances due to the less informative nature of potential measurements.

Amperometric biosensors measure the resulting current in electrode reactions to quantify the concentration of the target analyte.[130] Compared with potentiometric biosensors, the high signal magnitude in redox reactions and the employment of current amplifiers enhance the S/N ratio and sensitivity of amperometric sensors, facilitating the reliability of assays. Chronoamperometry (CA),[162] cyclic voltammetry (CV) methods,[163] and pulse voltammetry (*e.g.*, square-wave voltammetry, SWV)[164, 165] are commonly employed. As stated in Section **6.3.1**, CA method provides straightforward real-time monitoring of current, but the single potential step approach offers limited information about the system. CV methods deliver detailed insights into redox processes and reaction kinetics, allowing for the characterisation of complex systems. However, their sensitivity is constrained by the interference of double-layer charging,[143] making it challenging to detect low-concentration analytes (c_{bulk}~10^{-5} M). To address this challenge, SWV has been developed to enhance sensitivity (c_{bulk}~10^{-8} M) by minimising capacitance noise.[143, 147, 148] Despite their capabilities, these techniques require precise control of experimental conditions and careful data interpretation. It is noted that most biomarkers are inherently redox inactive, necessitating the labelling of analytes with electroactive tags in amperometric biosensors. This complicates sample preparation, increases costs, and may introduce potential interferences in measurements.

Impedimetric/capacitive biosensors employ either solution-phase or surface-bound electroactive species to probe changes in impedance or capacitance at the electrode surface resulting from of biorecognition events, with principles detailed in Section **6.3.1**.[141, 166] Upon introducing a biomarker onto a bio-receptive interface, the resulting

biomarker-bioreceptor complex typically hinders electron transfer kinetics and alters the dielectric properties of electrode interface, leading to an increase in charge transfer resistance R_{ct} and a decrease in redox capacitance C_r. These changes are utilised to establish analyte concentration-response curves. Unlike many amperometric sensors, impedimetric/capacitive biosensors offer label-free detections,[141, 167] eliminating the need for redox tags in sample preparation. Since measurements are conducted under equilibrium conditions with a small AC perturbation applied, these sensors are non-destructive,[19, 147] preserving biomolecular activity and interface stability. Additionally, the frequency-dependent information allows for distinguishing processes with different time scales, enhancing sensitivity comparative to SWV. However, the complex data interpretation and sophisticated modelling limit their accessibility.

Resistive pulse sensing operates by detecting transient disruptions in ionic current as individual analytes pass through a confined pore (*e.g.*, nanopores, nanopipettes) under an applied voltage.[168, 169] This technique offers high sensitivity and resolution, as each analyte generates a characteristic "pulse" based on its size, shape, charge, and surface chemistry, enabling label-free, single-entity detection and even biomolecular sequencing at the individual level.[169, 170]

Electrochemical biosensors offer numerous advantages,[19, 22, 130] including high sensitivity, rapid response times, cost-effectiveness, portability, and potentials for real-time monitoring and point-of-care applications. Several challenges can hinder its broader application, including issues with biofouling,[171] inefficient target recruitment,[172, 173] and limited turnaround efficiency.[174, 175] In clinical samples, the abundance of biomarkers is significant lower compared to non-specific biomolecules.[176, 177] This presents a major challenge in electrochemical biosensing due to biofouling, where unwanted interfering

substances accumulate to the electrode surface, resulting in reduced sensing specificity and an increased likelihood of false-positive results.[171, 172] Additionally, inefficient target recruitment can diminish assay sensitivity,[173] due to limited and unreliable bioreceptor coverage on a 2D electrode surface.[178] On the other hand, complex sample preparation procedures, such as redox tagging,[179] and prolonged assay times reduce the turnaround efficiency and practicality of electrochemical biosensing for real-world clinical applications.[180, 181]

To address these challenges, several solutions have been proposed.[182-185] Firstly, the integration of microfluidic techniques into electrochemical biosensing platforms has shown great promise in enhancing performance.[185, 186] Microfluidic devices offer precise control over small sample volumes, automate sample processing, minimise handling interferences, and facilitate high-throughput analysis.[185, 187] This integration can streamline the sample preparation process and enhance the overall turnaround efficiency. Additionally, mass transport in microfluidics is significantly accelerated by convection,[147, 148] resulting in enhanced biosensing performance. Unlike diffusion-limited transport in traditional biosensors, convective mass transport accelerates the delivery of target analytes to the bioreceptors, reducing response times and increasing the rate of biorecognition, as detailed in Section **1.3**. Consequently, this enhancement improves the sensitivity of biosensors, making them valuable in detecting low-volume and low-abundance analytes.

Another approach to improving the performance of electrochemical biosensors is the employment of nanomaterials,[183, 188, 189] as detailed in Section **1.4**. Nanomaterials, such as gold nanoparticles,[190] carbon nanotubes,[191] and graphene,[192-194] provide a high surface area for bioreceptor immobilisation, facilitating efficient target recruitment and

enhancing signal transduction. Additionally, the employment of these nanomaterials, particularly magnetic nanoparticles,[195, 196] can effectively concentrate target and reduce the presence of non-specific substances. This approach not only enhances the sensitivity of biosensors but also addresses the issue of biofouling,[85] ensuring robust and reliable detection. Surface modification of these particles can further minimise non-specific binding.[197, 198] Together, these advancements enable the development of highly sensitive, selective, and robust biosensing platforms for clinical applications.

1.3 MICROFLUIDICS AND BIOSENSING

Microfluidics, the manipulation of small volumes of fluids (μL to fL) at the microscale,[199] has emerged and revolutionised the field of biosensing,[182, 185] by providing automated, portable, user-friendly, and cost-effective solutions for high-throughput measurements. This section begins by introducing the fundamental concept of microfluidics, emphasizing the principles of mass transport under hydrodynamic conditions and its impact on biorecognition kinetics. Subsequently, the discussion will turn to the applications of microfluidics in electrochemical biosensing, highlighting its potential to advance analytical and diagnostic tools.

1.3.1 Concept of Microfluidics

Unlike diffusion-controlled processes in a stationary solution, microfluidic systems are typically operated under hydrodynamic conditions,[148] involving both diffusive and convective mass transport through controlled fluid flow.[200] This enhanced mass transport can result in significantly faster biorecognition kinetics,[201-203] thereby improving the performance of electrochemical biosensors. In this section, the fundamental concept of microfluidics will be outlined, elucidating the interplay between hydrodynamic flow and biosensing performance.

1.3.1.1 Mass Transport under Hydrodynamic Conditions

Under hydrodynamic conditions, the modified Nernst-Planck equation (*eqn.* **1.12**) is employed to depict the convection-diffusion controlled mass transport.[147, 148]

$$J_j(x) = J_{diff} + J_{conv} = -D_j \frac{\partial c_j(x)}{\partial x} + c_j(x)v(x) \tag{1.12}$$

where $J_j(x)$ is the flux of species j at distance x from the electrode, consisting of diffusive flux J_{diff} and convective flux J_{conv}; D_j is the diffusion coefficient of species j; $c_j(x)$ is the concentration of species j at distance x; and $v(x)$ is the local fluid at point x. As indicated in *eqn.* **1.12**, higher fluid velocity v enhance the convective transport J_{conv}, facilitating the delivery of reactants to the electrode surface.[203] Once the local velocity profile $v(x)$ is determined, the flux and distribution of species in the systems can be accurately predicted.

To evaluate the relative impact of convection versus diffusion, Reynolds number (R_e) is defined as ratio between inertial and viscous forces, as shown in *eqn.* **1.13**.[148]

$$R_e = \frac{vL}{\upsilon} = \frac{\rho v L}{\mu} \tag{1.13}$$

where v is the flow velocity in $\mathrm{m \cdot s^{-1}}$; L is the characteristic length, typically defined as the ratio between the volume of a system to its surface; υ is the kinematic viscosity of the fluid in $\mathrm{m^2 s^{-1}}$, which is the ratio of the fluid's dynamic viscosity μ and its density ρ.

The Reynolds number helps determine the type of fluid flow, either laminar ($R_e < 2300$) or turbulent ($R_e > 2900$).[147, 204] In laminar flow, the fluid moves in smooth, parallel layers, while in turbulent flow, the fluid motion is chaotic and unsteady.[148] The discussion of hydrodynamic problems is typically centred on laminar systems because of their

predictable and orderly flow patterns, which simplify the analysis and modelling of fluid behaviours.

For example, in a channel electrode, laminar flow typically results in a parabolic velocity profile,[205] as shown in Figure **1.7**. The velocity components are given by the following equations.[148]

$$v_x \approx \frac{2v_0 y}{h} = \frac{2v_f y}{3h^2 d};\ v_y = v_z = 0 \tag{1.14}$$

where v_x, v_y, and v_z donate the velocity components along the longitudinal x, axial y, and transverse z directions, respectively; v_0 is the maximum velocity at the centreline in $\mathrm{cm \cdot s^{-1}}$; v_f is the volume flow rate in $\mathrm{cm^3 s^{-1}}$; d and h are the width and half-height of the channel.

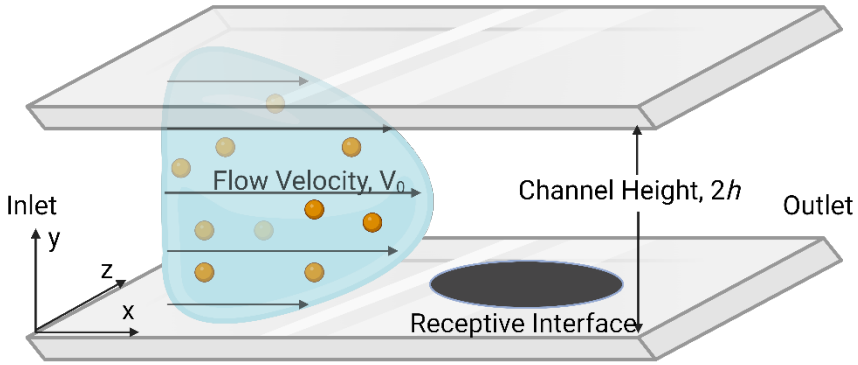


Figure 1.7. Schematic depiction of the channel electrode and a parabolic velocity profile.[148]

By combining Fick's 2nd law,[147] the temporal concentration change of species j at the electrode surface, after neglecting the small contributions of axial and transverse diffusion, is shown as follows.[148]

$$\frac{\partial c_j}{\partial t} = -\nabla J_j = D_j \frac{\partial^2 c_j}{\partial y^2} - v_x \cdot \frac{\partial c_j}{\partial x} \tag{1.15}$$

Under steady-state conditions ($\frac{\partial c_j}{\partial t} = 0$), The solution to *eqn.* **1.13** is known as the Levich equation (*eqn.* **1.16**),[148] where A represents the electrode surface area; the scale factor between flux J_j and species concentration c_j is defined as the Levich constant k_{Lev}, with a unit of $\mathrm{cm} \cdot \mathrm{s}^{-1}$.

$$J_j = 0.925 \cdot \left(\frac{D_j^2 v_f}{Ah^2}\right)^{\frac{1}{3}} \cdot c_j = k_{Lev} \cdot c_j \tag{1.16}$$

The Levich equation highlights the dependence of the flux on several key factors: the analyte concentration, the channel geometry, and the flow conditions. Specifically, a high analyte concentration increases the flux proportionally. Additionally, a channel confinement results in higher flux values.[203] The flow conditions, represented by the volume flow rate v_f, also play a crucial role, where an increase in flow rate enhances the flux. The Levich equation provides valuable insights into mass transport in hydrodynamic environments, paving the way for microfluidic system design and biosensor optimisation.

Distinct from diffusion-only transport with a decaying flux, as depicted by the Cottrell equation (*eqn.* **6.5**),[147, 148] convection ensures a constant and steady-state flux, enabling sustained delivery of reactants to the electrode surface and maintaining reaction rates over time.[148] This concept is essential in techniques such as hydrodynamic voltammetry and rotating disk electrode (RDE) experiments,[148, 200, 206] where controlled and stable laminar flows are established at the electrode surface. The enhanced mass transport improves assay sensitivity, while the time-independent response simplifies data interpretation and enhances the reproducibility of measurements.

1.3.1.2 Integration with Biorecognition Kinetics

Following a steady convective mass transport, analytes *A* are delivered from the bulk solution to the electrode surface, enabling the subsequent specific biorecognition with surface-bound ligands by an association rate constant k_{on} and a dissociation rate constant k_{off}.

$$A_b \xrightleftharpoons{MT} A_s + L_s \underset{k_{off}}{\overset{k_{on}}{\rightleftharpoons}} A - L_s$$

The overall biorecognition demonstrates pseudo first-order kinetics, as shown in *eqn.***1.17** (association phase v_{on}) and **1.18** (dissociation phase v_{off}),[207] where c_{A_s}, c_{L_s}, and c_{A-L_s} are surface concentration of analyte, ligand, and analyte-ligand complex, respectively.

$$v_{on} = \frac{dc_{A-L_s}}{dt} = k_{on} c_{A_s} c_{L_s} - k_{off} c_{A-L_s} \tag{1.17}$$

$$v_{off} = \frac{dc_{A-L_s}}{dt} = -k_{off} c_{A-L_s} \tag{1.18}$$

Unfortunately, the exact determination of the overall binding rate under hydrodynamic conditions is challenging, due to the mathematical complexity involved in solving coupled differential equations that describe both convective transport and surface reactions,[205, 208] necessitating introducing assumptions. In the initial phase of this consecutive process, the overall biorecognition kinetics is predominantly modulated only by the rate of mass transport and the association kinetics. This is because, at this stage, the formation of surface-bound analyte-ligand complexes is limited, and dissociation is negligible.[208, 209] Déjardin et al. suggest the initial overall rate constant $k_{overall}$ is the sum

of the inverse rate constants of the association process k_{on} and the transport process k_{Lev} (*eqn.* **1.19**).[208, 210]

$$k_{overall} = (k_{on}^{-1} + k_{Lev}^{-1})^{-1} \quad (1.19)$$

Accordingly, three distinct regimes can be identified based on the relative magnitudes of k_{on} and k_{Lev}: the mass-transport limit (MTL) regime, the partial MTL regime, and the binding-limited regime.[181] Within the MTL regime, the transport of analytes to the surface is the rate-determining step,[211-213] *i.e.*, $k_{Lev} \ll k_{on}$, $k_{overall} \approx k_{Lev}$. This scenario occurs in conditions such as low flow rates, highly viscous media, and high affinity between analytes and ligands. In the binding-limited regime, the formation of surface-bound analyte-ligand complexes limits the overall biorecognition kinetics,[211, 213] *i.e.*, $k_{Lev} \gg k_{on}$, $k_{overall} \approx k_{on}$. Besides the influence of environmental conditions, *e.g.*, pH, temperature, ionic strength, and medium viscosity, as well as a low affinity between analytes and ligands, the sluggish binding rate can result from the conformational changes and structural rearrangements of biomolecules involved in biorecognition to overcome energy barriers,[213, 214] as discussed in Section **1.1.1.2**. Finally, in the partial MTL regime,[215] the overall binding rate is governed by both the efficiency of analyte transport to the surface and the intrinsic binding kinetics of the analyte-ligand interaction, *i.e.*, $k_{Lev} \sim k_{on}$.

In the context of specific biorecognition, the high affinity and rapid binding kinetics ($k_{on} \geq 10^5\,\mathrm{M^{-1} \cdot s^{-1}}$) ensure that once the analyte reaches the surface,[181, 216] it binds ligands immediately, resulting in the overall biorecognition being in the MTL or partial MTL regime. Unlike specific binding, nonspecific binding, resulting from weaker and more general biomolecular interaction (Section **1.1.1.2**), is characterised by lower affinity

(K_d ~mM)) and a slower association rate constant ($k_{on} \leq 10^3\ \mathrm{M^{-1} \cdot s^{-1}}$).[217, 218] Consequently, the overall binding kinetics dominated by nonspecific binding tend to be binding-limited. Improvement in k_{Lev} through optimised flow conditions and the geometry of microfluidic devices can enhance the binding efficiency of processes in the MTL or partial MTL regime, *i.e.*, specific biorecognition. In contrast, nonspecific binding in binding-limited regime remains largely unchanged. This discrimination between specific and nonspecific binding is potential to enhance the sensitivity and selectivity of microfluidic setups in biosensing applications.

1.3.2 Microfluidics in Biosensing

Microfluidics is advantageous for developing compact, portable, and cost-effective biosensors due to the small sample volumes, reduced reagent consumption, and rapid, sensitive detection facilitated by enhanced mass transport and biorecognition efficiency,[187] as discussed in Section **1.31**. Additionally, the integration of multiple functions into a single microfluidic platform allows for the automation of analysis from sample preparation to target detection, facilitating high-throughput screening and multiplexed assays.[182] Additionally, this integration streamlines the workflow and minimises experimental variability, resulting in more reliable and reproducible outcomes.[219]

To precisely manipulate small volumes of fluids, microfluidic devices typically consist of several essential components,[220, 221] including pumps and valves, microchannels and microchambers, and substrate materials. Pumps and valves control the direction, speed, and volume of fluid flow.[220] These fluids are transported through microchannels to

microchambers, where they undergo mixing, reactions, and various biochemical or physical processes essential for the operation of devices.[220] Substrate materials provide mechanical support to microfluidic devices, and their properties, such as chemical affinity, functionality, and biocompatibility, significantly influence the device's fabrication, overall efficiency and performance.[222] Common substrate materials include glass, silicon, paper, and polymers (*e.g.*, hydrogel, polydimethylsiloxane).[223, 224]

Classified by their operational mechanisms, microfluidic biosensing devices can be broadly divided into: continuous flow microfluidics,[181, 225, 226] droplet microfluidics,[227] and Lab-on-a-Chip (LoC),[187, 220] as shown in Figure **1.8**. In continuous flow microfluidics, samples are delivered under steady-state condition, allowing for the real-time monitoring of analytes through microchannels. The ease of signal readout and high temporal resolution make these systems ideal for applications such as long-term cell metabolite detection and high-throughput biomarker analysis.[228, 229] Droplet microfluidics, also known as digital microfluidics,[230] involves the generation and manipulation of uniform, reproducible discrete droplets within microchannels. Serving as microreactors, these droplets can offer isolated environments that prevent cross-contamination, providing a powerful platform for single-cell analysis and high-throughput screening.[231, 232] By integrating multiple laboratory functions, Lab-on-a-Chip (LoC) devices can perform sample preparation, reaction, separation, and detection steps on a single micro-scale platform.[187, 220] This compact integration allows for the automation of complex biochemical processes and the miniaturisation of these processes, making LoC technology particularly well-suited for PoC diagnostics.

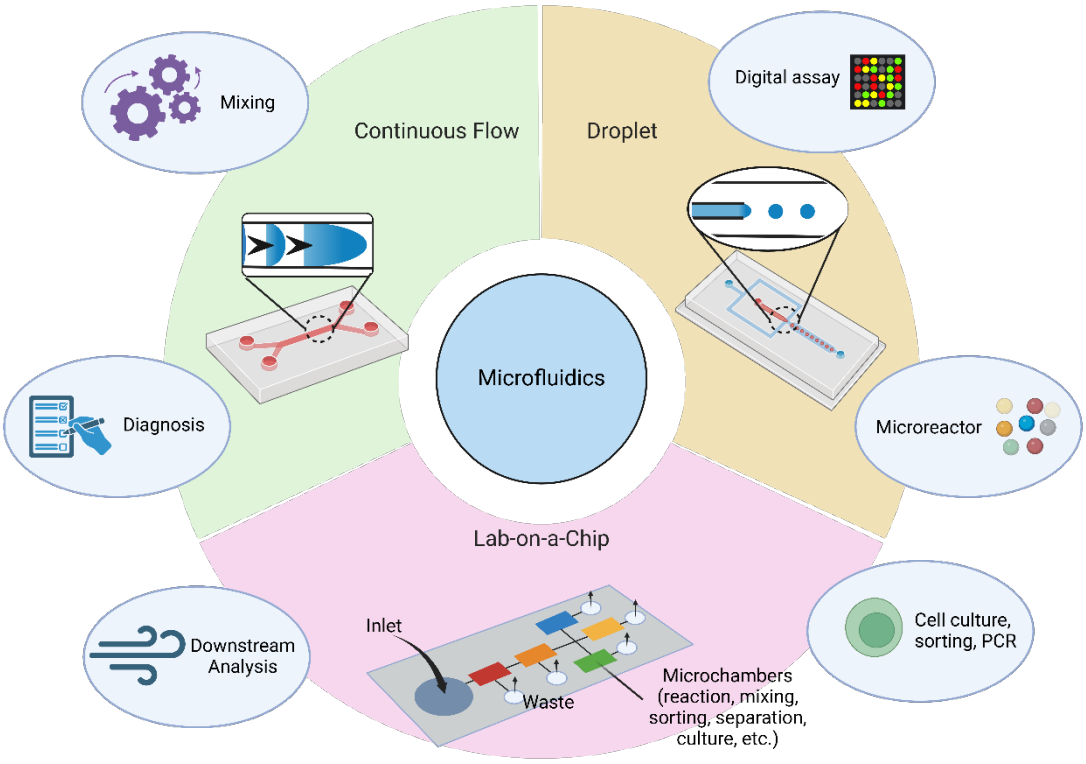


Figure 1.8. Schematic representation of microfluidic categorization and corresponding applications.[224, 230] Microfluidic devices are broadly divided into three types: continuous flow, droplet-based, and Lab-on-a-Chip configurations. Continuous flow microfluidics operates under steady-state conditions, facilitating efficient mixing, diagnosis, and downstream analysis. Droplet-based systems generate numerous microdroplets within microfluidic chips, enabling applications such as digital assays and microreactors. Lab-on-a-Chip devices are compact systems integrating multiple functionalized microchambers, ideal for cell culture, sorting, PCR, and various cell biology research applications

1.4 MAGNETIC NANOPARTICLES AND DOWNSTREAM ANALYSIS

Nanomaterials in biosensing have significantly advanced the field of diagnostics.[188, 189, 196] The employment of these nanomaterials in electrochemical biosensing, such as gold nanoparticles,[190] carbon nanotubes,[191] and graphene,[194] facilitates the development of highly sensitive and selective sensors, by providing a high surface area for bioreceptor loading and excellent conductivity for electron transfer.[188] This is also exemplified using quantum dots and plasmonic nanoparticles in optical biosensing.[233, 234] Among numerous nanomaterials, magnetic nanoparticles enable efficient target enrichment and recruitment from clinical samples,[85, 196, 235, 236] paving the way for diagnostic, proteomic, and genetic analysis. This section will explore the structural insights into magnetic nanoparticles, the origin of magnetisation, and their synthesis methods, providing a comprehensive overview of their applications and potential.

1.4.1 Magnetic Nanoparticles: Source of Magnetism, Structure, and Synthesis

Magnetic iron oxide nanoparticles, particularly magnetite (Fe_3O_4), are of increasing interest in scientific research and biomedical applications due to their unique magnetic characteristics, ease of functionalisation, and high biocompatibility.[237-239] The properties of these magnetic particles, including size distribution, surface functionalities, and magnetisation, are tailored through different synthesis approaches to enhance the efficiency of immunomagnetic separation for biomarker enrichment and cell recruitment.[85, 196, 236, 240]

1.4.1.1 Magnetism and Magnetic Nanoparticles: Structural Insights

Magnetism, originating from the movement of electrically charged particles, permeates every aspect of universe, from atomic interactions to the vast magnetic fields of celestial bodies.[239, 241] In materials, magnetism primarily results from the spin and orbital motion of electrons within atoms. Their magnetisation M, response to an external magnetic field H, is depicted by hysteresis loop.[239, 241] Four key parameters in the hysteresis loop characterise the magnetic properties of materials, namely magnetic susceptibility χ, coercivity H_c, remanence M_r, and saturation magnetisation M_s, each corresponding to specific features in the M *vs.* H curve.

As shown in Figure **1.9a**,[241] χ represented by the initial slope of the hysteresis loop, measuring the degree of material magnetisation in response to a small applied magnetic field. H_c is the value of the applied magnetic field required to reduce M to zero after the material has been magnetised, depicted by the intersection of the hysteresis loop with the H-axis. M_r is the residual magnetisation remaining in the material when $H = 0$, shown by the intersection of the hysteresis loop with the M-axis. M_s is the maximum magnetisation that the material can achieve, indicated by the plateau of the hysteresis loop at high H regimes. Defined by these four parameters, magnetic materials can be categorised into six types,[239, 242, 243] namely diamagnetism, paramagnetism, ferromagnetism, antiferromagnetism, ferrimagnetism, and superparamagnetism.

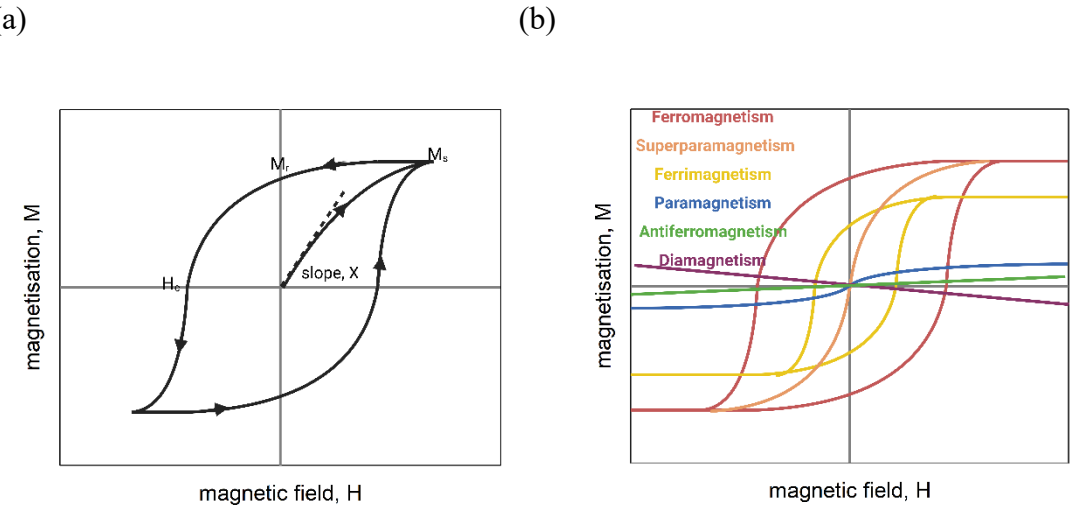


Figure 1.9. (a) Schematic depiction of magnetic susceptibility χ, coercivity H_c, remanence M_r, and saturation magnetisation M_s on a typical hysteresis loop. (b) Different types of magnetism represented by their characteristic magnetisation curves in response to an applied magnetic field, including ferromagnetism, superparamagnetism, ferrimagnetism, paramagnetism, antiferromagnetism, and diamagnetism.[239]

Diamagnetism and paramagnetism are two fundamental types of magnetism characterised by their weak magnetisation responses to external magnetic fields.[242] Diamagnetic materials consist of atoms with paired electrons and no net magnetic moment, while paramagnetic ones have weak magnetic moments resulting from unpaired electrons.[243] In hysteresis loops, both diamagnetic and paramagnetic materials exhibit a small linear response proportional to H, as shown in Figure **1.9b**.[241] The difference lies in the direction of this response: diamagnetic materials show a negative slope (*i.e.*, $\chi < 0$), while paramagnetic materials exhibit a positive slope (*i.e.*, $\chi > 0$). Neither type retains any magnetisation after the external field is removed, resulting in zero H_c and M_r.

In contrast, ferromagnetism, antiferromagnetism, and ferrimagnetism display significantly more complex behaviours and stronger magnetisation responses to external magnetic fields.[242, 243] These materials are typically composed of regions known as magnetic domains,[237] within which the magnetic moments of atoms are aligned in the

same direction. The strong magnetisation of ferromagnetic materials results from the parallel alignment of magnetic moments within domains in the material, such as Fe, Co, and Ni.[241] These materials exhibit substantial H_c and M_r, shown by the pronounced S-shaped hysteresis loop that flattens out at M_s in Figure **1.9b**.[241] This indicates that the material retains significant magnetisation even after the external field is removed. Ferrimagnetic materials, with partially cancelled magnetic moments within domains, show a hysteresis loop similar to ferromagnetic materials but with generally smaller H_c and M_r, as exemplified by magnetite.[244] Antiferromagnetic materials have a very narrow hysteresis loop with minimal H_c and M_r, due to the antiparallel alignment of neighbouring magnetic moments.[242] This alignment cancels out the net magnetic moments, resulting in no observed magnetisation.[243] However, antiferromagnetic behaviour can become paramagnetic once the spin alignment is disrupted, typically above the Néel temperature.[243]

Not only can unpaired electrons and the spin alignment modulate the magnetic properties of materials, but the size of the materials can also play a crucial role. In the context of superparamagnetism, ferromagnetic or ferrimagnetic nanoparticles are reduced to a single magnetic domain (*e.g.*, 35 nm for Fe_3O_4).[242, 243] These single-domain nanoparticles can achieve magnetisation approaching M_s of their bulk counterparts under an external field.[242] However, similar to paramagnetic materials, they exhibit zero H_c and M_r once the external magnetic field is removed.[242] This is because thermal fluctuations can overcome the magnetic anisotropy energy, resulting in no net magnetisation being retained. This unique size-dependent magnetic behaviours makes superparamagnetic materials particularly useful in applications such as magnetic resonance imaging (MRI) and drug delivery.[245-247]

Among the numerous candidates for magnetic materials, ferrites compounds, particularly iron oxides, are widely used due to their biocompatibility and ease of synthesis.[237, 238] Iron oxides exist in several different forms, including hematite (α-Fe_2O_3), akaganeite (β-FeOOH), maghemite (γ-Fe_2O_3), and magnetite (Fe_3O_4),[238] with their crystal structures shown in Figure **1.10**. α-Fe_2O_3 has a rhombohedral crystal structure characterised by hexagonally closed-packed layers of oxygen atoms,[238] with iron atoms occupying two-thirds of the octahedral sites. β-FeOOH features a monoclinic crystal structure,[248] where Fe-O octahedra share edges and corners to create tunnels running through the structure. Both γ-Fe_2O_3 and Fe_3O_4 share an inverse spinel crystal structure (AB_2O_4, space group $Fd\bar{3}m$),[238] consisting of a cubic close-packed arrangement of oxygen atoms with iron atoms occupying both tetrahedral and octahedral sites. In Fe_3O_4, the tetrahedral (A) sites are occupied exclusively by Fe^{3+} ions, while the octahedral (B) sites are occupied by an equal mixture of Fe^{2+} and Fe^{3+}, giving the formula $(Fe^{3+})[Fe^{2+}Fe^{3+}]O_4$. In contrast, in γ-$Fe_2O_3$, the B sites are occupied by Fe^{3+} along with a significant number of vacancies.[238]

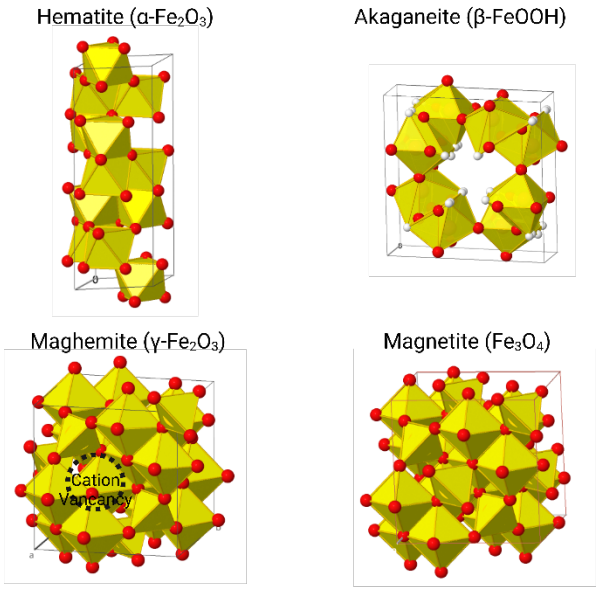


Figure 1.7. Crystal structures of iron oxides. Yellow polyhedral represent the coordination environment of iron atoms, while the red spheres indicate oxygen anions. Rhombohedral hematite (α-Fe_2O_3) and monoclinic akaganeite (β-FeOOH) are composed of Fe-O Fe-O octahedra sharing faces or corners. Both cubic maghemite (γ-Fe_2O_3) and magnetite (Fe_3O_4) consist of Fe-O octahedra and tetrahedra, although maghemite contains cation vacancies.

The distinct crystal structures significantly influence the magnetic properties of iron oxides. The coupling of magnetic moments in these compounds is primarily governed by superexchange interactions,[249, 250] where the bridging oxygen atoms align the spins of adjacent iron ions antiparallel to each other. Both α-Fe_2O_3 and β-FeOOH are antiferromagnetic due to this antiparallel alignment, which cancels out the net magnetic moment. In contrast, both γ-Fe_2O_3 and Fe_3O_4 are ferrimagnetic.[250] Superexchange interactions between Fe^{3+} in the tetrahedral sites and either cation vacancies (in γ-Fe_2O_3) or a mix of Fe^{2+}/Fe^{3+} (in Fe_3O_4) in the octahedral sites cannot completely cancel each other out. It is noted that the vacancies in γ-Fe_2O_3 disrupt partial magnetic coupling, resulting in a slightly weaker overall magnetisation (M_s = 74 - 80 emu $\cdot$ g^{-1}) compared with Fe_3O_4 (M_s = 92 emu $\cdot$ g^{-1}).[239]

1.4.1.2 Synthesis of Magnetite Nanoparticles

Although magnetite exhibits the highest saturation magnetisation among iron oxides, its properties in biosensing are also influenced by the sizes, geometries, and surface functionalities, which are tailored through different synthesis approaches, including co-precipitation, reverse micelle method, and hydrothermal synthesis.[238, 251]

Co-precipitation is a widely recognised method to generate large quantities of magnetite nanoparticles due to its simplicity and efficiency,[238, 251] involving the simultaneous precipitation of iron salts (Fe^{2+} and Fe^{3+}) in an alkaline medium. Practically, this method entails aging ferrous and ferric salts in a 1:2 stoichiometric ratio in a NaOH solution at room temperature, with the presence of inert gas to prevent oxidation, represented by the following formula.

$$Fe^{2+} + 2Fe^{3+} + 8OH^{-} \rightarrow Fe_3O_4 \downarrow + 4H_2O$$

Co-precipitation involves two distinct processes,[238] namely nucleation and growth. Nucleation is the initial step where small clusters form from the supersaturated solution. These clusters then grow by the diffusion of iron to the surface, leading to the formation of larger nanoparticles. To generate size-defined and uniformly dispersed nanoparticles, these two processes must be precisely controlled. A high pH promotes rapid nucleation, resulting in a larger number of smaller, more uniformly dispersed nanoparticles. Conversely, high iron concentrations can accelerate the growth rate, leading to larger and less uniform nanoparticles. Additionally, the ratio of ferrous and ferric salts also influences the synthesis. It is suggested that,[238] in the synthesis of Fe_3O_4, Fe^{3+} initially forms nuclei as akageneite (β-FeOOH), which subsequently convert to α-Fe_2O_3, γ-Fe_2O_3, and finally Fe_3O_4, under the catalysis of Fe^{2+}. A higher ratio of Fe^{2+} to Fe^{3+} can increase

the size of nanoparticles, but often results in less uniformity. Meticulous control of these factors is crucial for tailoring the magnetic properties and ensuring the high quality of magnetite nanoparticles.

To achieve precise control over particle size and distribution, the reverse micelle method, also known as the microemulsion method, has been developed. In this technique, reverse micelles are generated by dissolving surfactants in a non-polar solvent, with the surfactant molecules creating a microemulsion around water droplets.[244] These droplets act as nanoreactors for the synthesis of nanoparticles. In addition to pH, iron concentration, and the Fe^{2+}/Fe^{3+} ratio, the nature of the surfactant also impacts the size distribution of nanoparticles. These surfactants determine the size of micelles, facilitate the reaction, and stabilise the resulting nanoparticles.[244] Typical surfactants employed in Fe_3O_4 synthesis include sodium dodecyl sulfate (SDS),[252] polyvinylpyrrolidone (PVP),[253] and cetyltrimethylammonium bromide (CTAB).[254] However, the drawback of low-yield production makes the reverse micelle method less suitable for large-scale synthesis.[244]

Alternatively, hydrothermal synthesis offers significant advantages for producing shape-controlled, monodispersed, and highly crystalline Fe_3O_4 nanoparticles.[237] This method involves reducing and crystallising an Fe (III) source within a sealed autoclave, under temperatures ranging from 130 °C to 250 °C and high pressures of 0.3 to 4 MPa.[237] The high temperature increases the solubility of the precursor salts and provides sufficient thermal energy to overcome activation barriers for nucleation. The higher degree of supersaturation and accelerated nucleation rate result in efficiency synthesis. Meanwhile, high pressure facilitates and stabilises the formation of highly crystalline nanoparticles. Additionally, by adjusting the reducing agents and surfactants, hydrothermal synthesis can incorporate various surface functionalities directly during synthesis,[237] facilitating

the creation of tailored nanoparticles for specific applications. These advantages make the hydrothermal synthesis method an ideal choice for our study.

1.4.2 Nanoparticle-Assisted Biomarker Enrichment and Downstream Analysis

Magnetic nanoparticles, with their strong magnetic properties, biocompatibility, and ease of synthesis and functionalisation, enable the selective and efficient isolation of targets from clinical samples.[195, 196, 236] These particles have been extensively employed in immunomagnetic separation for biomarker enrichment and downstream analysis.[85, 235, 236] In these applications, antibody-coated magnetic beads are mixed with samples to bind to target biomarkers or cells. A magnetic field is then applied to separate the beads and their bound targets from the rest of the sample. Once separated, the bound targets can be analysed using various techniques, such as microscopy, immunoassays, or genetic analysis.[196, 255]

The importance of immunomagnetic separation lies in its ability to efficiently and specifically enrich biomarkers or cells from a plethora of interfering substances in clinical samples, as exemplified by the recruitment of tumour cells (CTCs) and Parkinson's disease biomarkers.[235, 236, 255] At the centre of these applications are magnetic beads with surface-bound antibodies, which provide the essential selectivity for targeting specific biomolecules or cells.[196] To covalently immobilise antibodies onto the bead surfaces, surface functionalities that are capable to bind to -NH_2 or -SH groups on the proteins are necessary. Common reactive functionalities on the surfaces of magnetic nanoparticles include carboxyl, amino, hydroxy, and epoxy groups..[196] Some of these surface functionalities must be activated prior to antibody immobilisation. For example, as shown

in Figure **1.11**, carboxyl groups are commonly activated through carbodiimide chemistry (*e.g.*, EDC, 1-ethyl-3-(3-dimethylaminopropyl)carbodiimide);[256] amino groups can be activated using glutaraldehyde to form Schiff bases with protein amino groups;[257] hydroxyl groups need to be converted into active tosyl or mesyl groups;[196, 258] while epoxy groups can directly react with amino or thiol groups under mild conditions.[259] Upon bioconjugations, antibodies can be firmly attached to the beads while retaining their ability to bind to their specific targets, ensuring effective immunomagnetic separation.

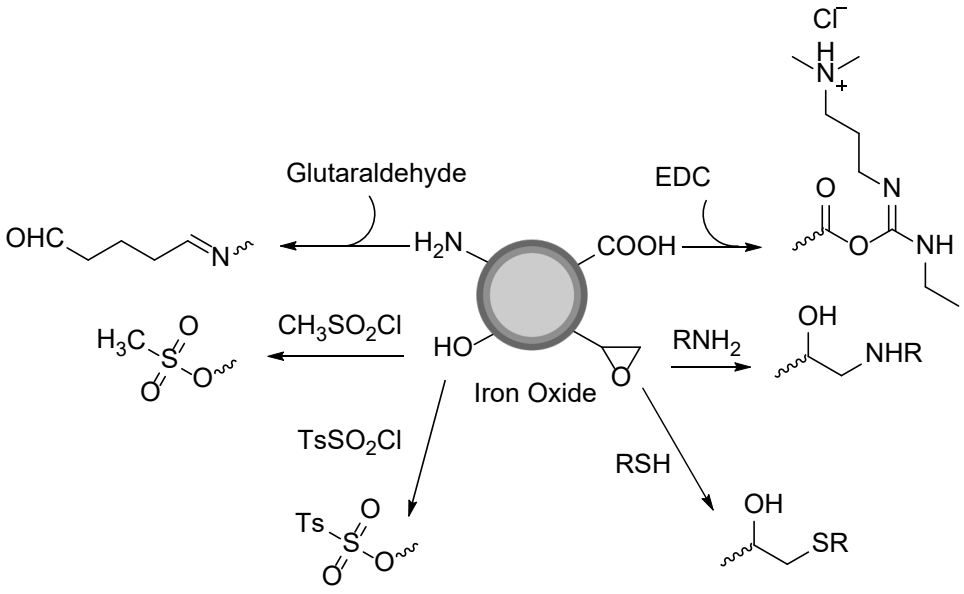


Figure 1.11. Examples of surface functionalization strategies for iron oxide nanoparticles:[196] Carboxyl groups are activated using EDC chemistry; amino groups are functionalized via glutaraldehyde, forming Schiff bases; hydroxyl groups are converted into sulfonates; and epoxy groups directly react with amino or thiol groups on proteins.

Not only the surface-bound antibodies but also the size and surface properties of magnetics nanoparticles can affect the performance of target recruitment.[240] Smaller nanoparticles provide a higher surface area-to-volume ratio, allowing for a high loading of bioreceptors on the surface. Additionally, magnetic nanoparticles smaller than 30 nm are superparamagnetic, meaning they do not retain residual magnetisation in the absence

of an external magnetic field,[242, 243] thereby reducing the tendency for aggregation. However, reducing particle size can potentially decrease the recruitment efficiency due to an insufficient magnetic force F_m, as shown in *eqn.* **1.20**.[195, 240]

$$F_m = \mu_0 V_p M_p \cdot \nabla H \tag{1.20}$$

where μ_0 is the permeability of free space; V_p is the volume of nanoparticles; M_p is the magnetisation of the nanoparticles, defined by product of magnetic susceptibility χ and the applied magnetic field H. As V_p reduces, the decrease in F_m can impair the efficiency of magnetic separation.[240, 260] For this reason, balancing nanoparticle size to optimise both the magnetic response and surface area is crucial for achieving efficient and effective target recruitment and separation. In addition to size, surface properties such as hydrophilicity and surface charge can also play significant roles in immunocapture. An ideal magnetic adsorbent should exhibit low non-specific binding to ensure high selectivity for target molecules. Hydrophilic surfaces with an appropriate charge can generate a hydration layer, reducing non-specific biofouling and improving colloidal stability.[261] Together, these properties optimise the performance of magnetic nanoparticles in immunomagnetic separation, ensuring efficient and specific target capture.

1.5 INTEGRATION OF MICROFLUIDICS AND ELECTROCHEMICAL BIOSENSORS: NEW AVENUES TOWARDS HIGH-SPEED AND HIGH-SENSITIVITY BIOSENSING PLATFORMS

In the context of the aforementioned discussions on challenges in electrochemical biosensing, regarding profound biofouling, inefficient target recruitment, and reduced turnaround efficiency discussed in Section **1.2.2,** integrating microfluidics with electrochemical biosensors combines the strengths of both technologies, providing more efficient, sensitive, and versatile platforms for biosensing applications. This thesis is dedicated to illustrating the application of these integrated systems, highlighting their potential to address existing limitations and advance the field of biosensing towards more robust, real-time, and high-throughput analytical capabilities. Based on the electrochemical transductions and specific biomarkers, Chapter 2 and Chapter 3 examine the microfluidic integration on a capacitive polyaniline (PANI) surface for the detection of CRP, while Chapter 4 is established on horseradish peroxidase-mediated voltammetric immunoassays for p53 autoantibody quantification.

Chapter 2

Building on a well-established biorecpetive PANI interface,[166] in this chapter, a reagentless assessment for rapidly quantifying biomarkers will be introduced. By real-time monitoring the capacitive fingerprint of PANI under continuous flow conditions, this technique allows the determination of biomolecular binding kinetics, offering valuable insights into interactions essential for developing effective diagnostics and therapeutics.[181] In addition, the temporal change in redox capacitance C_r is sensitive to

target concentration, enabling the assaying of biomarker in just 15 second.[181] Exemplified with the quantification of C-reactive protein, this methodology significantly enhances turnaround efficiency by simplifying sample preparation without redox labelling, automating processes via microfluidics, and the employment of kinetic assessment. The integration with microfluidics in biosensing facilitates a streamlined, efficient, and highly sensitive platform for rapid biomarker quantification.

Chapter 3

Microfluidic integration not only showcases versatility in biosensing applications but also significantly improves biosensor performance. Characterised by convective mass transport, microfluidics accelerates the delivery of target analytes to the bioreceptors, thereby enhancing biorecognition kinetics. This enhancement effectively distinguishes between specific and nonspecific binding, with specific interactions being more influenced by flow conditions within microfluidic channels. By leveraging microfluidic confinements, enhanced assay sensitivity and selectivity are achieved, without resorting to conventional methods such as the employment of nanomaterials or catalytic amplifications. Such advancements demonstrate the potential of microfluidic systems to revolutionise biosensing, opening new avenues for developing a more sensitive, selective, and versatile approach to biomarker detection.

Chapter 4

In addition to profound biofouling, inefficient target recruitment on the 2D electrode surface limits the performance of electrochemical biosensors. To address these challenges, in this chapter, antigen-mimicking and antibody-capturing peptide-coated magnetic nanoparticles were employed,[85] along with an alternating current (AC) magnetic field-

promoted sample mixing, to immunomagnetic recruit cancer-relative biomarker from serum-spiked samples, prior to the presentation of Fab-captured targets to simple lectin-modified screen-printed electrode surface. The high sequence specificity of peptide-based bioreceptors, their dense coverage on nanoparticle surface, and the powerful magnetic manipulation ensures the sufficient target recruitment efficiency, supporting a scalable, robust, ultrasensitive, and highly selective electrochemical approach for early cancer diagnosis.

1.6 REFERENCES

(1) Strimbu, K.; Tavel, J. A. What are biomarkers? *Current Opinion in HIV and AIDS* **2010**, *5* (6), 463-466.
(2) Aronson, J. K.; Ferner, R. E. Biomarkers-a general review. *Curr. Protoc. Pharmacol.* **2017**, *76* (1), 9.23.01-29.23.17.
(3) Califf, R. M. Biomarker definitions and their applications. *Experimental biology and medicine* **2018**, *243* (3), 213-221.
(4) Wagner, K.-H.; Cameron-Smith, D.; Wessner, B.; Franzke, B. Biomarkers of aging: from function to molecular biology. *Nutrients* **2016**, *8* (6), 338.
(5) Tucci, P.; González-Sapienza, G.; Marin, M. Pathogen-derived biomarkers for active tuberculosis diagnosis. *Front. Microbiol.* **2014**, *5*, 549.
(6) Sahu, P. K.; Satpathi, S.; Behera, P. K.; Mishra, S. K.; Mohanty, S.; Wassmer, S. C. Pathogenesis of cerebral malaria: new diagnostic tools, biomarkers, and therapeutic approaches. *Front. Cell. Infect. Microbiol.* **2015**, *5*, 75.
(7) Anderson, D.; Kodukula, K. Biomarkers in pharmacology and drug discovery. *Biochem. Pharmacol.* **2014**, *87* (1), 172-188.
(8) Sonawane, M. D.; Nimse, S. B. C-Reactive protein: a major inflammatory biomarker. *Anal. Methods* **2017**, *9* (23), 3400-3413.
(9) LuÃ, X. p53: A Target and a Biomarker of Cancer Therapy. *Recent Adv. Cancer Res. Ther.* **2012**, *197*.
(10) Schwarzenbach, H. Circulating nucleic acids as biomarkers in breast cancer. *Breast Cancer Res.* **2013**, *15*, 1-9.
(11) Zarrouk, A.; Debbabi, M.; Bezine, M.; Karym, E. M.; Badreddine, A.; Rouaud, O.; Moreau, T.; Cherkaoui-Malki, M.; El Ayeb, M.; Nasser, B. Lipid biomarkers in Alzheimer's disease. *Curr. Alzheimer Res.* **2018**, *15* (4), 303-312.
(12) Qiu, S.; Cai, Y.; Yao, H.; Lin, C.; Xie, Y.; Tang, S.; Zhang, A. Small molecule metabolites: discovery of biomarkers and therapeutic targets. *Signal Transduction Targeted Ther.* **2023**, *8* (1), 132.
(13) Yap, T. A.; Lorente, D.; Omlin, A.; Olmos, D.; De Bono, J. S. Circulating tumor cells: a multifunctional biomarker. *Clin. Cancer Res.* **2014**, *20* (10), 2553-2568.
(14) Lilja, H.; Ulmert, D.; Vickers, A. J. Prostate-specific antigen and prostate cancer: prediction, detection and monitoring. *Nat. Rev. Cancer* **2008**, *8* (4), 268-278.
(15) Blackwood, M. A.; Weber, B. L. BRCA1 and BRCA2: from molecular genetics to clinical medicine. *J. Clin. Oncol.* **1998**, *16* (5), 1969-1977.
(16) Rennert, G.; Bisland-Naggan, S.; Barnett-Griness, O.; Bar-Joseph, N.; Zhang, S.; Rennert, H. S.; Narod, S. A. Clinical outcomes of breast cancer in carriers of BRCA1 and BRCA2 mutations. *N. Engl. J. Med.* **2007**, *357* (2), 115-123.
(17) Schiess, R.; Wollscheid, B.; Aebersold, R. Targeted proteomic strategy for clinical biomarker discovery. *Mol. Oncol.* **2009**, *3* (1), 33-44.
(18) Kaysheva, A. L.; Kopylov, A. T.; Ponomarenko, E. A.; Kiseleva, O. I.; Teryaeva, N. B.; Potapov, A. A.; Izotov, A. A.; Morozov, S. G.; Kudryavtseva, V. Y.; Archakov, A. I. Relative abundance of proteins in blood plasma samples from patients with chronic cerebral ischemia. *J. Mol. Neurosci.* **2018**, *64*, 440-448.
(19) Guo, L.; Zhao, Y.; Huang, Q.; Huang, J.; Tao, Y.; Chen, J.; Li, H.-Y.; Liu, H. Electrochemical protein biosensors for disease marker detection: progress and opportunities. *Microsyst. Nanoeng.* **2024**, *10* (1), 65.

(20) Bodaghi, A.; Fattahi, N.; Ramazani, A. Biomarkers: Promising and valuable tools towards diagnosis, prognosis and treatment of Covid-19 and other diseases. *Heliyon* **2023**, *9* (2).
(21) Hayes, D. F. Biomarker validation and testing. *Mol. Oncol.* **2015**, *9* (5), 960-966.
(22) Sharafeldin, M.; Davis, J. J. Point of care sensors for infectious pathogens. *Anal. Chem.* **2020**, *93* (1), 184-197.
(23) Kissinger, P. T. Biosensors-a perspective. *Biosens. Bioelectron.* **2005**, *20* (12), 2512-2516.
(24) Alberts, B.; Bray, D.; Hopkin, K.; Johnson, A. D.; Lewis, J.; Raff, M.; Roberts, K.; Walter, P. *Essential Cell Biology*; W.W. Norton & Company, 2015.
(25) Dill, K.; Jernigan, R. L.; Bahar, I. *Protein Actions: Principles and Modeling*; Garland Science, 2017.
(26) Alberts, B.; Heald, R.; Johnson, A.; Morgan, D.; Raff, M. C.; Roberts, K.; Wilson, J.; Walter, P.; Hunt, T. *Molecular Biology of the Cell*; W. W. Norton, 2022.
(27) Kraut, J. How do enzymes work? *Science* **1988**, *242* (4878), 533-540.
(28) Von Ballmoos, C.; Wiedenmann, A.; Dimroth, P. Essentials for ATP synthesis by F1F0 ATP synthases. *Annu. Rev. Biochem.* **2009**, *78* (1), 649-672.
(29) Beard, W. A.; Wilson, S. H. Structure and mechanism of DNA polymerase β. *Chem. Rev.* **2006**, *106* (2), 361-382.
(30) Gosline, J.; Lillie, M.; Carrington, E.; Guerette, P.; Ortlepp, C.; Savage, K. Elastic proteins: biological roles and mechanical properties. *Phil. Trans. R. Soc. Lon. B* **2002**, *357* (1418), 121-132.
(31) Shoulders, M. D.; Raines, R. T. Collagen structure and stability. *Annu. Rev. Biochem.* **2009**, *78* (1), 929-958.
(32) Jørgensen, P. L. Na, K-ATPase, structure and transport mechanism. *New Compr. Biochem.* **1992**, *21*, 1-26.
(33) Deng, D.; Xu, C.; Sun, P.; Wu, J.; Yan, C.; Hu, M.; Yan, N. Crystal structure of the human glucose transporter GLUT1. *Nature* **2014**, *510* (7503), 121-125.
(34) Sun, P. D.; Foster, C. E.; Boyington, J. C. Overview of protein structural and functional folds. *Curr. Protoc. Protein Sci.* **2004**, *35* (1), 17.11. 11-17.11. 189.
(35) Chakrabarti, P.; Pal, D. The interrelationships of side-chain and main-chain conformations in proteins. *Prog. Biophys. Mol. Biol.* **2001**, *76* (1-2), 1-102.
(36) Dwyer, D. S. Electronic properties of the amino acid side chains contribute to the structural preferences in protein folding. *J. Biomol. Struct. Dyn.* **2001**, *18* (6), 881-892.
(37) Bhattacharyya, M.; Ghosh, S.; Vishveshwara, S. Protein structure and function: looking through the network of side-chain interactions. *Curr. Protein Pept. Sci.* **2016**, *17* (1), 4-25.
(38) Yang, A.-S.; Honig, B. Free energy determinants of secondary structure formation: II. Antiparallel β-sheets. *J. Mol. Biol.* **1995**, *252* (3), 366-376.
(39) Yang, A.-S.; Honig, B. Free energy determinants of secondary structure formation: I. α-helices. *J. Mol. Biol.* **1995**, *252* (3), 351-365.
(40) Sund, H.; Weber, K. The quaternary structure of proteins. *Angew. Chem., Int. Ed.* **1966**, *5* (2), 231-245.
(41) Frieden, E. Non-covalent interactions: Key to biological flexibility and specificity. *J. Chem. Educ.* **1975**, *52* (12), 754.
(42) Karshikoff, A.; Jelesarov, I. Salt bridges and conformational flexibility: effect on protein stability. *Biotechnol. Biotechnol. Equip.* **2008**, *22* (1), 606-611.
(43) Mian, I. S.; Bradwell, A. R.; Olson, A. J. Structure, function and properties of antibody binding sites. *J. Mol. Biol.* **1991**, *217* (1), 133-151.

(44) Weis, W. I.; Kobilka, B. K. The molecular basis of G protein-coupled receptor activation. *Annu. Rev. Biochem.* **2018**, *87* (1), 897-919.
(45) Reichmann, D.; Rahat, O.; Cohen, M.; Neuvirth, H.; Schreiber, G. The molecular architecture of protein-protein binding sites. *Curr. Opin. Struct. Biol.* **2007**, *17* (1), 67-76.
(46) Ivarsson, Y.; Jemth, P. Affinity and specificity of motif-based protein-protein interactions. *Curr. Opin. Struct. Biol.* **2019**, *54*, 26-33.
(47) Vajda, S.; Guarnieri, F. Characterization of protein-ligand interaction sites using experimental and computational methods. *Curr. Opin. Drug Discovery Dev.* **2006**, *9* (3), 354.
(48) Feyereisen, M. W.; Feller, D.; Dixon, D. A. Hydrogen bond energy of the water dimer. *J. Phys. Chem.* **1996**, *100* (8), 2993-2997.
(49) Kildahl, N. K. Bond energy data summarized. *J. Chem. Educ.* **1995**, *72* (5), 423.
(50) Bahadur, R. P.; Chakrabarti, P.; Rodier, F.; Janin, J. A dissection of specific and non-specific protein-protein interfaces. *J. Mol. Biol.* **2004**, *336* (4), 943-955.
(51) Frutiger, A.; Tanno, A.; Hwu, S.; Tiefenauer, R. F.; Voros, J.; Nakatsuka, N. Nonspecific binding—fundamental concepts and consequences for biosensing applications. *Chem. Rev.* **2021**, *121* (13), 8095-8160.
(52) Copeland, R. A. Protein-ligand binding equilibria. In *Enzymes: A Practical Introduction to Structure, Mechanism, and Data Analysis*, Wiley, New York, 2000; pp 76-108.
(53) Kim, B.; Dikova, E.; Sheller, U.; Dikov, M.; Gavrilova, E.; Egorov, A. Evaluation of dissociation constants of antigen-antibody complexes by ELISA. *J. Immunol. Methods* **1990**, *131* (2), 213-222.
(54) Johansson, H.; Jensen, M. R.; Gesmar, H.; Meier, S.; Vinther, J. M.; Keeler, C.; Hodsdon, M. E.; Led, J. J. Specific and nonspecific interactions in ultraweak protein-protein associations revealed by solvent paramagnetic relaxation enhancements. *J. Am. Chem. Soc.* **2014**, *136* (29), 10277-10286.
(55) Levi, V.; Flecha, F. L. G. Reversible fast-dimerization of bovine serum albumin detected by fluorescence resonance energy transfer. *Biochim. Biophys. Acta, Proteins Proteomics* **2002**, *1599* (1-2), 141-148.
(56) Mix, E.; Goertsches, R.; Zett, U. K. Immunoglobulins-basic considerations. *J. Neurol.* **2006**, *253*, v9-v17.
(57) Edelman, G. M. Antibody structure and molecular immunology. *Science* **1973**, *180* (4088), 830-840.
(58) North, J. R. Immunosensors: antibody-based biosensors. *Trends Biotechnol.* **1985**, *3* (7), 180-186.
(59) Noh, S.; Kim, J.; Kim, G.; Park, C.; Jang, H.; Lee, M.; Lee, T. Recent advances in CRP biosensor based on electrical, electrochemical and optical methods. *Sensors* **2021**, *21* (9), 3024.
(60) Chambers, J. P.; Arulanandam, B. P.; Matta, L. L.; Weis, A.; Valdes, J. J. Biosensor recognition elements. *Curr. Issues Mol. Biol.* **2008**, *10* (1-2), 1-12.
(61) Trier, N. H.; Houen, G. Antibody cross-reactivity in auto-immune diseases. *Int. J. Mol. Sci.* **2023**, *24* (17), 13609.
(62) Black, S.; Kushner, I.; Samols, D. C-reactive protein. *J. Biol. Chem.* **2004**, *279* (47), 48487-48490.
(63) Clyne, B.; Olshaker, J. S. The C-reactive protein. *J. Emerg. Med.* **1999**, *17* (6), 1019-1025.

(64) Tillett, W. S.; Francis Jr, T. Serological reactions in pneumonia with a non-protein somatic fraction of pneumococcus. *J. Exp. Med.* **1930**, *52* (4), 561.
(65) Volanakis, J. E. Human C-reactive protein: expression, structure, and function. *Mol. Immunol.* **2001**, *38* (2-3), 189-197.
(66) Salazar, J.; Martínez, M. S.; Chávez-Castillo, M.; Núñez, V.; Añez, R.; Torres, Y.; Toledo, A.; Chacín, M.; Silva, C.; Pacheco, E. C‐reactive protein: an in‐depth look into structure, function, and regulation. *Int. Scholarly Res. Not.* **2014**, *2014* (1), 653045.
(67) Shrive, A. K.; Gheetham, G. M.; Holden, D.; Myles, D. A.; Turnell, W. G.; Volanakis, J. E.; Pepys, M. B.; Bloomer, A. C.; Greenhough, T. J. Three dimensional structure of human C-reactive protein. *Nat. Struct. Biol.* **1996**, *3* (4), 346-354.
(68) Thompson, D.; Pepys, M. B.; Wood, S. P. The physiological structure of human C-reactive protein and its complex with phosphocholine. *Structure* **1999**, *7* (2), 169-177.
(69) Marnell, L.; Mold, C.; Du Clos, T. W. C-reactive protein: ligands, receptors and role in inflammation. *Clin. Immunol.* **2005**, *117* (2), 104-111.
(70) Agrawal, A.; Xu, Y.; Ansardi, D.; Macon, K. J.; Volanakis, J. Probing the phosphocholine-binding site of human C-reactive protein by site-directed mutagenesis. *J. Biol. Chem.* **1992**, *267* (35), 25352-25358.
(71) Osmand, A.; Mortensen, R.; Siegel, J.; Gewurz, H. Interactions of C-reactive protein with the complement system. III. Complement-dependent passive hemolysis initiated by CRP. *J. Exp. Med.* **1975**, *142* (5), 1065-1077.
(72) Marnell, L. L.; Mold, C.; Volzer, M. A.; Burlingame, R. W.; Du Clos, T. C-reactive protein binds to Fc gamma RI in transfected COS cells. *J. Immunol.* **1995**, *155* (4), 2185-2193.
(73) Sproston, N. R.; Ashworth, J. J. Role of C-reactive protein at sites of inflammation and infection. *Front. Immunol.* **2018**, *9*, 754.
(74) Jones, S. A.; Novick, D.; Horiuchi, S.; Yamamoto, N.; Szalai, A. J.; Fuller, G. M. C-reactive protein: a physiological activator of interleukin 6 receptor shedding. *J. Exp. Med.* **1999**, *189* (3), 599-604.
(75) Robertson, M. Innate immunity. *Curr. Biol.* **1998**, *8* (17), R595-R597.
(76) Dominici, R.; Luraschi, P.; Franzini, C. Measurement of C‐reactive protein: Two high sensitivity methods compared. *J. Clin. Lab. Anal.* **2004**, *18* (5), 280-284.
(77) Otsuji, S.; Shibata, H.; Umeda, M. Turbidimetric immunoassay of serum C-reactive protein. *Clin. Chem.* **1982**, *28* (10), 2121-2124.
(78) Montagne, P.; Laroche, P.; Cuilliere, M.; Varcin, P.; Pau, B.; Duheille, J. Microparticle‐enhanced nephelometric immunoassay for human C‐reactive protein. *J. Clin. Lab. Anal.* **1992**, *6* (1), 24-29.
(79) Whicher, J.; Price, C.; Spencer, K.; Ward, A. M. Immunonephelometric and immunoturbidimetric assays for proteins. *Crit. Rev. Clin. Lab. Sci.* **1982**, *18* (3), 213-260.
(80) Drieghe, S. A.; Alsaadi, H.; Tugirimana, P. L.; Delanghe, J. R. A new high-sensitive nephelometric method for assaying serum C-reactive protein based on phosphocholine interaction. *Clin. Chem. Lab. Med.* **2014**, *52* (6), 861-867.
(81) Zhang, L.; Li, H.-Y.; Li, W.; Shen, Z.-Y.; Wang, Y.-D.; Ji, S.-R.; Wu, Y. An ELISA assay for quantifying monomeric C-reactive protein in plasma. *Front. Immunol.* **2018**, *9*, 511.
(82) Borque, L.; Bellod, L.; Rus, A.; Seco, M. L.; Galisteo-González, F. Development and validation of an automated and ultrasensitive immunoturbidimetric assay for C-reactive protein. *Clin. Chem.* **2000**, *46* (11), 1839-1842.

(83) Oh, S. W.; Moon, J. D.; Park, S. Y.; Jang, H. J.; Kim, J. H.; Nahm, K. B.; Choi, E. Y. Evaluation of fluorescence hs-CRP immunoassay for point-of-care testing. *Clin. Chim. Acta* **2005**, *356* (1-2), 172-177.
(84) Pundir, S.; Pundir, C. Detection of tumor suppressor protein p53 with special emphasis on biosensors: A review. *Anal. Biochem.* **2020**, *588*, 113473.
(85) Kang, S.; Yuan, D.; Barber, R.; Davis, J. J. Antigen-mimic nanoparticles in ultrasensitive on-chip integrated anti-p53 antibody quantification. *ACS Sens.* **2024**, *9* (3), 1475-1481.
(86) Eaton, L. World cancer rates set to double by 2020. British Medical Journal Publishing Group: 2003.
(87) Christopher P. Wild, E. W., Bernard W. Stewart. *World Cancer Report: Cancer Research for Cancer Prevention*; IARC press Lyon, 2020.
(88) Henry, N. L.; Hayes, D. F. Cancer biomarkers. *Mol. Oncol.* **2012**, *6* (2), 140-146.
(89) Labrecque, S.; Naor, N.; Thomson, D.; Matlashewski, G. Analysis of the anti-p53 antibody response in cancer patients. *Cancer Res.* **1993**, *53* (15), 3468-3471.
(90) Xu, R.; Rai, A.; Chen, M.; Suwakulsiri, W.; Greening, D. W.; Simpson, R. J. Extracellular vesicles in cancer—implications for future improvements in cancer care. *Nat. Rev. Clin. Oncol.* **2018**, *15* (10), 617-638.
(91) Lane, R.; Korbie, D.; Hill, M.; Trau, M. Extracellular vesicles as circulating cancer biomarkers: opportunities and challenges. *Clin. Transl. Med.* **2018**, *7*, 1-11.
(92) Wang, W.; Rong, Z.; Wang, G.; Hou, Y.; Yang, F.; Qiu, M. Cancer metabolites: promising biomarkers for cancer liquid biopsy. *Biomark. Res.* **2023**, *11* (1), 66.
(93) Park, J.; Shin, Y.; Kim, T. H.; Kim, D.-H.; Lee, A. Plasma metabolites as possible biomarkers for diagnosis of breast cancer. *PLoS One* **2019**, *14* (12), e0225129.
(94) Surget, S.; Khoury, M. P.; Bourdon, J.-C. Uncovering the role of p53 splice variants in human malignancy: a clinical perspective. *OncoTargets Ther.* **2014**, *7*, 57.
(95) Aubrey, B. J.; Kelly, G. L.; Janic, A.; Herold, M. J.; Strasser, A. How does p53 induce apoptosis and how does this relate to p53-mediated tumour suppression? *Cell Death Differ.* **2018**, *25* (1), 104-113.
(96) Vousden, K. H.; Lane, D. P. p53 in health and disease. *Nat. Rev. Mol. Cell Biol.* **2007**, *8* (4), 275-283.
(97) Ananiev, J.; Tchernev, G.; Patterson, J.; Gulubova, M.; Ganchev, G. p53-"the guardian of genome". *Acta Med. Bulg.* **2011**, *38* (2), 73.
(98) Bai, L.; Zhu, W.-G. p53: structure, function and therapeutic applications. *J. Cancer Mol.* **2006**, *2* (4), 141-153.
(99) Naryzhny, S.; Legina, O. Structural-functional diversity of p53 proteoforms. *Biochem. (Mosc.) Suppl. B: Biomed. Chem.* **2019**, *13* (4), 293-307.
(100) Purvis, J. E.; Karhohs, K. W.; Mock, C.; Batchelor, E.; Loewer, A.; Lahav, G. p53 dynamics control cell fate. *Science* **2012**, *336* (6087), 1440-1444.
(101) Liang, S. H.; Clarke, M. F. Regulation of p53 localization. *Eur. J. Biochem.* **2001**, *268* (10), 2779-2783.
(102) Gencel-Augusto, J.; Lozano, G. p53 tetramerization: at the center of the dominant-negative effect of mutant p53. *Genes Dev.* **2020**, *34* (17-18), 1128-1146.
(103) Raj, N.; Attardi, L. D. The transactivation domains of the p53 protein. *Cold Spring Harbor Perspect. Med.* **2017**, *7* (1), a026047.
(104) Weinberg, R. L.; Freund, S. M.; Veprintsev, D. B.; Bycroft, M.; Fersht, A. R. Regulation of DNA binding of p53 by its C-terminal domain. *J. Mol. Biol.* **2004**, *342* (3), 801-811.

(105) Perri, F.; Pisconti, S.; Scarpati, G. D. V. P53 mutations and cancer: a tight linkage. *Ann. Transl. Med.* **2016**, *4* (24).
(106) Attallah, A. M.; Abdel-Aziz, M. M.; El-Sayed, A. M.; Tabll, A. A. Detection of serum p53 protein in patients with different gastrointestinal cancers. *Cancer Detect. Prev.* **2003**, *27* (2), 127-131.
(107) Luo, J. C.; Zehab, R.; Anttila, S.; Ridanpaa, M.; Husgafvel-Pursiainen, K.; Vainio, H.; Carney, W.; DeVivo, I.; Milling, C.; Brandt-Rauf, P. W. Detection of serum p53 protein in lung cancer patients. *J. Occup. Med.* **1994**, *36* (2), 155-160.
(108) Freed-Pastor, W. A.; Prives, C. Mutant p53: one name, many proteins. *Genes Dev.* **2012**, *26* (12), 1268-1286.
(109) Afsharan, H.; Navaeipour, F.; Khalilzadeh, B.; Tajalli, H.; Mollabashi, M.; Ahar, M. J.; Rashidi, M.-R. Highly sensitive electrochemiluminescence detection of p53 protein using functionalized Ru-silica nanoporous@ gold nanocomposite. *Biosens. Bioelectron.* **2016**, *80*, 146-153.
(110) Hasbek, Z.; Doğan, Ö. T.; Sarı, İ.; Yücel, B.; Şeker, M. M.; Turgut, B.; Berk, S.; Siliğ, Y. The diagnostic value of the correlation between serum Anti-p53 antibody and positron emission tomography parameters in lung cancer. *Mol. Imaging Radionucl. Ther.* **2016**, *25* (3), 107.
(111) Sabapathy, K.; Lane, D. P. Understanding p53 functions through p53 antibodies. *J. Mol. Cell Biol.* **2019**, *11* (4), 317-329.
(112) Nissim, A.; Hoogenboom, H. R.; Tomlinson, I.; Flynn, G.; Midgley, C.; Lane, D.; Winter, G. Antibody fragments from a 'single pot'phage display library as immunochemical reagents. *EMBO J.* **1994**, *13* (3), 692-698.
(113) Rehman, A.; Chahal, M. S.; Tang, X.; Bruce, J. E.; Pommier, Y.; Daoud, S. S. Proteomic identification of heat shock protein 90 as a candidate target for p53 mutation reactivation by PRIMA-1 in breast cancer cells. *Breast Cancer Res.* **2005**, *7*, 1-10.
(114) Haidacher, S.; Blaschrtz, A.; Desoye, G.; Dohr, G. Immunohistochemical evidence of p53 protein in human placenta and choriocarcinoma cell lines. *Mol. Hum. Reprod.* **1995**, *1* (2), 63-68.
(115) Wolff, A.; Technau, A.; Ihling, C.; Technau-Ihling, K.; Erber, R.; Bosch, F. X.; Brandner, G. Evidence that wild-type p53 in neuroblastoma cells is in a conformation refractory to integration into the transcriptional complex. *Oncogene* **2001**, *20* (11), 1307-1317.
(116) Hwang, L.-A.; Phang, B. H.; Liew, O. W.; Iqbal, J.; Koh, X. H.; Koh, X. Y.; Othman, R.; Xue, Y.; Richards, A. M.; Lane, D. P. Monoclonal antibodies against specific p53 hotspot mutants as potential tools for precision medicine. *Cell Rep.* **2018**, *22* (1), 299-312.
(117) Cruz-Pacheco, A. F.; Quinchia, J.; Orozco, J. Cerium oxide-doped PEDOT nanocomposite for label-free electrochemical immunosensing of anti-p53 autoantibodies. *Microchim. Acta* **2022**, *189* (6), 228.
(118) Clark, L. Monitoring and control blood and tissue oxygen. *Trans. Am. Soc. Artif. Intern. Organs* **1958**, *2*, 41-48.
(119) Clark Jr, L. C.; Lyons, C. Electrode systems for continuous monitoring in cardiovascular surgery. *Ann. N. Y. Acad. Sci.* **1962**, *102* (1), 29-45.
(120) Newman, J.; Turner, A. Biosensors for monitoring glucose. In *Sensors in Medicine and Health Care: Sensors Applications*, Vol. 3; 2004; pp 45-78.
(121) Sethi, R. S. Transducer aspects of biosensors. *Biosens. Bioelectron.* **1994**, *9* (3), 243-264.

(122) Wilson, G. S.; Hu, Y. Enzyme-based biosensors for in vivo measurements. *Chem. Rev.* **2000**, *100* (7), 2693-2704.
(123) Sharma, S.; Byrne, H.; O'Kennedy, R. J. Antibodies and antibody-derived analytical biosensors. *Essays Biochem.* **2016**, *60* (1), 9-18.
(124) Du, Y.; Dong, S. Nucleic acid biosensors: recent advances and perspectives. *Anal. Chem.* **2017**, *89* (1), 189-215.
(125) Bousse, L. Whole cell biosensors. *Sens. Actuators, B* **1996**, *34* (1-3), 270-275.
(126) Gui, Q.; Lawson, T.; Shan, S.; Yan, L.; Liu, Y. The application of whole cell-based biosensors for use in environmental analysis and in medical diagnostics. *Sensors* **2017**, *17* (7), 1623.
(127) Borisov, S. M.; Wolfbeis, O. S. Optical biosensors. *Chem. Rev.* **2008**, *108* (2), 423-461.
(128) Skládal, P. Piezoelectric biosensors. *TrAC, Trends Anal. Chem.* **2016**, *79*, 127-133.
(129) Raiteri, R.; Grattarola, M.; Butt, H.-J.; Skládal, P. Micromechanical cantilever-based biosensors. *Sens. Actuators, B* **2001**, *79* (2-3), 115-126.
(130) Ronkainen, N. J.; Halsall, H. B.; Heineman, W. R. Electrochemical biosensors. *Chem. Soc. Rev.* **2010**, *39* (5), 1747-1763.
(131) Ramanathan, K.; Danielsson, B. Principles and applications of thermal biosensors. *Biosens. Bioelectron.* **2001**, *16* (6), 417-423.
(132) Li, B.; Yu, Q.; Duan, Y. Fluorescent labels in biosensors for pathogen detection. *Crit. Rev. Biotechnol.* **2015**, *35* (1), 82-93.
(133) Hnatowich, D.; Layne, W.; Childs, R.; Lanteigne, D.; Davis, M.; Griffin, T. W.; Doherty, P. Radioactive labeling of antibody: a simple and efficient method. *Science* **1983**, *220* (4597), 613-615.
(134) Zhang, Y.; Park, K.-Y.; Suazo, K. F.; Distefano, M. D. Recent progress in enzymatic protein labelling techniques and their applications. *Chem. Soc. Rev.* **2018**, *47* (24), 9106-9136.
(135) Mayer, A.; Neuenhofer, S. Luminescent labels-more than just an alternative to radioisotopes? *Angew. Chem., Int. Ed.* **1994**, *33* (10), 1044-1072.
(136) Sang, S.; Wang, Y.; Feng, Q.; Wei, Y.; Ji, J.; Zhang, W. Progress of new label-free techniques for biosensors: A review. *Crit. Rev. Biotechnol.* **2016**, *36* (3), 465-481.
(137) Arya, S. K.; Estrela, P. Recent advances in enhancement strategies for electrochemical ELISA-based immunoassays for cancer biomarker detection. *Sensors* **2018**, *18* (7), 2010.
(138) Sipova, H.; Zhang, S.; Dudley, A. M.; Galas, D.; Wang, K.; Homola, J. Surface plasmon resonance biosensor for rapid label-free detection of microribonucleic acid at subfemtomole level. *Anal. Chem.* **2010**, *82* (24), 10110-10115.
(139) Singh, P. SPR biosensors: historical perspectives and current challenges. *Sens. Actuators, B* **2016**, *229*, 110-130.
(140) Noi, K.; Iwata, A.; Kato, F.; Ogi, H. Ultrahigh-frequency, wireless MEMS QCM biosensor for direct, label-free detection of biomarkers in a large amount of contaminants. *Anal. Chem.* **2019**, *91* (15), 9398-9402.
(141) Daniels, J. S.; Pourmand, N. Label‐free impedance biosensors: Opportunities and challenges. *Electroanalysis* **2007**, *19* (12), 1239-1257.
(142) Harvey, D. *Modern Analytical Chemistry*; McGraw-Hill New York, 2000.
(143) Robinson, J. W.; Frame, E. M. S.; Frame II, G. M. *Instrumental Analytical Ehemistry: An Introduction*; CRC Press, 2021.

(144) Aguilera, E.; Lucena, R.; Cárdenas, S.; Valcárcel, M.; Trullols, E.; Ruisánchez, I. Robustness in qualitative analysis: a practical approach. *TrAC, Trends Anal. Chem.* **2006**, *25* (6), 621-627.
(145) Bollella, P.; Gorton, L. Enzyme based amperometric biosensors. *Curr. Opin. Electrochem.* **2018**, *10*, 157-173.
(146) Ding, J.; Qin, W. Recent advances in potentiometric biosensors. *TrAC, Trends Anal. Chem.* **2020**, *124*, 115803.
(147) Bard, A. J.; Faulkner, L. R.; White, H. S. *Electrochemical Methods: Fundamentals and Applications*; Wiley, 2022.
(148) Compton, R. G.; Banks, C. E. *Understanding Voltammetry*; World Scientific, 2018.
(149) Elgrishi, N.; Rountree, K. J.; McCarthy, B. D.; Rountree, E. S.; Eisenhart, T. T.; Dempsey, J. L. A practical beginner's guide to cyclic voltammetry. *J. Chem. Educ.* **2018**, *95* (2), 197-206.
(150) Feiner, A.-S.; McEvoy, A. The nernst equation. *J. Chem. Educ.* **1994**, *71* (6), 493.
(151) Trasatti, S. The concept of absolute electrode potential an attempt at a calculation. *J. Electroanal. Chem. Interfacial Electrochem.* **1974**, *52* (3), 313-329.
(152) Faulkner, L. R. Understanding Electrochemistry: Some Distinctive Concepts. ACS Publications: 1983.
(153) Bamford, C. H.; Tipper, C.; Compton, R. Electrode kinetics: Principles and methodology. **1986**.
(154) Laidler, K. J. The kinetics of electrode processes. *J. Chem. Educ.* **1970**, *47* (9), 600.
(155) Groß, A.; Sakong, S. Modelling the electric double layer at electrode/electrolyte interfaces. *Curr. Opin. Electrochem.* **2019**, *14*, 1-6.
(156) Chen, L. D.; Urushihara, M.; Chan, K.; Nørskov, J. K. Electric field effects in electrochemical CO2 reduction. *ACS Catal.* **2016**, *6* (10), 7133-7139.
(157) Menshykau, D.; Streeter, I.; Compton, R. G. Influence of electrode roughness on cyclic voltammetry. *J. Phys. Chem. C* **2008**, *112* (37), 14428-14438.
(158) Dickinson, E. J.; Wain, A. J. The Butler-Volmer equation in electrochemical theory: Origins, value, and practical application. *J. Electroanal. Chem.* **2020**, *872*, 114145.
(159) Cha, J.-E.; Seo, M. H.; Choi, Y.-W.; Kim, W. B. A practical approach to measuring the ion-transport number of cation-exchange membranes: Effects of junction potential and analyte concentration. *J. Membr. Sci.* **2021**, *635*, 119471.
(160) Dickinson, E. J.; Limon-Petersen, J. G.; Rees, N. V.; Compton, R. G. How much supporting electrolyte is required to make a cyclic voltammetry experiment quantitatively "diffusional"? A theoretical and experimental investigation. *J. Phys. Chem. C* **2009**, *113* (25), 11157-11171.
(161) Sharafeldin, M.; James, T.; Davis, J. J. Open circuit potential as a tool for the assessment of binding kinetics and reagentless protein quantitation. *Anal. Chem.* **2021**, *93* (44), 14748-14754.
(162) El Harrad, L.; Amine, A. Chronoamperometric biosensor for protease activity assay and inhibitor screening. *Electroanalysis* **2017**, *29* (10), 2395-2400.
(163) Bergveld, P.; Eijkel, J. C.; Olthuis, W. Detection of protein concentrations with chronopotentiometry. *Biosens. Bioelectron.* **1997**, *12* (9-10), 905-916.
(164) Hassanain, W. A.; Sivanesan, A.; Izake, E. L.; Ayoko, G. A. An electrochemical biosensor for the rapid detection of erythropoietin in blood. *Talanta* **2018**, *189*, 636-640.
(165) Chen, A.; Shah, B. Electrochemical sensing and biosensing based on square wave voltammetry. *Anal. Methods* **2013**, *5* (9), 2158-2173.
(166) Baradoke, A.; Hein, R.; Li, X.; Davis, J. J. Reagentless redox capacitive assaying of C-reactive protein at a polyaniline interface. *Anal. Chem.* **2020**, *92* (5), 3508-3511.

(167) Garrote, B. L.; Santos, A.; Bueno, P. R. Label-free capacitive assaying of biomarkers for molecular diagnostics. *Nat. Protoc.* **2020**, *15* (12), 3879-3893.
(168) Pan, R.; Hu, K.; Jiang, D.; Samuni, U.; Mirkin, M. V. Electrochemical resistive-pulse sensing. *J. Am. Chem. Soc.* **2019**, *141* (50), 19555-19559.
(169) Shi, W.; Friedman, A. K.; Baker, L. A. Nanopore sensing. *Anal. Chem.* **2017**, *89* (1), 157-188.
(170) Harrell, C. C.; Choi, Y.; Horne, L. P.; Baker, L. A.; Siwy, Z. S.; Martin, C. R. Resistive-pulse DNA detection with a conical nanopore sensor. *Langmuir* **2006**, *22* (25), 10837-10843.
(171) Lin, P.-H.; Li, B.-R. Antifouling strategies in advanced electrochemical sensors and biosensors. *Analyst* **2020**, *145* (4), 1110-1120.
(172) Wu, Y.; Tilley, R. D.; Gooding, J. J. Challenges and solutions in developing ultrasensitive biosensors. *J. Am. Chem. Soc.* **2018**, *141* (3), 1162-1170.
(173) Tehrani, Z.; Abbasi, H. Y.; Devadoss, A.; Evans, J. E.; Guy, O. J. Assessing surface coverage of aminophenyl bonding sites on diazotised glassy carbon electrodes for optimised electrochemical biosensor performance. *Nanomaterials* **2021**, *11* (2), 416.
(174) Soleymani, L.; Li, F. Mechanistic challenges and advantages of biosensor miniaturization into the nanoscale. *ACS Sens.* **2017**, *2* (4), 458-467.
(175) Kikkeri, K.; Wu, D.; Voldman, J. A sample-to-answer electrochemical biosensor system for biomarker detection. *Lab Chip* **2022**, *22* (1), 100-107.
(176) Jaros, J. A.; Guest, P. C.; Bahn, S.; Martins-de-Souza, D. Affinity depletion of plasma and serum for mass spectrometry-based proteome analysis. In *Proteomics for Biomarker Discovery*, 2013; pp 1-11.
(177) Tonry, C. L.; Leacy, E.; Raso, C.; Finn, S. P.; Armstrong, J.; Pennington, S. R. The role of proteomics in biomarker development for improved patient diagnosis and clinical decision making in prostate cancer. *Diagnostics* **2016**, *6* (3), 27.
(178) Baker, M. Antibody anarchy: a call to order. *Nature* **2015**, *527* (7579), 545-551.
(179) Sharafeldin, M.; Fleschhut, F.; James, T.; Davis, J. J. A quantification of target protein biomarkers in complex media by faradaic shotgun tagging. *Anal. Chem.* **2022**, *94* (5), 2375-2382.
(180) Qi, H.; Hu, Z.; Yang, Z.; Zhang, J.; Wu, J. J.; Cheng, C.; Wang, C.; Zheng, L. Capacitive aptasensor coupled with microfluidic enrichment for real-time detection of trace SARS-CoV-2 nucleocapsid protein. *Anal. Chem.* **2022**, *94* (6), 2812-2819.
(181) Kang, S.; Sharafeldin, M.; Patrick, S. C.; Chen, X.; Davis, J. J. Ultrafast biomarker quantification through reagentless capacitive kinetics. *Anal. Chem.* **2023**, *95* (10), 4721-4727.
(182) Fernández-la-Villa, A.; Pozo-Ayuso, D. F.; Castaño-Álvarez, M. Microfluidics and electrochemistry: An emerging tandem for next-generation analytical microsystems. *Curr. Opin. Electrochem.* **2019**, *15*, 175-185.
(183) Farka, Z.; Jurik, T.; Kovar, D.; Trnkova, L.; Skládal, P. Nanoparticle-based immunochemical biosensors and assays: recent advances and challenges. *Chem. Rev.* **2017**, *117* (15), 9973-10042.
(184) Luo, X.; Morrin, A.; Killard, A. J.; Smyth, M. R. Application of nanoparticles in electrochemical sensors and biosensors. *Electroanalysis* **2006**, *18* (4), 319-326.
(185) Rackus, D. G.; Shamsi, M. H.; Wheeler, A. R. Electrochemistry, biosensors and microfluidics: a convergence of fields. *Chem. Soc. Rev.* **2015**, *44* (15), 5320-5340.
(186) Li, T.; Díaz-Real, J. A.; Holm, T. Design of electrochemical microfluidic detectors: A review. *Adv. Mater. Technol.* **2021**, *6* (12), 2100569.

(187) Lafleur, J. P.; Jönsson, A.; Senkbeil, S.; Kutter, J. P. Recent advances in lab-on-a-chip for biosensing applications. *Biosens. Bioelectron.* **2016**, *76*, 213-233.
(188) Wang, J. Nanomaterial-based electrochemical biosensors. *Analyst* **2005**, *130* (4), 421-426.
(189) Wang, Z.; Dai, Z. Carbon nanomaterial-based electrochemical biosensors: an overview. *Nanoscale* **2015**, *7* (15), 6420-6431.
(190) Pingarrón, J. M.; Yanez-Sedeno, P.; González-Cortés, A. Gold nanoparticle-based electrochemical biosensors. *Electrochim. Acta* **2008**, *53* (19), 5848-5866.
(191) Jacobs, C. B.; Peairs, M. J.; Venton, B. J. Carbon nanotube based electrochemical sensors for biomolecules. *Anal. Chim. Acta* **2010**, *662* (2), 105-127.
(192) Loo, A. H.; Bonanni, A.; Pumera, M. Thrombin aptasensing with inherently electroactive graphene oxide nanoplatelets as labels. *Nanoscale* **2013**, *5* (11), 4758-4762.
(193) Bonanni, A.; Chua, C. K.; Zhao, G.; Sofer, Z. k.; Pumera, M. Inherently electroactive graphene oxide nanoplatelets as labels for single nucleotide polymorphism detection. *ACS Nano* **2012**, *6* (10), 8546-8551.
(194) Bahadır, E. B.; Sezgintürk, M. K. Applications of graphene in electrochemical sensing and biosensing. *TrAC, Trends Anal. Chem.* **2016**, *76*, 1-14.
(195) Moeser, G. D.; Roach, K. A.; Green, W. H.; Alan Hatton, T.; Laibinis, P. E. High-gradient magnetic separation of coated magnetic nanoparticles. *AIChE J.* **2004**, *50* (11), 2835-2848.
(196) Olsvik, O.; Popovic, T.; Skjerve, E.; Cudjoe, K. S.; Hornes, E.; Ugelstad, J.; Uhlén, M. Magnetic separation techniques in diagnostic microbiology. *Clin. Immunol. Rev.* **1994**, *7* (1), 43-54.
(197) Zhu, N.; Ji, H.; Yu, P.; Niu, J.; Farooq, M.; Akram, M. W.; Udego, I.; Li, H.; Niu, X. Surface modification of magnetic iron oxide nanoparticles. *Nanomaterials* **2018**, *8* (10), 810.
(198) Boyer, C.; Priyanto, P.; Davis, T. P.; Pissuwan, D.; Bulmus, V.; Kavallaris, M.; Teoh, W. Y.; Amal, R.; Carroll, M.; Woodward, R. Anti-fouling magnetic nanoparticles for siRNA delivery. *J. Mater. Chem.* **2010**, *20* (2), 255-265.
(199) Whitesides, G. M. The origins and the future of microfluidics. *Nature* **2006**, *442* (7101), 368-373.
(200) Pungor, E.; Fehér, Z.; Váradi, M.; Campbell, B. H. Hydrodynamic voltammetry. **1980**.
(201) Li, B.; Chen, J.; Long, M. Measuring binding kinetics of surface-bound molecules using the surface plasmon resonance technique. *Anal. Biochem.* **2008**, *377* (2), 195-201.
(202) Rabbany, S. Y.; Kusterbeck, A. W.; Bredehorst, R.; Ligler, F. S. Binding kinetics of immobilized antibodies in a flow immunosensor. *Sens. Actuators, B* **1995**, *29* (1-3), 72-78.
(203) Hu, G.; Gao, Y.; Li, D. Modeling micropatterned antigen-antibody binding kinetics in a microfluidic chip. *Biosens. Bioelectron.* **2007**, *22* (7), 1403-1409.
(204) Barr, D. I. H. The Transition from Laminar to Turbulent Flow. *Proc. Instn. Civ. Engrs.* **1980**, *69* (2), 555-562.
(205) Cooper, J. A.; Compton, R. G. Channel electrodes-a review. *Electroanalysis* **1998**, *10* (3), 141-155.
(206) Bond, A. M.; Oldham, K. B.; Zoski, C. G. Steady-state voltammetry. *Anal. Chim. Acta* **1989**, *216*, 177-230.

(207) Hearty, S.; Leonard, P.; O'Kennedy, R. Measuring antibody-antigen binding kinetics using surface plasmon resonance. In *Antibody Engineering: Methods and Protocols*, Second Edition ed.; 2012; pp 411-442.
(208) Déjardin, P.; Vasina, E. N. An accurate simplified data treatment for the initial adsorption kinetics in conditions of laminar convection in a slit: application to protein adsorption. *Colloids Surf., B* **2004**, *33* (2), 121-127.
(209) Edwards, P. R.; Leatherbarrow, R. J. Determination of association rate constants by an optical biosensor using initial rate analysis. *Anal. Biochem.* **1997**, *246* (1), 1-6.
(210) Dejardin, P.; Le, M.; Johner, A.; Wittmer, J. Adsorption rate in the convection-diffusion model. *Langmuir* **1994**, *10* (10), 3898-3901.
(211) Gervais, T.; Jensen, K. F. Mass transport and surface reactions in microfluidic systems. *Chem. Eng. Sci.* **2006**, *61* (4), 1102-1121.
(212) Sigmundsson, K.; Másson, G.; Rice, R.; Beauchemin, N.; Öbrink, B. Determination of active concentrations and association and dissociation rate constants of interacting biomolecules: an analytical solution to the theory for kinetic and mass transport limitations in biosensor technology and its experimental verification. *Biochemistry* **2002**, *41* (26), 8263-8276.
(213) Jarmoskaite, I.; AlSadhan, I.; Vaidyanathan, P. P.; Herschlag, D. How to measure and evaluate binding affinities. *Elife* **2020**, *9*, e57264.
(214) Schreiber, G.; Haran, G.; Zhou, H.-X. Fundamental aspects of protein− protein association kinetics. *Chem. Rev.* **2009**, *109* (3), 839-860.
(215) Christensen, L. L. Theoretical analysis of protein concentration determination using biosensor technology under conditions of partial mass transport limitation. *Anal. Biochem.* **1997**, *249* (2), 153-164.
(216) Richalet-Sécordel, P. M.; Rauffer-Bruyère, N.; Christensen, L. L.; Ofenloch-Haehnle, B.; Seidel, C.; Van Regenmortel, M. H. Concentration measurement of unpurified proteins using biosensor technology under conditions of partial mass transport limitation. *Anal. Biochem.* **1997**, *249* (2), 165-173.
(217) Ogi, H.; Fukunishi, Y.; Nagai, H.; Okamoto, K.; Hirao, M.; Nishiyama, M. Nonspecific-adsorption behavior of polyethylenglycol and bovine serum albumin studied by 55-MHz wireless-electrodeless quartz crystal microbalance. *Biosens. Bioelectron.* **2009**, *24* (10), 3148-3152.
(218) Best, R. B.; Zheng, W.; Mittal, J. Balanced protein–water interactions improve properties of disordered proteins and non-specific protein association. *J. Chem. Theory Comput.* **2014**, *10* (11), 5113-5124.
(219) Gountia, D. Reliability issues in state-of-the-art microfluidic biochips: A survey. *IETE Tech. Rev.* **2023**, *40* (5), 694-709.
(220) Lim, Y. C.; Kouzani, A. Z.; Duan, W. Lab-on-a-chip: a component view. *Microsyst. Technol.* **2010**, *16*, 1995-2015.
(221) Haeberle, S.; Zengerle, R. Microfluidic platforms for lab-on-a-chip applications. *Lab Chip* **2007**, *7* (9), 1094-1110.
(222) Becker, H.; Locascio, L. E. Polymer microfluidic devices. *Talanta* **2002**, *56* (2), 267-287.
(223) Niculescu, A.-G.; Chircov, C.; Bîrcă, A. C.; Grumezescu, A. M. Fabrication and applications of microfluidic devices: A review. *Int. J. Mol. Sci.* **2021**, *22* (4), 2011.
(224) Pattanayak, P.; Singh, S. K.; Gulati, M.; Vishwas, S.; Kapoor, B.; Chellappan, D. K.; Anand, K.; Gupta, G.; Jha, N. K.; Gupta, P. K. Microfluidic chips: recent advances, critical strategies in design, applications and future perspectives. In *Microfluidics and Nanofluidics*, Vol. 25; 2021; pp 1-28.

(225) Cardoso Marques, M. P.; Lorente-Arevalo, A.; Bolivar, J. M. Biocatalysis in continuous-flow microfluidic reactors. In *Microfluidics in Biotechnology*, Springer, 2021; pp 211-246.
(226) Liu, G.; Huang, H.; Chen, Z.; Lin, H.; Liu, H.; Huang, X.; Guo, W. Design automation for continuous-flow microfluidic biochips: A comprehensive review. *Integration* **2022**, *82*, 48-66.
(227) Teh, S.-Y.; Lin, R.; Hung, L.-H.; Lee, A. P. Droplet microfluidics. *Lab Chip* **2008**, *8* (2), 198-220.
(228) Shi, J.; Tong, L.; Tong, W.; Chen, H.; Lan, M.; Sun, X.; Zhu, Y. Current progress in long-term and continuous cell metabolite detection using microfluidics. *TrAC, Trends Anal. Chem.* **2019**, *117*, 263-279.
(229) Marcus, J. S.; Anderson, W. F.; Quake, S. R. Parallel picoliter RT-PCR assays using microfluidics. *Anal. Chem.* **2006**, *78* (3), 956-958.
(230) Berthier, J. *Micro-drops and Digital Microfluidics*; William Andrew, 2012.
(231) Pan, L.-J.; Tu, J.-W.; Ma, H.-T.; Yang, Y.-J.; Tian, Z.-Q.; Pang, D.-W.; Zhang, Z.-L. Controllable synthesis of nanocrystals in droplet reactors. *Lab Chip* **2018**, *18* (1), 41-56.
(232) Joensson, H. N.; Andersson Svahn, H. Droplet microfluidics-A tool for single‐cell analysis. *Angew. Chem., Int. Ed.* **2012**, *51* (49), 12176-12192.
(233) Chung, S.; Revia, R. A.; Zhang, M. Graphene quantum dots and their applications in bioimaging, biosensing, and therapy. *Adv. Mater.* **2021**, *33* (22), 1904362.
(234) Nie, L.; Liu, F.; Ma, P.; Xiao, X. Applications of gold nanoparticles in optical biosensors. *J. Biomed. Nanotechnol.* **2014**, *10* (10), 2700-2721.
(235) Guo, L.; Liu, C.; Qi, M.; Cheng, L.; Wang, L.; Li, C.; Dong, B. Recent progress of nanostructure-based enrichment of circulating tumor cells and downstream analysis. *Lab Chip* **2023**, *23* (6), 1493-1523.
(236) Sharafeldin, M.; Yan, S.; Jiang, C.; Tofaris, G. K.; Davis, J. J. Alternating magnetic field-promoted nanoparticle mixing: the on-chip immunocapture of serum neuronal exosomes for Parkinson's disease diagnostics. *Anal. Chem.* **2023**.
(237) Nguyen, M. D.; Tran, H.-V.; Xu, S.; Lee, T. R. Fe3O4 nanoparticles: structures, synthesis, magnetic properties, surface functionalization, and emerging applications. *Appl. Sci.* **2021**, *11* (23), 11301.
(238) Wu, W.; Wu, Z.; Yu, T.; Jiang, C.; Kim, W.-S. Recent progress on magnetic iron oxide nanoparticles: synthesis, surface functional strategies and biomedical applications. *Sci. Technol. Adv. Mater.* **2015**, *16* (2), 023501.
(239) Shokrollahi, H. A review of the magnetic properties, synthesis methods and applications of maghemite. *J. Magn. Magn. Mater.* **2017**, *426*, 74-81.
(240) Rogers, H. B.; Anani, T.; Choi, Y. S.; Beyers, R. J.; David, A. E. Exploiting size-dependent drag and magnetic forces for size-specific separation of magnetic nanoparticles. *Int. J. Mol. Sci.* **2015**, *16* (8), 20001-20019.
(241) Coey, J. M. *Magnetism and Magnetic Materials*; Cambridge university press, 2010.
(242) Saini, S.; Frankel, R. B.; Stark, D. D.; Ferrucci Jr, J. Magnetism: a primer and review. *Am. J. Roentgenol.* **1988**, *150* (4), 735-743.
(243) Kong, L. B.; Liu, L.; Yang, Z.; Li, S.; Zhang, T.; Wang, C. Theory of ferrimagnetism and ferrimagnetic metal oxides. In *Magnetic, Ferroelectric, and Multiferroic Metal Oxides*, Elsevier, 2018; pp 287-311.
(244) Blaney, L. Magnetite (Fe3O4): Properties, synthesis, and applications. **2007**.

(245) Bonnemain, B. Superparamagnetic agents in magnetic resonance imaging: physicochemical characteristics and clinical applications a review. *J. Drug Targeting* **1998**, *6* (3), 167-174.
(246) Qiao, R.; Yang, C.; Gao, M. Superparamagnetic iron oxide nanoparticles: from preparations to in vivo MRI applications. *J. Mater. Chem.* **2009**, *19* (35), 6274-6293.
(247) Palanisamy, S.; Wang, Y.-M. Superparamagnetic iron oxide nanoparticulate system: synthesis, targeting, drug delivery and therapy in cancer. *Dalton Trans.* **2019**, *48* (26), 9490-9515.
(248) Ståhl, K.; Nielsen, K.; Jiang, J.; Lebech, B.; Hanson, J. C.; Norby, P.; van Lanschot, J. On the akaganéite crystal structure, phase transformations and possible role in post-excavational corrosion of iron artifacts. *Corros. Sci.* **2003**, *45* (11), 2563-2575.
(249) Gilleo, M. Superexchange interaction energy for Fe 3+-O 2−-Fe 3+ linkages. *Phys. Rev.* **1958**, *109* (3), 777.
(250) Curély, J. Magnetic orbitals and mechanisms of exchange II. Superexchange. *Monatsh. Chemie* **2005**, *136*, 1013-1036.
(251) Niculescu, A.-G.; Chircov, C.; Grumezescu, A. M. Magnetite nanoparticles: Synthesis methods-A comparative review. *Methods* **2022**, *199*, 16-27.
(252) Khani, A. H.; Rashidi, A.; Kashi, G. Synthesis of tungsten nanoparticles by reverse micelle method. *J. Mol. Liq.* **2017**, *241*, 897-903.
(253) Seo, K.; Sinha, K.; Novitskaya, E.; Graeve, O. A. Polyvinylpyrrolidone (PVP) effects on iron oxide nanoparticle formation. *Mater. Lett.* **2018**, *215*, 203-206.
(254) Graeve, O. A.; Fathi, H.; Kelly, J. P.; Saterlie, M. S.; Sinha, K.; Rojas-George, G.; Kanakala, R.; Brown, D. R.; Lopez, E. A. Reverse micelle synthesis of oxide nanopowders: Mechanisms of precipitate formation and agglomeration effects. *J. Colloid Interface Sci.* **2013**, *407*, 302-309.
(255) Ooi, C. C.; Park, S.-m.; Wong, D. J.; Gambhir, S. S.; Wang, S. X. Capture and genetic analysis of circulating tumor cells using a magnetic separation device (Magnetic Sifter). In *Circulating Tumor Cells: Methods and Protocols*, 2017; pp 153-162.
(256) Nakajima, N.; Ikada, Y. Mechanism of amide formation by carbodiimide for bioconjugation in aqueous media. *Bioconjugate Chem.* **1995**, *6* (1), 123-130.
(257) Richards, F.; Knowles, J. Glutaraldehyde as a protein cross-linking reagent. *J. Mol. Biol.* **1968**, *37* (1), 231-233.
(258) Heinze, T.; Rahn, K.; Jaspers, M.; Berghmans, H. p‐Toluenesulfonyl esters in cellulose modifications: acylation of remaining hydroxyl groups. *Macromol. Chem. Phys.* **1996**, *197* (12), 4207-4224.
(259) Mateo, C.; Fernández-Lorente, G.; Abian, O.; Fernández-Lafuente, R.; Guisán, J. M. Multifunctional epoxy supports: a new tool to improve the covalent immobilization of proteins. The promotion of physical adsorptions of proteins on the supports before their covalent linkage. *Biomacromolecules* **2000**, *1* (4), 739-745.
(260) Shojaee, P.; Niroomand-Oscuii, H.; Sefidgar, M.; Alinezhad, L. Effect of nanoparticle size, magnetic intensity, and tumor distance on the distribution of the magnetic nanoparticles in a heterogeneous tumor microenvironment. *J. Magn. Magn. Mater.* **2020**, *498*, 166089.
(261) Jiang, C.; Wang, G.; Hein, R.; Liu, N.; Luo, X.; Davis, J. J. Antifouling strategies for selective in vitro and in vivo sensing. *Chem. Rev.* **2020**, *120* (8), 3852-3889.

Chapter 2

Ultrafast Biomarker Quantification through

Reagentless Capacitive Kinetics

2.1 BACKGROUND

Polyaniline (PANI) is a conductive long-chain polymer composed of repeating units of aniline.[1] Its unique conductivity (ranging from 10^{-4} to $10^{2}\ S \cdot cm^{-1}$)[2-4] is attributed to transformations between quinoid (oxidised) and benzenoid (reduced) structures.[5, 6] Based on their relative proportions, three oxidation states can be identified: leucoemeraldine (fully reduced), emeraldine, and pernigraniline (fully oxidised),[5, 6] as shown in Figure **2.1**, which can be easily tailored by doping agents.[7] This tuneable conductivity, along with ease of synthesis, chemical stability, and great biocompatibility makes PANI versatile in electronics,[8, 9] supercapacitors,[10, 11] and biomedical applications.[12-14]

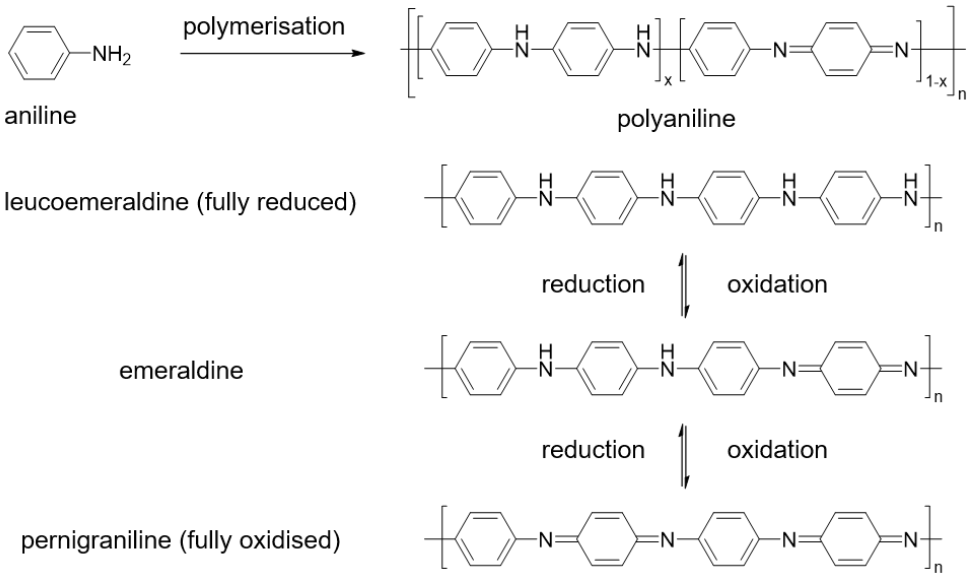


Figure 2.1. Schematic representation of the polymerisation process of polyaniline (PANI) and the interconversion among its three oxidation states: leucoemeraldine, emeraldine, and pernigraniline.[5]

Regarding electrochemical biosensing, the conductive nature of PANI facilitates efficient electron transfer between the biological recognition element and the electrode surface. Additionally, this rapid and reversible electron transfer generates capacitive fingerprints,[12, 15] allowing PANI to specifically probe and monitor biorecognition events.

The redox capacitance C_r of PANI decreases in response to the presence of specific biomarkers, making it an ideal material for developing advanced label-free electrochemical biosensors.[12]

Building on a well-established bio-receptive PANI interface,[12] herein, the potential of a microfluidic-integrated capacitive biosensor was explored for real-time monitoring of biorecognition events and the assessment of binding kinetics.[13] Additionally, exemplified by C-reactive protein, the temporal change in C_r enables the sensitive assaying of biomarker concentration in just 15 seconds, as shown in Figure **2.2**. This reagentless methodology provides a streamlined, efficient, and highly sensitive platform for rapid biomarker quantification, significantly improving assay turnaround efficiency for real-world applications.

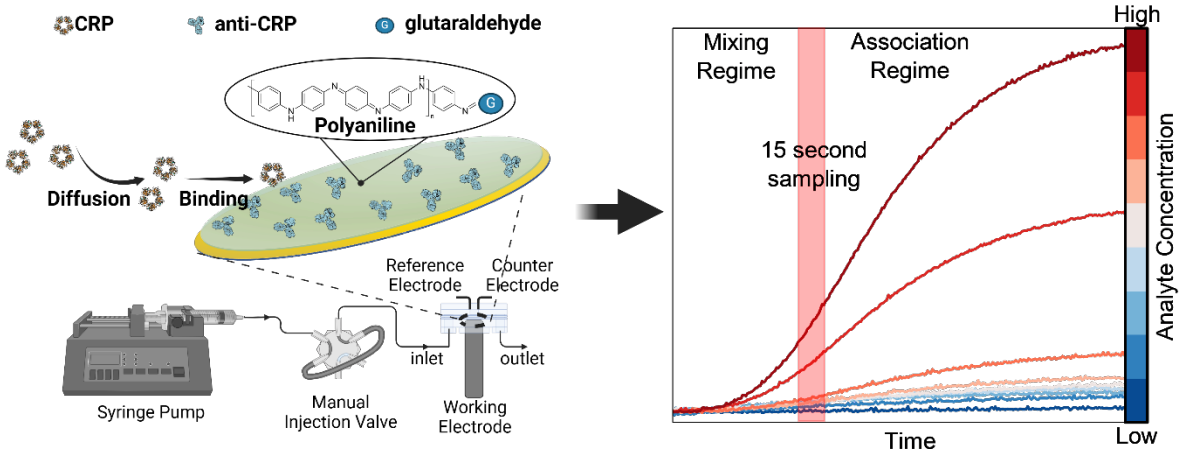


Figure 2.2. Schematic representation of a microfluidic-integrated electrochemical setup for real-time capacitive monitoring of CRP biorecognition sensogram.[13] The system features an antibody-modified Au disc electrode housed within a custom 3D-printed microfluidic cell, along with a Ag/AgCl reference wire electrode and a Pt counter wire electrode. Samples and running buffer are delivered via an automated syringe pump, with an adjustable flow rate of up to 500 $\mu L \cdot min^{-1}$. CRP quantification is derived from the temporal response, measured 15 seconds after sample mixing.

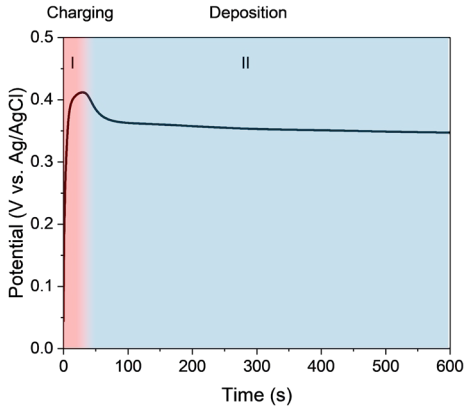
2.2 BIORECEPTIVE POLYANILINE PREPARATION

2.2.1 Electrochemical Deposition of PANI

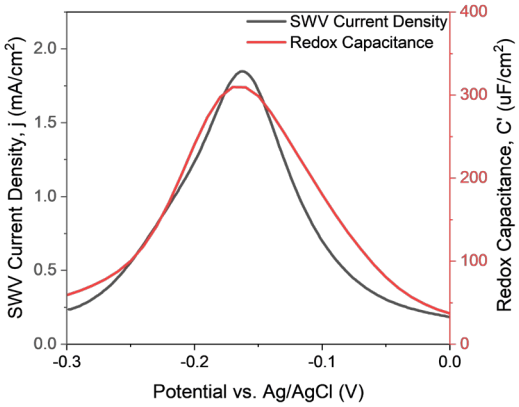
The PANI film was fabricated following our established electrodeposition protocol.[12] Briefly, an aniline solution was prepared by mixing 1 mL of 98% aniline with 2 mL of 50% phytic acid, followed by the addition of 17 mL of deionised water. Phytic acid, a hexaphosphorylated inositol derivative with a six-membered carbon ring attached to six phosphate groups, was essential in this process. It provided an acidic environment that enhances the solubility of aniline;[6] and, as a doping agent, facilitated the electron transfer within polyaniline, thereby enhancing the conductivity of the resulting coating.[16]

Electrodeposition was performed by immersing Au disc electrodes into the prepared solution and applying a chronopotentiometric scan at a current density of 10 $\mu A \cdot cm^{-2}$ for 10 minutes,[12] allowing the consistent thickness of the resulting PANI films. As shown in Figure **2.3a**, an initial sharp increase in potential during the electrodeposition process (Region I) was attributed to double layer charging.[17] This rise continued until the potential reached the deposition threshold (E_{dep} = + 0.41 V *vs.* Ag/AgCl), initiating aniline polymerisation and promoting uniform PANI film growth. As detailed in Section **6.3.1** and *eqn.* **6.2**, the electrodeposition of conductive PANI onto the electrode surface increased the interface capacitance (Figure **2.3b**), resulting in a gradual decrease in potential in Region II.[17] Subsequent capacitance potential scans and SWV measurements confirmed the formation of PANI films, with a distinct redox peak observed at E_{half} = -0.16 V (*vs.* Ag/AgCl), consistent with expectations.[12]

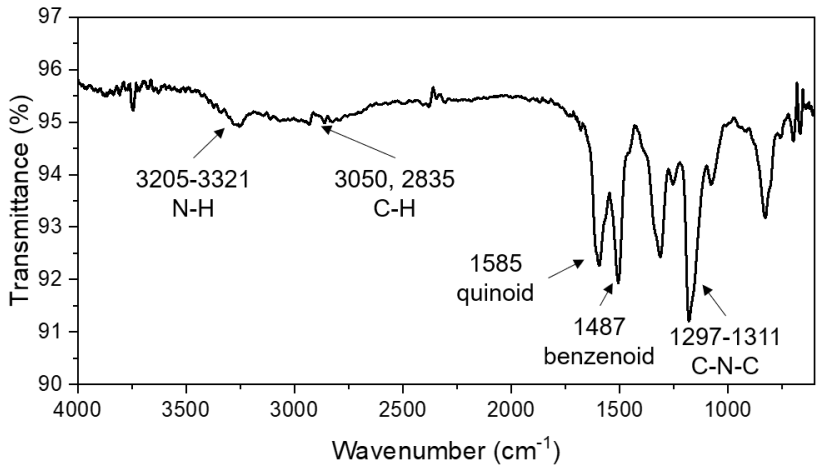
(a)


Charging
Deposition
I
II
Potential (V vs. Ag/AgCl)
Time (s)

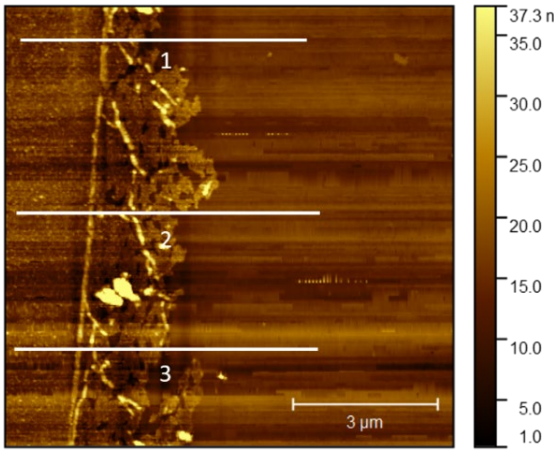
(b)


SWV Current Density
Redox Capacitance
SWV Current Density, j (mA/cm²)
Redox Capacitance, C' (uF/cm²)
Potential vs. Ag/AgCl (V)

(c)


Transmittance (%)
3205-3321
N-H
3050, 2835
C-H
1585
quinoid
1487
benzenoid
1297-1311
C-N-C
Wavenumber (cm-1)

(d)


1
2
3
3 µm

(e)

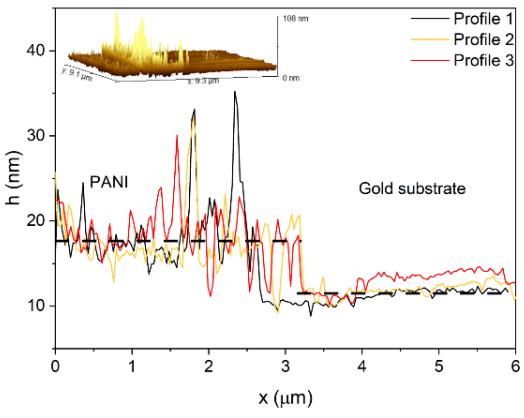

Profile 1
Profile 2
Profile 3
PANI
Gold substrate
h (nm)
x (µm)

Figure 2.3. (a) Representative electrodeposition of PANI on Au disc electrodes via a 10-min chronopotentiometric scan at a current density of 10 $\mu A \cdot cm^{-2}$. (b) Redox capacitance (red) and SWV (black) fingerprints of resulting PANI films.[13] (c) FT-IR spectrum of the PANI films. (d) AFM images showing the deposition boundary between the PANI film (left) and the gold substrate (right), with (e) three cross-sectional line profiles (inset: 3D view).[13] The thickness of the PANI layer was determined by averaging the height difference between the PANI film and the gold substrate across the profiles. Surface roughness was calculated as the arithmetic average of height deviations from the mean line.

The Fourier Transform Infrared spectra (FT-IR) of resulting PANI films, as shown in Figure **2.3c**, revealed characteristic peaks,[18] including a broad band corresponding to secondary amine N-H stretching vibrations between 3205 and 3321 cm^{-1}, a sharp peak of quinoid C=C stretching at 1586 cm^{-1}, and another distinct peak for benzenoid C=C stretching at 1487 cm^{-1}. The intensity ratio of the quinoid to benzenoid C=C stretching peaks was close to unity, indicating that the composition of the electrodeposited PANI films was primarily made up of the emeraldine oxidation state.[19] Atomic force microscopy (AFM) measurements were conducted on a PANI-coated gold substrate. As presented in Figure **2.3d**, a distinct deposition boundary was observed, with the left part corresponding to the PANI film and the right part to the gold substrate. Three cross-sectional line profiles were performed, as presented in Figure **2.3e**, and the thickness of the PANI interface was determined by averaging the height difference between the PANI layer and the gold substrate across these profiles. The AFM images demonstrated that the electro-grafted PANI films had an average thickness of 6.4 nm. The surface roughness (R_a) was estimated from the arithmetic average of profile height deviations from the mean line, yielding a value of 1.6 ± 0.12 nm.

2.2.2 Integration of Antibodies

Following electrodeposition, PANI-functionalised electrodes were activated by immersion in a 2.5% glutaraldehyde solution (in water) for 30 minutes at room temperature. Glutaraldehyde, a bifunctional aldehyde, reacts with lysine and cysteine residues in antibodies,[20] forming stable covalent bonds between the free amine groups on the PANI-coated electrode and the antibodies. This crosslinking enables the covalent immobilisation of anti-CRP onto the electrode surface, ensuring a stable attachment of the antibody. Antibody integration was confirmed by an increase in water contact angle from 43.7° (PANI) to 56.3° (anti-CRP/PANI),[12] as shown in Figure **2.4a**. Additionally, this process resulted in a decrease in C_r,[12, 13] as indicated by the shifts in the inflection point of capacitive Nyquist plots, shown in Figure **2.4b**. The surface coverage of anti-CRP was assessed using the standard Reichert SPR protocol,[21] revealing high levels of antibody integration ($192.9 \pm 9.0\ \mathrm{ng \cdot cm^{-2}}$), equating to approximately $60.8 \pm 2.8\%$ of a theoretical IgG antibody monolayer.[22]

The anti-CRP modified PANI interface exhibited great stability.[12] The C_r baseline, measured at the $E_{1/2}$ of PANI with an AC frequency determined from the inflection point of capacitive Nyquist plots, drifted less than 1% ($< 2.0\ \mathrm{\mu F \cdot cm^{-2}}$) over a 10-min measurement period in 0.1 M phosphate buffer (PB) solution, and < 5% across 3-4 hours of continuous measurement,[13] as shown in Figure **2.4c**. Upon introducing CRP, the interfacial C_r decreased, reflecting the presence of biomarkers (Figure **2.4**). Subsequent end-point assays, depicted in Figure **2.4d**, demonstrated a concentration-dependent C_r response, with a linear dynamic range spanning from $80.0\ \mathrm{ng \cdot mL^{-1}}$ (651 pM) to $10.0\ \mathrm{\mu g \cdot mL^{-1}}$ (87.7 nM) and a picomolar LoD of 58.1 pM (Figure **2.4e**, for the determination of LoD, see *eqn.* **1.4**). The affinity data (normalised to $C_{r,0}$, following the equation

$RR\% = (1/C_{r,t} - 1/C_{r,0})/(1/C_{r,0}) \cdot 100$; see details in the experimental chapter), empirically fitted with a Langmuir-Freundlich isotherm in Figure **2.4f**, yielded a dissociation constant K_d of 19.6 nM, consistent with previous reports and SPR results.[12]

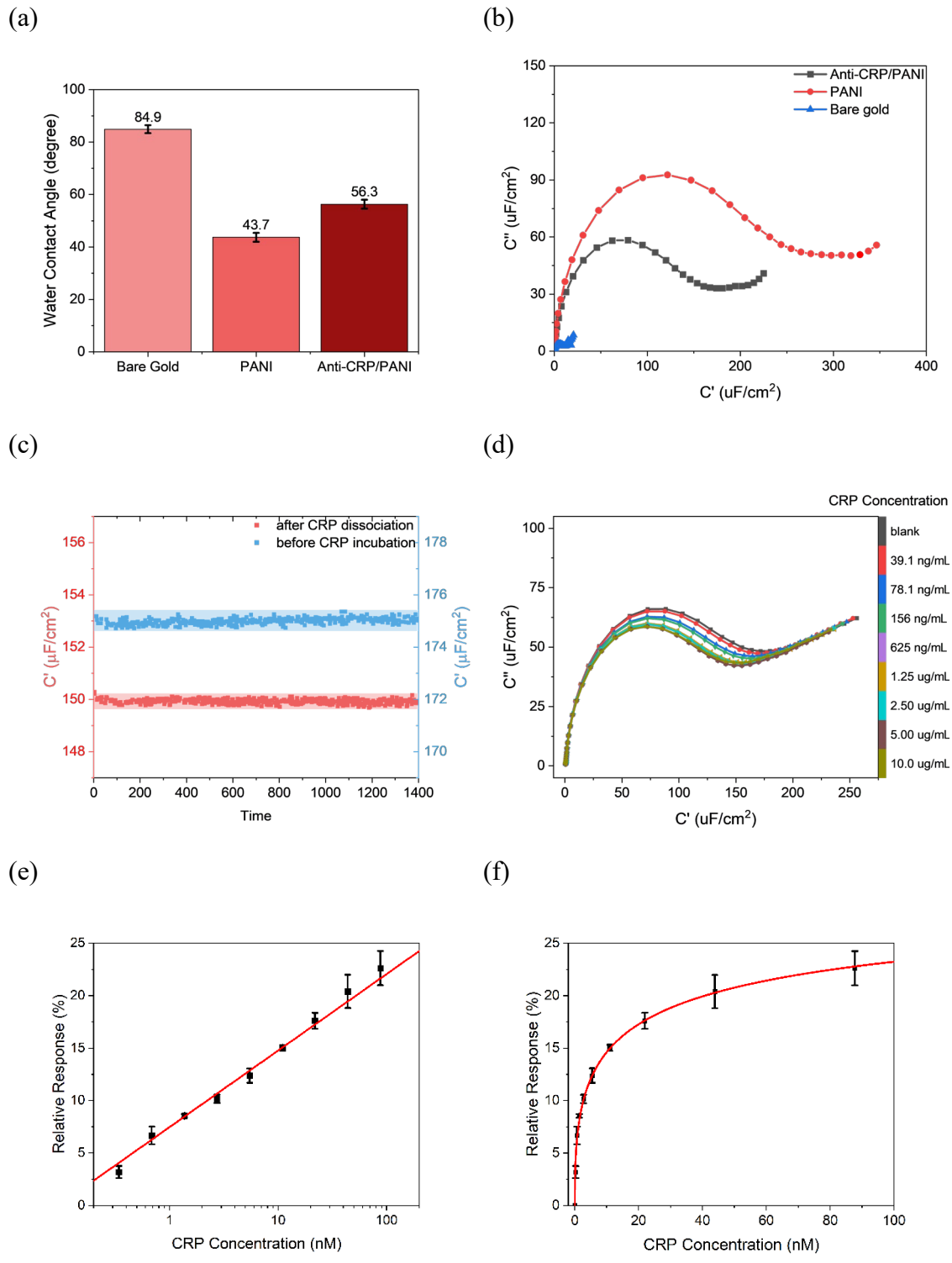


Figure 2.4. (a) Representative water contact angles and (b) electrochemical capacitance spectroscopy of bare gold disc electrode, electro-grafted PANI films, and anti-CRP modified PANI interfaces.[13] (c) Stability assessment of the capacitive baseline for the anti-CRP/PANI interface before (blue) and after 10-minute CRP incubation (red). (d) End-point capacitive Nyquist plots of the anti-CRP/PANI interface in response to varying CRP concentrations. (e) Linear and (f) Langmuir fitting of the end-point CRP capacitive response. C_r was obtained in 0.1 M PB buffer with a pH of 7.4, at the E_{half} of PANI with an AC frequency derived from the inflection point of capacitive Nyquist plots. Error bars represent the standard deviation from three individual electrodes (n = 3).

2.3 REAL-TIME MONITORING OF TARGET BINDING KINETICS

Real-time monitoring of CRP biorecognition was performed in custom 3D-printed microfluidic cells, fabricated with photocurable, light-sensitive resins. As shown in Figure **2.5a**, the chamber within the cell had a volume of 60 µL.[13, 23] To accurately measure the interfacial C_r, a three-electrode configuration was employed, consisting of a gold disc working electrode (ϕ = 1.6 mm), a Ag/AgCl wire pseudo-reference electrode (ϕ = 0.25 mm), and a Pt wire counter electrode (ϕ = 0.25 mm). Samples were introduced through a manual sample injection valve with a sample loop volume of 100 µL, at a controlled flow rate ranging from 1.0 to 500 $\mu L \cdot min^{-1}$.

Interfacial C_r was monitored at the E_{half} of PANI (*i.e.*, - 0.16 V *vs.* Ag/AgCl)) using an AC frequency derived from the inflection point of capacitive Nyquist plot. This frequency also determined the temporal resolution of data acquisition, approximately 0.5 s^{-1}. Both the association and dissociation phases were resolved, as shown in Figure **2.5b**, within four regimes (*i.e.*, mixing, association, equilibrium, and dissociation) being noted.[13] Initially, during the mixing stages, CRP samples were introduced into the chamber, gradually displacing the buffer solution.[23] As shown in Figure **2.5c**, the binding rate, evaluated by the temporal change in C_r or the first derivative of the capacitive relative response, increased due to the rising analyte concentration c_{A_s} and negligible dissociation c_{A-L_s} on the electrode surface,[24] as described in *eqn.* **1.17**. The duration of this stage was determined by the ratio of chamber volume to fluid flow rate. At a 25 $\mu L \cdot min^{-1}$ flow rate, the time required for complete buffer displacement was approximately 140 s.

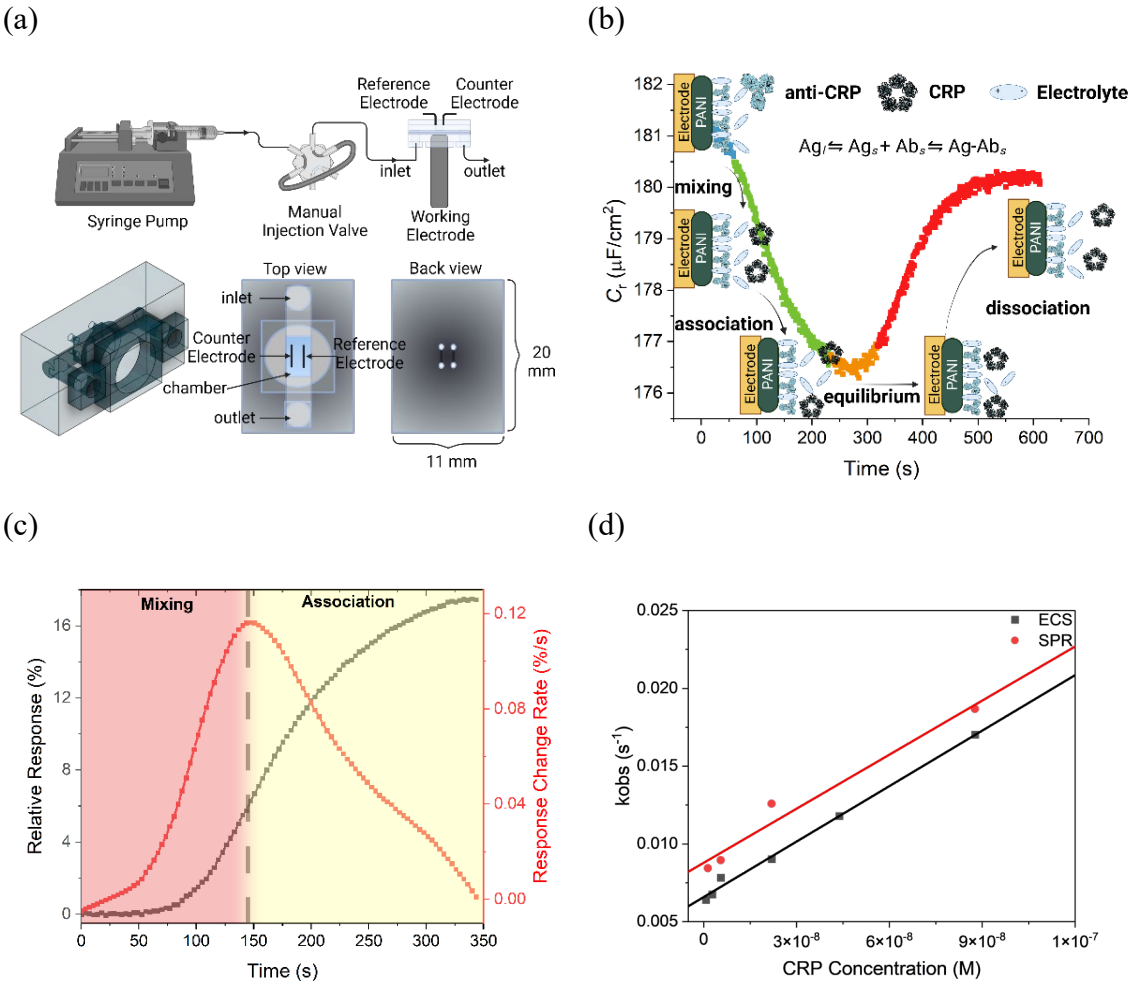


Figure 2.5. (a) Schematic depiction of the microfluidic setup, featuring a syringe pump linked to a manual injection valve for delivering samples into a 3D-printed microfluidic cell.[13] The cell was equipped with a Ag/AgCl wire pseudo-reference electrode, a Pt wire counter electrode, and a Au disc electrode. (b) Representative C_r changes during a CRP biorecognition event under continuous flow, with phases of mixing (blue), association (green), equilibrium (orange), and dissociation (red) resolved. The subscripts for antibody (Ab) and antigen (Ag) denote their respective states, with "*l*" indicating the bulk solution and "*s*" representing the interface. (c) The relative response (black) of C_r and the rate of response change (red) following a CRP injection, with the dashed line indicating the boundary between the mixing and association regimes. The rate of response change, derived directly from the first derivative of the capacitive relative response, represents the overall binding rate of CRP. (d) Analysis of the CRP binding rate constant, plotted as the observed rate constant k_{obs} against CRP concentration. The slope and intercept of the plot represent the association rate constant k_{on} and dissociation rate constant k_{off}, respectively. The k_{obs} values were determined from the association C_r data obtained in continuous-flow ECS (black) and SPR (red), and were fitted using *eqn.* **2.1**.

Once a steady flow was established following the 140 s mixing stage, the binding rate reached its maximum, marking the onset of the association regime. During this phase, as biorecognition occurred, the formation of the antigen-antibody complex altered the interfacial dielectric properties, leading to a decrease in C_r. Additionally, the dissociation rate v_{off} became significant, and biorecognition process followed a pseudo-first-order kinetic pattern (*eqn.* **2.1**), where f_b represents the fraction of bound target relative to the total number of available binding sites, $f_{b,eq}$ is the fraction bound at equilibrium, and k_{obs} is the observed rate constant defined as $k_{on} \cdot c_{\mathrm{A}} + k_{off}$.

$$f_b = f_{b,eq} \cdot [1 - \exp(-k_{obs}t)] \tag{2.1}$$

As shown in Figure **2.5c**, the surface concentration of resulting antigen-antibody complex c_{A-L_s} exhibited an exponential increase over time as the reaction progressed. By empirically fitting the association data to *eqn.* **2.1**, the observed rate constants k_{obs} were determined and plotted against the analyte concentration c_{A} (Figure **2.5d**). The slope and intercept corresponded to the association rate constant k_{on} and the dissociation rate constant k_{off}, respectively. For CRP biorecognition, a k_{on} of $1.19 \times 10^5\ \mathrm{M^{-1} \cdot s^{-1}}$ and a k_{off} of $6.58 \times 10^{-3}\ \mathrm{s^{-1}}$ was noted, consistent with values determined by SPR (*i.e.*, $k_{on,SPR} = 1.16 \times 10^5\ \mathrm{M^{-1} \cdot s^{-1}}$, $k_{off,SPR} = 8.78 \times 10^{-3}\ \mathrm{s^{-1}}$).

As discussed in Section **1.3.1.2**, the specific binding with rapid binding kinetics ($k_{on} \geq 10^5\ \mathrm{M^{-1} \cdot s^{-1}}$) likely falls within the regime of mass-transport limited (MTL) or partial MTL regime, [25-28] where the primary rate-determining step was attributed to the sluggish mass transport. In the context of CRP binding, the overall process remained in the partial MTL regime across all accessible flow rates (1.0 - 500 $\mu\mathrm{L \cdot min^{-1}}$). This was confirmed

by the absence of linearity in the response versus $t^{-\frac{1}{2}}$ (a characteristic of diffusion control, as described in *eqn.* **6.4**),[29, 30] and the observed exponential decay in binding rate (indicative of pseudo-first-order kinetics) even under near-static conditions at a flow rate of 1.0 $\mu L \cdot min^{-1}$.

Following the association stage, CRP binding gradually reached equilibrium, as shown in Figure **2.5b**. In this equilibrium regime, the temporal change in C_r (evaluated by the first derivative of the capacitive relative response) approached zero, indicating that the formation and dissociation of the antigen-antibody complexes occurred at equal rates. A plateau in the C_r value, corresponding to the end-point response, was noted, reflecting the maximum surface binding capacity. After the analyte supply was halted, dissociation started where the surface-bound CRP was gradually washed off, and the interfacial C_r recovered, with kinetics described by *eqn.* **1.18**. The entire window of biorecognition events under continuous flow was largely reversible, with approximately 90% of the C_r returning to its initial value. This real-time, microfluidic-assisted, non-destructive, and label-free electrochemical setup enabled highly sensitive and cost-effective monitoring the biorecognition events with great temporal resolution, providing detailed insights into the binding kinetics and biomolecular interactions.

2.4 ULTRAFAST BIOMARKER QUANTIFICATION

Following analysis of CRP binding kinetics, microfluidic-integrated electrochemical immunoassays were performed across various analyte concentrations. As shown in Figure **2.6**, the temporal C_r change during the initial association phase (~ 140 s, Figure **2.6b**),[13, 24] along with the capacitive response at the equilibrium plateau, both reported on the CRP concentration. As discussed in Section **2.3**, the signal growth during this time interval was primarily attributed to the significant CRP association, as negligible dissociation was insufficient to dominate the observed response.[24, 27]

This section offers theoretical insights into the principles and error analysis behind the initial temporal C_r response. Building on this foundation, a straightforward and rapid method for assessing biomarker concentration was developed, utilizing the capacitive fingerprint of PANI films and association kinetics to enable sensitive and efficient biosensing applications.

(a) (b)

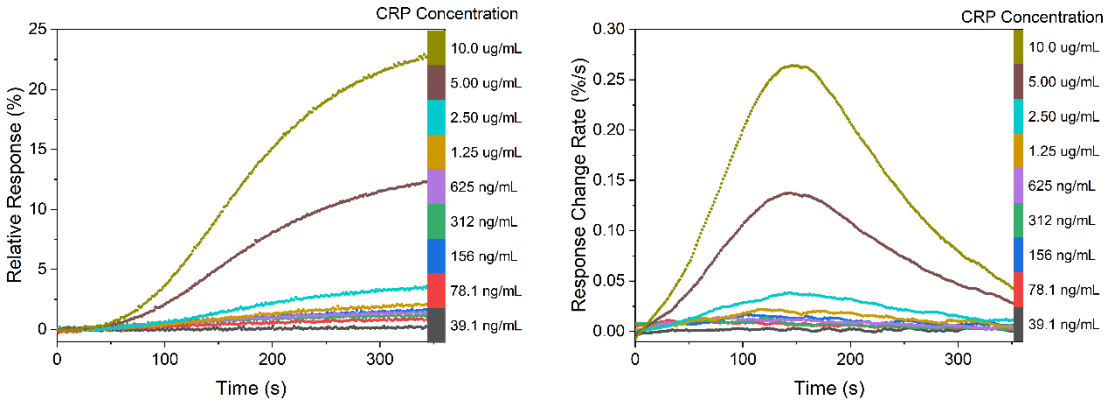


Figure 2.6. (a) Representative sensograms and (b) temporal C_r changes of anti-CRP modified PANI interface in response to varying concentrations of CRP, ranging from 39.1 ng · mL^{-1} to 10.0 µg · mL^{-1}.[13] C_r measurements were conducted in 0.1 M PB buffer (pH = 7.4), at the E_{half} of PANI using an AC frequency determined from the inflection point of capacitive Nyquist plots.

2.4.1 Theoretical Consideration

2.4.1.1 Linear Approximation of Association Kinetics

Within the microfluidic channel, analyte *A* was delivered to the electrode surface via a steady flux (discussed in Section **1.3.1.1**), allowing subsequent specific biorecognition with surface-bound ligands. The binding kinetics between the analyte and ligand are characterised by the association rate constant k_{on} and the dissociation rate constant k_{off}.

$$A_b \xrightleftharpoons{MT} A_s + L_s \xrightleftharpoons[k_{off}]{k_{on}} A - L_s$$

The signal transduction S_A was linearly related to the surface-bound analyte-ligand complex concentration c_{A-L_s}, as described by *eqn.* **2.2**. Here, K_A is the proportionality constant, and S_0 represents the baseline signal.

$$S_A = K_A \cdot c_{A-L_s} + S_0 \tag{2.2}$$

Derived from *eqn.* **1.17**, under a first-order kinetic approximation, the initial temporal response $\left.\frac{dS_A}{dt}\right|_{t\to 0}$ during the association phase was proportional to the analyte concentration c_{A_s},[13] as shown in *eqn.* **2.3**.

$$\left.\frac{dS_A}{dt}\right|_{t\to 0} = K_A \cdot \left.\frac{dc_{A-L_s}}{dt}\right|_{t\to 0} \approx K_A k_{on} c_{L_s} \cdot c_{A_s} = K \cdot c_{A_s} \tag{2.3}$$

where c_{A_s}, c_{L_s}, c_{A-L_s} represent the surface concentration of analyte, ligand, and analyte-ligand complex, respectively; the proportionality constant K between the initial temporal response and c_{A_s} is given by $K_A k_{on} c_{L_s}$.

Similarly, this relationship can also be derived from Taylor theorem. The exponential function can be expressed as a Taylor series, as shown in *eqn.* **2.4**.

$$\exp(-x) = 1 - x + \frac{x^2}{2!} - \frac{x^3}{3!} + \cdots \tag{2.4}$$

When $x \to 0$, the series approximates to the following (*eqn.* **2.5**).

$$\exp(-x) \approx 1 - x \tag{2.5}$$

The higher-order terms (the Taylor remainders R) are given by *eqn.* **2.6**.

$$R(-x) = \frac{x^2}{2!} - \frac{x^3}{3!} + \cdots \tag{2.6}$$

By combining *eqn.* **2.1** and **2.5**, the fraction of surface-bound analyte can be expressed as follows.[13]

$$f_b|_{t\to 0} \approx f_{b,eq} k_{obs} t = \frac{c_{A_s}}{c_{A_s} + K_d} \cdot \left(k_{on} \cdot c_{A_s} + k_{off}\right) \cdot t = k_{on} \cdot c_{A_s} \cdot t \tag{2.7}$$

Therefore, the initial temporal response is described by *eqn.* **2.8**.

$$\left.\frac{dS_A}{dt}\right|_{t\to 0} = K_A c_{L_s} \cdot \left.\frac{df_b}{dt}\right|_{t\to 0} \approx K_A k_{on} c_{L_s} \cdot c_{A_s} = K \cdot c_{A_s} \tag{2.8}$$

Both *eqn.* **2.3** and **2.8** highlight that the initial signal growth during the association phase is primarily driven by the rapid binding of analytes to surface-bound ligands. The rate of signal increase is directly proportional to the analyte concentration c_{A_s} and is heavily influenced by the association rate constant k_{on}, along with the surface coverage of ligands c_{L_s}. Once k_{on} and c_{L_s} are constants, an assay can be established, allowing for the quantification of biomarker concentration based on the association kinetics.

2.4.1.2 Error Analysis of Linear Approximation with Different Data Sampling Windows

Although the initial temporal response can be employed to directly assess the biomarker concentration, errors arise due to the inherent nonlinear behaviours in the first-order model. As indicated in *eqn.* **2.6**, these errors primarily stem from the higher-order terms in the Taylor series, which are neglected in the linear approximation. The magnitude of these errors significantly depends on the choice of data sampling windows, as larger windows increase the contribution of higher-order terms, leading to deviations from the ideal linear model and a relatively narrow dynamic range. Additionally, limited data points, due to insufficient temporal resolution, can compromise the reliability of results. Therefore, a thorough error analysis is necessary for selecting the appropriate sampling window, minimising deviations and ensuring accurate and reliable kinetic assessments.

In an association sensogram, the linear regression of $f_b(t)$ is expressed as follows,

$$f_b(t) = kt + b \tag{2.9}$$

where k and b represent the slope and intercept of $f_b(t)$, respectively. By combining *eqn.* **2.1**, the linear regression of $f_b(t)$ over the sampling window t_0 must pass through the data average $(\bar{t}, \bar{f_b})$, with the values given by *eqn.* **2.10** and **2.11**.[13]

$$\bar{t} = \frac{1}{t_0}\int_0^{t_0} t\,dt = \frac{t_0}{2} \tag{2.10}$$

$$\bar{f_b} = \frac{1}{t_0}\int_0^{t_0} f_b(t)\,dt = \frac{f_{b,eq}(k_{obs}t_0 + e^{-k_{obs}t_0} - 1)}{k_{obs}t_0} \tag{2.11}$$

The slope k is determined by calculating the covariance between the time points t_i and the corresponding values $f_{b,i}$, normalised by the variance of the time points, as shown below.[13]

$$k = \frac{\sum_{i=1}^{n}(t_i - \bar{t})(f_{b,i} - \bar{f_b})}{\sum_{i=1}^{n}(t_i - \bar{t})^2} = \frac{6f_{b,eq}e^{-k_{obs}t_0}(k_{obs}t_0e^{k_{obs}t_0} + k_{obs}t_0 - 2e^{k_{obs}t_0} + 2)}{k_{obs}^2t_0^3} \quad (2.12)$$

when $t \to 0$, the initial slope k_0 is the product of $f_{b,eq}$ and k_{obs}, given by *eqn.* **2.13**.

$$k_0 = f_{b,eq} \cdot k_{obs} = k_{on} \cdot c_{A_s} \quad (2.13)$$

This is consistent with *eqn.* **2.8**, where the initial rate of signal change rate is directly proportional to the analyte concentration c_{A_s} and the association rate constant k_{on}. The error of linear approximation E_r is therefore defined by the relative deviation between the slope k (over the sampling window t_0) and the initial slope k_0 (as t_0 approaches 0). By combining *eqn.* **2.12** and **2.13**, the error can be expressed as follows.[13]

$$E_r = \frac{|k - k_0|}{k_0} = \left|\frac{6e^{-k_{obs}t_0}(k_{obs}t_0e^{k_{obs}t_0} + k_{obs}t_0 - 2e^{k_{obs}t_0} + 2)}{k_{obs}^2t_0^3} - 1\right| \quad (2.14)$$

As shown in Figure **2.7**, E_r increases with longer data sampling windows, due to the accumulation of surface analyte-ligand complex resulting in the pronounced dissociation. While the error remains relatively low (< 5.0%) below the optimum sampling window time (*i.e.*, < 15 s), insufficient data points can compromise the accurate determination of the temporal response. Consequently, an optimal sampling window of 15 seconds balances minimal error and data sampling frequency,[13] providing a reliable temporal analysis for ultrafast biomarker quantification.

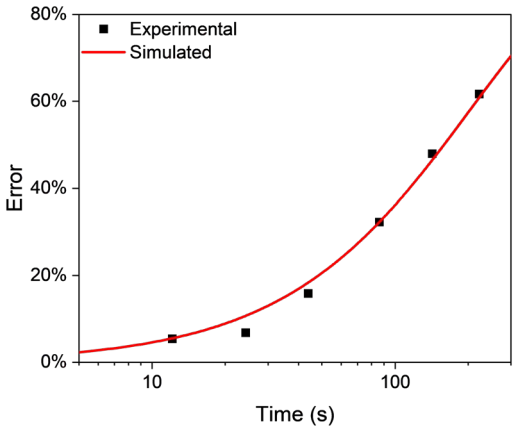


Figure 2.7. Simulated (red line) and experimental (black) error in the linear approximation of CRP initial temporal response across different data sampling windows.[13] The red line was generated using *eqn.* **2.14**, assuming a k_{obs} of 9.38×10^{-3} s^{-1}, determined from SPR measurements of 625 $ng \cdot mL^{-1}$ CRP binding (see Figure **2.5d)**. Experimental error was normalised to 5% for a 15-second data sampling window.

2.4.2 Ultrafast Biomarker Quantification through Reagentless Capacitive Kinetics

Following the determination of the optimal sampling window, CRP dose-response curves were generated by monitoring the temporal C_T change during the initial association phase, on the anti-CRP modified PANI electrodes within the microfluidic channel. As shown in Figure **2.8a**, the 15-second temporal analysis enabled the assaying of CRP with a dynamic range spanning from 80.0 $ng \cdot mL^{-1}$ (651 pM) to 10.0 $\mu g \cdot mL^{-1}$ (87.7 nM), and a picomolar LoD of 70 pM. These results meet the clinical requirements for CRP detection,[31, 32] as discussed in Section **1.1.2.1**. Additionally, they were comparable to those of the end-point assay (Figure **2.4e**),[12] offering similar sensitivity in a significantly shorter timeframe of 15 seconds rather than over tens of minutes. Additionally, this ultrafast kinetic assessment demonstrated excellent reproducibility,[13] with low variability

observed in three repeated measurements on the same electrode (standard deviations < 3%) and across three different electrodes (< 5%).

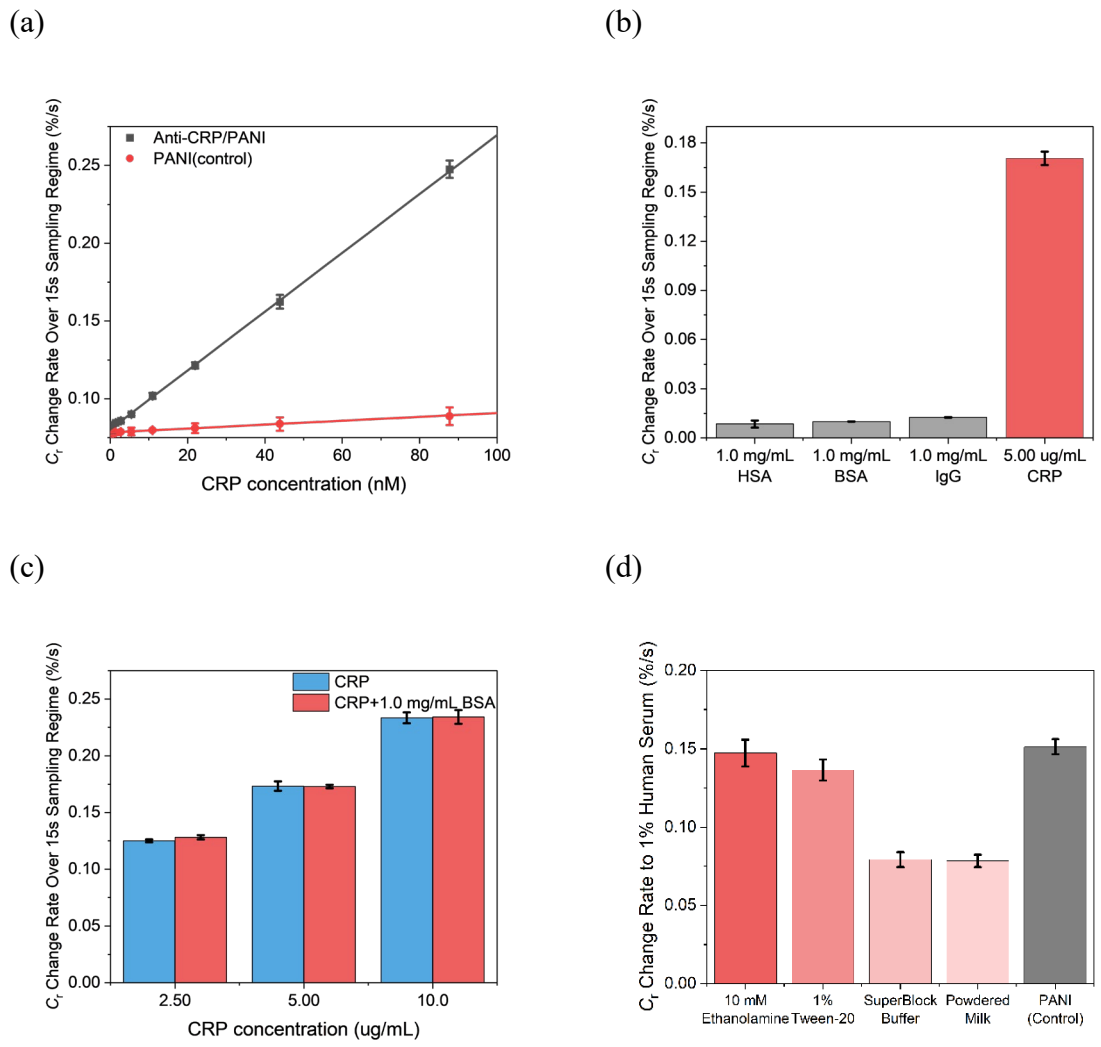


Figure 2.8. (a) 15-second temporal C_r response of anti-CRP modified PANI electrodes (black) and PANI control (red) to increasing concentrations of CRP.[13] (b) Specificity assessment of anti-CRP modified PANI electrode, evaluating initial temporal responses toward 1.0 mg · mL^{-1} HSA, BSA, IgG, and 5.00 µg · mL^{-1} CRP. (c) Recovery of 2.50, 5.00, and 10.0 µg · mL^{-1} CRP spiked in a 1.0 mg · mL^{-1} BSA substrate. (d) Antifouling performance of PANI electrodes treated with several blocking agents, including ethanolamine, Tween-20, SuperBlock™ blocking buffer, and powdered milk. Antifouling performance was assessed based on the 15-second temporal C_r response during 1.0% human serum injection. Error bars represent the standard deviations of three individual electrodes (n = 3).

As indicated in *eqn.* **2.9**, the initial temporal response is significantly influenced by k_{on}, enabling clear discrimination between specific and nonspecific binding events. As shown

in Figure **2.8b**, interfacial specificity was evaluated by comparing the 15-second temporal response in C_r during a 5.00 $\mu g \cdot mL^{-1}$ CRP injection, with those observed for 1.0 $mg \cdot mL^{-1}$ human serum albumin (HSA), bovine serum albumin (BSA), and bovine immunoglobulin G (IgG), respectively, under identical flow conditions. The slopes of the 15-second sampling window for nonspecific bindings were generally less than 5% of those observed following CRP injection,[13] with a selectivity coefficient $K_{A,I}$ consistently greater than 3000.

This high selectivity facilitated the effective recruitment of the specific target from an interference-containing substrate, supporting robust assaying of biomarkers for real-world applications. As indicated in Section **1.1.3.2**, the robustness of the assay is assessed by recovery, which is calculated as the ratio of the detected concentration to the known spiked concentration, expressed as a percentage. As shown in Figure **2.8c**, the recoveries of CRP in BSA-spiked samples averaged 100.9 $\pm$ 1.1%.[13] Additionally, CRP recovery in 1.0% human serum was quantified at 108.9 $\pm$ 2.2%, demonstrating excellent agreement with independent SPR measurements (103.6 $\pm$ 4.6%).[13] However, poor recoveries (> 150%) were noted in serum-spiked samples when the CRP concentration was below 1.0 $\mu g \cdot mL^{-1}$. This reduction in performance can be attributed to the accumulation of nonspecific serum proteins on the electrode surface, particularly fibrinogen,[33, 34] which has a selectivity coefficient $K_{\mathrm{CRP,fibrinogen}}$ of less than 500.

To address this issue, a 1-hour surface-blocking procedure was employed to minimise nonspecific binding. The efficiency of several common blocking agents was evaluated, including ethanolamine,[35] Tween-20,[36] SuperBlock™ blocking buffer,[37] and powdered milk. As shown in Figure **2.8d**, a significant reduction in fouling was noted upon 1.0% human serum injection in blocked PANI electrodes, compared to the unblocked PANI

control. Additionally, the antifouling performance of blocking agents improved with increasing molecular size.[36] The small molecule ethanolamine (M_r = 61.08 $\mathrm{g \cdot mol^{-1}}$) provided minimal improvement, followed by the polymer Tween-20 (M_r = 1225 $\mathrm{g \cdot mol^{-1}}$). In contrast, both protein-based blocking agents, SuperBlock™ blocking buffer (containing glycoproteins) and powdered milk, exhibited the best performance in reducing nonspecific binding, with similar levels of improvement, as reflected in their lowest 15-second temporal response in C_r during human serum injection. Despite these, the improvements remain limited, necessitating further surface engineering to optimise antifouling performance and ensure robust and reliable assaying of biomarkers in clinical applications.

2.5 CONCLUSION AND FUTURE OUTLOOK

In this chapter, we innovatively monitored the biomolecular binding kinetics in real-time utilising the capacitive fingerprint of an antibody-functionalised electro-grafted PANI film as the signal generator on a reagentless microfluidic electrochemical biosensor. Exemplified with the immunorecognition of C-reactive protein (CRP), within a custom 3D-printed microfluidic channel, four distinct phases were identified in the binding sensogram, including mixing, association, equilibrium, and dissociation. The association rate constant k_{on} , determined from the association data, indicated that CRP immunorecognition operated within the regime of partial mass-transport limitation (MTL), where both mass transport and binding kinetics significantly influenced the overall reaction rate. Across all accessible flow rates, a pseudo-first-order kinetics was observed.

Additionally, we noted that the temporal change in redox capacitance C_r during the association phrase reported on the CRP concentration, as the initial signal growth at this time interval was primarily attributed to the rapid binding of analytes to surface-bound ligands. This proportional relationship between signal increase rate and analyte concentration enabled the sensitive and rapid assaying of biomarker concentration. The linear approximation, of course, introduced errors due to the inherent nonlinear behaviours of the first-order model. Error analysis revealed that a 15-second sampling window, which balanced minimal error and data sampling frequency, allows for accurate and reliable kinetic assessments of biomarker concentrations. The proposed approach is promising to significantly improve the turnaround efficiency of electrochemical biosensing for detecting clinically relevant targets.

Accordingly, CRP dose-response curves were generated using kinetic assessments. A dynamic range spanning from 80.0 $ng \cdot mL^{-1}$ (651 pM) to 10.0 $\mu g \cdot mL^{-1}$ (87.7 nM), along with a picomolar LoD of 70 pM, was achieved, covering clinical requirements. These results were comparable to those of the standard end-point assays, with shorter sample-to-result time in just 15 seconds rather than over tens of minutes. The method can robustly and specifically quantify CRP concentration in BSA-spiked samples, given the significant discrimination in k_{on} between specific and nonspecific binding events.

To further enhance biosensing performance in serum samples, protein-based blocking agents, including SuperBlock^{TM} blocking buffer and powdered milk, were employed to minimise nonspecific binding. While these agents demonstrated reduced biofouling in serum, their effectiveness remained limited. Advanced surface engineering strategies,[38-41] such as covalent modification of PANI films or improving surface hydrophilicity, can be applied to enhance the selectivity and practicality of electrochemical biosensors in high-protein environments for clinical applications.

2.6 REFERENCES

(1) Syed, A. A.; Dinesan, M. K. Polyaniline-A novel polymeric material. *Talanta* **1991**, *38* (8), 815-837.
(2) Stejskal, J.; Hlavatá, D.; Holler, P.; Trchová, M.; Prokeš, J.; Sapurina, I. Polyaniline prepared in the presence of various acids: a conductivity study. *Polym. Int.* **2004**, *53* (3), 294-300.
(3) Stejskal, J.; Sapurina, I.; Trchová, M.; Prokeš, J.; Křivka, I.; Tobolková, E. Solid-state protonation and electrical conductivity of polyaniline. *Macromolecules* **1998**, *31* (7), 2218-2222.
(4) Bhadra, S.; Chattopadhyay, S.; Singha, N. K.; Khastgir, D. Improvement of conductivity of electrochemically synthesized polyaniline. *J. Appl. Polym. Sci.* **2008**, *108* (1), 57-64.
(5) Beygisangchin, M.; Abdul Rashid, S.; Shafie, S.; Sadrolhosseini, A. R.; Lim, H. N. Preparations, properties, and applications of polyaniline and polyaniline thin films-A review. *Polymers* **2021**, *13* (12), 2003.
(6) Boeva, Z. A.; Sergeyev, V. G. Polyaniline: Synthesis, properties, and application. *Polym. Sci., Ser. C* **2014**, *56* (1), 144-153.
(7) Hatchett, D. W.; Josowicz, M.; Janata, J. Acid doping of polyaniline: spectroscopic and electrochemical studies. *J. Phys. Chem. B* **1999**, *103* (50), 10992-10998.
(8) Lee, S.-Y.; Choi, G.-R.; Lim, H.; Lee, K.-M.; Lee, S.-K. Electronic transport characteristics of electrolyte-gated conducting polyaniline nanowire field-effect transistors. *Appl. Phys. Lett.* **2009**, *95* (1).
(9) Guo, X.; Li, J.; Wang, F.; Zhang, J. H.; Zhang, J.; Shi, Y.; Pan, L. Application of conductive polymer hydrogels in flexible electronics. *J. Polym. Sci.* **2022**, *60* (18), 2635-2662.
(10) Eftekhari, A.; Li, L.; Yang, Y. Polyaniline supercapacitors. *J. Power Sources* **2017**, *347*, 86-107.
(11) Gupta, V.; Miura, N. Polyaniline/single-wall carbon nanotube (PANI/SWCNT) composites for high performance supercapacitors. *Electrochim. Acta* **2006**, *52* (4), 1721-1726.
(12) Baradoke, A.; Hein, R.; Li, X.; Davis, J. J. Reagentless redox capacitive assaying of C-reactive protein at a polyaniline interface. *Anal. Chem.* **2020**, *92* (5), 3508-3511.
(13) Kang, S.; Sharafeldin, M.; Patrick, S. C.; Chen, X.; Davis, J. J. Ultrafast biomarker quantification through reagentless capacitive kinetics. *Anal. Chem.* **2023**, *95* (10), 4721-4727.
(14) Zare, E. N.; Makvandi, P.; Ashtari, B.; Rossi, F.; Motahari, A.; Perale, G. Progress in conductive polyaniline-based nanocomposites for biomedical applications: a review. *J. Med. Chem.* **2019**, *63* (1), 1-22.
(15) Bueno, P. R.; Mizzon, G.; Davis, J. J. Capacitance spectroscopy: a versatile approach to resolving the redox density of states and kinetics in redox-active self-assembled monolayers. *J. Phys. Chem. B* **2012**, *116* (30), 8822-8829.
(16) Huang, M.; Xie, L.; Wang, Y.; He, H.; Yu, H.; Cui, J.; Feng, X.; Lou, Z.; Xiong, Y. Efficient uranium electrochemical deposition with a functional phytic Acid-Doped Polyaniline/Graphite sheet electrode by Adsorption-electrodeposition strategy. *Chem. Eng. J.* **2023**, *457*, 141221.
(17) Ali, Y.; Kumar, V.; Sonkawade, R.; Dhaliwal, A. Fabrication of polyaniline nanofibers by chronopotentiometry. *Adv. Mater. Lett* **2012**, *3*, 388-392.

(18) Shoba, S.; Bankole, O. M.; Ogunlaja, A. S. Electrocatalytic Oxidation of Dibenzothiophene and 4, 6-Dimethyldibenzothiophene at Gold-Polyaniline (Au-PANI) Composite Electrodes. *Electrocatalysis* **2020**, *11*, 593-603.
(19) Quillard, S.; Louarn, G.; Lefrant, S.; MacDiarmid, A. Vibrational analysis of polyaniline: A comparative study of leucoemeraldine, emeraldine, and pernigraniline bases. *Phys. Rev. B* **1994**, *50* (17), 12496.
(20) Migneault, I.; Dartiguenave, C.; Bertrand, M. J.; Waldron, K. C. Glutaraldehyde: behavior in aqueous solution, reaction with proteins, and application to enzyme crosslinking. *Biotechniques* **2004**, *37* (5), 790-802.
(21) Markey, F. Principles of Surface Plasmon Resonance. In *Real-Time Analysis of Biomolecular Interactions: Applications of BIACORE*, Nagata, K., Handa, H. Eds.; Springer Japan, 2000; pp 13-22.
(22) Macchia, E.; Manoli, K.; Holzer, B.; Di Franco, C.; Picca, R. A.; Cioffi, N.; Scamarcio, G.; Palazzo, G.; Torsi, L. Selective single-molecule analytical detection of C-reactive protein in saliva with an organic transistor. *Anal. Bioanal. Chem.* **2019**, *411* (19), 4899-4908.
(23) Sharafeldin, M.; James, T.; Davis, J. J. Open circuit potential as a tool for the assessment of binding kinetics and reagentless protein quantitation. *Anal. Chem.* **2021**, *93* (44), 14748-14754.
(24) Karlsson, R.; Fägerstam, L.; Nilshans, H.; Persson, B. Analysis of active antibody concentration. Separation of affinity and concentration parameters. *J. Immunol. Methods* **1993**, *166* (1), 75-84.
(25) Sigmundsson, K.; Másson, G.; Rice, R.; Beauchemin, N.; Öbrink, B. Determination of active concentrations and association and dissociation rate constants of interacting biomolecules: an analytical solution to the theory for kinetic and mass transport limitations in biosensor technology and its experimental verification. *Biochemistry* **2002**, *41* (26), 8263-8276.
(26) Schuck, P.; Zhao, H. The Role of Mass Transport Limitation and Surface Heterogeneity in the Biophysical Characterization of Macromolecular Binding Processes by SPR Biosensing. In *Surface Plasmon Resonance: Methods and Protocols*, Mol, N. J., Fischer, M. J. E. Eds.; Humana Press, 2010; pp 15-54.
(27) Christensen, L. L. Theoretical analysis of protein concentration determination using biosensor technology under conditions of partial mass transport limitation. *Anal. Biochem.* **1997**, *249* (2), 153-164.
(28) Svitel, J.; Balbo, A.; Mariuzza, R. A.; Gonzales, N. R.; Schuck, P. Combined affinity and rate constant distributions of ligand populations from experimental surface binding kinetics and equilibria. *Biophys. J.* **2003**, *84* (6), 4062-4077.
(29) Trurnit, H. J. Studies on enzyme systems at a solid-liquid interface. II. The kinetics of adsorption and reaction. *Arch. Biochem. Biophys.* **1954**, *51* (1), 176-199.
(30) Bard, A. J.; Faulkner, L. R.; White, H. S. *Electrochemical Methods: Fundamentals and Applications*; Wiley, 2022.
(31) Black, S.; Kushner, I.; Samols, D. C-reactive protein. *J. Biol. Chem.* **2004**, *279* (47), 48487-48490.
(32) Pepys, M. B.; Hirschfield, G. M. C-reactive protein: a critical update. *J. Clin. Invest.* **2003**, *111* (12), 1805-1812.
(33) Mohanraj, G. Electrochemical Mitigation of Biofouling on Metallic Implants. State University of New York at Buffalo, 2022.

(34) Dargahi, M.; Konkov, E.; Omanovic, S. Influence of surface charge/potential of a gold electrode on the adsorptive/desorptive behaviour of fibrinogen. *Electrochim. Acta* **2015**, *174*, 1009-1016.
(35) Frederix, F.; Bonroy, K.; Reekmans, G.; Laureyn, W.; Campitelli, A.; Abramov, M. A.; Dehaen, W.; Maes, G. Reduced nonspecific adsorption on covalently immobilized protein surfaces using poly (ethylene oxide) containing blocking agents. *J. Biochem. Biophys. Methods* **2004**, *58* (1), 67-74.
(36) Che, Y.; Li, Y.; Slavik, M. Detection of Campylobacter jejuni in poultry samples using an enzyme-linked immunoassay coupled with an enzyme electrode. *Biosens. Bioelectron.* **2001**, *16* (9-12), 791-797.
(37) Contreras-Naranjo, J. E.; Aguilar, O. Suppressing non-specific binding of proteins onto electrode surfaces in the development of electrochemical immunosensors. *Biosensors* **2019**, *9* (1), 15.
(38) Jiang, C.; Wang, G.; Hein, R.; Liu, N.; Luo, X.; Davis, J. J. Antifouling strategies for selective in vitro and in vivo sensing. *Chem. Rev.* **2020**, *120* (8), 3852-3889.
(39) Lin, P.-H.; Li, B.-R. Antifouling strategies in advanced electrochemical sensors and biosensors. *Analyst* **2020**, *145* (4), 1110-1120.
(40) Ye, H.; Wang, L.; Huang, R.; Su, R.; Liu, B.; Qi, W.; He, Z. Superior antifouling performance of a zwitterionic peptide compared to an amphiphilic, non-ionic peptide. *ACS applied materials & interfaces* **2015**, *7* (40), 22448-22457.
(41) Sabaté del Río, J.; Henry, O. Y.; Jolly, P.; Ingber, D. E. An antifouling coating that enables affinity-based electrochemical biosensing in complex biological fluids. *Nat. Nanotechnol.* **2019**, *14* (12), 1143-1149.

Chapter 3

Leveraging Microfluidic Confinement to Boost Assay Sensitivity and Selectivity

3.1 BACKGROUND

Electrochemical biosensors are advantageous due to their high sensitivity, cost-effectiveness, and portability.[1] The detection of clinically relevant biomarkers at a planar electrode surface, however, comes with limitations associated with their sluggish binding kinetics and the scale of specific signal development relative to nonspecific fouling.[2] In specific biorecognition, slow diffusion of target analytes to surface-bound receptors severely limits binding efficiency,[3, 4] resulting in a marked reduction in sensitivity. Additionally, this sluggish mass transport can blur the distinction between specific and nonspecific binding, as the observed kinetic constants for both interactions become levelled, making it difficult to differentiate target responses from background, thereby diminishing the overall biosensor specificity.

To address these limitations, a range of amplification strategies — aimed at enhancing selectivity — have become increasingly common.[5-7] These strategies typically involve either expanding the electrochemical surface area by incorporating nanomaterials (*e.g.*, nanoparticles, graphene),[8-12] or employing catalytic and chain reactions in "double recognition" sandwich assays to selectively magnify the specific signals (*e.g.*, current). Despite their effectiveness, the integration of nanomaterials, catalysts, redox tags, or enzyme-modified secondary antibodies increases both the assay cost and complexity. These approaches can significantly compromise reproducibility and scalability, due to the numerous variables associated with the multi-step procedures and repeated washing protocols.

Microfluidic configurations are increasingly employed in biosensing applications,[13, 14] as reduced sample volumes and automated sample processing provide a cost-effective

solution that minimises user intervention and thus improves assay reproducibility.[15] Additionally, mass transport of analytes within microfluidic channels is accelerated by convection and is strongly influenced by the channel geometry. At the microscale, even slight changes in channel dimensions can have a significant impact on flow dynamics, as depicted by the Levich equation (*eqn.* **1.16**).[16] The resulting increase in channel flux promotes interfacial binding kinetics (*eqn.* **1.19**), facilitating more efficient target accumulation on the bio-receptive interface within a shorter time frame,[17-19] ultimately improving assay sensitivity. This enhancement is closely related to the association rate constant k_{on}, making it particularly significant in processes where mass transport is the rate-limiting step (*e.g.*, specific binding with $k_{on} \geq 10^5\,\mathrm{M^{-1}\cdot s^{-1}}$).[20, 21] Consequently, the differential enhancement of specific over nonspecific binding enables selective recruitment of analytes while minimising background interference, thereby increasing the specificity and robustness of assays.

The previous chapter demonstrated that the capacitive fingerprint of a polyaniline film can effectively transduce the recruitment of C-reactive protein,[20] within a custom 3D-printed microfluidic channel. Additionally, an analysis of target recruitment kinetics enabled biomarker quantification in just 15 seconds, with sensitivity and picomolar limit of detection (LoD) generally better than established ELISA or electrochemiluminescence formats.[22] Its real-world application, however, remains limited due to the natively high biofouling in serum samples. In this chapter, the concepts developed earlier will be integrated, along with the previously introduced kinetic quantification approach (see Chapter **2**),[20] to significantly enhance both assay sensitivity and selectivity using microfluidic confinement (Figure **3.1**), in a manner that is streamlined, broadly applicable and COMSOL validated.[23]

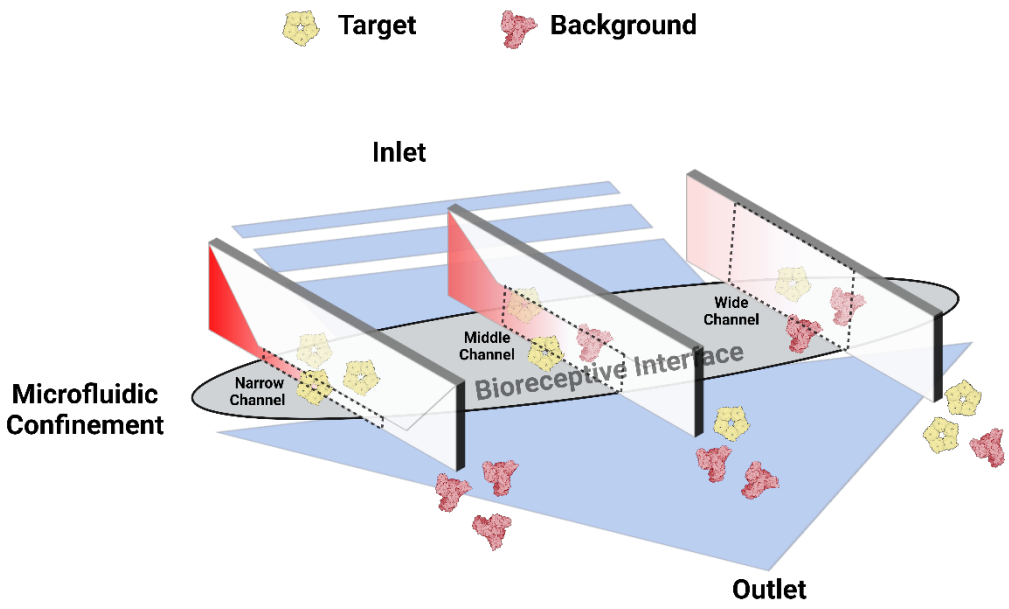


Figure 3.1. Schematic representation of microfluidic confinement in enhancing assay sensitivity and improving the selectivity of target recruitment. The three cross-sectional slides represent microfluidic channels with varying channel heights, from left (smallest) to right (largest). The red-colour gradient within the channels illustrates analyte flux toward the bio-receptive interface, with darker colour being indicative of higher flux. Within more confined volumes, increased convective flow facilitates enhanced mass transport, leading to rapid accumulation of analytes on the bio-receptive surface and significantly boosting assay sensitivity. This process, governed by association rate constants, significantly improves selectivity of targeted recruitment by concentrating analytes at the detection interface while minimising nonspecific background interference.

3.2 MICROFLUIDIC CONFINEMENT IN BOOSTING ASSAY SENSITIVITY

3.2.1. Enhanced Analyte Flux Within Microfluidic Confinement

The study of microfluidic confinement began with an investigation into enhanced analyte flux within the microfluidic channels (the fabrication of microfluidic confinement see Figure **3.2**). In a cyclic voltammogram (CV) within microfluidic confinement, the behaviour of redox reactions is influenced by the competition between the electrochemical reaction consumption of the redox probe and its convective delivery. At the electrode surface, the redox probe undergoes electrode reaction, depleting its concentration near the interface. The rate at which the electrochemical reaction occurs is the function of over potential η and potential scan rate v, as depicted by Butler-Volmer equation (*eqn.* **1.9**) and the Randles-Sevcik equation (*eqn.* **6.7**), respectively. Within microfluidic channels, the flow rate-dependent convection delivers fresh redox species to the electrode surface at a constant flux, as depicted by the Levich equation (*eqn.* **1.16**).

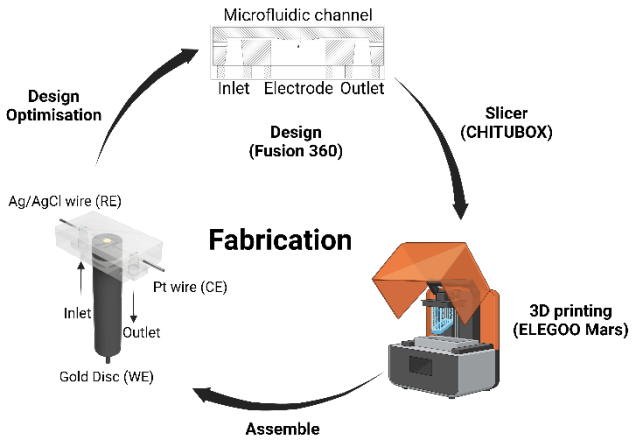


Figure 3.2. Schematic representation of the fabrication for custom 3D-printed microfluidic channels, from design to final functional integration. The microfluidic channels were designed in Fusion 360 with adjustable channel heights (20 -1000 µm) and fabricated using stereolithography 3D printing (ELEGOO

Mars, 5 μm layer thickness). After post-processing treatment (isopropanol washing and UV curing), Pt and Ag/AgCl wires were integrated into the microfluidic cells and securely affixed to establish a three-electrode system with gold disc electrodes. Iterative design optimization was performed to ensure precise microchannel dimensions and reliable device performance.[23]

At low flow rates, the convective delivery of redox probes is insufficient to match their rapid consumption at the electrode surface, leading to diffusion-limited behavior. This is reflected in the cyclic voltammogram as a reduction in peak current. Conversely, at higher flow rates, enhanced mass transport ensures a continuous supply of redox probes, maintaining a stable current until the electrode reaction kinetics once again exceed the rate of convective delivery (*e.g.*, under high scan rates). Microfluidic confinement amplifies this effect, as even minor changes in channel geometry at the microscale can significantly impact flow dynamics and mass transport efficiency.

As shown in Figure **3.3a**, two 3D-printed microfluidic channels were fabricated, with channel heights of 100 μm and 1000 μm, respectively, above gold disc electrodes. The microfluidic channel a height of 1000 μm is expected to exhibit minimal sensitivity to changes in flow dynamics due to its larger volume, which reduces the influence of flow on mass transport. As expected, under continuous flow of a 5 mM ferrocyanide and ferricyanide in PBS mixture (pH = 7.4), voltammograms at a scan rate of 100 $\mathrm{mV \cdot s^{-1}}$ within the 1000 μm channel exhibited a typical diffusion-controlled pattern across all accessible flow rate (0 - 300 $\mu\mathrm{L \cdot min^{-1}}$),[24] characterised by a pair of reversible redox peaks centred at $E_{1/2}$= + 0.17 V (*vs.* Ag/AgCl).[20, 25] Peak currents increased with flow rate, reaching a plateau at 15.0 $\pm$ 0.27 μA once the flow rate exceeded 25 $\mu\mathrm{L \cdot min^{-1}}$.

In contrast, voltammograms within the 100 μm microfluidic confinement demonstrated a strong dependence on flow rate. As shown in Figure **3.3b**, diffusion-control behaviour

was noted in a stationary solution (*i.e.*, v_f = 0 $\mu L \cdot min^{-1}$), consistent with the results in the 1000 µm channel. However, with increasing flow rates, the voltammograms progressively changed into a convection-dominated curve,[16] where steady-state currents were generated at high overpotentials ($\eta \gg 0$ V). As expected, the relationship between steady-state currents and flow rate followed the Levich equation (*eqn.* **1.16**),[16] shown in Figure **3.3c**. As discussed in Section **6.3.1.1**, the current is a direct measure of analyte flux, indicating a constant and steady-state analyte flux, facilitated by forced convection, was achieved within the microfluidic confinement.

Unlike the "Randles-Sevcik" dependence (*eqn.* **6.7**) between peaks currents and scan rates observed in the 1000 µm channel,[24] the steady-state currents in the 100 µm microfluidic confinement remained nearly constant at 20.8 $\pm$ 0.59 µA up to scan rates of 500 $mV \cdot s^{-1}$. Beyond this point, the mass transport within the microfluidic confinement became insufficient to support such high electrochemical reaction rate, resulting in the regeneration of redox peaks (Figure **3.3d**). These results highlight that reduced microfluidic channel height altered the mass transport pattern and facilitated an enhanced, steady analyte flux, demonstrating the significant impact of channel geometry on electrochemical performance.

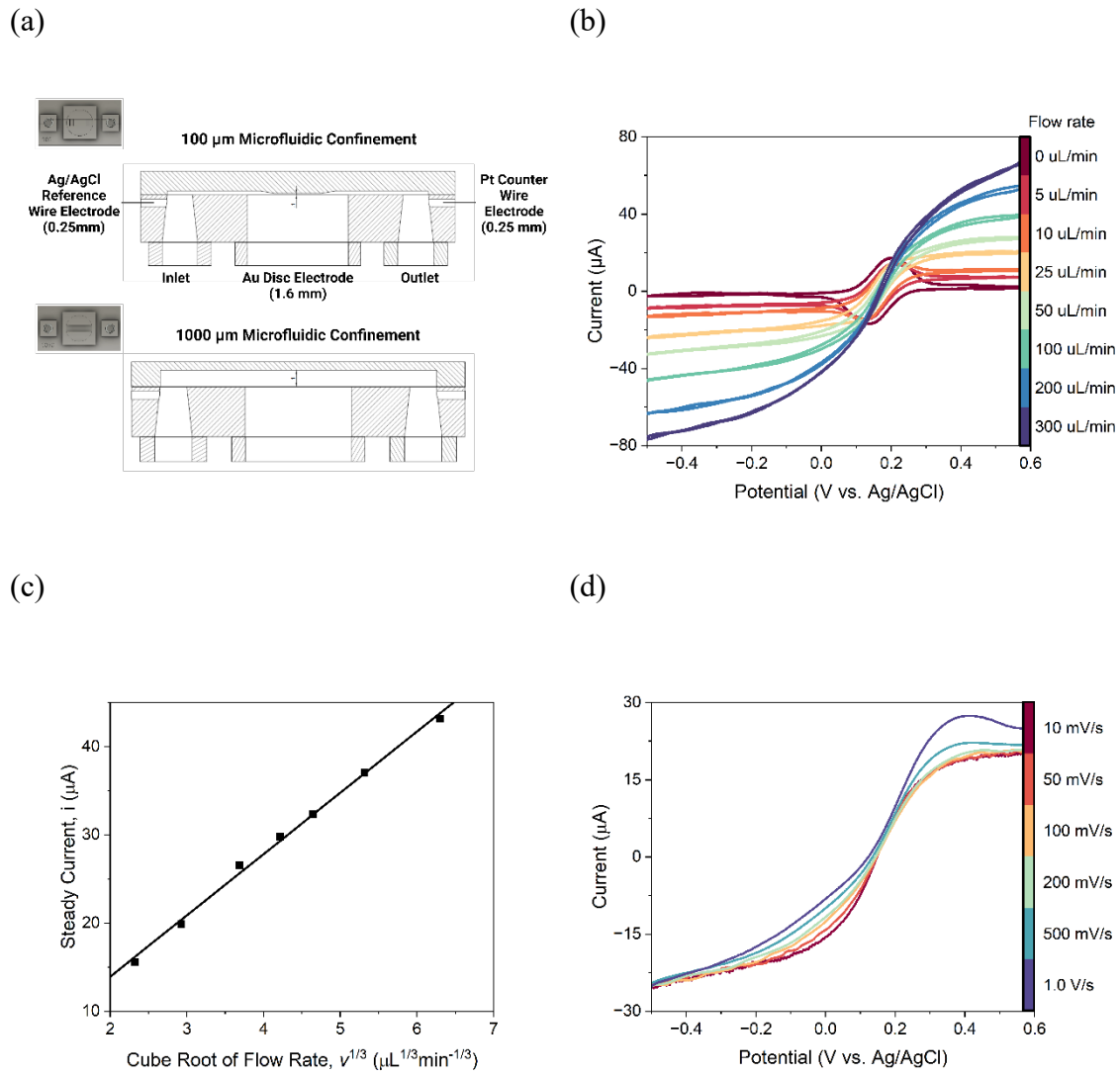


Figure 3.3. (a) Schematic representation of the custom 3D-printed microfluidic channels with 100 µm (top) and 1000 µm (bottom) channel heights above a gold disc electrode (ϕ = 1.6 mm). The Ag/AgCl reference wire electrode and Pt counter wire electrode were positioned at the inlet and outlet of the microfluidic cells, respectively. (b) Cyclic voltammograms for the 100 µm microfluidic channel at varying flow rates (0 - 300 $\mu L \cdot min^{-1}$) with a scan rate of 100 $mV \cdot s^{-1}$, using a 5 mM ferrocyanide/ferricyanide PBS solution (pH = 7.4). As the flow rate increased, the system shifted from a diffusion-controlled to a convection-dominated regime, with steady-state currents noted at high overpotentials ($\eta \gg 0$ V). (c) The Levich dependence between steady-state currents and flow rate in the 100 µm microfluidic channel under a scan rate of 100 $mV \cdot s^{-1}$, demonstrating convection-dominated mass transport behaviour. (d) Effect of scan rate on cyclic voltammograms in the 100 µm microfluidic channel at a constant flow rate of 25 $\mu L \cdot min^{-1}$. Redox peaks reappeared when the scan rate exceeded 500 $mV \cdot s^{-1}$.

3.2.2. Boosted Assay Sensitivity Within Microfluidic Confinement

The enhanced analyte flux within the microfluidic channel not only shifted the mass transport pattern from a diffusion-controlled to a convection-dominated regime, but also facilitated the rapid accumulation of targets on the bio-receptive interface within a shorter time frame.[17, 19] Notably, assay sensitivity and temporal assay sensitivity are distinct concepts. Assay sensitivity refers to a biosensor's ability to detect low concentrations of a target analyte, primarily determined by the total number of target molecules bound to the sensor surface at equilibrium or at end-points. In contrast, temporal assay sensitivity focuses on how quickly the system generates a detectable signal in response to the analyte, which is governed by the rate of binding kinetics. Though different, these two forms of sensitivity are interrelated. The surface-bound target concentration is the result of cumulative binding events over the entire time course of the analyte injection. Faster binding kinetics, facilitated by increased analyte flux, lead to a more rapid approach to equilibrium, thereby improving assay sensitivity.

Specific recruitment of targets was achieved on the well-established antibody-functionalised PANI interface,[20, 25] utilising its capacitive fingerprint to enable reagentless monitoring of biorecognition events, as discussed in Sections **2.2** and **2.3**. As shown in Figure **3.4a**, the normalised capacitive response C_r (relative to baseline, calculated using the equation $RR\% = (1/C_{r,t} - 1/C_{r,0})/(1/C_{r,0}) \cdot 100$) was highly sensitive to the microfluidic confinement size. The smaller channel heights induced higher C_r responses in plateau. Specifically, the capacitive response at binding equilibrium (C_r plateau) in the 20 μm microfluidic confinement was nearly 10 times greater than that observed in the 1000 μm channel (167% *vs.* 19.8%) at a flow rate of 10 $\mu L \cdot min^{-1}$, resulting in 600% enhancement in binding affinity K_a (Figure **3.4c**).

Additionally, as shown in Figure **3.4b**, the temporal C_r response over the 15-second sampling window demonstrated a strong dependence on both analyte concentration (discussed in Section **2.4**) and microfluidic confinement size. Reducing the channel height from 1000 μm to 20 μm led to an approximately 2000% increase in binding rate, as reflected by the steeper slope in the "dose-response" curves in Figure **3.4b**. This increased temporal sensitivity then supported a 2000% decrease in the LoD ($LoD_{20\mu m}$ = 1.50 ng · mL^{-1} *vs.* $LoD_{1000\mu m}$ = 30.5 ng · mL^{-1}). These initial observations highlighted the pivotal value of controlling local analyte flux by simply manipulating channel dimensions (Figure **3.4c**),[16] and the profound impact this can have on assay performance.

The enhancement of temporal sensitivity in CRP binding is not only dependent on microfluidic confinement size, but is also significantly influenced by analyte capture probability, which is governed by antibody surface coverage. As depicted in *eqn.* **2.8**, the initial signal growth during the association phase directly reported on the analyte concentration c_{A_s}, the association rate constant k_{on}, along with the surface coverage of ligands c_{L_s}. A higher analyte capture probability, resulting from increased antibody surface coverage, leads to more efficient target binding and faster signal generation, thereby significantly boosting temporal sensitivity. As shown in Figure **3.4d**, increasing antibody surface coverage by adjusting its concentration in the preparation solution led to a substantial rise in the selectivity enhancement factor (assessed by the temporal binding rate within microfluidic confinements). This enhancement reached near saturation at a 10-fold increase when anti-CRP surface coverage exceeded 150 ng · cm^{-2}. These results implied the interplay between analyte capture probability and microfluidic dynamics, indicating the importance of optimisation in microfluidics for maximum assay performance.

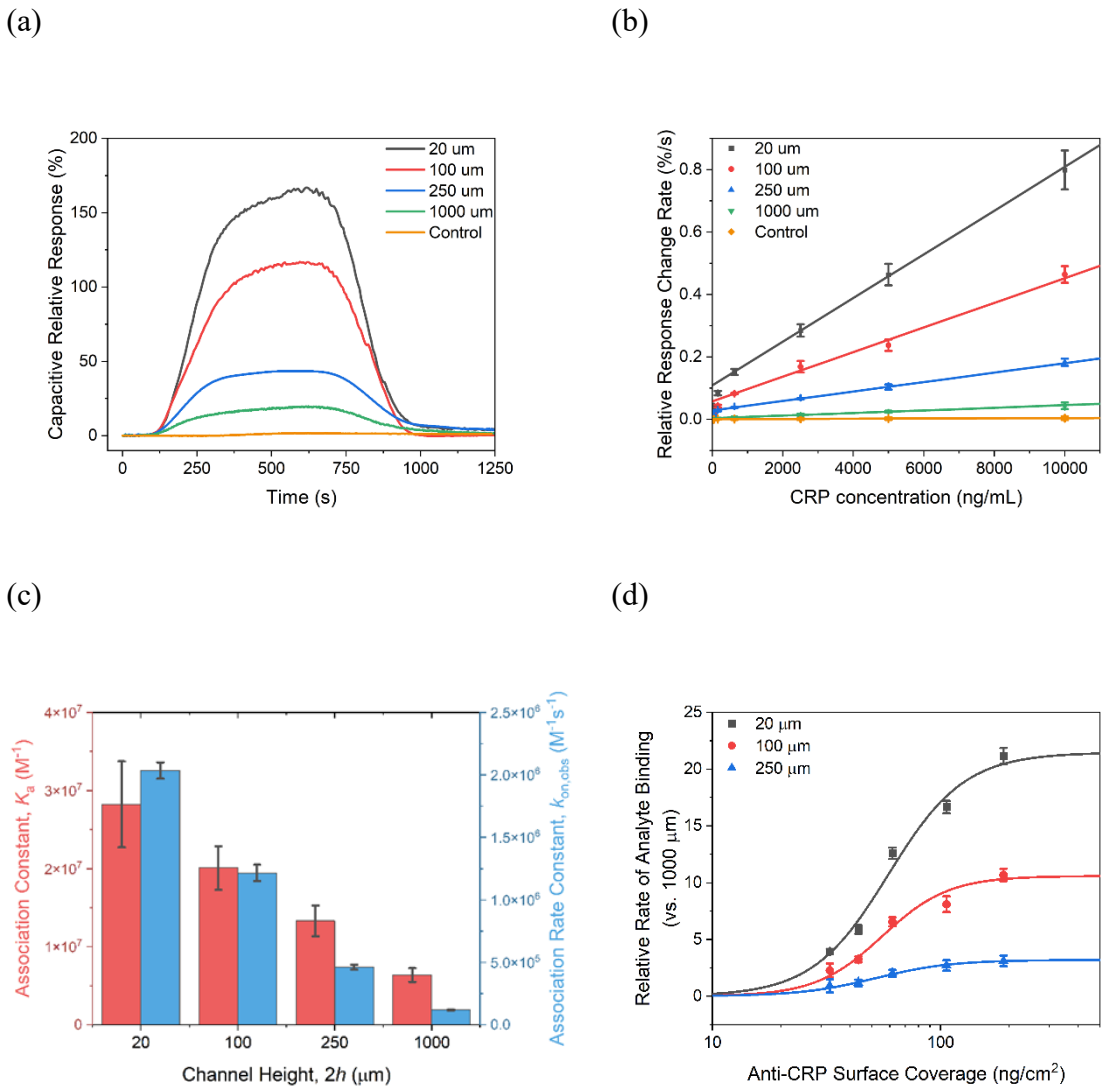


Figure 3.4. (a) Representative sensograms of anti-CRP modified PANI interface in response to 10.0 μg · mL^{-1} CRP within varying microfluidic confinement sizes, ranging from 1000 μm to 20 μm, under a flow rate of 10 μL · min^{-1}. (b) Dose-response curves of bio-receptive PANI films within microfluidic confinements, derived from the 15-second temporal changes during the association regime. (c) Effect of microfluidic channel height 2h on the association constant K_a (red) and the observed association rate constant $k_{on,obs}$ (blue). K_a was determined using the Langmuir-Freundlich isotherms model by fitting equilibrium data of the capacitive response (C_r in plateau) versus analyte concentration. $k_{on,obs}$ was derived from the first-order kinetic fitting of association C_r response, as detailed in Experimental Section. (d) Effect of anti-CRP surface coverage on temporal selectivity enhancement within microfluidic confinements, fitted with a sigmoid curve. Antibody surface coverage was controlled by varying its concentration in the preparation solution and quantified using SPR, following the standard Reichert SPR protocol.

3.3 ENHANCED TARGET SELECTIVITY INSIDE A CONFINED CHANNEL

In contrast to nonspecific interactions, specific biorecognition exhibits high affinity (nM to pM K_d)[26] and fast association kinetics ($k_{on} \geq 10^5\,\mathrm{M^{-1}\cdot s^{-1}}$),[4, 20] ensuring that the analyte binds to the surface-immobilised ligands almost immediately upon contact. The distinction between specific and nonspecific binding, however, is blurred by the sluggish mass transport, resulting in diminishing the target specificity in typical electrochemical biosensor setups. As discussed in Section **1.3.1.2**, the introduction of forced convective flow within microfluidic confinements enhances binding kinetics in proportion to the association rate constants k_{on}. Binding, occurring within the mass-transport limit (MTL) or the partial MTL regime (*i.e.*, specific biorecognition),[20, 27, 28] is highly sensitive to flow conditions such as flow rate, viscosity of media, and channel geometry (*eqn.* **1.16**). In contrast, nonspecific binding, occurring in the binding-limited regime,[3, 4, 20] remains primarily governed by the intrinsic biomolecular association independent of flow dynamics. The impact of increased analyte flux is expected to be significantly more pronounced when mass transport dominates the binding events, that is, specific biorecognition (Figure **3.9d**, discussed later).

This discrimination between specific and nonspecific recruitment can, therefore, be leveraged to improve target selectivity in assays. This was indeed experimentally demonstrated in Figure **3.5a**, where a four-order difference in k_{on} between specific and nonspecific events resulted in a remarkable 300% enhancement in selectivity (see selectivity coefficient $K_{CRP/BSA}$ over an anti-CRP modified PANI electrode in Figure **3.5b**) when analyte flux was boosted by compressing the delivery channel. Pearson

correlation coefficients (PCC), which measure the linear correlation between two variables, were noted to be 0.999 and 0.874 between the selectivity enhancement factor (see definition in Section **3.2**) and the SPR-resolved association rate constant ($\log_{10} k_{on}$, see Section **2.3**) and binding constant ($\log_{10} K_a$), respectively. The stronger correlation with k_{on} indicates that the selectivity enhancement is more directly influenced by the rate at which the analyte binds to the surface, highlighting the importance of rapid association in achieving high target selectivity under improved flow conditions. Additionally, the observed k_{on} value for the Streptavidin/Biotin interaction, as determined by SPR, was two orders of magnitude lower than the reported value ($k_{on} \sim 10^7\ \mathrm{M^{-1} \cdot s^{-1}}$),[29] potentially due to the mass transport limits under give flow conditions.

(a) (b)

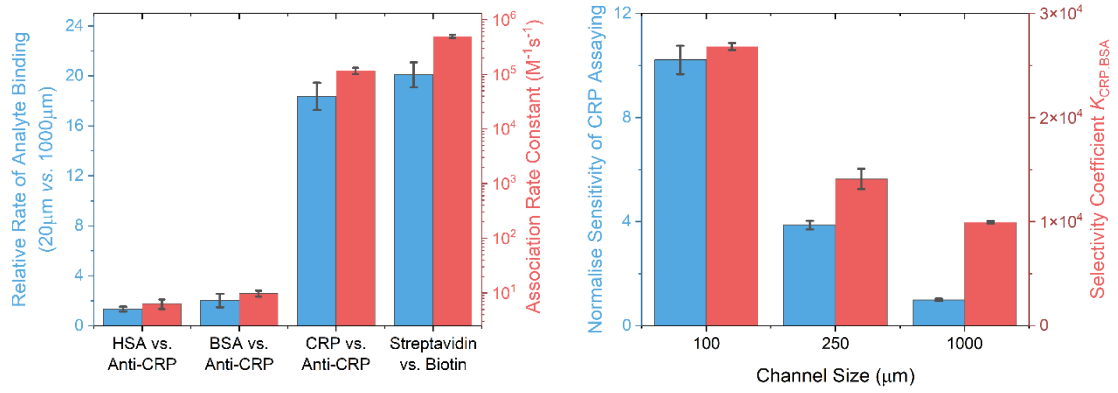


Figure 3.5 (a) Effect of association rate constant (k_{on}, red) and selectivity enhancement factor (blue) for nonspecific (HSA/anti-CRP, BSA/anti-CRP) and specific (CRP/anti-CRP, Streptavidin/biotin) biorecognition within microfluidic confinements of 20 μm and 1000 μm channel heights. The selectivity enhancement factor calculated as the ratio of the temporal sensitivity of analyte response at five increasing concentrations in the 20 μm channel compared to the 1000 μm channel. k_{on} was determined using SPR (see Section **2.3**). (b) Influence of microfluidic confinement channel height on CRP target sensitivity (blue) and the selectivity coefficient over BSA ($K_{CRP/BSA}$, red). CRP temporal sensitivity was normalised to the response in the 1000 μm channel. $K_{CRP/BSA}$ was determined from the ratio of temporal sensitivity between

CRP and BSA over an anti-CRP modified PANI electrode. All error bars represent the standard deviation across three individual electrodes (n = 3).

This target selectivity enhancement can be directly employed to support reliable and robust CRP assaying on unprotected electrodes even in protein-rich environments, such as serum-spiked samples. Building upon the above observations, the robustness (see definition in Section **1.1.3.2**) of the unprotected bio-receptive PANI interface was evaluated by measuring target recovery (as defined in Section **2.4.2**) in serum-spiked samples. As discussed in Section **2.4**, poor recoveries (> 150%) were noted for the anti-CRP modified PANI interface in serum-spiked samples when the CRP concentration was below 1.0 $\mu g \cdot mL^{-1}$. The effectiveness of applying protein blocking agents (*e.g.*, SuperBlock™ blocking buffer and powdered milk) to mitigate nonspecific binding, however, was limited. Alternatively, significant improvement in CRP recovery was achieved within microfluidic confinements without pretreatment or blocking, as shown in Figure **3.6a**. CRP recovery approached unity as the microfluidic channel height was reduced, with a 25% improvement in CRP recovery observed in the 20 μm channel compared to the 1000 μm. These results highlighted the potential of microfluidic confinement as a streamlined and versatile strategy for enhancing target selectivity and specificity in complex biological matrices without the need for additional pretreatment or blocking steps, as shown in Figure **3.6b**.

(a) (b)

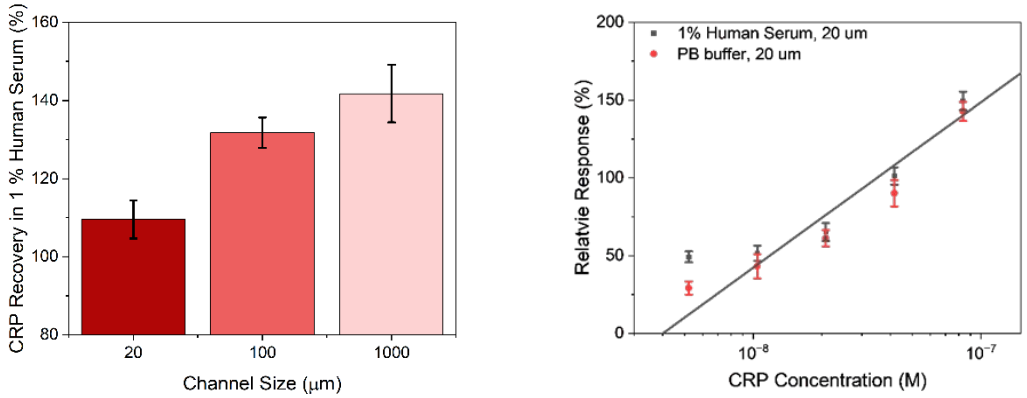


Figure 3.6. (a) Effect of microfluidic confinement channel height on CRP recovery in 1% human serum-spiked samples. Recovery values were averaged from measurements at three different concentrations. (b) "Dose-Response" curves for the assaying of CRP spiked in 1% human serum (black) and PB buffer (red) within a 20 μm microfluidic channel at an unblocked receptive PANI interface. A LoD of 4.0 nM was noted. Error bars represent the standard deviation across three individual electrodes (n = 3).

3.4 MECHANISTIC INSIGHTS INTO MICROFLUIDIC CONFINEMENT: THEORETICAL FRAMEWORK AND COMSOL SIMULATION

As demonstrated in previous observations, analyte flux was selectively improved within microfluidic confinement, resulting in significantly increased assay sensitivity and enhanced target selectivity. In this section, the underlying mechanisms governing the impact of microfluidic confinement on assay performance will be explored. Theoretical frameworks are established to quantify the effects of analyte transport, binding kinetics, surface composition, and microfluidic dynamics under varying channel heights. Additionally, numerical simulations with COMSOL Multiphysics are employed to visualise and validate these theoretical predictions, offering detailed insights into the influence of microchannel dimensions, flow rates, and ligand surface coverage on analyte flux and binding efficiency. Together, these insights serve as a foundation for optimising microfluidic assay designs, enabling more effective and robust assaying of biomarkers in real-world applications.

3.4.1. Theoretical Considerations

Boosted Assay Sensitivity Within Microfluidic Confinement

As shown in *eqn.***3.1**, the specific signal development S_A is directly proportional to the surface concentration of the complex A-B, with a proportionality constant K_A.

$$S_A = K_A \cdot c_{A-B,S} \tag{3.1}$$

Under convective conditions, the observed association rate constant $k_{obs,on}$ depends on the intrinsic association rate constant k_{on} and the mass transport coefficient k_{Lev}, as described in *eqn.* **1.19** (${k_{obs,on}}^{-1} = {k_{on}}^{-1} + {k_{Lev}}^{-1}$).[30, 31] While the observed equilibrium binding constant $K_{a,obs}$ is derived as follows,

$$K_{a,obs} = \frac{k_{on,obs}}{k_{off}} = \frac{\left({k_{on}}^{-1} + {k_{Lev}}^{-1}\right)^{-1}}{k_{off}} \tag{3.2}$$

As the rate constant k_{off} is generally significantly smaller than k_{on} and k_{Lev}, the dissociation process, unlike association, remains relatively unaffected by increases in mass transport ($k_{off,obs} = ({k_{off}}^{-1} + {k_{Lev}}^{-1})^{-1} \approx k_{off}$).

Reducing the channel height increases the mass transport coefficient k_{Lev} (Figure **3.7**), resulting in enhancements in $k_{on,obs}$ and, consequently, $K_{a,obs}$. Assuming Langmuir adsorption behaviour, *eqn.***3.1** can be expressed as follows, where θ is the fractional coverage of receptors by the analyte.

$$S_A = K_A \cdot c_{B,s} \cdot \theta = K_A \cdot c_{B,s} \cdot \frac{c_{A,b} \cdot K_{a,obs}}{\left(1 + c_{A,b} \cdot K_{a,obs}\right)} \tag{3.3}$$

As indicated in *eqn.* **2.8**, the rate of signal change over time ($\frac{\partial S_A}{\partial t}$) becomes,

$$\frac{\partial S_A}{\partial t} = K_A \cdot \frac{\partial c_{A-B,S}}{\partial t} = K_A \cdot \left({k_{on}}^{-1} + {k_{Lev}}^{-1}\right)^{-1} \cdot c_{A,b} \cdot c_{B,s} \tag{3.4}$$

where K_A is the proportionality constant, representing the signal transduction S_A per unit concentration of the surface-bound analyte-ligand complex c_{A_s}, as defined in *eqn.* **2.2**. It is evident that both equilibrium S_A and temporal $\frac{\partial S_A}{\partial t}$ responses increase with the mass transport coefficient k_{Lev}, as indicated by positive derivatives,

$$\frac{dS_A}{dk_{Lev}} = \frac{K_A \cdot c_{B,s} \cdot {c_A}^2 \cdot k_{on} \cdot k_{off}}{\left[\left(c_A \cdot k_{on} + k_{off}\right) \cdot k_{Lev} + k_{on} \cdot k_{off}\right]^2} > 0 \tag{3.5}$$

$$\frac{d}{dk_{Lev}}\left(\frac{\partial S_A}{\partial t}\right) = \frac{K_A \cdot c_{B,s} \cdot c_A \cdot {k_{on}}^2}{(k_{Lev} + k_{on})^2} > 0 \tag{3.6}$$

As shown in *eqn.* **3.5** and **3.6**, these positive derivatives indicate that increasing k_{Lev} by compressing the delivery channel can boost both the magnitude of the signal response and the rate of signal generation. The Levich constant, k_{Lev}, quantifies the influence of microfluidic dynamics — including microchannel dimensions, analyte diffusivity, and flow rate — on mass transport under hydrodynamic conditions, as described by *eqn.* **1.16**.[16, 32] Reducing the microfluidic channel height, particularly below 100 μm, significantly increases k_{Lev} (Figure **3.7**), thereby accelerating overall biorecognition kinetics $k_{overall}$. This enhancement in mass transport facilitates more efficient analyte binding to the surface, ultimately boosting assay sensitivity and lowering detection limits.

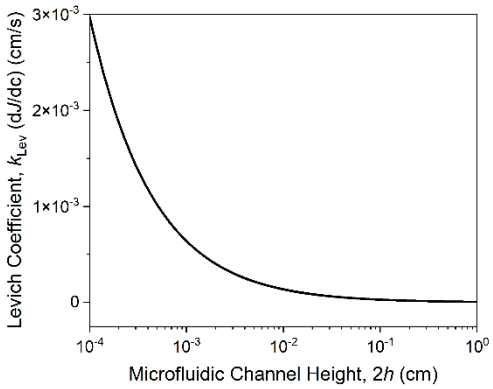


Figure 3.7. Simulated effect of microfluidic channel height on the Levich coefficient (k_{Lev}), using a diffusion coefficient of 1×10^{-7} cm$^2 \cdot$ s^{-1}, a flow rate of 10 μL $\cdot$ min^{-1}, and a receptive disc electrode with a diameter of 1.6 mm, in accordance with *eqn.* **1.16**.[16]

Enhanced Target Selectivity Inside a Confined Channel

Microfluidic confinement not only enhances assay sensitivity but also significantly improves target selectivity within the confined space. By combining *eqn.* **1.5** and **1.6**, target selectivity can be defined as the ratio between the temporal sensitivities of target A and interferent I.

$$Selectivity \equiv \frac{\partial S_A}{\partial t} \Big/ \frac{\partial S_I}{\partial t} = \frac{K_A \cdot k_{obs,on,A}}{K_I \cdot k_{obs,on,I}} = K_{A,I} \cdot \frac{k_{obs,on,A}}{k_{obs,on,I}} \tag{3.8}$$

Using *eqn.* **1.19** and **3.4**, this expression can be simplified as follows, where K_A and K_I represent the proportionality constants of signal transduction for per unit concentration of the surface-bound target A and interferent I, respectively. The ratio of these constants defines the selectivity coefficient of signal transduction between the target and interferent, $K_{A,I}$.

As shown in *eqn.* **3.8**, target selectivity within microfluidic confinement depends not only on the selectivity coefficient ($K_{A,I}$), but also on the relative differences in the overall binding kinetics ($k_{overall,A}/k_{overall,I}$). As discussed in Section **1.3.1.2**, the overall binding kinetics of specific biorecognition, $k_{overall,A}$, which occurs in the MTL regime (*i.e.*, $k_{on} \gg k_{Lev}$), is dominated by k_{Lev}. In contrast, nonspecific binding $k_{overall,I}$ occurring in the binding-limited regime (*i.e.*, $k_{on} \ll k_{Lev}$) is primarily regulated by k_{on}. Considering these approximations, *eqn.* **3.8** can be further simplified as follows.

$$Selectivity \approx K_{A,I} \cdot \frac{k_{Lev}}{k_{on,I}} \tag{3.9}$$

This simplification indicates that the enhanced selectivity is primarily attributed to the increase in mass transport efficiency for specific biorecognition, while impact of

microfluidic enhancements in binding-limited reaction (*i.e.*, nonspecific binding) remains negligible. These results imply that, in heterogeneous processes involving both mass transport and surface binding, enhanced discrimination in target selectivity can be easily achieved by finely controlling flow conditions and geometries of microfluidic devices. Such strategy enables more efficient and selective targeting of specific analytes in the presence of interferent, providing a versatile and streamlined approach for real-world applications. Additionally, it highlights how precise control over reaction environments can significantly enhance the efficiency and specificity of reactions, paving the way for innovative advancements in synthetic methodologies.

3.4.2. COMSOL Simulation

To further validate the theoretical framework, COMSOL simulations were employed to model and visualise the microfluidic confinement (Figure **3.8a** and **b**) and investigate its impact on surface binding kinetics (see details in the experimental chapter). As depicted in Figure **3.8c** and **d**, a crescent-shape analyte surface concentration profile was noted, consistent with expectations.[16] This distribution pattern results from the formation of a 'non-uniform' diffusion layer over the electrode surface (Figure **3.8e**),[16] leading to analyte accumulation predominantly at the upstream edge of the electrode. Additionally, the surface-bound analyte concentration within a 20 μm microfluidic channel, after a 100-second injection, is 30 times higher than in a 1000 μm channel at equilibrium, with a significantly faster binding rate (as indicated by the first derivative of analyte surface concentration) during the initial association phase, as shown in Figure **3.8f**.

It was also confirmed that analyte binding to the receptive interface within microfluidic confinement is highly sensitive to the channel geometry, flow dynamics, target capture probability, and the magnitude of association kinetics, consistent with theoretical expectations.[32] As shown in Figure **3.9a**, the binding rate increased significantly as the microfluidic channel height was reduced. Similarly, at smaller channel heights, the flow rates generated a more pronounced impact on the binding kinetics (Figure **3.9b**). However, the influence of flow rate did not strictly adhere to the Levich equation (*eqn.* **1.16**),[16, 32] which predicts that analyte flux within a microfluidic channel should follow a cube-root dependence on flow rate ($v_f^{1/3}$). Instead, two distinct linear regimes were identified: one below 1 $\mathrm{mm \cdot s^{-1}}$ and another above 1 $\mathrm{mm \cdot s^{-1}}$, as shown in Figure **3.9b**.

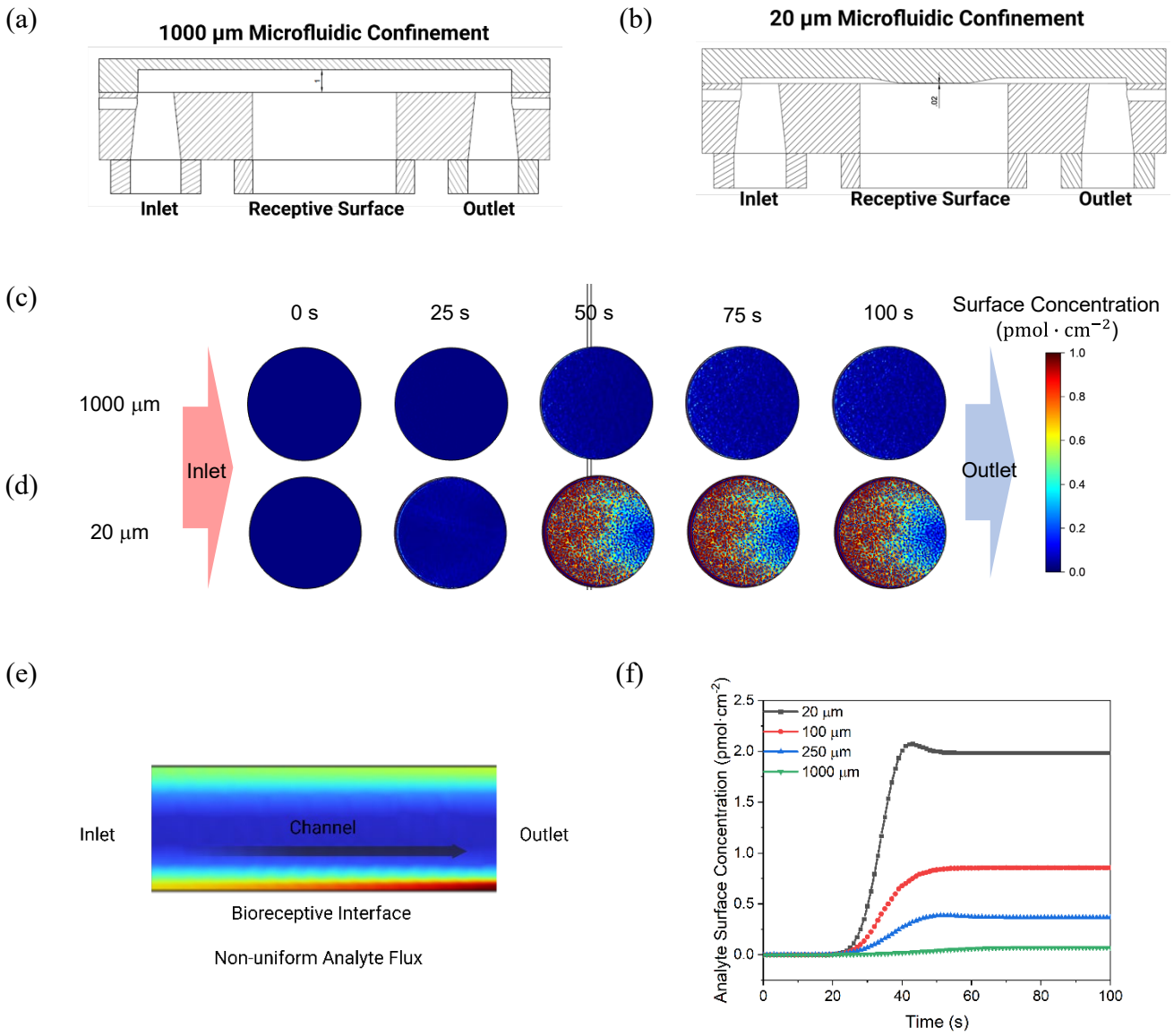


Figure 3.8. Schematic representation of the COMSOL simulation model for (a) 1000 µm and (b) 20 µm microfluidic confinements. Simulated surface-bound analyte concentration profiles on the bio-receptive disc electrode surface within (c) 1000 µm and (d) 20 µm microfluidic confinements. (e) Schematic representation of the non-uniform analyte flux over the electrode surface (bottom), with a higher analyte concentration at the upstream edge (right). (f) Simulated sensograms of analyte surface concentration over a 100-second injection. The colour gradient represents the analyte concentration, with red indicating high concentration and blue indicating low concentration. The parameters used in the simulation are as follows: a diffusion coefficient of the parameters utilised in the simulation are shown as follows: the diffusion coefficient of analyte of 1×10^{-7} $cm^2 \cdot s^{-1}$, a flow rate of 10 $\mu L \cdot min^{-1}$, a receptive disc electrode with a diameter of 1.6 mm and a bioreceptor surface coverage of 1×10^{-5} $mol \cdot m^{-2}$, the association rate constant k_{on} of 1×10^{8} $m \cdot s^{-1}$, the dissociation rate constant k_{off} of 1 $mol \cdot m^{-2} \cdot s^{-1}$, the analyte concentration of 1×10^{-4} $mol \cdot m^{-3}$.

At low flow rates, convective forces are relatively weak, and analyte transport to the receptive surface is primarily governed by diffusion. Increasing the flow rate in this regime has minimal impact on improving mass transport efficiency, resulting in a gradual, linear dependence. In contrast, when the flow rate exceeds 1 $\mathrm{mm \cdot s^{-1}}$ (Reynolds number Re = 0.1, as defined in *eqn.***1.13**), the system enters a convection-dominated regime. Higher flow rates proportionally reduce the thickness of the diffusion boundary layer, significantly accelerating the analyte-to-surface mass transport. This leads to a steeper, "Levich-like" relationship, as shown in Figure **3.9b**.

As depicted in *eqn.* **3.4**, the temporal sensitivity of analyte assaying depends not only on microfluidic dynamics but also on the target capture probability, which is influenced by the interfacial ligand density. As shown in Figure **3.9c**, the simulated selectivity enhancement factor increased with higher bioreceptor surface coverage, reaching a threshold at approximately 10^{-2} $\mathrm{pmol \cdot cm^{-2}}$, consistent with the experimental results shown in Figure **3.4d**.

Finally, the impact of association kinetics on biorecognition within microfluidic confinement was investigated. As shown in Figure **3.9d**, three distinct regimes can be identified accordingly: the MTL regime ($k_{on} \geq 1 \times 10^8$ $\mathrm{M^{-1} \cdot s^{-1}}$), the partial MTL regime (1×10^4 $\mathrm{M^{-1} \cdot s^{-1}} \leq k_{on} \leq 1 \times 10^8$ $\mathrm{M^{-1} \cdot s^{-1}}$), and binding-limited regime ($k_{on} \leq 1 \times 10^4$ $\mathrm{M^{-1} \cdot s^{-1}}$). It is evident that the microfluidic confinement can only selectively improve the reaction kinetics of those involved sluggish mass transport occurring in MTL or partial MTL regimes. However, for processes occurring in the binding-limited regime such as nonspecific binding, microfluidic confinement has little to no effect on improving analyte recruitment efficiency. These results reveal the underlying mechanism that microfluidic confinement enhances assay sensitivity and

target selectivity — by creating a confined space to significantly improve local flow dynamics and increases analyte flux, effectively minimising mass transport limitations. This reduction of the mass transport boundary allows for more efficient target delivery and facilitates the rapid and substantial accumulation of specific analytes at the bio-receptive surface, ultimately enhancing assay sensitivity and target selectivity.

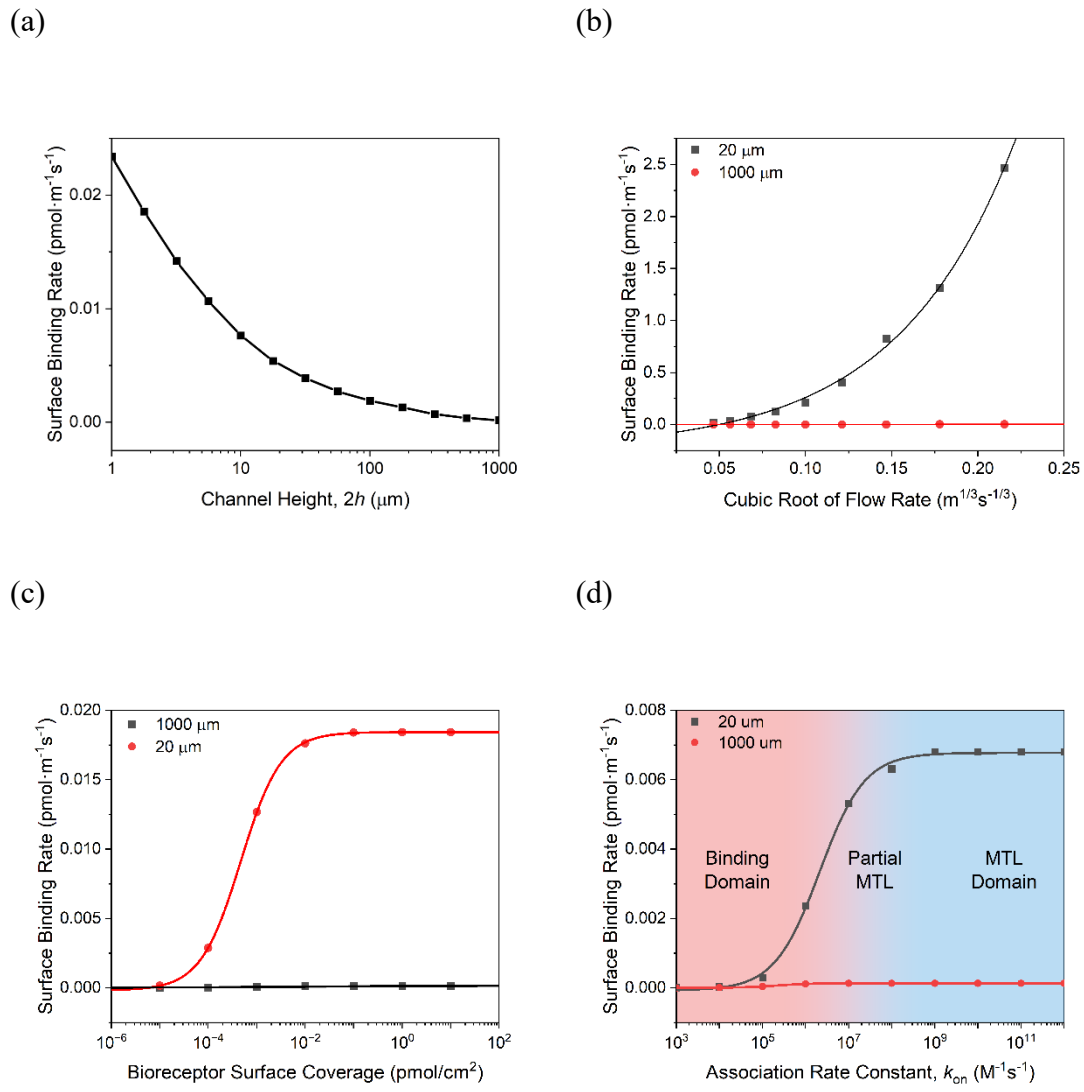


Figure 3.9. Simulation studies on the effects of (a) microfluidic channel height, (b) flow rate, and (c) bioreceptor surface coverage on analyte binding kinetics. (d) Simulated impact of the association rate constant on the overall binding rate within 1000 µm and 20 µm microfluidic confinements. The binding rate was determined from the first derivative of the analyte surface concentration, as resolved from the COMSOL simulation. Simulation parameters are as listed in Figure **3.8** caption.

Since numerical results are highly sensitive to parameters — such as flow rate, analyte concentration and diffusivity, receptive surface area, and surface-bound receptor density — a dimensionless analysis was employed to generalise these findings.[23, 33] Two key dimensionless numbers were considered: the Peclet number Pe and the Damköhler number Da. The Peclet number, also referred to as the dimensionless flow rate, quantifies the relative contribution of convection to diffusion, as shown in *eqn*.**3.10**.

$$Pe = \frac{convection\ rate}{diffusion\ rate} = \frac{2h \cdot U}{D} = \frac{v_f}{w \cdot D} \tag{3.10}$$

Here, $2h$ represents the channel height (cm), w is the channel width (cm), U is the flow velocity ($\mathrm{cm} \cdot \mathrm{s}^{-1}$), v_f the volume flow rate ($\mathrm{cm}^3 \cdot \mathrm{s}^{-1}$), and D is the analyte diffusion coefficient ($\mathrm{cm}^2 \cdot \mathrm{s}^{-1}$). A high Pe indicates convection-dominated transport, while a low one signifies diffusion-driven transport. As shown in Figure **3.10a**, the dimensionless surface binding rate (normalised to receptor surface coverage $c_{B,S}$, analyte bulk concentration $c_{A,b}$, diffusivity D, and channel dimensions) strongly depended on Pe, transitioning from a diffusion-limited regime ($Pe < 10^3$) to a convection-enhanced binding regime ($Pe > 10^3$), consisting with results shown in Figure **3.9b**. Additionally, the Damköhler number Da was introduced as a dimensionless reaction rate constant, defined as follows:

$$Da_{on} = \frac{2d \cdot k_{on} c_{B,S}}{D} \tag{3.11}$$

As shown in Figure **3.10b**, three regimes were identified, namely those of MTL (mass-transfer limited), partial MTL, and binding regimes, aligning with the simulation results in Figure **3.9d**. Both COMSOL simulations and dimensionless analysis supported that the confined geometry of microchannels enhances the likelihood of analyte-receptor

interaction, effectively boosting the local binding rate, increasing sensor sensitivity and selectivity.

(a) (b)

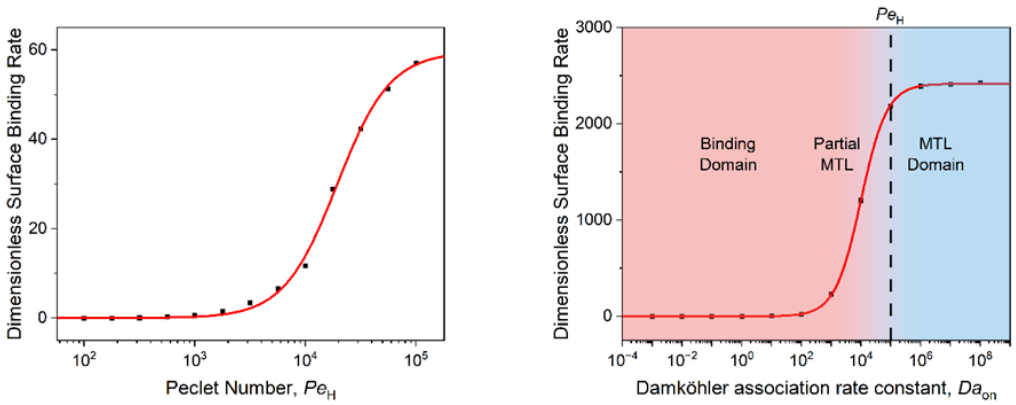


Figure 10. (a) (a) The dimensionless surface binding rate is plotted against the Peclet number, illustrating a shift from a diffusion-limited regime ($Pe_H \leq 10^3$) to a convection-enhanced binding regime ($Pe_H \geq 10^3$). As convective transport becomes more dominant relative to diffusion, surface binding efficiency increases markedly, leading to improved analyte capture at rapid flow rates. (b) The dimensionless binding rate is shown as a function of the Damköhler association rate constant, revealing a transition from a reaction-limited regime to partial mass transport-limited (partial MTL), and eventually to a fully mass transport-limited (MTL) regime. This shift aligns with the characteristic Peclet number (dashed line), signifying the point at which analyte capture becomes primarily governed by transport rather than binding kinetics.

3.5 CONCLUSION AND FUTURE OUTLOOK

Building on the well-established bio-receptive PANI interface,[20, 25] this chapter explored the effects of microfluidic confinement on improving assay sensitivity and enhancing target selectivity. By reducing channel height to just a few micrometres, microfluidic confinement was shown to significantly improve mass transport efficiency through forced convection, resulting in an enhanced and static analyte flux within the confined channel. This constant analyte flux facilitates the rapid and substantial accumulation of specific targets at the bio-receptive interface under flow conditions. When applied to biosensing, reducing the channel height from 1000 μm to 20 μm led to a remarkable 2000% increase in binding rate, 600% enhancement in sensitivity for CRP biosensing. Additionally, the enhancement benefited from microfluidic confinement is selective and shows a more pronounced effect on target-specific biorecognition than nonspecific binding events, with a 300% increase in target selectivity and a 25% improvement in CRP recovery on unprotected electrodes in serum-spiked samples, achieved without the need for pretreatment or blocking.

Subsequently, theoretical frameworks were developed to elucidate the underlying mechanisms driving these improvements. It was suggested that these enhancements are highly sensitive to the channel geometry, flow dynamics, target capture probability, and the magnitude of association kinetics, consistent with experimental results. Further COMSOL simulations revealed that microfluidic confinement can effectively minimise mass transport limitations and significantly improve the reaction kinetics of processes involving sluggish mass transport, particularly in the MTL or partial MTL regimes, that is, specific biorecognition. These results highlighted the potential of tailoring the electrochemical biosensor performance by optimising the device designs, offering a

versatile and powerful strategy for advancing sensitive, robust, and reliable platforms for real-world application.

As microfluidic confinement leverages the mass transport boundary at micrometre-scale dimensions to differentiate between specific biorecognition and nonspecific interactions, it presents exciting opportunities for further applications in sorting and selectively recruiting specific cells, based on both mass transport discrimination and molecular size. Additionally, as mentioned in Section **3.4.1**, microfluidic confinement is particularly advantageous in heterogeneous processes that involve both mass transport and surface binding. This approach is exemplified by electrosynthesis and electrocatalysis, where substrate molecules must approach the electrode surface to facilitate subsequent transformations. Exploring the application of microfluidic confinement in synthetic chemistry and catalytic reactions could open new avenues for optimising reaction efficiency, selectivity, and product yield, particularly in flow-based systems in industrial settings.

3.6 REFERENCES

(1) Ronkainen, N. J.; Halsall, H. B.; Heineman, W. R. Electrochemical biosensors. *Chem. Soc. Rev.* **2010**, *39* (5), 1747-1763.
(2) Jiang, C.; Wang, G.; Hein, R.; Liu, N.; Luo, X.; Davis, J. J. Antifouling strategies for selective in vitro and in vivo sensing. *Chem. Rev.* **2020**, *120* (8), 3852-3889.
(3) Gervais, T.; Jensen, K. F. Mass transport and surface reactions in microfluidic systems. *Chem. Eng. Sci.* **2006**, *61* (4), 1102-1121.
(4) Jarmoskaite, I.; AlSadhan, I.; Vaidyanathan, P. P.; Herschlag, D. How to measure and evaluate binding affinities. *Elife* **2020**, *9*, e57264.
(5) Cho, I.-H.; Lee, J.; Kim, J.; Kang, M.-s.; Paik, J. K.; Ku, S.; Cho, H.-M.; Irudayaraj, J.; Kim, D.-H. Current technologies of electrochemical immunosensors: Perspective on signal amplification. *Sensors* **2018**, *18* (1), 207.
(6) Arya, S. K.; Estrela, P. Electrochemical ELISA-based platform for bladder cancer protein biomarker detection in urine. *Biosens. Bioelectron.* **2018**, *117*, 620-627.
(7) Lee, T. M.-H.; Carles, M. C.; Hsing, I.-M. Microfabricated PCR-electrochemical device for simultaneous DNA amplification and detection. *Lab Chip* **2003**, *3* (2), 100-105.
(8) Wang, Z.; Dai, Z. Carbon nanomaterial-based electrochemical biosensors: an overview. *Nanoscale* **2015**, *7* (15), 6420-6431.
(9) Malhotra, B. D.; Ali, M. A. *Nanomaterials in biosensors: Fundamentals and applications*; Elsevier, 2018.
(10) Su, S.; Sun, Q.; Gu, X.; Xu, Y.; Shen, J.; Zhu, D.; Chao, J.; Fan, C.; Wang, L. Two-dimensional nanomaterials for biosensing applications. *TrAC, Trends Anal. Chem.* **2019**, *119*, 115610.
(11) Wang, J. Nanomaterial-based electrochemical biosensors. *Analyst* **2005**, *130* (4), 421-426.
(12) Luo, X.; Morrin, A.; Killard, A. J.; Smyth, M. R. Application of nanoparticles in electrochemical sensors and biosensors. *Electroanalysis* **2006**, *18* (4), 319-326.
(13) Fernández-la-Villa, A.; Pozo-Ayuso, D. F.; Castaño-Álvarez, M. Microfluidics and electrochemistry: An emerging tandem for next-generation analytical microsystems. *Curr. Opin. Electrochem.* **2019**, *15*, 175-185.
(14) Rackus, D. G.; Shamsi, M. H.; Wheeler, A. R. Electrochemistry, biosensors and microfluidics: a convergence of fields. *Chem. Soc. Rev.* **2015**, *44* (15), 5320-5340.
(15) Gountia, D. Reliability issues in state-of-the-art microfluidic biochips: A survey. *IETE Tech. Rev.* **2023**, *40* (5), 694-709.
(16) Compton, R. G.; Banks, C. E. *Understanding Voltammetry*; World Scientific, 2018.
(17) Li, B.; Chen, J.; Long, M. Measuring binding kinetics of surface-bound molecules using the surface plasmon resonance technique. *Anal. Biochem.* **2008**, *377* (2), 195-201.
(18) Rabbany, S. Y.; Kusterbeck, A. W.; Bredehorst, R.; Ligler, F. S. Binding kinetics of immobilized antibodies in a flow immunosensor. *Sens. Actuators, B* **1995**, *29* (1-3), 72-78.
(19) Hu, G.; Gao, Y.; Li, D. Modeling micropatterned antigen-antibody binding kinetics in a microfluidic chip. *Biosens. Bioelectron.* **2007**, *22* (7), 1403-1409.
(20) Kang, S.; Sharafeldin, M.; Patrick, S. C.; Chen, X.; Davis, J. J. Ultrafast biomarker quantification through reagentless capacitive kinetics. *Anal. Chem.* **2023**, *95* (10), 4721-4727.

(21) Richalet-Sécordel, P. M.; Rauffer-Bruyère, N.; Christensen, L. L.; Ofenloch-Haehnle, B.; Seidel, C.; Van Regenmortel, M. H. Concentration measurement of unpurified proteins using biosensor technology under conditions of partial mass transport limitation. *Anal. Biochem.* **1997**, *249* (2), 165-173.
(22) Pultar, J.; Sauer, U.; Domnanich, P.; Preininger, C. Aptamer–antibody on-chip sandwich immunoassay for detection of CRP in spiked serum. *Biosens. Bioelectron.* **2009**, *24* (5), 1456-1461.
(23) Kang, S.; Davis, J. J. Leveraging Microfluidic Confinement to Boost Assay Sensitivity and Selectivity. *Chem. Sci.* **2025**.
(24) Bard, A. J.; Faulkner, L. R.; White, H. S. *Electrochemical Methods: Fundamentals and Applications*; Wiley, 2022.
(25) Baradoke, A.; Hein, R.; Li, X.; Davis, J. J. Reagentless redox capacitive assaying of C-reactive protein at a polyaniline interface. *Anal. Chem.* **2020**, *92* (5), 3508-3511.
(26) Kim, B.; Dikova, E.; Sheller, U.; Dikov, M.; Gavrilova, E.; Egorov, A. Evaluation of dissociation constants of antigen-antibody complexes by ELISA. *J. Immunol. Methods* **1990**, *131* (2), 213-222.
(27) Schreiber, G.; Haran, G.; Zhou, H.-X. Fundamental aspects of protein− protein association kinetics. *Chem. Rev.* **2009**, *109* (3), 839-860.
(28) Christensen, L. L. Theoretical analysis of protein concentration determination using biosensor technology under conditions of partial mass transport limitation. *Anal. Biochem.* **1997**, *249* (2), 153-164.
(29) Duan, X.; Li, Y.; Rajan, N. K.; Routenberg, D. A.; Modis, Y.; Reed, M. A. Quantification of the affinities and kinetics of protein interactions using silicon nanowire biosensors. *Nat. Nanotechnol.* **2012**, *7* (6), 401-407.
(30) Déjardin, P.; Vasina, E. N. An accurate simplified data treatment for the initial adsorption kinetics in conditions of laminar convection in a slit: application to protein adsorption. *Colloids Surf., B* **2004**, *33* (2), 121-127.
(31) Dejardin, P.; Le, M.; Johner, A.; Wittmer, J. Adsorption rate in the convection-diffusion model. *Langmuir* **1994**, *10* (10), 3898-3901.
(32) Cooper, J. A.; Compton, R. G. Channel electrodes-a review. *Electroanalysis* **1998**, *10* (3), 141-155.
(33) Squires, T. M.; Messinger, R. J.; Manalis, S. R. Making it stick: convection, reaction and diffusion in surface-based biosensors. *Nat. Biotechnol.* **2008**, *26* (4), 417-426.

Chapter 4

Antigen-Mimic Nanoparticles in Ultrasensitive on-Chip Integrated Anti-p53 Antibody Quantification

4.1 BACKGROUND

Anti-p53 antibodies, trigged by the abnormal accumulation of p53 proteins,[1, 2] are important candidate biomarkers for early cancer diagnosis,[1-3] due to their structurally consistent and accessible abundance ($\sim$100 ng $\cdot$ mL^{-1}) at hundreds of times higher than those of antigen in serum,[3, 4] as discussed in Section **1.1.2.2**. Among the various anti-p53 antibody quantification approaches,[5-7] their electrochemical assaying, which typically rely on electrode-confined p53 antigens,[6, 7] are advantageous due to their cost-effectiveness, portable, and scalability.[8, 9] However, on planar two-dimensional interfaces, the electrochemical transduction of these antibodies is hindered by the inefficient target recruitment, resulting from relatively low epitope surface density ($\sim$pmol $\cdot$ cm^{-2}),[10] restricted target accessibility, and sluggish planar diffusion. Additionally, their robust assaying in protein-rich samples (*e.g.*, serum) remains challenges due to pronounced background interference.[4, 11]

Peptide-based recognition elements have emerged as a promising alternative to immunoprotein counterparts,[4] offering several advantages, such as high binding specificity and affinity (nM K_d), excellent chemical stability, synthetic tunability, and significantly reduced costs.[12-14] As these versatile receptors are typically small in size, they can be densely packed on electrode surfaces, enabling higher receptor densities and improving target accessibility. These features make them highly valuable across a wide range of applications in both diagnostics and therapeutics.[12, 13, 15, 16]

Nanomaterials have been increasingly incorporated into sensor formats due to their rich interfacial functionality and high specific surface area,[17-20] which allow for significantly greater bioreceptor loading compared to planar surfaces, thereby enhancing target

recruitment efficiency. When free in solution, their associated three-dimensional (3D) target recruitment is particularly advantageous,[21] as exemplified by the iron oxide nanoparticles (IONPs) assisted biomarker enrichment,[22-25] discussed in Section **1.4.2**. Additionally, when combined with microfluidic techniques,[25] background noise can be reduced, as continuous flow efficiently minimises nonspecific fouling, allowing for the robust target recruitment and assaying of anti-p53 antibodies in serum.[4]

Building on the concepts developed earlier, this chapter details the use of antigen-mimicking, dual-modified IONPs — featuring a 2.1 kDa 18-amino acid peptide recognition element (including the Ser-Asp-Leu-Trp-Lys-Leu epitope for the anti-p53 antibody DO-1,[2] as discussed in Section **1.1.2.2**), and horseradish peroxidase (HRP).[4] These nanoparticles, along with an alternating current (AC) magnetic field-promoted sample mixing,[4, 25] were employed to specifically and efficiently recruit antibodies from serum, prior to presenting the captured targets to lectin (Concanavalin A)-modified screen-printed sensors, as shown in Figure **4.1**. The antigenic peptide displays high sequence specificity and demonstrates superior target recruitment efficiency compared to the full antigen (*i.e.*, p53 proteins) under equivalent conditions. Subsequently, HRP-mediated catalytic oxidation of the TMB substrate generates a voltammetric response that directly reports on the anti-p53 antibody concentration.[26] These sub-femtomolar assays exhibit exceptional sensitivity and selectivity,[4] supporting robust assaying in serum-spiked samples within minutes, with potential for clinical translation.

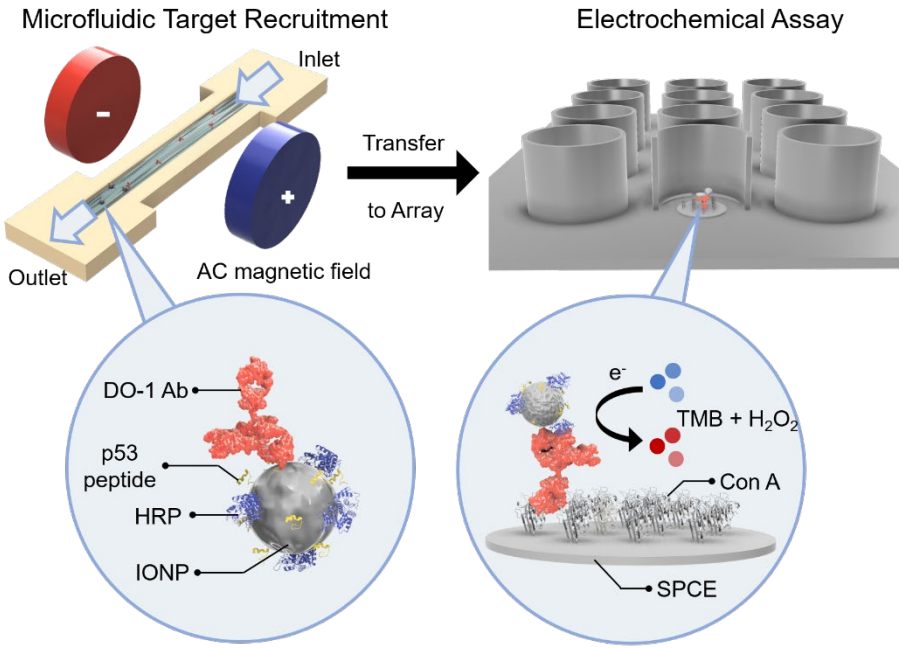


Figure 4.1. Schematic representation of the nanoparticle-assisted biomarker enrichment and subsequent downstream electrochemical enzyme-amplified assay for the DO-1 antibody quantification.[4] The synthesised antigen-mimicking peptide receptor (p53 peptide) was covalently attached to the surface of IONPs, along with HRP (bottom left). An AC magnetic field was then employed to efficiently mix the dual-modified IONPs with DO-1 antibody samples within a microfluidic channel (upper left). Following immunocapture, the nanoparticle-antibody complexes were manually transferred onto Con A-modified screen-printed carbon electrodes (SPCE, upper right). In the presence of the tetramethylbenzidine (TMB) substrate and hydrogen peroxide (H_2O_2),[26, 27] a concentration-dependent square wave voltammetry (SWV) response was generated (bottom right).

4.2 DO-1 ANTIBODY RECRUITMENT: PEPTIDE SEQUENCE SELECTION AND BINDING PERFORMANCE ASSESSMENT

4.2.1. Antigen-mimicking p53 Peptide: SPR Study

As detailed in Section **1.1.2.2**, the DO-1 antibody specifically recognises a conserved epitope located within amino acids residues 20-25 (Ser-Asp-Leu-Trp-Lys-Leu) of the transactivation domain (TAD) in the human p53 protein.[2, 28] This sequence forms part of the antigen α-helix (Gln-Glu-Thr-Phe-Ser-Asp-Leu-Trp-Lys-Leu), as elucidated through crystallographic studies (PDB: 8F2I). To emulate the native antigen, a selected peptide sequence (DO-1 peptide, Cys-Gln-Glu-Thr-Phe-Ser-Asp-Leu-Trp-Lys-Leu-Leu-Pro-Glu-Asn-Asn-Val-Leu) was designed as a functional mimic. As shown in Figure **4.2a**, surface plasmon resonance (SPR) analysis (detailed in the experimental section) revealed that the DO-1 peptide exhibited a binding affinity to the DO-1 antibody (dissociation constant $K_{d,peptide}$ = 0.34 nM) comparable to that of the full recombinant p53 protein ($K_{d,protein}$ = 0.12 nM).[29]

Validation of peptide sequence specificity was conducted by assessing the SPR response of peptide-modified interfaces toward 10.0 $\mu g \cdot mL^{-1}$ DO-1 antibodies, with the synthesised sequence compared against two control peptides: Ser-Pro-Asp-Asp-Ile-Glu-Gln-Trp-Phe-Thr (control peptide 1, mimicking a nonbinding region of the p53 protein)[30] and Cys-Pro-Pro-Pro-Pro-Glu-Lys-Glu-Lys-Glu-Lys (control peptide 2, a non-p53 related, nonfouling peptide). As shown in Figure **4.2b**, at comparable peptide surface densities (~100 $ng \cdot cm^{-2}$), the DO-1 peptide-modified interface demonstrated a 100-fold higher recruitment of DO-1 antibodies compared to the control peptides, confirming the great sequence specificity of the antigen-mimicking peptide.[4]

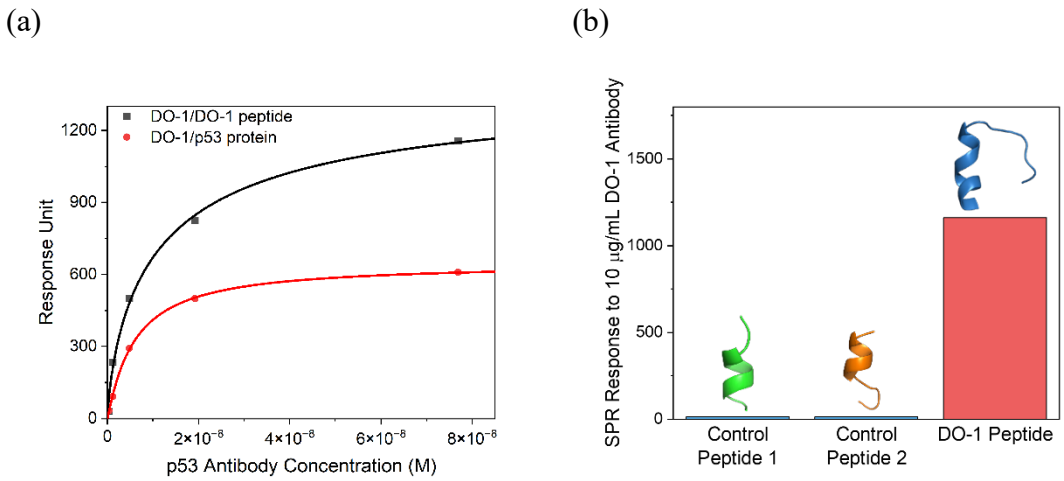


Figure 4.2. SPR analysis of (a) the binding affinity of the DO-1 peptide (black) and full p53 protein (red) to DO-1 antibodies, and (b) the peptide specificity of the synthesised DO-1 sequences (Cys-Gln-Glu-Thr-Phe-Ser-Asp-Leu-Trp-Lys-Leu-Leu-Pro-Glu-Asn-Asn-Val-Leu, blue) compared to control peptides upon exposure to 10.0 μg · mL^{-1} DO-1 antibodies.[4] Control peptide 1 (Ser-Pro-Asp-Asp-Ile-Glu-Gln-Trp-Phe-Thr, green) corresponds to a non-target p53 epitope (amino acids 46-55),[2] while control peptide 2 (Cys-Pro-Pro-Pro-Pro-Glu-Lys-Glu-Lys-Glu-Lys, orange) serves as a non-p53, non-fouling control. SPR measurements were performed at room temperature (298 K) with a flow rate of 30 μL · min^{-1} using 10 mM PBS solution (pH = 7.4) as the running buffer.

4.2.2. Generation of a Sandwich Structure: Concanavalin A

Following the formation of the peptide-antibody complex, Concanavalin A (Con A), a lectin with high affinity for mannose and glucose residues commonly found in antibodies (*e.g.*, immunoglobulin G),[31-36] was employed to immobilise the anti-p53 complexes onto the planar electrode surfaces. The interactions between Con A and DO-1 antibody were mapped using Electrochemical impedance spectroscopy (EIS). A high level of stability of Con A-modified screen-printed carbon electrode (SPCE) interface was noted,[4] with a baseline drift of less than 3% over a one-hour successive EIS measurement. As shown in Figure **4.3a**, the introduction of antibodies resulted in an increase in charge transfer resistance R_{ct}. Empirically fitting these dose-response curves to a Langmuir-Freundlich

isotherm yielded a dissociation constant K_d of 13.6 ± 2.3 nM,[4] consistent with previous reports and SPR results.[37]

Additionally, the specificity of Con A-modified interface was further evaluated using both EIS and SPR. As shown in Figure **4.3b**, a good level of antibody selectivity was confirmed,[4] with significantly lower responses (<10% of the DO-1 signal) to nonspecific protein (*i.e.*, 1.0 mg · mL^{-1} human serum albumin, HSA, and bovine serum albumin, BSA). These results highlighted the role of Con A in leveraging its glycan-binding properties to facilitate the selective and robust attachment of antibody complexes to the electrode surfaces.[34, 36] This immobilisation ensures that the target antibodies are effectively anchored, forming a stable sandwich structure for subsequent electrochemical detection.

(a) (b)

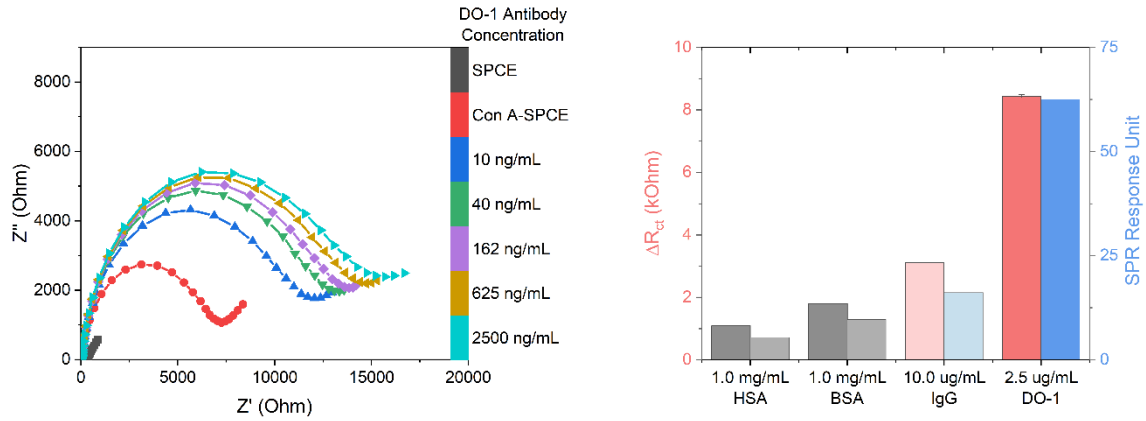


Figure 4.3. (a) Representative impedimetric Nyquist plots of a plasma-cleaned SPCE electrode (black), Con A-modified SPCE electrode before (red) and after exposed to varying concentrations of DO-1 antibody.[4] (b) Impedimetric (left) and SPR (right) assessments of the specificity of the Con A-modified surface toward 2.5 μg · mL^{-1} DO-1 antibody (target), compared to nonspecific proteins (*i.e.*, 10.0 μg · mL^{-1} IgG, 1.0 mg · mL^{-1} HSA and BSA). EIS measurements were conducted on the Con A-modified SPCE interface, using a 5 mM ferrocyanide and ferricyanide in PBS mixture (pH = 7.4). SPR measurements were performed at room temperature (298 K) with a flow rate of 30 μL · min^{-1} in 10 mM PBS solution (pH = 7.4) as the running buffer.

4.2.3. TMB-HRP Catalysis in High-throughput SPCE Array

The electrochemical transduction of captured anti-p53 antibodies was performed on a high-throughput, plasma-cleaned SPCE array. Leveraging advanced scalable screen-printing fabrication techniques,[38] SPCEs provide a cost-effective and highly adaptable platform for multiplexed electrochemical analysis. By depositing conductive carbon ink (*e.g.*, graphite, graphene, or carbon nanotubes)[39, 40] and integrating multiple electrodes onto a substrate (*e.g.*, glass, ceramic, or flexible polymer)[41] within a compact array, this process enables the production of consistent and reproducible electrode arrays. The resulting uniform electrochemical performance across large batches makes SPCEs ideal for large-scale, high-throughput diagnostic applications.

However, during the production of SPCEs, additives such as insulating binders are typically employed to enhance improve ink adhesion to the substrate.[41] While necessary, these additives can reduce electrochemical transduction efficiency and increase background noise. To mitigate these issues, thorough cleaning of SPCEs prior to use is essential, typically involving solvent washing, electrochemical cleaning, or plasma pre-treatment.[41] As shown in Figure **4.4a**, following a 30-min plasma cleaning, the peak separation ΔE_p in a 5 mM ferrocyanide and ferricyanide in PBS mixture (pH = 7.4) was significantly reduced from 739 mV to 153 mV, closely matching that of the glassy carbon electrode (GC, ΔE_p = 160 mV). The reduction in R_{ct} from 42.6 kOhm to 0.276 kOhm, and the corresponding increase in the Tafel analysis-resolved charge transfer coefficient (β, as defined in Section **6.3.1.2**) from 0.15 to 0.47 confirmed the enhanced conductivity and improved electrochemical performance of the SPCEs after plasma cleaning.

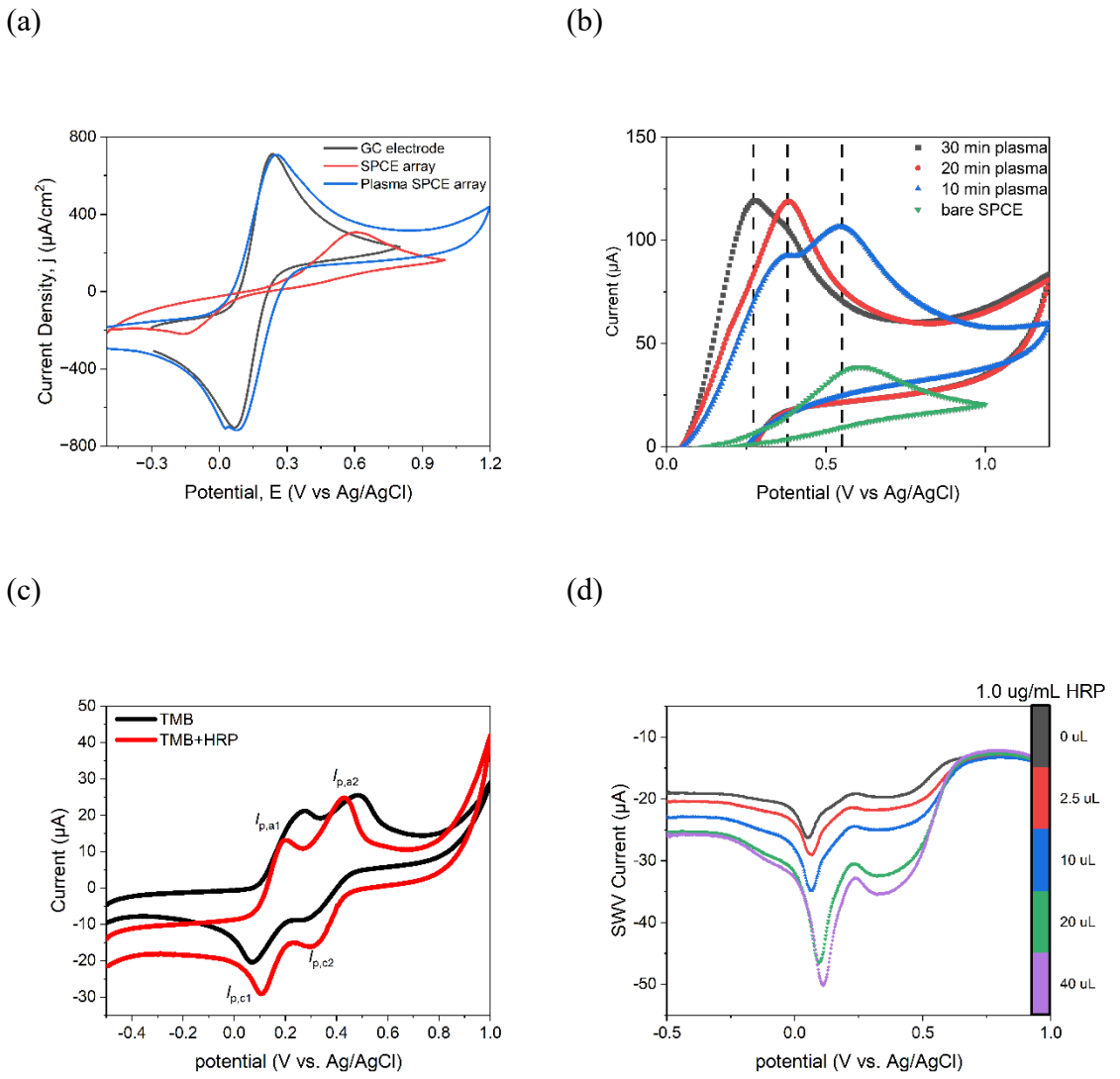


Figure 4.4. (a) Representative cyclic voltammograms of a GC disc electrode (ϕ = 3.0 mm, black), an SPCE array (ϕ = 3.0 mm, red) and a plasma-cleaned SPCE array (blue),[4] and (b) Time-course study of plasma cleaning effect on the electrochemical performance of SPCEs. The electrochemical characterisation of carbon electrodes was performed using a 5 mM ferrocyanide and ferricyanide in PBS mixture (pH = 7.4) at a scan rate of 100 mV · min^{-1}. (c) Electrochemical oxidation of TMB with (red) or without (black) the presence of HRP scanning from - 0.5 V to + 1.0 V *vs.* Ag/AgCl at a scan rate of 100 mV · min^{-1}, using a commercially available TMB substrate (see experimental section). (d) SWV response for the TMB reduction at varying volumes of 1.0 μg · mL^{-1} HRP additions. SWV measurements were performed with an amplitude of 20 mV, a potential step of 5 mV, and a frequency of 50 Hz.

A time-course study demonstrated that the improvement in SPCE performance is progressive with extended plasma cleaning, as shown in Figure **4.4b**. After 10 minutes of plasma treatment, the current density of the oxidation peak at E_p = + 0.61 V *vs.* Ag/AgCl

increased notably. With further cleaning, the oxidation peak shifted progressively to lower potentials, first to + 0.37 V *vs.* Ag/AgCl in 20 mins and eventually to + 0.27 V *vs.* Ag/AgCl after a 30-min pretreatment while consistently maintaining a high current density. This gradual shift in E_p suggests that plasma activation of SPCEs primarily involves two stages: the removal of surface contaminants within the first 10 minutes, followed by the generation of a defect-rich electrode surface[42]. These defects servers as electrochemically active centres, significantly enhancing electron transfer kinetics over time and contributing to the overall improvement in the electrode performance.

Following the immunocapture of DO-1 antibodies, the resulting nanoparticle-antibody complexes were manually transferred onto Con A-modified SPCEs. The particle-bound HRP then catalyses the oxidation of the TMB substrate,[26] producing a concentration-dependent signal. To initial assay, it is essential to investigate the underlying mechanism of HRP-mediated TMB oxidation and understand the specific role of HRP in enhancing the electrochemical signal in this system. As shown in Figure **4.4c**, two pairs of well-defined redox peaks were noted, centred at + 0.168 V and + 0.381 V *vs.* Ag/AgCl, corresponding to a reversible two-electron transfer process, as anticipated.[26, 27] Tafel analysis further revealed that the charge transfer from the cation radical to di-imine (*i.e.*, $\beta_{p,a2}$ = 0.12) was significantly slower compared to the previous redox step (*i.e.*, $\beta_{p,a1}$ = 0.50). This sluggish behaviour is attributed to the formation of charge-transfer complexes during TMB oxidation,[43] as illustrated in Figure **4.5**, which hinders electron transfer in the second step of the process.

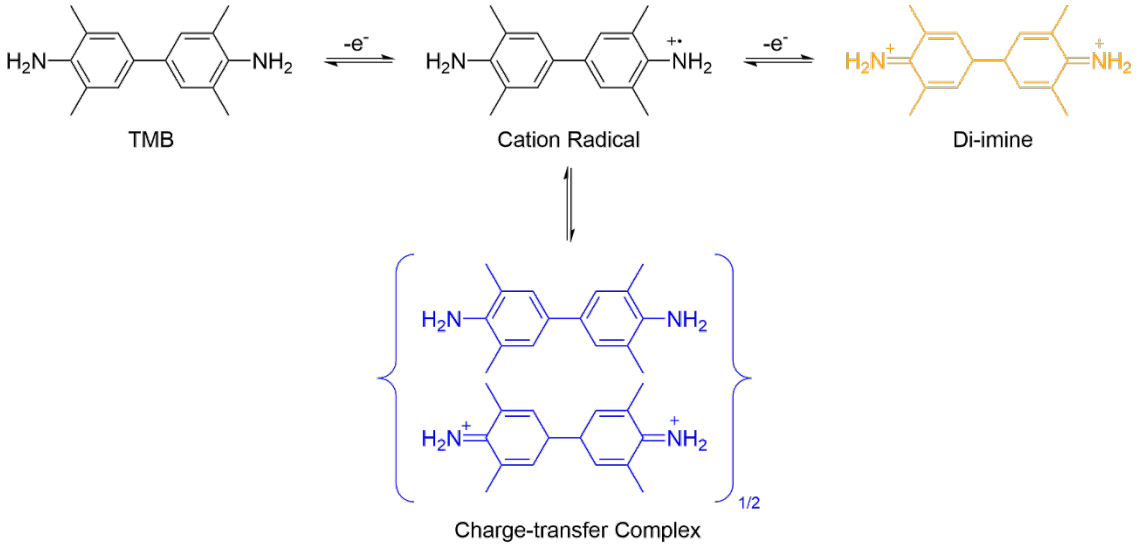


Figure 4.5. Schematic representation of the TMB oxidation mechanism.[43] TMB undergoes a two-step, two-electron oxidation, initially forming a cation radical intermediate, followed by further oxidation to the yellow di-imine form. The cation radicals can be stabilised through the formation of blue charge-transfer complexes.

In the presence of HRP, the cleavage of H_2O_2 generates two equivalents of activated HRP intermediates.[26, 27] These intermediates catalyse the oxidation of TMB to its di-imine form via a successive two-step electron transfer process. The introduction of HRP significantly lowers the activation energy for TMB oxidation, enabling faster electron transfer, as evidenced by the steeper Tafel slope shown in Figure **4.4c**. This rapid oxidation depleted the available TMB substrate, leading to a reduction in current density during the forward scans (*e.g.*, $i_{p,a1}$). Simultaneously, the accumulation of di-imine compounds enhanced the reduction current in the reverse scans (*e.g.*, $i_{p,c1}$ and $i_{p,c2}$). This increase in reduction current was directly proportional to the HRP concentration, as shown in Figure **4.4d**. To ensure sensitive and reliable assaying of HRP-bound complexes, the reduction peak at around $E_{p,c1}$ = + 0.1 V *vs.* Ag/AgCl was chosen for subsequent experiments.

4.3 PREPARATION OF ANTIGEN-MIMIC DUAL-FUNCTIONALISED IRON OXIDE NANOPARTICLES

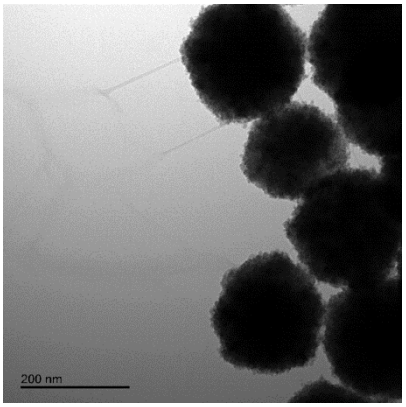
4.3.1. Hydrothermal Synthesis of IONPs

Low-polydispersity IONPs were prepared by hydrothermal synthesis.[4, 44] Briefly, a mixture of 50 mL ethylene glycol, 0.65 g anhydrous trisodium citrate, 0.97 g anhydrous iron (III) chloride and 3.00 g anhydrous sodium acetate was thoroughly sonicated and stirred at room temperature for 30 minutes. After adding a small amount of water (0.25 mL), the yellow solution was transferred to an autoclave and heated at 200℃ for 10 hours, followed by overnight cooling. The resulting nanoparticles were purified through three rounds of washing with water and ethanol, collected with a Neodymium magnet, and dried at 60℃ overnight. During hydrothermal synthesis,[45] iron (III) ions undergo two processes to form iron oxide nanoparticles: reduction and hydration, as detailed in Section **1.4.1.2**. Ethylene glycol and citrate serve as reducing agents, effectively facilitating the reduction of iron (III) ions to iron (II). In addition to aiding in reduction, citrate functions as a capping agent, stabilising the resulting nanoparticles and preventing agglomeration. The generation of low-polydispersity IONPs requires precise control over the hydration rate, which is finely modulated by viscous solvent ethylene glycol ($\eta_{\text{ethylene glycol}}$ = 17.01 $\text{mPa} \cdot \text{s}^{-1}$ *vs.* η_{water} = 0.894 $\text{mPa} \cdot \text{s}^{-1}$ at room temperature),[46] the water volume, and the acetate buffering capacity. This controlled hydration process, coupled with fine-tuned reduction conditions, ensures the formation of uniform, high-quality IONPs.[45]

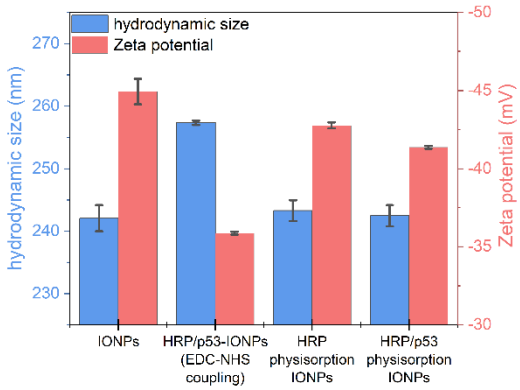
As shown in Figure **4.6a**, transmission electron microscopy (TEM) revealed that the synthesised IONPs exhibited a uniform spherical morphology with an average size of approximately 200 nm.[4] This observation aligns closely with dynamic light scattering

(DLS) measurements (Figure **4.6b**), which reported a hydrodynamic size of 242.1 $\pm$ 2.1 nm (PDI < 0.06).[4] As shown in Figure **4.6c**, the Fourier-transform infrared spectroscopy (FTIR) results were as expected.[47] In addition to the characteristic peak of the Fe–O stretching at 562 cm^{-1}, distinct peaks were noted, at 1565 cm^{-1} and 1407 cm^{-1} corresponds to the asymmetric and symmetric stretching vibrations of carboxylate groups (COO), respectively. The presence of surface-bound carboxylate groups was also confirmed by zeta potential measurements (Figure **4.6b**), where the strong negative charge (ζ_{IONPs} = - 44.9 $\pm$ 0.8 mV) was indicative of the abundant carboxylate groups on the nanoparticle surface. Powder X-ray diffraction (PXRD, Figure **4.6d**) confirmed the inverse spinel crystal structure of synthesised nanoparticles (discussed in Section **1.4.1.1**),[47, 48] giving the formula $(Fe^{3+})[Fe^{2+}Fe^{3+}]O_4$. Based on the Scherrer equation,[49] the crystallite size of the synthesised IONPs was calculated to be 8.55 nm, corresponding to the size of individual magnetic domains within particles. These small magnetic domains facilitate the superparamagnetic behaviour of the synthesised IONPs (discussed in Section **1.4.1.1**),[50] as evidenced by the absence of coercivity H_c and remanence M_r once the external magnetic field is removed (*i.e.*, magnetic field H = 0), shown in Figure **4.6e**. Additionally, the synthesised IONPs exhibited a saturation magnetisation M_s of approximately 100 $emu \cdot g^{-1}$, closely aligning with the expected value for Fe_3O_4 (M_s = 92 $emu \cdot g^{-1}$),[51] confirming the strong magnetic properties of the nanoparticles.

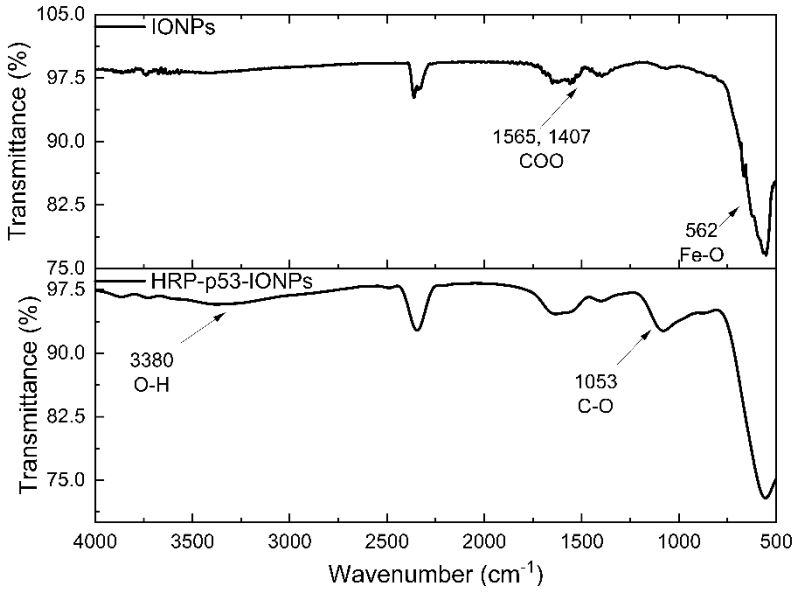
(a)


200 nm

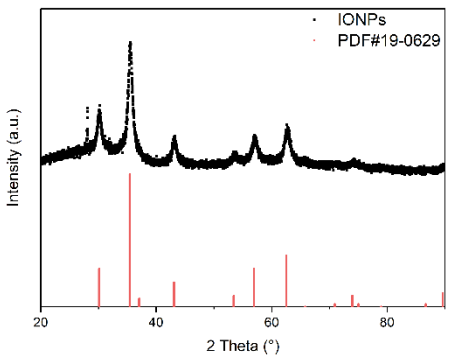
(b)


hydrodynamic size
Zeta potential
hydrodynamic size (nm)
Zeta potential (mV)
270
260
250
240
230
-50
-45
-40
-35
-30
IONPs
HRP/p53-IONPs (EDC-NHS coupling)
HRP physisorption IONPs
HRP/p53 physisorption IONPs

(c)


IONPs
Transmittance (%)
105.0
97.5
90.0
82.5
75.0
1565, 1407
COO
562
Fe-O
HRP-p53-IONPs
3380
O-H
1053
C-O
4000
3500
3000
2500
2000
1500
1000
500
Wavenumber (cm-1)

(d)


IONPs
PDF#19-0629
Intensity (a.u.)
20
40
60
80
2 Theta (°)

(e)

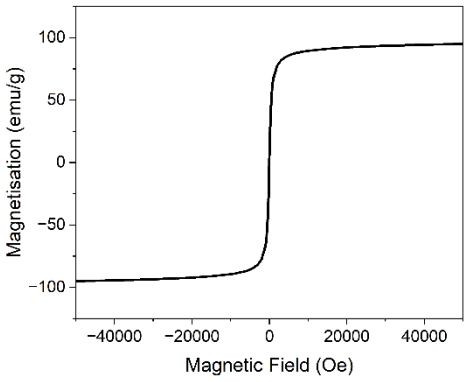

Magnetisation (emu/g)
100
50
0
−50
−100
−40000
−20000
0
20000
40000
Magnetic Field (Oe)

Figure 4.6. (a) Representative TEM image of citrate-chelated IONPs, showing a uniform spherical morphology with an average diameter of approximately 200 nm.[4] (b) DLS (blue) and zeta potential (red) measurements of IONPs, and HRP-p53-IONPs prepared via EDC-NHS coupling or physisorption. Measurements were performed at room temperature, with IONPs samples dispersed in a 10 mM phosphate buffer (pH = 7.4). Error bars represent the standard deviations across three individual measurements (n = 3). (c) FTIR spectrums of the IONPs and HRP-p53 peptide-IONPs. In addition to characteristic peaks, the peak around 2349 cm^{-1} corresponds to the asymmetric stretching of CO_2 from the atmosphere. (d) PXRD pattern of hydrothermal synthesised iron oxide nanoparticles (upper, Cu $K_{\alpha 1}$), with reference diffraction peaks for Fe_3O_4 (PDF #19-0629) shown below for comparison. (e) Representative magnetisation curve of synthesized IONPs, demonstrating superparamagnetic behaviour with a great saturation magnetisation M_s of approximately 100 emu/g.[50]

4.3.2. Integration with p53 Epitope and HRP: Dual-Functionalised IONPs Preparation

Dual-functionalised interfaces were constructed by immobilising the DO-1 peptide and HRP onto the synthesised IONPs using EDC-NHS coupling chemistry.[4, 52] In brief, the nanoparticles were first dispersed and activated in a solution of 0.2 M EDC and 0.05 M NHS in MES buffer (pH = 5.5) for 1 hour at room temperature. Following activation, these particles were incubated overnight in a solution containing 50 $\mu g \cdot mL^{-1}$ HRP and 5.0 $\mu g \cdot mL^{-1}$ DO-1 peptide in MES buffer (pH = 5.5). Bioconjugation was conducted in an acidic environment to promote efficient activation of carboxyl groups, thereby facilitating the formation of the reactive ester intermediate and enhancing the overall coupling efficiency.[52] Both activation and incubation steps were carried out on a roller to ensure thorough mixing and efficient conjugation. After incubation, the particles were washed with PBS (pH = 7.4) to remove unbound reagents, and the particle surfaces were subsequently blocked with 1.0 $mg \cdot mL^{-1}$ BSA in PBS-T to prevent nonspecific binding.

The bioconjugation process was monitored using DLS and zeta-potential measurements, as shown in Figure **4.6b**. Compared to the HRP and HRP/p53 peptide physiosorbed IONPs, the hydrodynamic size of the resulting dual-functionalised IONPs increased to 257.3 $\pm$ 0.3 nm , accompanied by a slight positive shift in zeta potential to $\zeta_{HRP/p53\ peptide-IONPs}$ = - 35.9 $\pm$ 0.1 mV. Additionally, upon functionalisation with HRP and DO-1 peptide, a new broad peak around 3380 cm^{-1}, corresponding to O-H stretching, and a C-O stretching peak at 1053 cm^{-1} were noted in the FTIR spectrum. These changes indicated successful covalent attachment of the biomolecules to the IONP surface.

The surface densities of HRP and DO-1 peptide on the IONPs were quantified using 2,2'-azino-bis(3-ethylbenzothiazoline-6-sulfonic acid) (ABTS) UV-vis and micro-BCA assays, respectively.[4, 53] As shown in Figure **4.7a**, the peptide surface coverage was highly tuneable, ranging from 6% to >80% of the geometric surface area. In contrast, the surface-bound HRP accounted for less than 5% of the geometric surface area, and diminished at higher peptide coverage levels, likely due to competition for binding sites on the nanoparticle surface.[4] This balance between peptide and HRP loading has a direct impact on assay performance. As shown in Figure **4.7b**, a quadratic correlation was noted between the SWV response and DO-1 peptide coverage on the dual-functionalised IONPs.[4] In this system, the DO-1 peptide serves as a bioreceptor, specifically recruiting anti-p53 antibodies, while HRP acts as an electrocatalyst to amplify the electrochemical signal. At lower peptide densities, the limited number of bioreceptors reduces the likelihood of target capture, compromising assay sensitivity. Conversely, at higher peptide densities, competition for surface binding sites limits HRP attachment, thereby diminishing the catalytic signal. Therefore, optimal antibody responses were obtained at

~50% geometric peptide coverage, prepared using a solution containing 50 $\mu g \cdot mL^{-1}$ HRP and 5.0 $\mu g \cdot mL^{-1}$ DO-1 peptide, maximising both assay sensitivity and target capture efficiency. Notably, the surface coverage of the full-length p53 protein was substantially lower than that of peptide coverage (5% *vs.* 50%) under identical preparation conditions (*i.e.*, bioreceptor and nanoparticle concentrations, incubation time), as shown in Figure **4.7b** (black square).[4] This significant difference in surface coverage likely arises from the larger size of the full-length protein, which restricts the accessibility of bioconjugation on the nanoparticle surface. The impact of this disparity on the sensing performance of peptide and protein-modified IONPs will be further discussed in Section **4.4.2**.

(a) (b)

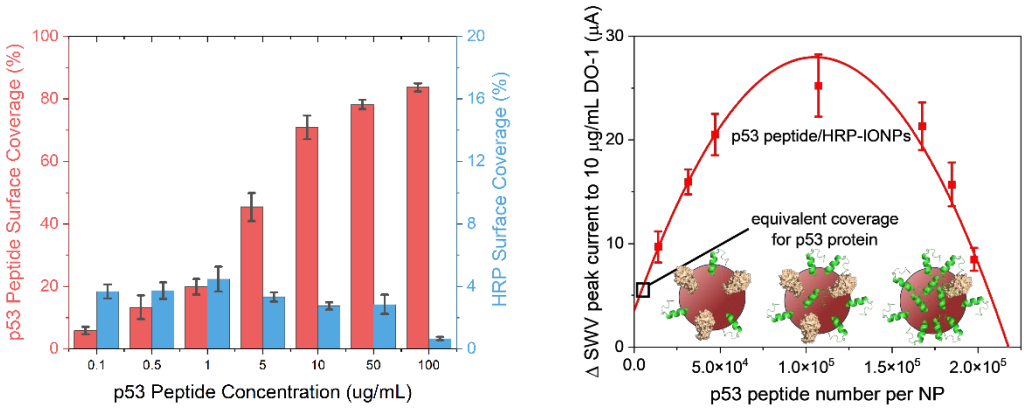


Figure 4.7. (a) Surface coverage of DO-1 peptide (red) and HRP (blue) on IONPs as a function of peptide concentration in the preparation solution.[4] DO-1 peptide surface coverage was determined using the micro-BCA assay, while the HRP surface coverage was quantified through the ABTS UV-vis study. (b) SWV analysis showing the relationship between dual-functionalised IONP surface composition (represented by DO-1 peptide surface coverage) and sensing performance, when exposed to 10.0 $\mu g \cdot mL^{-1}$ DO-1 antibody. The red curve represents a quadratic correlation (R^2 = 0.95) between peptide loading and the corresponding electrochemical signal. The black square denotes the equivalent surface coverage and SWV response using the full antigen protein. SWV measurements were conducted in 100 µL of TMB substrate solution, ranging from + 1.0 V to - 0.5 V (*vs.* Ag/AgCl), with an amplitude of 20 mV, a potential step of 5 mV, and a

frequency of 50 Hz. All error bars represent the standard deviations across three individual measurements (n = 3).

4.4 AC MAGNETIC FIELD-ASSISTED IMMUNOCAPTURE AND AMPLIFIED ELECTROCHEMICAL P53 ANTIBODY QUANTIFICATION

4.4.1. AC Magnetic Field-Assisted Magnetic Separation for Enhanced Biomarker Recruitment

A 100 μL aliquot of 10 $\mu g \cdot mL^{-1}$ peptide-modified IONPs was employed for the recruitment of DO-1 antibodies, initially from a buffer solution.[4] As discussed in Section **4.1**, target recruitment on planar receptor surfaces is typically hindered by sluggish binding kinetics and nonspecific fouling, particularly in protein-rich media such as serum, which necessitates either extended incubation times or the implementation of antifouling strategies. As expected, significant fouling was noted in serum-spiked samples after 1-hour of static recruitment, accounting for more than 25% of the specific response (Figure **4.9c**). To address these challenges, a microfluidic setup paired with a programmable AC electromagnetic field was introduced to improve recruitment efficiency and specificity, as shown in Figure **4.9a**.[4] IONPs oscillated within microfluidic channel, with their oscillation frequency and intensity regulated by the AC electromagnetic field's frequency and strength. As the sample was delivered to the channel at a controlled flow rate, the dynamic movement of the oscillating magnetic nanoparticles increased the likelihood of target binding between the functionalised IONPs and DO-1 antibodies, while minimising nonspecific fouling, ensuring effective and specific recruit of the DO-1 antibodies from serum-spiked samples.

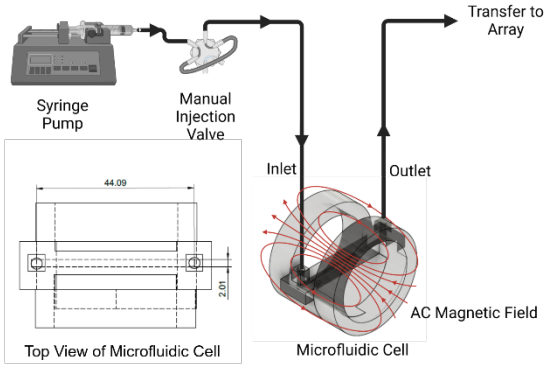
As shown in Figure **4.9b** and **c**, a time-course study revealed that AC magnetic field-assisted (MAC) magnetic separation significantly improved both target recruitment

efficiency and specificity.[4] The SWV response to 50.0 $ng \cdot mL^{-1}$ rapidly reached a plateau within just 10 minutes, while nonspecific background response in serum-spiked samples were reduced by 60%. In comparison, a 10-minute vortex shaking — another approach used to promote mixing — also accelerated target recruitment, as evidenced by the similar SWV response shown in Figure **4.9d**.[4] However, 100% higher nonspecific binding was noted in vortex shaking. These results highlighted the capability of AC magnetic field-assisted magnetic separation, which not only sped up the target recruitment but also significantly minimised undesired biofouling.

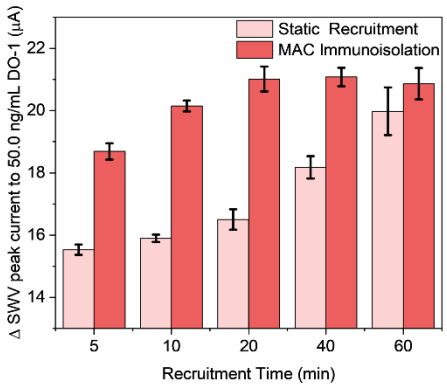
As noted in a previous work,[25] target capture efficiency is highly dependent on the particle oscillation frequency, field strength, and microfluidic flow rate.[4] As shown in Figure **4.9e**, the heatmap demonstrated the correlation between the target recruitment efficiency (normalised to 100% using the SWV response of IONPs capturing 1.0 $ng \cdot mL^{-1}$ DO-1 antibody under optimised microfluidic isolation conditions) and both the strength (regulated by electromagnetic potential) and frequency of the AC magnetic field. High oscillation frequencies and electromagnetic potentials (upper right corner of the heatmap) increased particle mobility and improved mixing efficiency, thereby accelerating target recruitment. The increased oscillation frequency notably enhanced target recruitment efficiency, but was herein capped at 2.0 Hz due to equipment limitations and concerns about potential nanoparticle-induced hyperthermia at higher frequencies.[4, 54] Elevated temperatures could lead to undesired protein denaturation, compromising assay sensitivity and reliability. The impact of flow rate on target capture efficiency is shown in Figure **4.9f**. As the flow rate increased from 25 $\mu L \cdot min^{-1}$ to 100 $\mu L \cdot min^{-1}$, capture efficiency remained consistently high. However, at higher flow rates, faster sample passage through the microfluidic channel resulted in reduced interaction

time between the target molecules and the functionalized nanoparticles. This is evidenced by the significant drop in capture efficiency when the flow rate increased to 200 $\mu L \cdot min^{-1}$. Therefore, the optimised conditions for microfluidic isolation were determined to be 2 Hz oscillation frequency, 11.5 V electromagnetic potential, and a flow rate of 100 $\mu L \cdot min^{-1}$.[4]

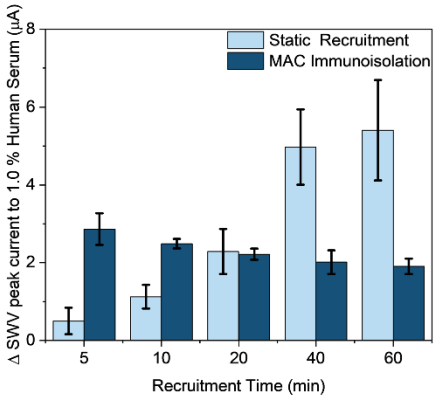
(a)



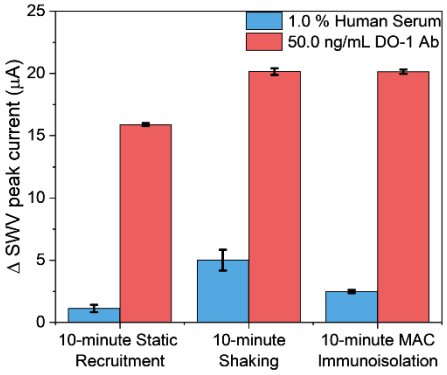
(b)



(c)



(d)



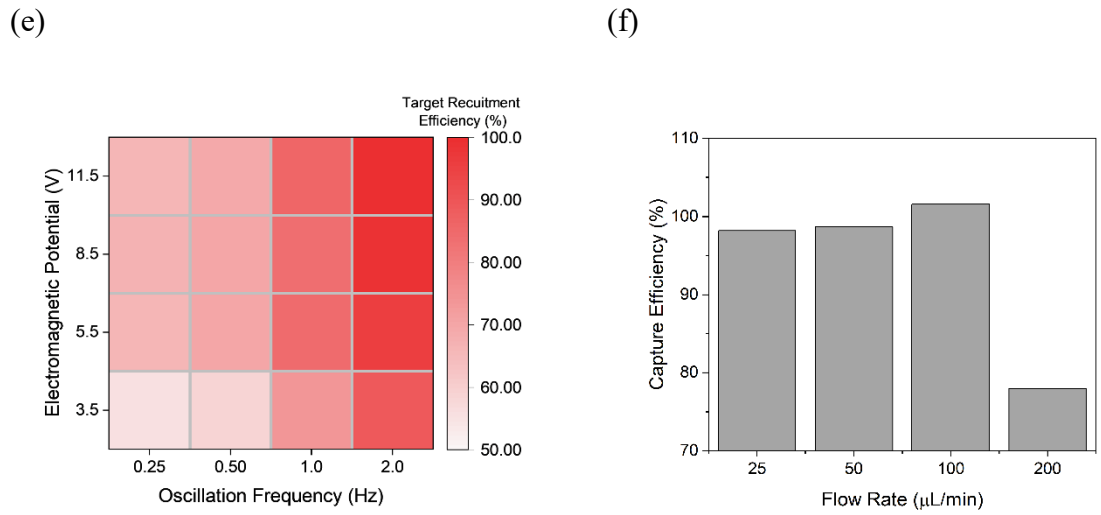


Figure 4.8. (a) Schematic depiction of the microfluidic setup for biomarker immunocapture, featuring a microfluidic channel, syringe pump, manual injection valve, and programmable electromagnets housed in two rings on either side of the channel.[4, 25] The microfluidic channel was fabricated using 3D printing, with the dimensions in millimetres provided in the top view. Samples and running buffer were delivered by an automated syringe pump at a controlled flow rate, accessible up to 200 $\mu L \cdot min^{-1}$. The AC magnetic field was precisely tuned by adjusting the oscillation frequency (up to 2.0 Hz) and electromagnetic field strength (regulated by potential, up to 12.0 V). Time-course studies included: (b) target recruitment efficiency (measured by the SWV response to 50.0 $ng \cdot mL^{-1}$ DO-1 antibody) and (c) nonspecific binding in serum over a 1-hour static incubation and MAC immunoisolation. (d) Comparative target recruitment efficiency and nonspecific binding in serum under three incubation conditions: 10 minutes of static recruitment, 10 minutes of vortex shaking (using a vortex mixer), and magnetic mixing (10 minutes of MAC immunoisolation under optimised AC magnetic conditions). (e) The effect of nanoparticle oscillation frequency and AC magnetic field strength and (f) flow rate on microfluidic DO-1 antibody immunoisolation. SWV measurements were conducted in 100 µL of TMB substrate solution, ranging from + 1.0 V to - 0.5 V (*vs.* Ag/AgCl), with an amplitude of 20 mV, a potential step of 5 mV, and a frequency of 50 Hz. Recruitment efficiency was normalised to 100% using the SWV current response of IONPs capturing 1.0 $ng \cdot mL^{-1}$ DO-1 antibody under optimised microfluidic isolation conditions (*i.e.*, electromagnetic potential = 11.5 V; nanoparticle oscillation frequency = 2.0 Hz; flow rate = 100 $\mu L \cdot min^{-1}$). All error bars represent the standard deviations across three individual measurements (n = 3).

4.4.2. Amplified Electrochemical p53 Antibody Quantification

After immunoisolation, the antibody-IONP complexes were carefully collected using a pipette and manually transferred to Con A-modified SPCEs, as shown in Figure **4.10a**. The complexes were allowed to incubate on the lectin-modified surface for 1 hour, ensuring effective binding of the captured antibodies. Subsequently, these captured antibodies were subjected to an electrochemical assay in the presence of TMB and H_2O_2. As shown in Figure **4.10b**, the HRP-mediated SWV response reported sensitively on DO-1 antibody concentrations. The assay demonstrated a broad dynamic range, spanning from 5.0 $pg \cdot mL^{-1}$ to 0.5 $\mu g \cdot mL^{-1}$, with great repeatability (standard deviation <5% across the entire range),[4] as shown in Figure **4.10c**. Following *eqn.* **1.4**, the limit of detection (LoD) was determined to be as low as 1.0 $pg \cdot mL^{-1}$ (8.3 fM), comfortably surpassing clinical requirements.

Notably, the peptide-coated IONPs exhibited much higher bioreceptor loading compared to the full-length p53 protein under equivalent preparation conditions (50% *vs.* 5.0% geometric surface area; as confirmed by the micro-BCA assay in Figure **4.7b**). This substantial increase in bioreceptor surface density greatly enhanced the probability of target capture, resulting in a 400% increase in assay sensitivity, as shown in Figure **4.10d**.[4] This result highlighted the potential of peptide-based recognition elements in improving target recruitment efficiency and assay performance. Their smaller size, compared to full-length proteins, allows for higher surface loading and greater target accessibility, making them more effective for biosensing applications.

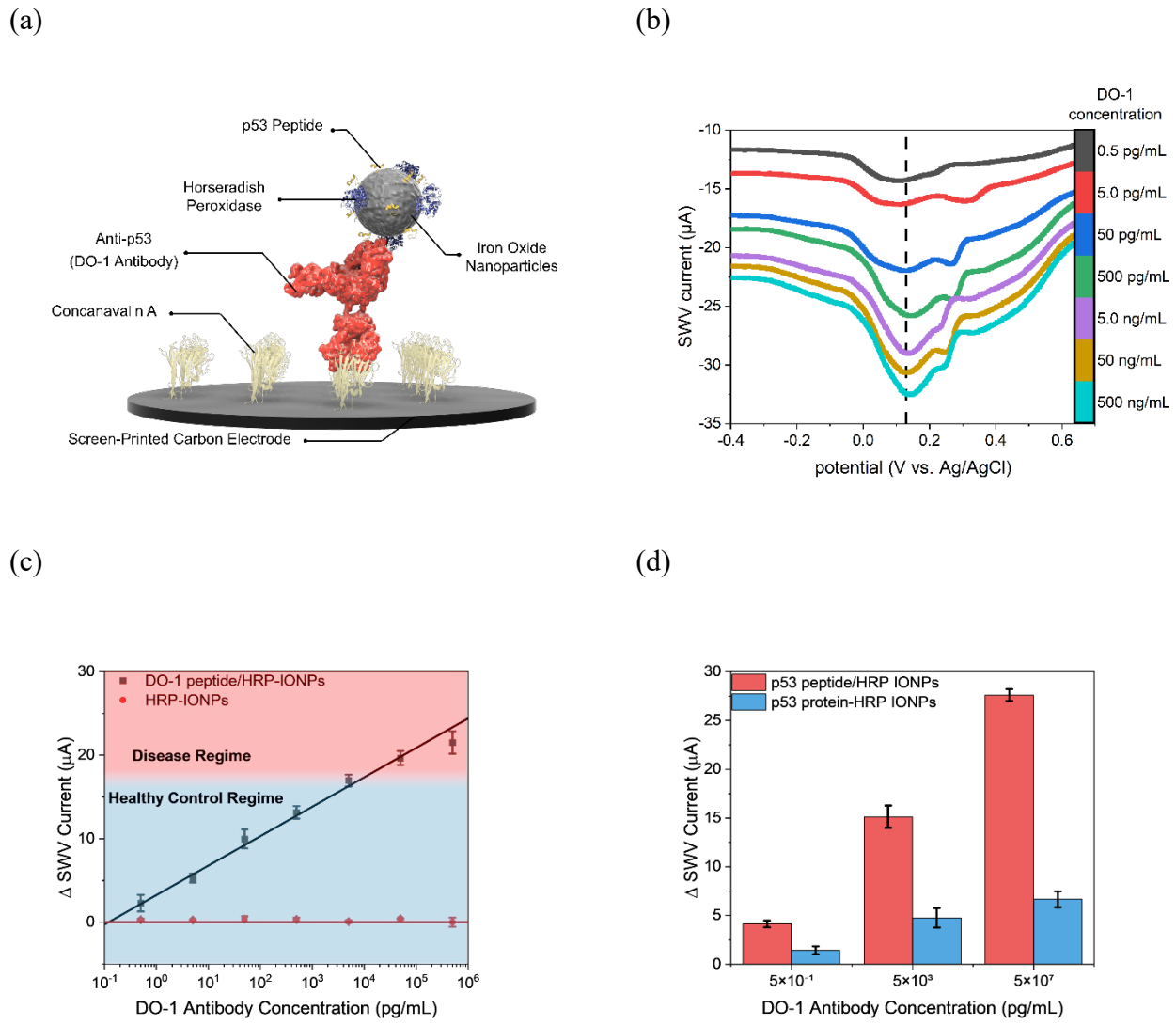


Figure 4.9. (a) Schematic depiction of the sandwich structure generated on the Con A-modified SPCEs surface. The structure features antigen-mimicking, dual-functionalised IONPs bound to the cancer-relevant anti-p53 antibody (DO-1), forming an IONP-antibody complex. This complex is then immobilised on the lectin-modified surface, facilitating subsequent electrochemical assays. (b) Representative SWV response showing HRP-mediated electrochemical detection of DO-1 antibodies across a broad concentration range (0.5 $pg \cdot mL^{-1}$ to 500 $ng \cdot mL^{-1}$) on Con A-modified SPCEs.[4] (c) Linear fitting of the voltammetric response to DO-1 antibodies recruited by DO-1 peptide/HRP-IONPs (black, R^2 = 0.99) and control, nonreceptive HRP-IONPs (red). Two regimes (healthy control and disease) were defined based on literature values,[3] extrapolated to the calibration curve. (d) Comparison of SWV response for target antibody detection (immunoisolation under optimised MAC conditions) using DO-1 peptide (red) and full antigen (blue) capture. Error bars represent standard deviation from three individual electrodes (n = 3).

Assay specificity was evaluated using 1.0 $mg \cdot mL^{-1}$ BSA, HSA, 1.0% human serum, and 10.0 $\mu g \cdot mL^{-1}$ immunoglobulin G (IgG) as antibody controls. Under optimised MAC immunoisolation conditions (see Section **4.4.1**), nonspecific binding was effectively minimised, with negligible voltammetric responses (<10% of the specific signal observed for 50 $ng \cdot mL^{-1}$ DO-1 antibody),[4] as shown in Figure **4.11a**. Additionally, as shown in Figure **4.11b**, recovery rates (as defined in Section **2.4.2**) averaged 96.7 $\pm$ 3.2% in BSA (n = 3) and 100.7 $\pm$ 5.0% in human serum (n = 5). These results highlighted the robustness and selectivity of MAC-assisted target recruitment, supporting the sensitive and reliable assaying of sub-femtomolar concentrations of cancer-relevant antibodies in serum-spiked samples, with potential for clinical translation.

(a) (b)

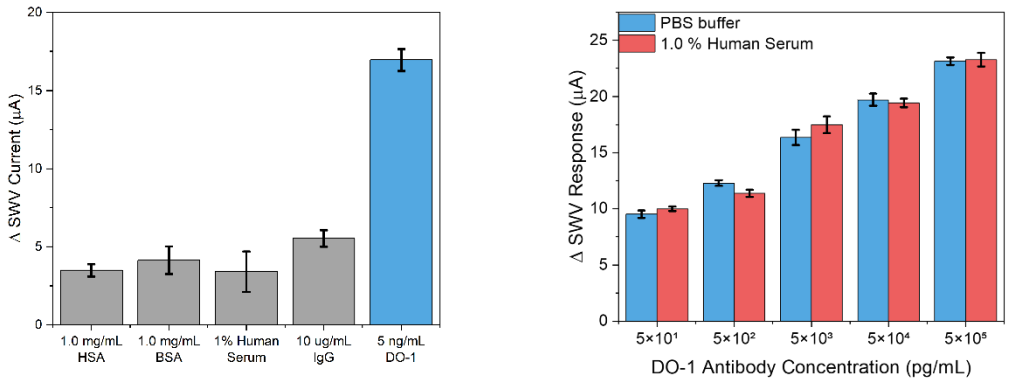


Figure 4.10. (a) Specificity assessment of MAC-assisted electrochemical quantification of anti-p53 antibodies, showing SWV current responses for nonspecific controls (grey; 1.0 $mg \cdot mL^{-1}$ HSA and BSA, 10.0 $\mu g \cdot mL^{-1}$ IgG, and 1% human serum) and specific detection of the DO-1 antibody (blue).[4] (b) Recovery rates for DO-1 antibody recruitment across clinically relevant concentrations spiked into 1.0% human serum. All error bars represent the standard deviation across three individual electrodes (n = 3).

4.5 CONCLUSION AND FUTURE OUTLOOK

This chapter demonstrated the development and application of antigen-mimicking, dual-functionalised iron oxide nanoparticles (IONPs) for the ultrasensitive detection of anti-p53 antibodies. The antigenic DO-1 peptide exhibited high sequence specificity, and when immobilised onto IONPs, its high surface loading resulted in a 400% enhancement in target recruitment efficiency, surpassing that of the full antigen under equivalent conditions. Paired with AC magnetic field-promoted sample mixing, these peptide-coated IONPs efficiently recruited DO-1 antibodies from serum-spiked samples within minutes, while significantly reducing nonspecific fouling, as confirmed by the time-course studies discussed in Section **4.4.1**.

The captured targets, when transferred to a lectin-modified SPCEs surface, generated an electrochemical readout through HRP-mediated TMB oxidation. This process delivered a dynamic range spanning from 5.0 $pg \cdot mL^{-1}$ to 0.5 $\mu g \cdot mL^{-1}$ for DO-1 antibodies, with a detection limit as low as 1.0 $pg \cdot mL^{-1}$ (8.3 fM) following optimised MAC immunoisolation conditions (*i.e.*, 2 Hz oscillation frequency, 11.5 V electromagnetic potential, and a flow rate of 100 $\mu L \cdot min^{-1}$). Additionally, with negligible voltammetric responses to nonspecific proteins, these assays enabled the reliable and robust recruitment of DO-1 antibodies in the presence of nonspecific interference, as evidenced by the great recovery rate (*i.e.*, 100.7 $\pm$ 5.0%) in serum-spiked samples. The integration of nanoparticle-based electrochemical assays with advanced immunoisolation techniques highlighted the potential for clinical translation, particularly in the early detection of cancer biomarkers, offering a robust, sensitive, and scalable solution for real-world applications.

Future research could focus on exploring sequence specificity, particularly in the context of subtle differences between closely related epitopes. For instance, the human DO-1 epitope (SDLWKL) and the mouse DO-7 epitope (SGLWKL) differ by only a single amino acid,[2] yet this minor variation may have significant effects on binding affinity and sensor performance. Investigating the impact of site-specific mutations on antibody recognition could provide valuable insights into the underlying mechanisms of binding, facilitating the development of biosensors tailored for detecting homologous proteins with slight epitope variations, thereby broadening their application across species and disease models.

Beyond sequence specificity, a critical next step in translating this technology to clinical practice is conducting extensive clinical trials. While the results from serum-spiked samples are promising, it is essential to validate the performance of these assays in real-world settings using diverse clinical samples. Additionally, further research should focus on developing multiplexed sensing platforms capable of detecting multiple cancer-relevant biomarkers simultaneously. For example, the simultaneous quantification of DO-1 and AB-2 antibody — both belonging to the anti-p53 family — could offer a more comprehensive assessment of disease progression.[2] Correlating the levels of these antibodies may provide valuable insights into p53 pathway dynamics, aiding in the elucidation of potential mechanisms underlying tumour development, and advancing cancer research.

4.6 REFERENCES

(1) Labrecque, S.; Naor, N.; Thomson, D.; Matlashewski, G. Analysis of the anti-p53 antibody response in cancer patients. *Cancer Res.* **1993**, *53* (15), 3468-3471.
(2) Sabapathy, K.; Lane, D. P. Understanding p53 functions through p53 antibodies. *J. Mol. Cell Biol.* **2019**, *11* (4), 317-329.
(3) Hasbek, Z.; Doğan, Ö. T.; Sarı, İ.; Yücel, B.; Şeker, M. M.; Turgut, B.; Berk, S.; Siliğ, Y. The diagnostic value of the correlation between serum Anti-p53 antibody and positron emission tomography parameters in lung cancer. *Mol. Imaging Radionucl. Ther.* **2016**, *25* (3), 107.
(4) Kang, S.; Yuan, D.; Barber, R.; Davis, J. J. Antigen-mimic nanoparticles in ultrasensitive on-chip integrated anti-p53 antibody quantification. *ACS Sens.* **2024**, *9* (3), 1475-1481.
(5) Aubrey, B. J.; Kelly, G. L.; Janic, A.; Herold, M. J.; Strasser, A. How does p53 induce apoptosis and how does this relate to p53-mediated tumour suppression? *Cell Death Differ.* **2018**, *25* (1), 104-113.
(6) Cruz-Pacheco, A. F.; Quinchia, J.; Orozco, J. Cerium oxide-doped PEDOT nanocomposite for label-free electrochemical immunosensing of anti-p53 autoantibodies. *Microchim. Acta* **2022**, *189* (6), 228.
(7) Elshafey, R.; Siaj, M.; Tavares, A. C. Au nanoparticle decorated graphene nanosheets for electrochemical immunosensing of p53 antibodies for cancer prognosis. *Analyst* **2016**, *141* (9), 2733-2740.
(8) Wang, J. Electrochemical biosensors: towards point-of-care cancer diagnostics. *Biosens. Bioelectron.* **2006**, *21* (10), 1887-1892.
(9) Sharafeldin, M.; Davis, J. J. Point of care sensors for infectious pathogens. *Anal. Chem.* **2020**, *93* (1), 184-197.
(10) Tehrani, Z.; Abbasi, H. Y.; Devadoss, A.; Evans, J. E.; Guy, O. J. Assessing surface coverage of aminophenyl bonding sites on diazotised glassy carbon electrodes for optimised electrochemical biosensor performance. *Nanomaterials* **2021**, *11* (2), 416.
(11) Lin, P.-H.; Li, B.-R. Antifouling strategies in advanced electrochemical sensors and biosensors. *Analyst* **2020**, *145* (4), 1110-1120.
(12) Xiao, X.; Kuang, Z.; Slocik, J. M.; Tadepalli, S.; Brothers, M.; Kim, S.; Mirau, P. A.; Butkus, C.; Farmer, B. L.; Singamaneni, S. Advancing peptide-based biorecognition elements for biosensors using in-silico evolution. *ACS Sens.* **2018**, *3* (5), 1024-1031.
(13) Kuang, Z.; Kim, S. N.; Crookes-Goodson, W. J.; Farmer, B. L.; Naik, R. R. Biomimetic chemosensor: designing peptide recognition elements for surface functionalization of carbon nanotube field effect transistors. *ACS Nano* **2010**, *4* (1), 452-458.
(14) Kim, S. S.; Kuang, Z.; Ngo, Y. H.; Farmer, B. L.; Naik, R. R. Biotic-abiotic interactions: factors that influence peptide-graphene interactions. *ACS Appl. Mater. Interfaces* **2015**, *7* (36), 20447-20453.
(15) Tadepalli, S.; Kuang, Z.; Jiang, Q.; Liu, K.-K.; Fisher, M. A.; Morrissey, J. J.; Kharasch, E. D.; Slocik, J. M.; Naik, R. R.; Singamaneni, S. Peptide functionalized gold nanorods for the sensitive detection of a cardiac biomarker using plasmonic paper devices. *Sci. Rep.* **2015**, *5* (1), 1-11.
(16) Soto, D.; Orozco, J. Peptide-based simple detection of SARS-CoV-2 with electrochemical readout. *Anal. Chim. Acta* **2022**, *1205*, 339739.

(17) Su, S.; Sun, Q.; Gu, X.; Xu, Y.; Shen, J.; Zhu, D.; Chao, J.; Fan, C.; Wang, L. Two-dimensional nanomaterials for biosensing applications. *TrAC, Trends Anal. Chem.* **2019**, *119*, 115610.
(18) Kong, D.; Bi, S.; Wang, Z.; Xia, J.; Zhang, F. In situ growth of three-dimensional graphene films for signal-on electrochemical biosensing of various analytes. *Anal. Chem.* **2016**, *88* (21), 10667-10674.
(19) Bansi Dhar Malhotra, M. A. A. *Nanomaterials in Biosensors: Fundamentals and Applications*; Elsevier, 2018.
(20) Wang, J. Nanomaterial-based electrochemical biosensors. *Analyst* **2005**, *130* (4), 421-426.
(21) Campuzano, S.; Pedrero, M.; González-Cortés, A.; Yáñez-Sedeño, P.; Pingarrón, J. M. Electrochemical biosensors for autoantibodies in autoimmune and cancer diseases. *Anal. Methods* **2019**, *11* (7), 871-887.
(22) Moeser, G. D.; Roach, K. A.; Green, W. H.; Alan Hatton, T.; Laibinis, P. E. High-gradient magnetic separation of coated magnetic nanoparticles. *AIChE J.* **2004**, *50* (11), 2835-2848.
(23) Olsvik, O.; Popovic, T.; Skjerve, E.; Cudjoe, K. S.; Hornes, E.; Ugelstad, J.; Uhlén, M. Magnetic separation techniques in diagnostic microbiology. *Clin. Immunol. Rev.* **1994**, *7* (1), 43-54.
(24) Guo, L.; Liu, C.; Qi, M.; Cheng, L.; Wang, L.; Li, C.; Dong, B. Recent progress of nanostructure-based enrichment of circulating tumor cells and downstream analysis. *Lab Chip* **2023**, *23* (6), 1493-1523.
(25) Sharafeldin, M.; Yan, S.; Jiang, C.; Tofaris, G. K.; Davis, J. J. Alternating magnetic field-promoted nanoparticle mixing: the on-chip immunocapture of serum neuronal exosomes for Parkinson's disease diagnostics. *Anal. Chem.* **2023**.
(26) Fanjul-Bolado, P.; González-García, M. B.; Costa-García, A. Amperometric detection in TMB/HRP-based assays. *Anal. Bioanal. Chem.* **2005**, *382* (2), 297-302.
(27) Volpe, G.; Draisci, R.; Palleschi, G.; Compagnone, D. 3, 3' 5, 5'-Tetramethylbenzidine as electrochemical substrate for horseradish peroxidase based enzyme immunoassays. A comparative study. *Analyst* **1998**, *123* (6), 1303-1307.
(28) Lin, J.; Chen, J.; Elenbaas, B.; Levine, A. J. Several hydrophobic amino acids in the p53 amino-terminal domain are required for transcriptional activation, binding to mdm-2 and the adenovirus 5 E1B 55-kD protein. *Genes Dev.* **1994**, *8* (10), 1235-1246.
(29) Cohen, P. A.; Mani, J.-C.; Lane, D. P. Characterization of a new intrabody directed against the N-terminal region of human p53. *Oncogene* **1998**, *17* (19), 2445-2456.
(30) Makhija, S.; Taylor, D.; Gibb, R.; Gercel-Taylor, C. Taxol-induced bcl-2 phosphorylation in ovarian cancer cell monolayer and spheroids. *Int. J. Oncol.* **1999**, *14* (3), 515-536.
(31) Dang, K.; Zhang, W.; Jiang, S.; Lin, X.; Qian, A. Application of lectin microarrays for biomarker discovery. *ChemistryOpen* **2020**, *9* (3), 285-300.
(32) Qiu, R.; Regnier, F. E. Use of multidimensional lectin affinity chromatography in differential glycoproteomics. *Anal. Chem.* **2005**, *77* (9), 2802-2809.
(33) Sharon, N.; Lis, H. Lectins as cell recognition molecules. *Science* **1989**, *246* (4927), 227-234.
(34) Klaamas, K.; Kodar, K.; Kurtenkov, O. An increased level of the Concanavalin A-positive IgG in the serum of patients with gastric cancer as evaluated by a lectin enzyme-linked immunosorbent assay (LELISA). *Neoplasma* **2008**, *55* (2), 143-150.

(35) Saleemuddin, M.; Husain, Q. Concanavalin A: a useful ligand for glycoenzyme immobilization-a review. *Enzyme Microb. Technol.* **1991**, *13* (4), 290-295.
(36) Babac, C.; Yavuz, H.; Galaev, I. Y.; Pişkin, E.; Denizli, A. Binding of antibodies to concanavalin A-modified monolithic cryogel. *React. Funct. Polym.* **2006**, *66* (11), 1263-1271.
(37) Saha, K.; Bender, F.; Gizeli, E. Comparative study of IgG binding to proteins G and A: nonequilibrium kinetic and binding constant determination with the acoustic waveguide device. *Anal. Chem.* **2003**, *75* (4), 835-842.
(38) Fletcher, S. Screen‐printed carbon electrodes. In *Electrochemistry of Carbon Electrodes*, 2015; pp 425-444.
(39) Wang, J.; Tian, B.; Nascimento, V. B.; Angnes, L. Performance of screen-printed carbon electrodes fabricated from different carbon inks. *Electrochim. Acta* **1998**, *43* (23), 3459-3465.
(40) Wahyuni, W. T.; Putra, B. R.; Fauzi, A.; Ramadhanti, D.; Rohaeti, E.; Heryanto, R. A brief review on fabrication of screen-printed carbon electrode: materials and techniques. *Indones. J. Chem. Res.* **2021**, *8* (3), 210-218.
(41) Suresh, R. R.; Lakshmanakumar, M.; Arockia Jayalatha, J.; Rajan, K.; Sethuraman, S.; Krishnan, U. M.; Rayappan, J. B. B. Fabrication of screen-printed electrodes: opportunities and challenges. *J. Mater. Sci.* **2021**, *56*, 8951-9006.
(42) Berczeli, M.; Weltsch, Z. Enhanced wetting and adhesive properties by atmospheric pressure plasma surface treatment methods and investigation processes on the influencing parameters on HIPS polymer. *Polymers* **2021**, *13* (6), 901.
(43) Guo, Y.; Ma, Q.; Cao, F.; Zhao, Q.; Ji, X. Colorimetric detection of hypochlorite in tap water based on the oxidation of 3, 3′, 5, 5′-tetramethyl benzidine. *Anal. Methods* **2015**, *7* (10), 4055-4058.
(44) Liu, J.; Sun, Z.; Deng, Y.; Zou, Y.; Li, C.; Guo, X.; Xiong, L.; Gao, Y.; Li, F.; Zhao, D. Highly water‐dispersible biocompatible magnetite particles with low cytotoxicity stabilized by citrate groups. *Angew. Chem., Int. Ed.* **2009**, *48* (32), 5875-5879.
(45) Nguyen, M. D.; Tran, H.-V.; Xu, S.; Lee, T. R. Fe3O4 nanoparticles: structures, synthesis, magnetic properties, surface functionalization, and emerging applications. *Appl. Sci.* **2021**, *11* (23), 11301.
(46) Hayduk, W.; Malik, V. K. Density, viscosity, and carbon dioxide solubility and diffusivity in aqueous ethylene glycol solutions. *J. Chem. Eng. Data* **1971**, *16* (2), 143-146.
(47) Li, S.; Zhang, T.; Tang, R.; Qiu, H.; Wang, C.; Zhou, Z. Solvothermal synthesis and characterization of monodisperse superparamagnetic iron oxide nanoparticles. *J. Magn. Magn. Mater.* **2015**, *379*, 226-231.
(48) Wu, W.; Wu, Z.; Yu, T.; Jiang, C.; Kim, W.-S. Recent progress on magnetic iron oxide nanoparticles: synthesis, surface functional strategies and biomedical applications. *Sci. Technol. Adv. Mater.* **2015**, *16* (2), 023501.
(49) Patterson, A. The Scherrer formula for X-ray particle size determination. *Phys. Rev.* **1939**, *56* (10), 978.
(50) Saini, S.; Frankel, R. B.; Stark, D. D.; Ferrucci Jr, J. Magnetism: a primer and review. *Am. J. Roentgenol.* **1988**, *150* (4), 735-743.
(51) Shokrollahi, H. A review of the magnetic properties, synthesis methods and applications of maghemite. *J. Magn. Magn. Mater.* **2017**, *426*, 74-81.

(52) Fischer, M. J. *Amine coupling through EDC/NHS: a practical approach*; Humana Totowa, NJ, 2010.
(53) Matsuda, H.; Tanaka, H.; Blas, B.; Nosenas, J.; Tokawa, T.; Ohsawa, S. Evaluation of ELISA with ABTS, 2-2'-azino-di-(3-ethylbenzthiazoline sulfonic acid), as the substrate of peroxidase and its application to the diagnosis of schistosomiasis. *J. Exp. Med.* **1984**, *54* (3), 131-138.
(54) Perigo, E. A.; Hemery, G.; Sandre, O.; Ortega, D.; Garaio, E.; Plazaola, F.; Teran, F. J. Fundamentals and advances in magnetic hyperthermia. *Appl. Phys. Rev.* **2015**, *2* (4), 041302.

Chapter 5

Conclusions and Future Outlooks

Conclusion

This thesis demonstrates the integration of electrochemical biosensors with advanced microfluidic techniques to address longstanding challenges in protein biomarker quantification, that is, persistent biofouling, inefficient target recruitment, and prolonged assay turnaround times. Specifically focusing on the inflammation marker C-reactive protein (CRP) and the cancer-related anti-p53 antibody, this research showcases the use of kinetics assessment, microfluidic confinement, and nanoparticle-assisted electrochemical assays to significantly enhances assay sensitivity, selectivity, and efficiency. This integration not only streamlines sample preparation and reduces handling errors, but also improves target recruitment efficiency and facilitates high-throughput analysis, thereby supporting robust, sensitive, and rapid assaying of biomarkers.

Chapter **2** presents the development of a microfluidic-integrated capacitive biosensor, for real-time, reagentless monitoring of CRP binding kinetics. By leveraging the unique capacitive fingerprint of polyaniline (PANI) films, the system allows for continuous monitoring of binding events and the resolution of binding regimes and kinetic constants without the need for external labels. Notably, the temporal change in redox capacitance C_r during the initial association phase is a sensitive function to the analyte concentration, yielding a sample-to-result time of just 15 seconds. Compared to established ELISA or electrochemiluminescence formats, this system demonstrates a comparable assay sensitivity (picomolar LoD) while significantly reducing assay turnaround times. Despite its advantages, the real-world application of this setup remains limited due to biofouling issues in serum-spiked samples, necessitating advanced surface engineering or antifouling strategies.

Building on this foundation, Chapter **3** demonstrates the use of microfluidic confinement to boost assay sensitivity and selectivity. Within the confined microfluidic channel, enhanced forced convection effectively minimises mass transport limitations, resulting in the substantial and rapid accumulation of specific target, compared to nonspecific protein, onto the bioreceptive electrode surface. By reducing the channel height to just a few micrometres, a notable 2000% increase in binding rate, a 600% enhancement in assay sensitivity, and a 300% increase in target selectivity were observed, all without the need for electrode pretreatment or transduction amplification. This approach enables the robust assaying of sub-picomolar concentrations of CRP in serum-spiked samples, in a manner that is streamlined, broadly applicable and COMSOL validated.

To address the issue of inefficient target recruitment caused by limited epitope surface density on two-dimensional electrode interfaces and slow diffusion of biomarkers across planar surfaces, in Chapter **4**, antigen-mimicking, dual-functionalised iron oxide nanoparticles (IONPs) were introduced, paired with AC magnetic field-assisted immunoisolation, to efficiently recruit anti-p53 antibodies from serum while significantly reducing nonspecific fouling. The antigenic DO-1 peptide, designed as a functional mimic of the native p53 protein, exhibited high sequence specificity. When immobilised onto IONPs, its high surface loading resulted in a 400% enhancement in target recruitment efficiency, surpassing that of the full antigen under equivalent conditions. The captured targets, when pulled down to a lectin-modified SPCE surface, generated an electrochemical readout through HRP-mediated TMB oxidation. This process supports the sensitive and robust recruitment of subfemtomolar concentrations of cancer-relevant biomarkers in serum-spiked samples within minutes, with potential for clinical translation.

In conclusion, the integration of microfluidic techniques with electrochemical biosensing represents a transformative approach to advancing the reliability and efficiency of biomarker quantification. By overcoming limitations such as biofouling, slow diffusion, and inefficient target recruitment, this approach not only enhances the sensitivity and specificity of detection but also establishes a robust platform for real-time, high-throughput diagnostics, providing a cost-effective and practical solution to improve patient outcomes.

Outlooks

While the integration of microfluidic techniques has significantly advanced the field of electrochemical biosensing, as demonstrated in this work, several promising avenues for future research remain:

Microfluidic Confinement in Broader Applications: As microfluidic confinement is particularly advantageous in heterogeneous processes that require efficient mass transport and surface binding, it holds potential beyond biomarker detection, especially in fields such as electrosynthesis and electrocatalysis. In these applications, microfluidic confinement can facilitate the transformation of substrate molecules in a more selective manner. Applying microfluidic confinement in synthetic chemistry and catalytic reactions could unlock new opportunities for optimising reaction efficiency, selectivity, and product yield, especially in flow-based industrial systems where selectivity and scalability are critical.

Multiplexed Sensing for Comprehensive Diagnostics: A critical next step in advancing the potential of antigen-mimicking IONP-assisted immunoisolation and amplified

electrochemical assays for clinical applications is the exploration of multiplexed sensing capabilities. The ability to simultaneously detect multiple biomarkers, such as various antibodies within the anti-p53 family, would enable a more comprehensive assessment of disease progression. By correlating the levels of these antibodies, this approach could offer deeper insights into the dynamics of the p53 pathway, facilitating the identification of underlying mechanisms in tumour development.

Chapter 6

Experimental Materials and Methods

6.1 GENERAL MATERIALS AND METHODOLOGY

All chemicals and solvents were sourced from commercial suppliers in the United Kingdom, including Biolegend, Inc., Bio-Rad Laboratories, Inc., Cayman Chemistry Company, ISCA Biochemicals Ltd, Proteintech Group, Santa Cruz Biotechnology, Sigma-Aldrich, and Thermo Fisher Scientific. Unless otherwise noted, these reagents were used as received without further purification. All solvents were of analytical grade.

All electrochemical experiments were conducted using a PalmSens potentiostat (PalmSens BV, UK) with a three-electrode setup, comprising a gold (Au) working electrode (ϕ = 1.6 mm diameter, BASi), a platinum (Pt) wire as the counter electrode, and a silver/silver chloride (Ag/AgCl) reference electrode, unless otherwise specified. The Au working electrodes underwent a thorough cleaning process, following established protocols.[1] Initially, the electrodes were mechanically polished using a sequence of MicroPolish alumina powder slurries (Buehler) with decreasing particle sizes (1.0 μm, 0.3 μm, and 0.05 μm). After each polishing step, the electrodes were briefly sonicated in a 1:1 deionised water/ethanol solution, repeated three times, and rinsed with deionised water. They were then immersed in a piranha solution (*conc.* H_2SO_4/30% H_2O_2, 3:1 v/v) for approximately 15 minutes. After a thorough rinse with deionised water, the electrodes were electrochemical polished. This process involved cyclic voltammetry in 0.5 M KOH solution over a potential range of - 0.7 V to - 1.7 V (*vs.* Ag/AgCl) and in 0.5 M H_2SO_4 solution from - 0.15 V to + 1.35 V (*vs.* Ag/AgCl) at a scan rate of 0.1 $V \cdot s^{-1}$, each step lasting approximately one hour. The electroactive surface area of the Au disc electrode was estimated by dividing the integral of the gold reduction peak in 0.5 M H_2SO_4 by a conversion factor of 420 $\mu C \cdot cm^{-2}$.

6.2 GENERAL CHARACTERISATIONS

6.2.1. Surface Plasmon Resonance (SPR)

All Surface Plasmon Resonance (SPR) experiments were performed using a Biacore X100 SPR instrument (Cytiva, UK) with SIA kit Au chips (Cytiva, UK). Prior to use, the SPR gold chips were cleaned by sequentially rinsing them with ethanol and deionised water, followed by immersion in piranha solution (composition as described previously) for 10 minutes. Afterward, the chips were thoroughly rinsed with deionised water. The cleaned chips were then mounted in the SPR spectrometer, and the interface was flushed with running buffer at a flow rate of 30 $\mu L \cdot min^{-1}$ at room temperature. Once a stable baseline was achieved (with fluctuations less than 1.0 $RU \cdot min^{-1}$), receptors were injected for in situ immobilization onto the chip surface. In cases where covalent attachment was required, appropriate crosslinking chemistry was employed to ensure stable binding. The receptor coverage, c_s, was estimated using the equation $c_s = 1.0 \cdot \Delta RU\ pg \cdot mm^{-1}$, where ΔRU represents the difference in response units between the sample-injected and control channels (buffer-only injection). To minimise nonspecific binding, both channels were blocked with a 1% BSA buffer solution.

A full SPR sensogram was generated by injecting a series of increasing target concentrations, with association and dissociation phases lasting approximately 270 seconds and 600 seconds, respectively. Binding affinity was evaluated by calculating the dissociation constant K_d using Langmuir fitting of the SPR response at equilibrium following each injection. Kinetic analysis was performed by fitting both the association and dissociation phase of each sample injection to *eqn.* **1.17** and **1.18**, respectively, yielding the association rate constant k_{on} and dissociation rate constant k_{off}.

6.2.2. Attenuated Total Reflection Fourier Transform Infrared Spectroscopy (ATR-FTIR).

Fourier Transform Infrared (FT-IR) spectra were recorded using an FT-IR spectrophotometer (IRTracer-100, Shimadzu, Japan) equipped with an attenuated total reflectance (ATR) accessory featuring a diamond crystal. Prior to sample analysis, the ATR crystal was thoroughly cleaned with ethanol and dried using lens-cleaning tissue to avoid contamination. Solid samples were placed directly onto the ATR crystal and a consistent pressure clamp was applied to ensure optimal contact. For liquid samples, careful pipetting was used to ensure complete coverage of the crystal surface. Background spectra were recorded before each sample measurement to correct for atmospheric and instrumental noise. Spectra were acquired in the mid-infrared region, typically between 4000 and 400 cm^{-1}. After each measurement, the ATR crystal was cleaned thoroughly to prevent cross-contamination between samples.

6.2.3. Dynamic Light Scattering (DLS) and Zeta Potential Measurements

The hydrodynamic size and zeta potential of the nanoparticles were measured using a Zetasizer (Malvern Panalytical, UK). Prior to analysis, all samples were freshly prepared and diluted in 10 mM phosphate buffer (pH = 7.4) to a concentration of 0.5 $mg \cdot mL^{-1}$. Samples were then carefully transferred into disposable folded capillary zeta cell (DTS1070, Malvern Panalytical, UK) for both DLS and zeta potential measurements. The cells were pre-rinsed with deionised water to eliminate contamination. DLS measurements were conducted at room temperature (*i.e.*, 25℃) with a detection angle of 173 ° (*i.e.*, backscatter mode). Each sample was analysed in triplicate to ensure

reproducibility, and the results were processed using the software to determine the Z-average size and polydispersity index (PDI). For zeta potential measurements, similar procedures were followed, with electrophoretic mobility measurements performed to assess the surface charge of the nanoparticles. Three replicates were carried out for each sample to ensure consistent and reliable results. Following the measurements, the cells were thoroughly rinsed with deionised water to prevent cross-contamination between samples.

6.2.4. Water Contact Angle Measurements (CAM)

Water contact angle measurements were performed using a goniometer (FTA1000B, First Ten Angstroms, Inc., USA) to evaluate the wettability of the sample surfaces (*e.g.*, electrodes). Prior to measurement, samples were rinsed with deionised water followed by N_2 drying to remove any dust. For each measurement, a 5 µL droplet of deionised water was carefully dispensed onto the sample surface using a microsyringe. Real-time imaging of the droplet was captured immediately after deposition. The contact angle was calculated using the instrument's built-in software, which measured the angle formed between the baseline of the liquid-solid interface and the tangent at the liquid-air boundary of the droplet. To ensure reproducibility, each sample was measured in triplicate.

6.3 GENERAL PROTOCOLS FOR ELECTROCHEMICAL STUDIES

6.3.1. Theory of Several Key Techniques in Electrochemistry

Based on the states of applied stimulus, electrochemical techniques can be broadly categorised into steady-state and transient methods, and those based on the concepts of impedance and capacitance. In this section, several key techniques in electrochemical measurements will be examined, with an emphasis on their underlying principles and significance in electrochemical studies.

6.3.1.1 Steady-State Electrochemical Techniques

Steady state in electrochemical systems refers to a condition where the variables of interest, such as current, potential, and concentration of species, remain constant over time.[2] Distinct from equilibrium, steady state is achieved when a dynamic balance is attained between the flux of electroactive species to the electrode surface and the rate of their electrochemical transformation.[3] This balance ensures that the reaction rate and resulting measurements remain stable over time. The time-independent nature of the steady state offers significant advantages for electrochemical analysis, as it simplifies measurement procedures and data interpretation.[4] This stability is particularly beneficial for long-term monitoring and continuous analysis in real-world applications.[5]

Achieving a steady state in electrochemical measurements can be accomplished through either enhanced mass transport or controlled electrode kinetics is employed.[2, 3] The former is exemplified by techniques such as microelectrode amperometry and

hydrodynamic voltammetry, while controlled electrode kinetics are demonstrated by chronopotentiometry (CP).[6] Microelectrode amperometry leverages the unique mass transport properties of microelectrodes,[2] which allow for rapid attainment of steady-state conditions. This technique is particularly powerful for studying fast reaction kinetics and detecting low concentrations of analytes with high sensitivity and precision. Similarly, hydrodynamic voltammetry,[3, 7] such as rotating disk electrode (RDE) voltammetry,[8] employs forced convection to create a controlled and stable hydrodynamic environment. By uniformly rotating the electrode, a continuous supply of reactants is delivered to the electrode surface, ensuring a steady-state current is generated. This method provides a reliable means of studying reaction mechanisms and kinetics under well-defined conditions.[9, 10] The details of hydrodynamic kinetics are discussed further in Section **1.3.1**.

Chronopotentiometry

Controlled electrode kinetics, exemplified by CP method, also contribute to achieving steady-state conditions. In electrochemistry, the current density j is a direct measure of electrode reaction rates,[11] derived from Faraday's law, as shown in *eqn.* **6.1**.[3, 4]

$$j = \frac{dQ}{Adt} = nF \cdot \frac{d(n/A)}{dt} = nFv \tag{6.1}$$

where Q is the total charge in coulombs; F is the Faraday constant; A represents the surface area of electrode; n is the number of electrons transferred in the electrochemical reaction per molecule of reactant; and v donates the rate of heterogeneous reactions on the electrode surface in $\mathrm{mol} \cdot \mathrm{s}^{-1}\mathrm{cm}^{-2}$. In CP method, a constant current is applied, and the resulting potential is monitored over time.[4, 6] This constant current ensures a steady flux of reactants to the electrode, facilitating the attainment of a steady state. The precise

control of electrode kinetics in CP method enables detailed studies of reaction mechanisms and surface properties.[6, 12]

The potential change in CP method is a result of double-layer charging and electrode reaction, as expressed in *eqn.* **6.2**.[6]

$$I = \frac{dQ}{dt} = \frac{d(C \cdot E)}{dt} = C\frac{dE}{dt} + E\frac{dC}{dt} \tag{6.2}$$

where I is the applied current in CP method; E is the resulting potential; C donates the electrode capacitance.

In a typical electrolysis process without changes in electrode surface composition, the chronopotentiometry plot begins with a phase of double-layer charging.[6] Once this initial charging is complete, the potential gradually shifts towards the electrode potential at which the electrochemical reaction occurs. As the reaction proceeds, the concentration of reactive species near the electrode surface decreases, leading to a gradual increase in electrode potential, as described by the Nernst equation (*eqn.* **1.6**).[4] As the concentration of the reactants decreases further, diffusion becomes insufficient to supply the necessary reactants. Consequently, most current is transferred through the double-layer capacitance, causing a rapid change in the electrode potential until it reaches a new reaction point. However, the electrodeposition of conductive materials onto the electrode surface can gradually reduce the potential as the result of increased electrode capacitance.[13, 14] The valuable insights provided by CP method aid in elucidating the mechanisms of electrode reactions,[6, 15] surface modifications,[16] and enhancing the understanding of complex electrochemical systems.

6.3.1.2 Transient Electrochemical Methods

Compared with steady-state techniques, transient methods employ a time-dependent change in potential or current to electrochemical systems,[4, 17] while recording the temporal response. This approach can provide valuable insights into the kinetics and mechanisms of electrochemical reactions, as exemplified by several key techniques including chronoamperometry (CA), cyclic voltammetry (CV), and square wave voltammetry (SWV).

Chronoamperometry

In CA method, a constant potential is applied to the working electrode, and the resulting current response is recorded over time.[4] Unlike CP method, a diffusion-controlled mass transport is achieved in CA method,[4, 18] rather than the steady state. This is because, in CA, the constant potential initially causes an increase in current as the electroactive species near the electrode surface are rapidly consumed. However, the rate of mass transport, primarily driven by diffusion, is slower compared with the electrode kinetics, resulting in a characteristic decay of current over time as described by the Cottrell equation (*eqn.* **6.5**).[3, 4] The temporal changes in reactant concentration c at the distance x from the electrode, flux J at the electrode surface, and the resulting current I are shown in *eqn.* **6.3**-**6.5**.[3]

$$c = c_{bulk}\mathrm{erf}\left(\frac{x}{2\sqrt{Dt}}\right) \tag{6.3}$$

$$J = -D\left(\frac{\partial c}{\partial x}\right)_{x=0} = \frac{\sqrt{D}\cdot c_{bulk}}{\sqrt{\pi t}} \tag{6.4}$$

$$I = nFAJ = \frac{nFA\sqrt{D} \cdot c_{bulk}}{\sqrt{\pi t}} \quad (6.5)$$

where c_{bulk} and D are the bulk concentration and diffusion coefficient of the reactant, respectively; erf denotes the error function; n is the number of electrons transferred in the reaction; A is the surface area of the electrode; F represents Faraday constant. The diffusion-controlled characteristic in CA method enables the determination of diffusion coefficients and provides a deep understanding of mass transport processes and electrode kinetics.[19]

Cyclic Voltammetry

In principle, one can thoroughly investigate the electrochemical behaviour of species by applying a series of potential steps in CA method to construct a three-dimensional I - t - E surface.[4] Such efforts, however, can be tedious and challenging. Alternatively, CV method can efficiently and readily capture the essentials of electrochemical systems by linearly sweeping the potential over time (Figure **6.1a**) and recording the voltammograms (I- E plots),[20] allowing the quick identification of redox species, determination of their electrode potentials and reversibility, and providing a deeper understanding of their electrode kinetics and mechanisms.

The shape of voltammograms is characterised by several peaks corresponding to the oxidation and reduction of electroactive species,[20] as shown in Figure **6.1b**. During the forward scans, limit current generates due to double-layer charging when potential is insufficient to oxidase electroactive species. As the potential increases, the electrode kinetics accelerate, resulting in a surge in oxidation current (*eqn.* **1.9**). This continues until the potential leads to the rapid consumption of electroactive species near the

electrode surface, creating an anodic peak. From this point, diffusion control is achieved, and the current drops beyond the peak follows a $t^{-1/2}$ dependence,[3] as described in *eqn.* **6.5**. Conversely, during the reverse sweep, the reduction of analyte creates a cathodic peak, following a similar pattern.

(a) (b)

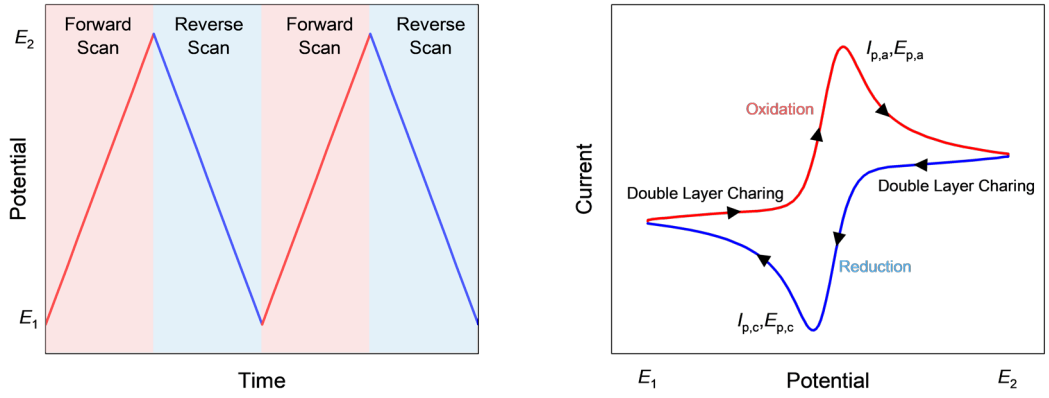


Figure 6.1. (a) Applied potential diagram in cyclic voltammetry,[4, 20] showing the forward scan (red) and reverse scan (blue) over time. (b) Schematic representation of a typical cyclic voltammogram, where the current is plotted against the applied potential. During the forward scan, oxidation occurs, resulting in an anodic peak, while the reverse scan shows reduction, resulting in a cathodic peak.

These peaks in CV voltammograms provide valuable information regarding the reversibility,[21] electrode potentials,[22] and diffusion coefficient of electroactive species.[23] The electrochemical systems, based on the electrode kinetics of oxidation and reduction relative to mass transport process,[3] can be categorised into reversible, quasi-reversible and irreversible systems. Since the diffusion kinetics in CV depends on the voltage scan rate v, Matsuda et al. introduced a parameter Λ to quantify the reversibility of redox couples,[21] as shown in *eqn.* **6.6**, where k° is the standard rate constant of electrochemical reactions; F is Faraday constant; D is the diffusion coefficient of electroactive species; R represents the gas constant; and T is the temperature in Kelvin.

$$\Lambda = \frac{k^{\circ}}{\left(\frac{FDv}{RT}\right)^{\frac{1}{2}}} \tag{6.6}$$

In a reversible system ($\Lambda \geq 15$),[3] the peak current ratio $I_{p,a}/I_{p,c}$ approaches unity.[20, 24] The peak current I_p values align with the Randles-Sevcik equation (*eqn.* **6.7**).[4, 25]

$$I_p = 2.69 \times 10^5 n^{\frac{3}{2}} A D^{\frac{1}{2}} c_{bulk} v^{\frac{1}{2}} \tag{6.7}$$

where n is the number of electrons transferred in the reaction; A is the electrode area; c_{bulk} and D are the bulk concentration and diffusion coefficient of the reactant; v is the voltage scan rate. Meanwhile, the formal potential E° and peak separation ΔE_p satisfy *eqn.* **6.8** and **6.9**, respectively.[3, 24]

$$E^{\circ} = \frac{E_{p,a} + E_{p,c}}{2} \tag{6.8}$$

$$\Delta E_p = E_{p,a} - E_{p,c} = \frac{59}{n} mV \tag{6.9}$$

In the quasi-reversible ($15 > \Lambda > 10^{-3}$) and irreversible ($\Lambda \leq 10^{-3}$) systems,[3] the sluggish charge transfer kinetics result in the peak current ratios $I_{p,a}/I_{p,c}$ deviating from unity.[4] The peak current I_p is impacted by charge transfer coefficient α, as shown in *eqn.* **6.10**.[3] The peak separation ΔE_p is larger and related to voltage scan rate v.[4]

$$I_p = 2.99 \times 10^5 n^{\frac{3}{2}} \alpha^{\frac{1}{2}} A D^{\frac{1}{2}} c_{bulk} v^{\frac{1}{2}} \tag{6.10}$$

Besides these peaks, CV can also provide valuable information about electrode kinetics. A crucial method for extracting kinetic information from CV is Tafel analysis, as shown in *eqn.* **6.11**.[26, 27] Derived from Butler-Volmer equation (*eqn.* **1.8**), Tafel analysis

examines the relationship between overpotential η and the logarithm of the current density j, enabling the determination of kinetic parameters of electrode reactions, such as the charge transfer coefficient α, the exchange current density j°, and the standard rate constant k°.[4]

$$\eta = a + b \log j \tag{6.11}$$

where b is the Tafel slope, given by $2.303RT/\alpha nF$; a represents the Tafel intercept, with a value of $-b \log j^{\circ}$. A small b indicates efficient charge transfer, and a small a suggests a high exchange current density j°, implying fast charge transfer kinetics k°. This analysis, together with CV voltammograms, offer an invaluable tool for understanding and optimising electrochemical systems, providing detailed insights into reaction mechanisms, kinetics, and material properties.

Square Wave Voltammetry

While cyclic voltammetry (CV) provides valuable information about redox processes and reaction kinetics, it often lacks the sensitivity in detecting low-concentration analytes ($c_{bulk} \sim 10^{-5}$ M) due to the interference of double-layer charging.[4, 24] Pulse voltammetry, particularly square wave voltammetry (SWV), addresses this limitation by applying a series of potential pulses superimposed on a staircase waveform.[4, 24, 28] This approach minimises capacitive currents, thereby enhancing the signal-to-noise ratio and providing more accurate measurements down to 10^{-8} M.[24]

The high resolution of SWV is accomplished through its unique waveform design and differential current sampling technique. As shown in Figure **6.2a**, SWV employs a series of symmetric square wave potential pulses superimposed on a staircase waveform, and

the resulting current is sampled at the end of each forward ($I_{forward}$) and reverse pulse ($I_{reverse}$), respectively, before the potential is switched. With a large amplitude typically recommended in SWV ($\Delta E_p \sim 50/n$ mV),[4] redox species undergo oxidation in the forward pulse and reduction during the reverse pulse. The difference in current $\Delta I = I_{forward} - I_{reverse}$ is plotted against the staircase potential (Figure **6.2b**), significantly reducing the influence of double-layer charging.[28]

(a) (b)

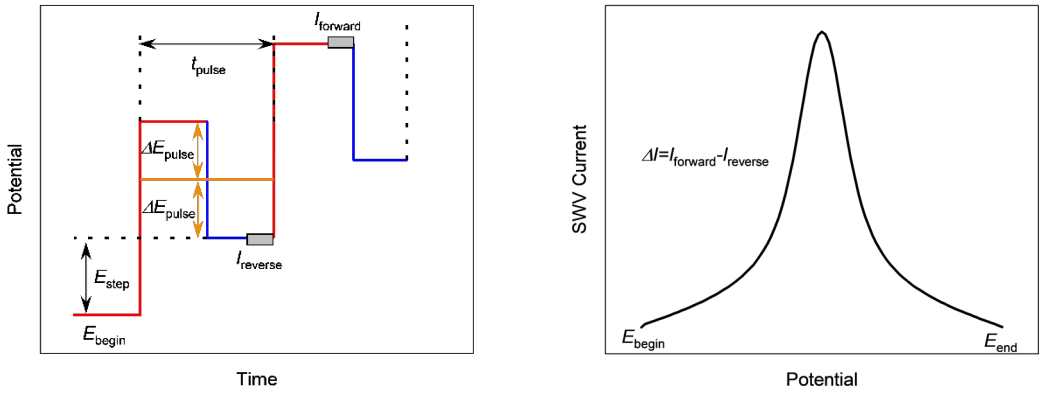


Figure 6.2. (a) Applied potential diagram in square wave voltammetry.[29] Square wave pulses, with amplitude ΔE_p and pulse time t_p, are superimposed on a staircase waveform step E_s. Current is sampled twice in each step, before and after the application of the pulse, corresponding to the forward current $I_{forward}$ and reverse current $I_{reverse}$. (b) Schematic representation of a typical SWV voltammogram, where the difference in current ΔI is plotted against the applied potential.

The sensitivity of SWV is modulated by several parameters, including the pulse high ΔE_p and voltage scan rate (regulated by the staircase shifts E_s and pulse width $t_p = 1/2f$, where f is the square-wave frequency), as described in *eqn.* **6.12**,[4, 28, 29] where n is the number of electrons transferred; F is the Faraday constant, A is the electrode area, c_{bulk} and D are the bulk concentration and diffusion coefficient of the species, $\Delta\Psi_p$ is a dimensionless constants determined by E_s and ΔE_p.

$$\Delta I_p = \frac{nFAD^{\frac{1}{2}}c_{bulk}}{\pi^{\frac{1}{2}}t_p^{\frac{1}{2}}}\Delta\Psi_p \quad (6.12)$$

Practically, a E_s of $10/n$ mV and a ΔE_p of $50/n$ mV are recommend,[3, 4] while t_p varies from 0.25 to100 ms. It is noted that the double-layer charging become negligible only when the condition $t_p > 5R_uC_{dl}$ is met (R_u is the uncompensated resistance between the working electrode and the reference electrode; C_{dl} is the double layer capacitance).[4] Selecting appropriate parameters in SWV ensures the minimisation background currents, while enhancing the sensitivity and reliability of electrochemical measurements.

6.3.1.3 Electrochemical Techniques Based on Concepts of Impedance and Capacitance

Unlike transient and steady-state methods, electrochemical impedance spectroscopy (EIS) and derived electrochemical capacitance spectroscopy (ECS) are operated by applying a small AC perturbation to the system and measuring the resulting current response,[4, 30] allowing for the analysis of impedance or capacitance over a range of frequencies to determine the properties of electrochemical systems. These techniques offer the advantages of being non-destructive, highly sensitive, and informative, enabling in-situ and real-time monitoring in energy storage,[31] corrosion protection,[32] and sensor development.[33]

Electrochemical Impedance Spectroscopy

Impedance Z represents the opposition to current flow in an electrical circuit and is determined from the ratio of the Laplace transform of the voltage, $L[E(t)]$, to the Laplace transform of the current, $L[i(t)]$, as shown in *eqn.* **6.13**.[34, 35]

$$Z = \frac{L[E(t)]}{L[i(t)]} \tag{6.13}$$

In electrochemical systems, impedance encompasses the combined contributions of resistance R, capacitance C, and inductance L.[34] Resistance typically arises from the ion flow within the electrolyte solution, charge transfer in electrode reactions, sluggish mass transport processes, and the connections between the electrode and external circuitry.[4] Capacitance, defined as the ability of electrochemical systems to accumulate and store charge, primarily consist of double layer capacitance,[4] due to the formation of an electric double layer at the electrode-electrolyte interface as detailed in Section **6.3.1.2**, and pseudo-capacitance,[36] which involves charge transfer in electrochemical processes. Inductance, although less common, can be present due to the magnetic fields generated by current-carrying conductors within the system.[4]

To accurately model and understand these contributions, equivalent circuits are employed.[4] These circuits simplify the representation of individual processes contributing to the overall impedance, allowing for a more straightforward interpretation of electrochemical processes and facilitating the optimisation of electrochemical systems. For examples, the Randles circuit is utilised to analyse a general electrochemical reaction in the presence of mass transfer.[4, 34]

(a) (b)

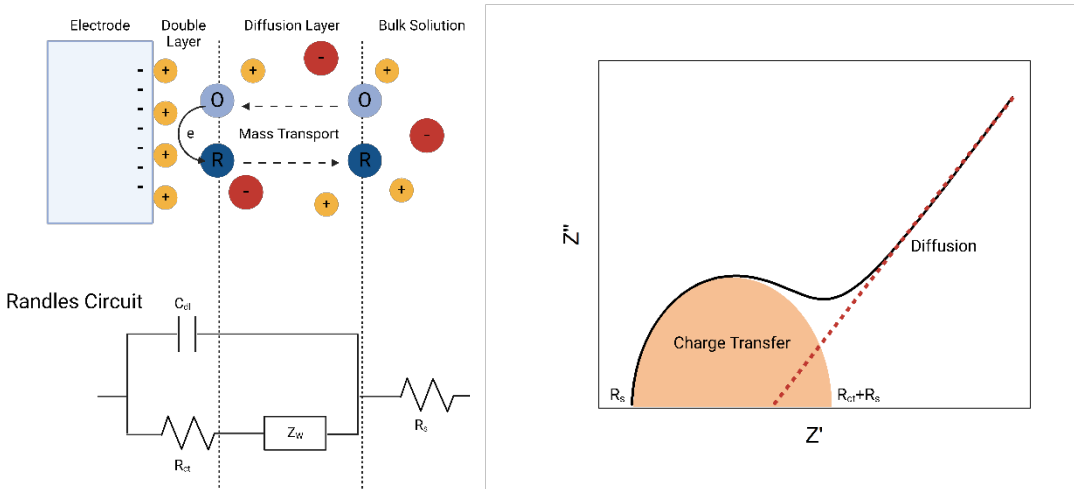


Figure 6.3. Schematic representation of (a) the Randles circuit and (b) its corresponding Nyquist plot.[34] The Randles equivalent circuit consists of a solution resistance R_s, a charge transfer resistance R_{ct}, a double-layer capacitance C_{dl}, and a Warburg impedance Z_w representing diffusion. In the Nyquist plot, charge transfer process is characterised by semicircle, starting at R_s with a diameter R_s. The low-frequency tail represents the diffusion impedance.

As shown in Figure **6.3a** the solution resistance R_s is arranged in series with a parallel combination of double-layer capacitance C_{dl} and the charge transfer resistance R_{ct}, often coupled with a Warburg impedance Z_w to account for the diffusion processes. This configuration effectively models the distinct physical and electrochemical processes: the parallel arrangement of C_{dl} and R_{ct} reflects the simultaneous storage of charge and charge transfer processes occurring at the electrode-electrolyte interface, while the coupling of R_{ct} and Z_w depicts the kinetics of the electrode reaction, which is regulated by both charge transfer and mass transport processes. The overall impedance Z is described in *eqn.* **6.14**.[34]

$$Z = R_s + \frac{1}{\frac{1}{R_{ct} + Z_w} + i\omega C_{dl}} \tag{6.14}$$

where i is the imaginary unit; and ω is the angular frequency of the applied AC perturbation. Under the condition where the applied DC potential E_{DC} equals the standard electrode potential E°, R_{ct} and Z_w are presented as follows.[4, 31]

$$R_{ct} = \frac{RT}{nFj_0} = \frac{RT}{n^2F^2Ak^{\circ}c_O^{1-\alpha}c_R^{\alpha}} \tag{6.15}$$

$$Z_w = \frac{\sigma}{\sqrt{\omega}}(1-i) = \frac{RT}{n^2F^2A\sqrt{2\omega}}\left(\frac{1}{D_O^{\frac{1}{2}}c_O} + \frac{1}{D_R^{\frac{1}{2}}c_R}\right)\cdot(1-i) \tag{6.16}$$

where R is the gas constant; T is the temperature in Kelvin; n is the number of electrons transferred; F is the Faraday constant; j° is the exchange current density; A is the electrode area; k° is the standard rate constant; α is the transfer coefficient; σ is the Warburg coefficient; c_O, c_R and D_O, D_R are the bulk concentration and the diffusion coefficients of the oxidised and reduced species, respectively. As shown in *eqn.* **6.15** and **6.16**, a high concentration of electroactive species and a faster electron transfer rate result in a reduced R_{ct}, while increased concentrations also facilitate mass transfer processes, thereby reducing Z_w. Additionally, the value of R_{ct} enables the determination of the exchange current density j°, offering valuable insights into charge transfer kinetics.

The overall impedance, as indicated in *eqn.* **6.14**, consists of in-phase components (*i.e.*, resistance) and out-of-phase components (*i.e.*, capacitance).[31] To visualise the contributions of these components, the complex impedance is typically represented in a Nyquist plot,[4, 31] where the real part is plotted on the x-axis and the imaginary part on the y-axis. As shown in Figure **6.3b**, the Randles circuit, in the Nyquist plot, is characterised by a semicircle that begins at R_s in the high-frequency domain and transitions into a 45° straight line due to Z_w in the low-frequency domain.[34] At high frequencies, the low

reactance of double layer results in the impedance being dominated by R_s. As the frequency decreases, the increased capacitive reactance and charge transfer generate the semicircle. At even lower frequencies, diffusion effects become significant, represented by Z_w. The diameter of the semicircle corresponds to R_{ct}, measured as the impedance between R_s and the inflection point of the curve.[4] Besides the Nyquist plot, the Bode plot is another useful representation,[34, 35] where impedance magnitude and phase angle are plotted against the logarithm of frequency, providing insight into frequency-dependent behaviours of the electrochemical system.

Practically, to obtain reliable impedance data, several key considerations need to be addressed. First, balancing signal linearity, derived from the Kramers-Kronig relations,[35] and measurement sensitivity requires an AC perturbation amplitude of around 5 mV.[31] Nonlinear responses from a large amplitude can distort and produce incorrect impedance data (*e.g.*, artificially reduced R_{ct}),[31] while an amplitude that is too small can result in an insufficient signal-to-noise ratio. Second, pre-equilibrium conditions must be established before measurements to ensure system stability throughout the experiment.[30, 31] Additionally, to minimize noise interference, it is essential to use a three-electrode system and enclose the setup in a Faraday cage.[30] By carefully managing these factors, accurate and reliable EIS measurements can be achieved, facilitating the understanding of electrochemical systems.

Electrochemical Capacitance Spectroscopy

Derived from EIS, electrochemical capacitance spectroscopy (ECS) is a technique to probe the capacitance of electrochemical systems. Although some techniques, such as CP and CA methods, can also determine capacitance,[4] ECS is unique in providing frequency-

dependent capacitive information. This frequency dependence offers a detailed profile that distinguishes electrochemical processes occurring at difference time scales,[30, 37] providing deeper insights into the properties of the electrochemical systems.

Capacitance in electrochemical systems can be broadly categorised into double-layer capacitance C_{dl} and pseudo-capacitance C_{pseudo}. C_{dl} is influenced by the electrode surface characteristics (*e.g.*, surface area, roughness, porosity, materials, and conductivity), electrolyte composition (*e.g.*, ion concentration, size, charge, and solvents), applied potential, and temperature.[4] As stated in Section **6.3.1.2**, the electrical double layer is typical composed of the compact Helmholtz layer (*i.e.*, IHP and OHP) and the diffusive layer. Thereby, C_{dl} is arranged as the Helmholtz capacitance C_H and the diffuse layer capacitance C_D in series, as shown in *eqn.* **6.17**.[4]

$$\frac{1}{C_{dl}} = \frac{1}{C_H} + \frac{1}{C_D} = \frac{x_2}{\varepsilon\varepsilon_0} + \frac{1}{\left(\frac{2\varepsilon\varepsilon_0 z^2 e^2 c_{ion}}{k_B T}\right)^{\frac{1}{2}} \cosh\left(\frac{ze\phi_2}{2k_B T}\right)} \tag{6.17}$$

where x_2 is the position of OHP; ε is the dielectric constant of the electrolyte; ε_0 is the permittivity of free space, with a value of 8.854×10^{-12} F · m^{-1}; z is the valence of the ion, with a concentration of c_{ion}; e is the elementary charge; k_B is the Boltzmann constant, with a value of 1.381×10^{-23} J · K^{-1}; T is the temperature; ϕ_2 is the potential at OHP.

Unlike an ideal capacitor, C_{dl} is influenced by the applied potential, as this potential alters the distribution and density of ions at the electrode interface. It is noted that C_H remains independent of the potential (ϕ_2),[4] while C_D exhibits a V-shape dependence,[38] reaching a minimum at the potential of zero charge (PZC). Additionally, C_{dl} is sensitive to the

local environment at the electrode-electrolyte interface; higher valence ions and increased ion concentrations in the electrolyte can enhance C_{dl}. The size of ions, represented by x_2 directly impact C_H. Smaller ions can approach the electrode surface more closely, reducing x_2 and thereby increasing C_{dl}. Typically, C_{dl} ranges around 10 - 40 $\mu F \cdot cm^{-2}$ in aqueous solutions at room temperature.[4]

C_{pseudo}, on the other hand, is primarily related to the presence of electroactive species (*e.g.*, transition metal and conducting polymers) and phase changes on the electrode surface.[36] Faradic C_{pseudo} involves charge storage through electrode reactions, also known as redox capacitance C_r,[37] allowing for a significantly greater amount of charge to be stored compared to the physical adsorption of ions at the electrode surface. As a result, C_r typically exhibits much higher values than C_{dl} and often dominates the overall capacitance of electrochemical systems. The value of C_r is related to the coverage of electroactive species Γ and their percentage density of redox states θ at the electrode surface,[37, 39] as shown in *eqn.* **6.18**, where A is the electrode area; e is the elementary charge; k_B is the Boltzmann constant; T is the temperature in Kelvin; θ is the percentage surface concentration of oxidised or reduced electroactive species relative to Γ.

$$C_r = \frac{Ae^2\Gamma}{k_B T}\theta(1-\theta) \tag{6.18}$$

It is noted that C_r is directly proportional to the surface concentration of redox species (Γ), as denser species can store more charge through electrode reactions. Additionally, C_r is sensitive to the redox form ratio (θ), regulated by the applied potential. As shown in the Nernst equation (*eqn.* **1.6**), the surface concentrations of redox species depend on

the electrode potential. When the applied potential equals the standard electrode potential E°, C_r reaches its maximum value of $\frac{Ae^2\Gamma}{4k_BT}$.[37]

In practice, capacitance C is determined by EIS and presented in a capacitive Nyquist plot using the following transformation (*eqn.* **6.19**),[34] where i is the imaginary unit; ω is the angular frequency; and Z is the complex impedance.

$$C = \frac{1}{i\omega Z} \tag{6.19}$$

The real part on the x-axis of the capacitive Nyquist plot represents the contribution of out-of-phase components (*i.e.*, capacitance), while the imaginary part on the y-axis is in-phase contributions (*i.e.*, resistance). ECS does not require solution-phase redox couples to probe electrochemical processes and surface properties. Instead, it integrates electroactive species directly onto the electrode surface, facilitating reagentless measurements.[1] This approach simplifies the experimental setup, reduces potential interference from the redox probes, providing a more direct, convenient and sustainable approach to assess electrochemical characteristics and surface properties.

6.3.2. General Protocols for CV and SWV Measurements

Both CV and SWV measurements were performed using a three-electrode configuration connected to a potentiostat (PalmSens BV, UK). The detailed cleaning procedure for the working electrode is described in Section **6.1**. The electrolyte solution, such as 0.1 M phosphate buffer or phosphate buffered saline (PBS) at pH of 7.4, was freshly prepared and degassed with nitrogen prior to each experiment. The potential range and scan rate were selected based on the specific electrochemical system under study, and the resulting voltammograms were analysed as discussed in Section **6.3.1.2**.

To assess the electrochemical performance of the electrodes, a pair of redox probes consisting of 5 mM potassium ferrocyanide and ferricyanide in PBS (pH = 7.4) was used. The peak-to-peak separation ΔE_p and current density j were determined from the cyclic voltammograms, providing insight into the electron-transfer kinetics and overall conductivity of the electrode material. Additionally, the charge transfer coefficient β, obtained through Tafel analysis, revealed the charge-transfer characteristics of electrode. Randles-Sevcik analysis was employed to determine the electrochemically active surface area and the surface roughness of the electrodes.

SWV measurements are conducted similarly to CV. As discussed in Section **6.3.1.2**, the sensitivity of SWV is highly dependent on the precise selection of experimental parameters. To optimise the signal-to-noise ratio and obtain reliable results, a potential step E_s in the range of 1 to 5 mV, a square wave amplitude of 20 to 50 mV, and a frequency between 10 and 25 Hz are typically recommended.[3, 4] For consistency, all SWV measurements in this thesis were performed using a square wave amplitude of 20 mV, a potential step of 5 mV, and a frequency of 50 Hz.

6.3.3. General Protocols for EIS and ECS Measurements

EIS measurements were also conducted using a three-electrode configuration with a redox probe mixture of 5 mM potassium ferrocyanide and ferricyanide in PBS (pH = 7.4). After stabilising the system at open-circuit potential (OCP) for at least 5 minutes, a small AC voltage perturbation of 5 mV was applied across a broad frequency range, spanning from 100 kHz to 0.1 Hz, over 40 discrete frequency points. The charge transfer resistance R_{ct} was determined from the Nyquist plot, either the diameter of the Randles semicircle or the inflection point, as discussed in Section **6.3.1.3.** To ensure the reproducibility of measurements, each sample was analysed in triplicate, with sufficient equilibration time provided before each set of measurements.

the capacitance of the electrode interface was measured using a three-electrode configuration in PBS or phosphate buffer (pH = 7.4), without the presence of solution-phase redox probes. The impedance data obtained during these measurements were converted into capacitance values using *eqn.* **6.19**. The redox capacitance C_r of the electrode interface was determined from the inflection point in the capacitive Nyquist plot.

6.4 EXPERIMENTAL PROTOCOLS FOR ULTRAFAST BIOMARKER QUANTIFICATION STUDIES

6.4.1. Materials and Instruments

Sodium phosphate dibasic, sodium phosphate monobasic, phytic acid solution (50% w/w in H_2O), aniline, glutaraldehyde solution (25% in water), human serum albumin (HSA), IgG from bovine serum (≥ 95%), and bovine serum albumin (BSA) were obtained from Sigma (UK). Native human C-reactive protein (CRP) and goat anti-CRP antibodies were sourced from Bio-Rad Laboratories, Inc. (UK). SuperBlock^{TM} TBS blocking buffer was purchased from ThermoFisher Scientific (UK). All chemicals and reagents were used without further purification.

Atomic force microscopy (AFM) images were acquired using a NanoWizard 3 AFM system (JPK Instruments, Germany). The experimental setup for continuous flow measurements consisted of a custom 3D-printed microfluidic channel with an approximate cell volume of 60 µL, fabricated using an ELEGOO Mars UV photocuring 3D printer (ELEGOO, Inc., China). The system was connected to a Rheodyne 9725 injector, featuring a 100 µL sample loop, and controlled by a PHD ULTRA Syringe Pump (Harvard Apparatus, UK) to ensure precise fluid delivery. Additionally, a three-electrode configuration was integrated, as shown in Figure **2.2**. The Ag/AgCl reference electrode was prepared by electrochemically oxidising a silver wire (ϕ = 0.25 mm) in 0.5 M HCl using a two-electrode setup. Prior to oxidation, the silver wire was polished with sandpaper. Cyclic voltammetry was performed between the potential range from 0 to + 0.5 V at a scan rate of 10 $\mathrm{mV \cdot s^{-1}}$ for 20 cycles. After the electrochemical treatment, the Ag/AgCl wire was rinsed with deionised water and dipped in a Nafion solution to provide

a protective coating. The dipping process was repeated at least 20 times, allowing the wire to dry between each dip. Once the preparation was complete, both the Ag/AgCl and platinum wires were inserted into the microfluidic cell and securely fixed in place with glue.

6.4.2. Bioreceptive Interface Preparation

Polyaniline (PANI) films were fabricated via electrodeposition in a solution composed of 1 mL of 98% aniline, 2 mL of 50% phytic acid, and 17 mL of deionised water. The electrodeposition process was carried out by applying a chronopotentiometric scan at a constant current density of 10 $\mu A \cdot cm^{-2}$ for 10 minutes, resulting in the formation of uniform PANI films. After deposition, the PANI-functionalised electrodes were thoroughly rinsed with deionised water and incubated in a 2.5% glutaraldehyde solution for 30 minutes at room temperature to facilitate the covalent attachment of antibodies. Following this, the electrodes were incubated with a 100 $\mu g \cdot mL^{-1}$ solution of polyclonal anti-CRP for 18 hours to immobilise the antibodies onto the PANI surface. To minimise nonspecific binding, the anti-CRP/PANI electrodes were subsequently washed with PB buffer and blocked with SuperBlock™ TBS blocking buffer for 30 minutes. These antibody-modified electrodes were then stored in PB buffer at 4 ℃ until use.

6.4.3. Continuous Flow Assays and Data Analysis

Real-time monitoring of interfacial C_r changes was performed in a custom 3D-printed microfluidic channel, ensuring the removal of all air bubbles (Figure **2.3a**).

Measurements were conducted at a fixed potential of E_{half} = - 0.16 V (*vs.* Ag/AgCl) and a fixed frequency, determined from the inflection point of the capacitive Nyquist plot, with a temporal resolution of 2 seconds. Under a controlled flow rate of 25 $\mu L \cdot min^{-1}$, increasing concentrations of CRP, ranging from 40.0 $ng \cdot mL^{-1}$ to 10.0 $\mu g \cdot mL^{-1}$, were sequentially introduced into the microfluidic channel once a stable baseline was established (baseline shift $< 0.1\%$ over a 5-minute interval). Following each CRP injection, a 30-minute washing step with PB buffer was performed to re-establish the baseline before the next injection.

The raw C_r data collected in real time were converted into a relative response using the equation $RR\% = (1/C_{r,t} - 1/C_{r,0})/(1/C_{r,0}) \cdot 100$, where $C_{r,t}$ represents the redox capacitance at time t, and $C_{r,0}$ is the initial baseline capacitance. Data were normalised to the re-established baseline prior to each CRP injection. Analyte concentrations were quantified based on the initial temporal change in C_r over a 15-second window, calculated as the maximum first derivative of the relative capacitive response following a 140-second mixing stage, as shown in Figure **2.5c**.

The specificity of the interface was assessed by injecting 1.0 $mg \cdot mL^{-1}$ solutions of HSA, IgG, and BSA under identical conditions. Percentage recoveries were calculated by comparing the 15-second temporal C_r responses to CRP samples (2.50, 5.00, and 10.0 $\mu g \cdot mL^{-1}$), with or without the presence of 1.0 $mg \cdot mL^{-1}$ BSA or 1.0% human serum.

6.5 EXPERIMENTAL PROTOCOLS FOR MICROFLUIDIC CONFINEMENT STUDIES

6.5.1. Materials and Instruments

Sodium phosphate dibasic, sodium phosphate monobasic, phytic acid solution (50% w/w in H_2O), aniline, glutaraldehyde solution (25% in water), human serum albumin (HSA), bovine serum albumin (BSA), potassium hexacyanoferrate(III), and Potassium hexacyanoferrate(II) trihydrate were purchased from Sigma-Aldrich (UK). Biotin-BSA, streptavidin, native human C-reactive protein (CRP) and goat anti-CRP were obtained from Bio-Rad Laboratories, Inc. (UK). All chemicals and agents were used without further purification.

Microfluidic channels with heights of 20, 100, 250, and 1000 µm were fabricated using an ELEGOO Mars UV photocuring 3D printer (ELEGOO, Inc., China), as shown in Figure **3.2a**. During the 3D printing process, the layer thickness was optimised to 10 µm, with a print time of 4 seconds per layer to minimise the risk of clogging and ensure precise feature resolution. Following the completion of printing, the microfluidic structures were thoroughly cleaned using iso-propanol to remove any residual uncured resin and ensure the integrity of the channels.

6.5.2. Boosted Assay Sensitivity and Enhanced Target Selectivity Within Microfluidic Confinement

A full sensogram for the anti-CRP-modified PANI interface in response to varying concentrations of CRP was generated, as detailed in Section **6.4.3**, using custom 3D-

printed microfluidic channels with different channel heights (*i.e.*, 20, 100, 250, and 1000 μm). The initial temporal change in C_r over a 15-second association window was plotted against the analyte concentration, and the slopes of these dose-response curves were defined as the temporal sensitivity of the assays. To assess the influence of microfluidic channel geometry on biomolecular recognition, the temporal sensitivities observed in channels of varying heights were normalised to the response in the 1000 μm channel.

The effect of microfluidic confinement on target selectivity was evaluated by comparing the temporal sensitivity of CRP with that of a nonspecific protein control, BSA. Temporal sensitivity for BSA was determined from the 10.0, 25.0, and 50.0 $\mathrm{mg \cdot mL^{-1}}$ BSA injections on the anti-CRP modified PANI interface. Percentage recoveries were calculated, as outlined in Section **6.4.3**, across microfluidic channels with varying heights.

6.5.3. Surface Coverage and Binding Affinity Impact on Temporal Selectivity Enhancement

The surface coverage of immobilised anti-CRP was controlled by varying its concentration in the preparation solution, using concentration of 0.01, 0.1, 1.0, 10.0 and 100 $\mathrm{\mu g \cdot mL^{-1}}$. After antibody immobilisation, the surface was backfilled with 10.0 $\mathrm{mg \cdot mL^{-1}}$BSA to quench the remaining glutaraldehyde and minimise nonspecific binding. For the biotin-modified PANI interface, biotinylated-BSA was incubated on the activated PANI electrode overnight, followed by a backfilling step with 10.0 $\mathrm{mg \cdot mL^{-1}}$ BSA, as performed with the anti-CRP films. The surface coverage of the receptors, along with their binding constant K_d and association rate constant k_{on} to target molecules, was determined using SPR under equivalent preparation conditions. The relationship between

receptor surface coverage and selectivity enhancement was further evaluated by the enhancement factor, defined as the temporal sensitivity difference between microfluidic confinements with 100 μm and 1000 μm channel heights. The correlation between this enhancement and binding constant K_d, or rate constant k_{on} was assessed using Pearson correlation coefficients.

6.5.4. COMSOL Simulation

The mass transport and surface biorecognition processes within microfluidic confinements were modelled using COMSOL Multiphysics to simulate the dynamics of analyte binding under varying experimental conditions. Parameters for these simulations — including channel height, flow rate, association rate constants, and bioreceptor surface coverage — are detailed below. The module of Surface Reactions, Transport of Diluted Species, and Laminar Flow were utilised, with a simulation time scale of 100 seconds.

In the simulations, the analyte diffusion coefficient was set at 1×10^{-11} $m^2 \cdot s^{-1}$, and the bulk analyte concentration was fixed at 1×10^{-4} $mol \cdot m^{-3}$. The surface coverage of the bioreceptor varied between 10^{-6} to 10^{2} $pmol \cdot cm^{-2}$, and an infusion flow rate of 0.02 $cm \cdot s^{-1}$ was applied. The association rate constants ranged from 10^3 to 10^{12} $M^{-1} \cdot s^{-1}$, while the dissociation rate constant was set at 1 s^{-1}.

Analyte surface concentration profiles were integrated across the surface and differentiated with respect to time to determine the initial binding rate, represented by the maximum in the first derivative of the association sensogram. These binding rates were examined under various conditions, such as microfluidic channel height, flow rate,

association rate constants, and bioreceptor surface coverage, allowing for detailed analysis of the interplay between mass transport and biomolecular recognition within microfluidic confinements.

To carry out dimensionless analysis in COMSOL Multiphysics, all relevant variables — such as dimension of channel, analyte concentration in bulk concentration, diffusion coefficient, surface coverage of receptor, flow rate, and simulation timescale — must first be expressed in non-dimensional form, with corresponding dimensionless parameters defined. In this study, two key dimensionless numbers were used: the Peclet number (Pe_H), representing the ratio of convective to diffusive transport (defined in *eqn.***3.10**), and the Damköhler number (Da), representing the ratio of the reaction rate (analyte binding at the surface) to diffusion rate (defined in *eqn*.**3.11**). The COMSOL model was scaled based on the characteristic length, specifically the channel height. Dimensionless surface concentration profiles of the analyte were generated and integrated across the surface as previously described. Parametric sweeps available in the COMSOL study module were utilized to evaluate the influence of varying Pe_H and Da_{on} values, enabling a systematic investigation of their effect on the dimensionless surface binding rate.

6.6 EXPERIMENTAL PROTOCOLS FOR ON-CHIP INTEGRATED ANTI-P53 QUANTIFICATION STUDIES

6.6.1. Materials and Instruments

Sodium chloride, disodium hydrogen phosphate, potassium chloride, potassium dihydrogen phosphate, sodium acetate, trisodium citrate, ethylene glycol, anhydrous iron (III) chloride, 2,2′-Azino-bis(3-ethylbenzothiazoline-6-sulfonic acid) diammonium salt (ABTS, ≥ 98%), N-(3-Dimethylaminopropyl)-N′-ethylcarbodiimide (EDC, ≥ 97%), N-Hydroxysuccinimide (NHS), hydrogen peroxide solution (30% w/w in water), horseradish peroxidase (HRP), human serum albumin (HSA), bovine serum IgG (≥ 95%), and bovine serum albumin (BSA) were obtained from Sigma-Aldrich (UK). Tween-20 and the Pierce^{TM} Micro BCA protein assay kit were sourced from ThermoFisher Scientific (UK). TMB high-sensitivity substrate solution was purchased from Biolegend, Inc (UK). Concanavalin A was acquired from Cayman Chemistry Company. Monoclonal p53 antibody (DO-1) was p sourced from Santa Cruz Biotechnology (UK). p53 protein was obtained from Proteintech Group (UK), and p53 peptides (DO-1 peptides: H-CQETFSDLWKLLPENNVLSPL-OH; AB-2 peptide: H-SPDDIEQWFT-OH) and control peptide (CPPPPEKEKEK) were supplied by ISCA Biochemicals Ltd. All chemicals and reagents were used without further purification.

Fourier Transform Infrared Spectra (FT-IR) were recorded using an IRTracer-100 FT-IR spectrophotometer (Shimadzu, Japan). Surface Plasmon Resonance (SPR) measurements were performed on a Biacore X100 SPR instrument (Cytiva, UK). Nanoparticle hydrodynamic size and zeta potential were determined using a Zetasizer (Malvern Panalytical, UK). Protein quantification via BCA assays was conducted in a microwell

format and analysed using an iMark Microplate Absorbance Reader (Bio-Rad Laboratories, Inc., UK). Transmission Electron Microscopy (TEM) images were obtained using an FEI Tecnai T12 Transmission Electron Microscope (120 kV, USA). Plasma cleaning was performed using a low-pressure plasma system (FEMTO, Diener Electronic, Germany). Immunoisolation was carried out using a custom 3D-printed microfluidic setup, which incorporated an injector, a syringe pump, and a pair of electromagnets controlled by a programmable power supply, as depicted in Figure **4.9a**.

All electrochemical experiments were performed on screen-printed carbon electrode (SPCE) arrays (FlexMedical Solutions, UK). Each SPCE featured a 3.0 mm diameter carbon working electrode, a carbon counter electrode, and a silver/silver chloride reference electrode. Prior to use, the SPCE arrays were thoroughly cleaned by washing three times with ethanol and deionized water, followed by a 30-minute plasma cleaning under an atmosphere of 0.1 atm O_2.

6.6.2. Preparation of Antigen-Mimicking Dual-Functionalized IONPs

Low-polydispersity IONPs were synthesised by sonicating and stirring of a mixture containing ethylene glycol (50 mL), anhydrous trisodium citrate (0.65 g), anhydrous iron(III) chloride (0.97 g), and anhydrous sodium acetate (3.00 g) at room temperature for 30 minutes. Following this, 0.25 mL of water was added, and the yellow mixture was transferred to an autoclave and heated at 200 ℃ for 10 hours. After cooling to room temperature overnight, the synthesised IONPs were purified by washing three times with water and ethanol. The particles were then collected using a Neodymium disc magnet and dried overnight at 60 ℃

For bioreceptive functionalisation, the synthesised IONPs were washed three times with 15 mM MES buffer (pH = 5.5) and suspended in a 0.2 M EDC and 0.05 M NHS solution in MES buffer for activation, by incubating for 1 hour at room temperature on a roller. The activated nanoparticles were then suspended in a solution containing 50 $\mu g \cdot mL^{-1}$ HRP and 5.0 $\mu g \cdot mL^{-1}$ p53 peptide in MES buffer (pH = 5.5), and incubated overnight on a roller at room temperature. After washing with 10 mM PBS (pH = 7.4), these particles were blocked with 1.0 $mg \cdot mL^{-1}$ BSA in PBS-T solution, and stored in PBS until use.

6.6.3. Micro-BCA Assay for p53 Peptide Surface Coverage Determination

A series of p53 peptide standards (150 µL each) were prepared in PBS buffer (pH = 7.4), with concentrations ranging from 0.5 $mg \cdot mL^{-1}$ to 40.0 $mg \cdot mL^{-1}$. Two IONP samples at a particle concentration of 1.0 $mg \cdot mL^{-1}$ were also prepared: p53 peptide-modified IONPs and bare IONP controls. Each standard and sample (150 µL) was dispensed into individual wells of a microplate, followed by the addition of an equal volume of Micro-BCA working solution to each well. The mixtures were thoroughly mixed on a plate shaker for 30 seconds and incubated at 37℃ for two hours.

Following incubation, the microplate was allowed to cool to room temperature. A magnet was then used to concentrate the IONPs to one side of each well, minimising scattering errors during subsequent measurements. Absorbance was measured at 590 nm using a microplate reader. Calibration curves were established, and the difference in absorbance between the p53 peptide-modified and bare IONPs was analysed to estimate the surface coverage of p53 peptide on the IONPs.

6.6.4. ABTS Assay for HRP Surface Coverage Quantification

A 1.0 mM ABTS solution was prepared in PBS buffer (pH = 5.0). This solution was mixed with 5.0 µL of serially diluted HRP solution, and the UV-vis absorption was monitored at 415 nm. After achieving a stable baseline, 10.0 µL of a 0.3% (w/w) H_2O_2 solution was added, and the mixture was left undisturbed for two minutes before recording the absorption at 415 nm again to construct a calibration curve. Subsequently, 5.0 µL of HRP-modified IONPs was introduced into the ABTS-H_2O_2 mixture, and the absorption at 415 nm was measured after two minutes. The difference in absorbance between HRP-modified and bare IONPs was used to estimate the surface coverage of HRP on the nanoparticles.

6.6.5. Nanoparticle-Assisted Immunoisolation

The sample and running buffer were introduced into the microfluidic channel at a controlled flow rate (ranging from 25 to 200 $\mu L \cdot min^{-1}$) using an automated syringe pump. A pair of opposing 150 N electromagnets (RS Components Ltd., UK) were mounted to the microfluidic system, connected to a programmable power supply capable of generating an alternating electromagnetic field with adjustable field strength.

To initiate the assay, a 100 µL aliquot of peptide-modified IONPs (10.0 $mg \cdot mL^{-1}$) was introduced into the microfluidic channel. Upon activation of the alternating electromagnetic field, DO-1 antibody samples were injected into the channel at a controlled flow rate of 100 $\mu L \cdot min^{-1}$. After a 10-minute immunoisolation process under optimised microfluidic conditions (*i.e.*, electromagnetic potential = 11.5 V; nanoparticle

oscillation frequency = 2.0 Hz), the resulting antibody-IONP complexes were eluted from the channel. These complexes were then manually transferred via pipette onto Con A-modified SPCEs for subsequent electrochemical analysis.

6.6.6. Electrochemical Enzyme-Amplified Assay

After a 10-minute incubation of the antibody-IONP immunocomplexes on Con A-modified SPCEs, followed by thorough washing with PBS, 100 µL of high-sensitivity TMB substrate was added and allowed to react for 5 minutes. SWV scans were then performed, with potential range from + 1.0 V to - 0.5 V (*vs.* Ag/AgCl), an amplitude of 20 mV, a potential step of 5 mV, and a frequency of 50 Hz.

Assay specificity was evaluated by comparing the SWV response to nonspecific proteins following immunoisolation, including 1.0 $mg \cdot mL^{-1}$ HSA, BSA, 1.0% human serum, and 10.0 $\mu g \cdot mL^{-1}$, all prepared in PBS buffer. Recovery assays were conducted using a similar procedure, with DO-1 antibodies spiked into 1.0 $mg \cdot mL^{-1}$ BSA or 1.0% human serum.

6.7 REFERENCES

(1) Baradoke, A.; Hein, R.; Li, X.; Davis, J. J. Reagentless redox capacitive assaying of C-reactive protein at a polyaniline interface. *Anal. Chem.* **2020**, *92* (5), 3508-3511.
(2) Bond, A. M.; Oldham, K. B.; Zoski, C. G. Steady-state voltammetry. *Anal. Chim. Acta* **1989**, *216*, 177-230.
(3) Compton, R. G.; Banks, C. E. *Understanding Voltammetry*; World Scientific, 2018.
(4) Bard, A. J.; Faulkner, L. R.; White, H. S. *Electrochemical Methods: Fundamentals and Applications*; John Wiley & Sons, 2022.
(5) Kye, J.; Hwang, S. In situ real time monitoring of kinetics of thiol adsorption on gold based on electrochemical steady-state current. *Electrochem. Commun.* **2011**, *13* (11), 1209-1212.
(6) Lingane, P. J.; Peters, D. G. Chronopotentiometry. *Crit. Rev. Anal. Chem.* **1971**, *1* (4), 587-634.
(7) Pungor, E.; Fehér, Z.; Váradi, M.; Campbell, B. H. Hydrodynamic voltammetry. **1980**.
(8) Nikolic, J.; Expósito, E.; Iniesta, J.; González-Garcia, J.; Montiel, V. Theoretical concepts and applications of a rotating disk electrode. *J. Chem. Educ.* **2000**, *77* (9), 1191.
(9) Bruckenstein, S.; Miller, B. Unraveling reactions with rotating electrodes. *Acc. Chem. Res.* **1977**, *10* (2), 54-61.
(10) Prats, H.; Chan, K. The determination of the HOR/HER reaction mechanism from experimental kinetic data. *Phys. Chem. Chem. Phys.* **2021**, *23* (48), 27150-27158.
(11) Faulkner, L. R. Understanding Electrochemistry: Some Distinctive Concepts. ACS Publications: 1983.
(12) Reinmuth, W. Chronopotentiometric potential-time curves and their interpretation. *Anal. Chem.* **1960**, *32* (11), 1514-1517.
(13) Lin, X.; Xu, Y. Facile synthesis and electrochemical capacitance of composites of polypyrrole/multi-walled carbon nanotubes. *Electrochim. Acta* **2008**, *53* (15), 4990-4997.
(14) Martinez, J.; Otero, T. Structural electrochemistry. Chronopotentiometric responses from rising compacted polypyrrole electrodes: experiments and model. *RSC Adv.* **2014**, *4* (55), 29139-29145.
(15) Laitinen, H.; Chambers, L. A Chronopotentiometric Study of Adsorption. *Anal. Chem.* **1964**, *36* (1), 5-11.
(16) Belgherbi, O.; Messaoudi, M.; Bezi, H.; Seid, L.; Chouder, D.; Lamiri, L.; Tounsi, A.; Akhtar, M. S.; Saeed, M. Incorporation of nickel particles into a polyaniline thin film for non-enzymatic glucose sensing in alkaline medium. *J. Appl. Electrochem.* **2024**, *54* (4), 851-863.
(17) Macdonald, D. *Transient Techniques in Electrochemistry*; Springer Science & Business Media, 2012.
(18) Hepel, T.; Osteryoung, J. Chronoamperometric transients at the stationary disk microelectrode. *J. Phys. Chem.* **1982**, *86* (8), 1406-1411.
(19) Yamada, A.; Kato, Y.; Yoshikuni, T.; Tanaka, Y.; Tanaka, N. Computer-assisted measurement of ion-diffusion coefficients by use of the cottrell equation. *Anal. Chim. Acta* **1979**, *112* (1), 55-63.
(20) Elgrishi, N.; Rountree, K. J.; McCarthy, B. D.; Rountree, E. S.; Eisenhart, T. T.; Dempsey, J. L. A practical beginner's guide to cyclic voltammetry. *J. Chem. Educ.* **2018**, *95* (2), 197-206.
(21) Matsuda, H.; Ayabe, Y. The theory of the cathode-ray polarography of Randles-Sevcik. *Z. Elektrochmie* **1955**, *59*, 494-503.

(22) Lim, H. S.; Barclay, D. J.; Anson, F. C. Formal potentials and cyclic voltammetry of some ruthenium-ammine complexes. *Inorg. Chem.* **1972**, *11* (7), 1460-1466.
(23) Asakawa, T.; Sunagawa, H.; Miyagishi, S. Diffusion coefficients of micelles composed of fluorocarbon surfactants with cyclic voltammetry. *Langmuir* **1998**, *14* (25), 7091-7094.
(24) Robinson, J. W.; Frame, E. M. S.; Frame II, G. M. *Instrumental Analytical Ehemistry: An Introduction*; CRC Press, 2021.
(25) Randles, J. E. A cathode ray polarograph. Part II.—The current-voltage curves. *Trans. Faraday Soc.* **1948**, *44*, 327-338.
(26) Bamford, C. H.; Tipper, C.; Compton, R. Electrode kinetics: Principles and methodology. **1986**.
(27) Li, D.; Lin, C.; Batchelor-McAuley, C.; Chen, L.; Compton, R. G. Tafel analysis in practice. *J. Electroanal. Chem.* **2018**, *826*, 117-124.
(28) Osteryoung, J. G.; Osteryoung, R. A. Square wave voltammetry. *Anal. Chem.* **1985**, *57* (1), 101-110.
(29) Ramaley, L.; Krause, M. S. Theory of square wave voltammetry. *Anal. Chem.* **1969**, *41* (11), 1362-1365.
(30) Garrote, B. L.; Santos, A.; Bueno, P. R. Label-free capacitive assaying of biomarkers for molecular diagnostics. *Nat. Protoc.* **2020**, *15* (12), 3879-3893.
(31) Qu, D.; Wang, G.; Kafle, J.; Harris, J.; Crain, L.; Jin, Z.; Zheng, D. Electrochemical impedance and its applications in energy‐storage systems. *Small Methods* **2018**, *2* (8), 1700342.
(32) Mansfeld, F. Use of electrochemical impedance spectroscopy for the study of corrosion protection by polymer coatings. *J. Appl. Electrochem.* **1995**, *25* (3), 187-202.
(33) Daniels, J. S.; Pourmand, N. Label‐free impedance biosensors: Opportunities and challenges. *Electroanalysis* **2007**, *19* (12), 1239-1257.
(34) Lasia, A. Electrochemical impedance spectroscopy and its applications. In *Modern Aspects of Electrochemistry*, Springer, 2002; pp 143-248.
(35) Wang, S.; Zhang, J.; Gharbi, O.; Vivier, V.; Gao, M.; Orazem, M. E. Electrochemical impedance spectroscopy. *Nat. Rev. Methods Primers* **2021**, *1* (1), 41.
(36) Waqas Hakim, M.; Fatima, S.; Rizwan, S.; Mahmood, A. Pseudo-capacitors: Introduction, Controlling Factors and Future. In *Nanostructured Materials for Supercapacitors*, Springer, 2022; pp 53-70.
(37) Bueno, P. R.; Mizzon, G.; Davis, J. J. Capacitance spectroscopy: a versatile approach to resolving the redox density of states and kinetics in redox-active self-assembled monolayers. *J. Phys. Chem. B* **2012**, *116* (30), 8822-8829.
(38) Huang, J. Zooming into the inner Helmholtz plane of Pt (111)-aqueous solution interfaces: chemisorbed water and partially charged ions. *JACS Au* **2023**, *3* (2), 550-564.
(39) Santos, A.; Carvalho, F. C.; Roque-Barreira, M.-C.; Bueno, P. R. Impedance-derived electrochemical capacitance spectroscopy for the evaluation of lectin-glycoprotein binding affinity. *Biosens. Bioelectron.* **2014**, *62*, 102-105.